

# The generation and characterisation of a physiologically relevant porcine model of inflammatory bowel disease

Thomas Winogrodzki

Vollständiger Abdruck der von der TUM School of Life Sciences der Technischen Universität München zur Erlangung des akademischen Grades eines

## Doktors der Naturwissenschaften

genehmigten Dissertation.

Vorsitz: Prof. Dr. Harald Luksch

Prüfer\*innen der Dissertation:

1. Prof. Angelika Schnieke, Ph. D.
2. Prof. Dr. Dirk Haller

Die Dissertation wurde am 19.04.2023 bei der Technischen Universität München eingereicht und durch die TUM School of Life Sciences am 02.08.2023 angenommen.

## Zusammenfassung

Morbus Crohn (MC) ist ein Subtyp chronisch-entzündlicher Darmerkrankungen (CED) mit steigender Inzidenz und Prävalenz. Neuartige Therapieansätze aus verfügbaren Tiermodellen zeigen oft eine geringe Übertragbarkeit auf Patienten. Auch existieren nur wenige Krankheitsmodelle, die eine vergleichbare Dünndarmopathie aufweisen. Schweine haben sich aufgrund ihrer Ähnlichkeiten zum Menschen als überaus geeignetes Krankheitsmodell herausgestellt. Dadurch sind sie ideal geeignet für das Testen experimenteller Ernährungsinterventionen und Technologien. Um die Übertragung von Erkenntnissen und Maßnahmen in die Klinik zu erleichtern, wurde im Rahmen dieser Dissertation ein physiologisch relevantes CED-Schweinmodell erstellt und charakterisiert. Zu diesem Zweck wurden befruchtete Eizellen aus dem Schwein mit CRISPR/Cas9-Vektoren mikroinjiziert, um eine 93-Basenpaar-Deletion des Adenosin-Uracil-reichen Elements (ARE) und des konstitutiven-Abbauelements (CDE) im 3' UTR-Bereich des *TNF*-Gens zu erreichen. Es wurde eine vergleichende Analyse physiologischer, molekularer, histologischer und immunologischer Merkmale zwischen Wildtyp-, *TNF<sup>ΔARE/+</sup>* und *TNF<sup>ΔARE/ΔARE</sup>*-Tieren durchgeführt. Die genetische Modifikation führte zu ulzerativer transmuraler Ileokolitis, einer erhöhten Abundanz proinflammatorischer Zytokine, der Einwanderung von Immunzellen ins Darmgewebe, sowie dysbiotischen mikrobiellen Gemeinschaften. Das Immunsystem der Mutantentiere war durch eine Zunahme der *TNF* Transkript-Halbwertszeit, die dadurch bedingte Anreicherung von *TNF*<sup>+</sup> Zellpopulationen, sowie durch eine Zunahme von Monozyten und eine Abnahme von Lymphozyten charakterisiert. Sequenzierungen der 16s rRNA Gene in Kot, sowie luminalen und Gewebeproben aus dem Darm haben zudem eine im Vergleich mit Kontrolltieren erhöhte Zahl CED-assoziiierter Bakterien gezeigt. Diese Befunde spiegeln den Pathophänotyp einer MC-ähnlichen Ileokolitis wider. Darüber hinaus wurden in *TNF<sup>ΔARE/+</sup>* Schweinen *Campylobacteria* mit der Intensität der Entzündung korreliert. Belege für die Existenz einer spezies-unabhängigen mikrobiellen Signatur basierend auf der Schwere der Erkrankung wurden durch PCoA-Clusterbildung von *TNF<sup>ΔARE/ΔARE</sup>* Schweineproben mit einigen Proben von *TNF<sup>ΔARE/+</sup>* Mäusen und CED-Patienten beobachtet.

Zusammengefasst ist es gelungen, ein physiologisch relevantes Großtiermodell mit einer dem menschlichen MC-ähnlichen Ileokolitis zu entwickeln. Das Schweinmodell spiegelt die wichtigsten Merkmale der menschlichen Krankheit wider. Aufgrund des Krankheitsverlaufs und der Pathophysiologie eignet sich das Modell für das Testen innovativer ernährungsbezogener und technologischer Interventionen.

## Abstract

Crohn's Disease (CD) is a subtype of inflammatory bowel diseases (IBD) with growing incidence and prevalence. Frequently used murine models for IBD often show poor translatability to patients and limited small intestinal pathology. Pigs have become a compelling translational disease model owing to their similarities in gastrointestinal physiology with humans, rendering them well-suited for the assessment of innovative nutritional and technological interventions. Thus, the aim of this dissertation was to establish and characterise a porcine IBD model. For this purpose, porcine fertilized oocytes were microinjected with a CRISPR/Cas9 targeting vector to achieve a 93 bp deletion of the adenosine-uracil-rich element (ARE) and the constitutive-decay element (CDE) in the 3' UTR of the *TNF* gene. The genetic modification led to ulcerative transmural ileocolitis, increased abundance of proinflammatory cytokines, immune cell infiltration into intestinal tissue, and dysbiotic microbial communities. The mutants' circulating immunity was characterised by an increase in *TNF* transcript half-life, an enrichment in  $TNF^+$  cell populations, an increase in monocytes and a decrease in lymphocytes. 16s rRNA gene amplicon sequencing revealed an enrichment of inflammation-associated gut bacteria in faecal, luminal and intestinal tissue samples derived from *TNF<sup>ΔARE</sup>* pigs. These findings resemble the human Crohn's disease-like ileocolitis pathophenotype. Noteworthy, *Campylobacteria* were associated with inflammation intensity in mutant pigs. A species-independent microbial signature based on disease severity was found by PCoA-clustering in a comparison of pigs with a subset of *TNF<sup>ΔARE/+</sup>* mice and human IBD patients. The clusters were characterised by a low bacterial diversity and the presence of disease-associated taxa. In summary, a pig model of Crohn's disease was generated and characterised. The pig model mirrors the major features of the human disease. The disease progression and pathophysiology make the model suitable for investigating innovative nutritional and technological interventions.

Zusammenfassung.....	1
Abstract .....	2
1. Introduction .....	8
1.1. Anatomy and function of the intestine .....	8
1.2. Microbe-host-interactions in health and disease .....	9
1.3. Inflammatory bowel disease – Complexity of a multihit disorder.....	12
1.4. The <i>TNF<sup>ΔARE/+</sup></i> mouse and other models of IBD .....	14
1.4.1. TNF as a central mediator of immunology and cell death control.....	14
1.4.2. Post-transcriptional control through AU-rich element-binding factors.....	17
1.5. Benefits of large animal models: Understanding their necessity.....	18
1.6. Porcine biotechnology .....	19
1.6.1. DNA repair mechanisms for double-strand breaks .....	20
1.6.2. Precision gene editing: Site-specific nucleases in Biotechnology.....	21
1.6.3. The generation of Genetically Modified Pigs.....	23
1.7. Aims of this thesis.....	25
2. Materials and methods.....	26
2.1. Materials .....	26
2.1.1. Laboratory equipment.....	26
2.1.2. Consumables.....	28
2.1.3. Chemicals.....	29
2.1.4. Enzymes and enzyme buffers .....	34
2.1.5. Antibodies.....	35
2.1.6. Kits.....	37
2.2. Cells.....	38
2.2.1. Prokaryotic cells .....	38
2.2.2. Eukaryotic cells.....	38
2.3. Nucleotides .....	39
2.3.1. Primers .....	39
2.3.2. gRNA oligonucleotides .....	41
2.3.3. Molecular cloning vectors and DNA constructs.....	41



2.4.	Software and Webtools.....	42
2.5.	Length and molecular weight standards.....	43
2.6.	Buffers and solutions .....	43
3.	Methods .....	47
3.1.	Reference gene annotations.....	47
3.2.	Plasmid construction.....	47
3.2.1.	Oligonucleotide annealing .....	47
3.2.2.	Restriction digest.....	47
3.2.3.	Ligation .....	47
3.2.4.	Electroporation of prokaryotes .....	48
3.2.5.	Polymerase chain reaction .....	48
3.2.6.	Colony PCR.....	49
3.2.7.	Agarose gel-electrophoresis.....	49
3.2.8.	PCR Amplicon sequencing.....	49
3.2.9.	Plasmid Midiprep and freezing of prokaryotic cells .....	50
3.2.10.	Measurement of DNA-concentration .....	50
3.3.	Eukaryotic cell culture.....	50
3.3.1.	Isolation of primary cells.....	50
3.3.2.	Thawing of eukaryotic cells .....	51
3.3.3.	Culture of porcine kidney fibroblasts .....	51
3.3.4.	Passaging of eukaryotic cells .....	51
3.3.5.	Lipofection of eukaryotic cells .....	52
3.3.6.	Selection of transfected cells.....	52
3.3.7.	Separation of single cell clones .....	52
3.3.8.	Upscaling of single cell clones .....	53
3.3.9.	DNA-Isolation from porcine kidney cells.....	53
3.3.10.	Assessment of gRNA targeting efficiencies in eukaryotic somatic cell culture .....	53
3.4.	<i>In vitro</i> embryo culture .....	53
3.4.1.	Collection of ovaries and <i>in vitro</i> -maturation of oocytes.....	53
3.4.2.	<i>In vitro</i> -fertilization .....	54

3.4.3.	Microinjection.....	54
3.4.4.	Assessment of plasmid genotoxicity and targeting efficiency in blastocysts .....	55
3.4.5.	Embryo Transfer.....	55
3.5.	Housing and animal husbandry .....	56
3.5.1.	Animal housing and termination criteria .....	56
3.5.2.	Gross phenotyping .....	56
3.6.	Sample isolation .....	57
3.6.1.	Sampling procedure .....	57
3.6.2.	Isolation of mammalian genomic DNA from ear clip biopsies.....	58
3.6.3.	PBMC isolation.....	58
3.6.4.	Isolation of RNA from macrophage and intestinal organoid culture.....	58
3.6.5.	Isolation of RNA from tissue biopsies.....	59
3.6.6.	Isolation of proteins from tissue biopsies .....	59
3.6.7.	Isolation of proteins from feces .....	59
3.7.	Macrophage culture and LPS challenge.....	59
3.8.	Transcript analyses.....	60
3.8.1.	cDNA synthesis .....	60
3.8.2.	Real-time quantitative polymerase chain reaction .....	60
3.8.3.	Determination of housekeeping genes.....	60
3.8.4.	Prediction of RNA structures .....	61
3.9.	Protein analyses .....	61
3.9.1.	Measurement of protein concentrations .....	61
3.9.2.	Determination of protein abundance via Western Blot.....	61
3.9.3.	Determination of protein abundance via ELISA .....	61
3.10.	Guaiac resin-based faecal occult blood test.....	62
3.11.	Immunohistochemistry and Pas/AB-staining.....	62
3.12.	Microbiomics.....	63
3.12.1.	High-throughput sequencing of 16s rRNA gene amplicons .....	63
3.12.2.	16s rRNA amplicon processing .....	63
3.12.3.	16s rRNA amplicon sequence analyses.....	64

3.12.4.	Absolute quantitation of SFBs in samples.....	64
3.13.	Flow cytometry.....	65
3.14.	Statistical analysis .....	65
4.	Results .....	66
4.1.	gRNA design and vector cloning .....	66
4.1.1.	Annotation and identification of protein isoforms of the porcine <i>IL10</i> gene .....	66
4.1.2.	gRNA candidate selection .....	68
4.1.3.	Generation and preliminary testing of CRISPR/Cas9 targeting vectors .....	69
4.2.	<i>In vitro</i> analysis of vector genotoxicity and gene editing efficiency .....	71
4.2.1.	<i>IL10</i> knockout .....	71
4.2.2.	<i>TNF ARE/CDE1</i> deletion .....	71
4.3.	Generation of <i>TNF<sup>ΔARE</sup></i> pigs .....	73
4.4.	Genetic analyses and establishment of the pig line .....	74
4.4.1.	Genotyping .....	74
4.4.2.	Comparative structural analysis of transcripts .....	74
4.4.3.	Analysis of off-target and random integration events.....	75
4.4.4.	SNP identification in the <i>TNF</i> gene .....	76
4.4.5.	Breeding strategy of <i>TNF<sup>ΔARE</sup></i> pigs .....	77
4.4.6.	Influence of sex on genotype and phenotype .....	78
4.5.	Phenotypic characterization of the <i>TNF<sup>ΔARE</sup></i> pig model .....	79
4.5.1.	Phenotyping.....	79
4.5.2.	Microscopic findings .....	85
4.5.3.	Complete blood count and qualitative pathobiont analysis .....	89
4.6.	Molecular analyses .....	90
4.6.1.	Selection of housekeeping genes for RT-qPCR .....	90
4.6.2.	<i>TNF</i> transcript half-life assessment in macrophages .....	91
4.6.3.	Transcript and protein quantification in biopsy samples .....	93
4.7.	Flow cytometric analysis of peripheral immune cells .....	95
4.8.	Analysis of the gut microbial composition.....	103
4.8.1.	Testing for sample contaminations.....	104

4.8.2.	Defining a wild-type reference microbial signature .....	105
4.8.3.	Assessment of genotype-associated shifts in microbial communities .....	113
4.8.4.	Exploring the temporal relationship between gut microbiota and inflammation .....	123
4.8.4.1.	Comparison of faecal consistency and markers of intestinal inflammation across genotypes.....	123
4.8.4.2.	Assessing inflammation-associated bacterial profile changes in <i>TNF<sup>ΔARE/+</sup></i> pigs.....	123
4.8.4.3.	Temporal relationship between gut microbiota changes and inflammation in <i>TNF<sup>ΔARE/+</sup></i> pigs.....	124
4.8.5.	Identification of bacterial taxa associated with severely inflamed <i>TNF<sup>ΔARE/+</sup></i> swine ..	125
4.8.6.	Cross-species comparison of bacterial profiles.....	128
5.	Discussion.....	140
5.1.	<i>TNF<sup>ΔARE</sup></i> pigs develop a CD-like ileocolitis pathophenotype that is associated with impaired barrier integrity and hyperresponsive immunity .....	140
5.2.	Intestinal inflammation is linked to human IBD-like alterations in the gut microbiome, but occurs earlier in development.....	141
5.3.	<i>TNF<sup>ΔARE</sup></i> pigs and mice differ in transcript regulation, biogeography of manifestations and pathophenotype-associated differentially abundant taxa .....	142
5.4.	Microbial similarities in highly inflamed individuals indicate the presence of a species-independent microbial signature of inflammation .....	143
5.5.	Ease of sampling vs. accuracy: stool-based analyses are a less invasive but only provide weak reflection of intestinal inflammatory hotspots .....	144
5.6.	Rodents to Pigs to People: Optimizing Pre-Clinical Testing.....	145
	Supplementary .....	147
	Abbreviations .....	176
	List of figures .....	181
	List of tables .....	194
	References .....	195
	Acknowledgement.....	215
	Curriculum Vitae.....	216

# 1. Introduction

## 1.1. Anatomy and function of the intestine

The gut plays a crucial role in the breakdown and absorption of nutrients and the immunological and physical separation of the human organism from environmental factors. Additionally, it facilitates communication between the host and the intestinal microbiota. Starting from the pylorus, the gut is divided by the valva ileocaecalis into the small and large intestine, with the former comprising the duodenum, jejunum, and ileum, and the latter consisting of the caecum, colon, and rectum. The intestinal tract is composed of four tissue layers, including the mucosa, submucosa, muscularis propria, and serosa<sup>1</sup>. Each region of the intestine has unique anatomical and physiological characteristics<sup>2</sup>, with villous structures present in the small intestine for surface enhancement and nutrient absorption<sup>3</sup>, and absent in the flat mucosa of the large intestine, which primarily regulates water and electrolyte transport. Stem cell niches known as Lieberkühn-crypts are found throughout the intestine, containing specialized cells for mucus secretion and antimicrobial peptide production<sup>3</sup>. Within these crypts, intestinal leucine-rich repeat-containing G-protein coupled receptor 5<sup>+</sup> (LGR5<sup>+</sup>) stem cells, Paneth cells, +4 reserve stem cells, mucus-secreting goblet cells and transit-amplifying cells are residing. Originating from these crypts, the single-layered mucosal gut epithelial cell layer is formed, which is constantly renewed every 3-4 days ensuring maintenance of the epithelial barrier despite intense contact with antigens and noxious agents at the luminal side<sup>4</sup>. It consists of differentiated and polarized, highly specialized absorptive enterocytes, goblet cells, Tuft cells, microfold cells (M-cells) and enteroendocrine cells, which are interconnected via tight junctions and adherens junction proteins<sup>5</sup>. On the apical side, this gut epithelial cell barrier is covered with an immunoglobulin A (IgA)-rich mucus layer that aids the transport of luminal content and acts as a primary barrier between gut microbiota and host cells<sup>6</sup>. Within the small intestine, this layer consists of a dense mucus layer, while in the large intestine additionally a loose outer layer is found<sup>7</sup>. On the basolateral side, the epithelial lining is connected to the lamina propria via the basal membrane. Within the lamina propria, between the epithelial cells and in organized gut-associated lymphatic tissues (GALT) such as lymph follicles, as well as in the ileal Peyer's Patches (PPs) a variety of immune cells is found, adding a further layer to the intestinal barrier integrity<sup>5</sup> (Figure 1).

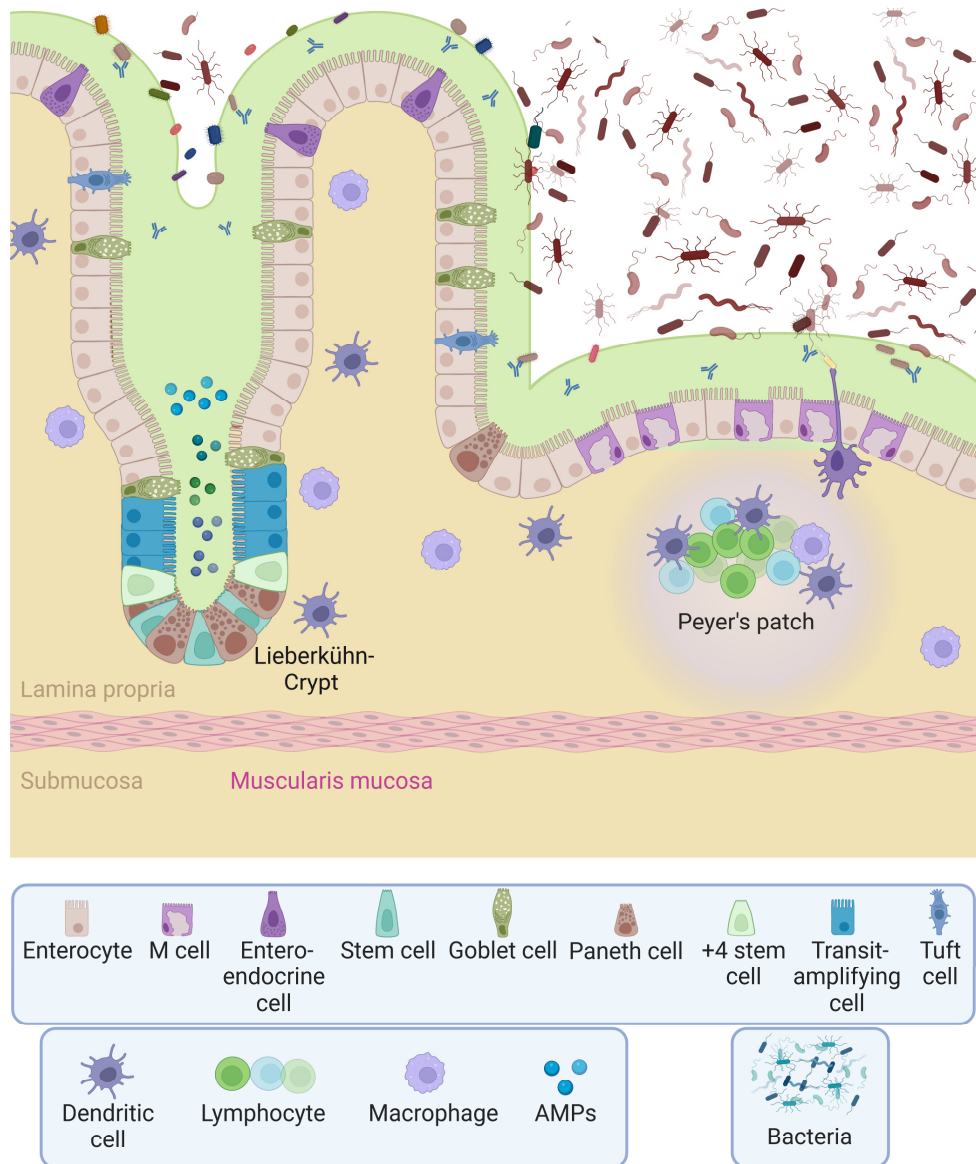


Figure 1: Schematic presentation of the small intestinal crypts. The intestinal microbiota and the goblet cell-derived and immunoglobulin A-rich mucus layer are separated by the single epithelial layer from the lamina propria harbouring the gut-associated lymphatic tissue (e.g. Peyer's patches) that senses the gut microbiota directly or indirectly through M-cell-mediated or -independent mechanisms. Lieberkühn-crypts are found throughout the gut and harbour a variety of stem cells, stem cell niche-supporting and antimicrobial peptide- (AMP) secreting cells. Adapted from "Small Intestine Villus Background (Layout)" by BioRender (2023).

## 1.2. Microbe-host-interactions in health and disease

Microorganisms have successfully colonized virtually every habitat on earth, regardless of present conditions. Evolutionary adaptations have enabled prokaryotic growth at the edge of survivability, including extreme temperature and pressure, various pH ranges, and the presence of organic solvents or radiation<sup>8</sup>. It is therefore not surprising that microorganisms have also adapted to coexist with their respective mammalian hosts through co-evolution<sup>9</sup>. It is estimated that humans consist of approximately  $3 \times 10^{13}$  endogenous cells ( $0.3 \times 10^{13}$  nucleated cells) and are home to roughly  $4 \times 10^{13}$  microbiota, 99% of which are found in the gut<sup>10</sup>. Mutualistic gut-resident bacteria are essential in the breakdown of

otherwise indigestible nutrients, the displacement of pathogenic microorganisms, and the maturation of a healthy immune system<sup>11</sup>. As environmental conditions vary considerably between distinctive gut sections, with differences in luminal content transit times, oxygen availability, water content and pH value, the composition and richness of the microbiota differ accordingly<sup>10,12</sup> (Figure 2).

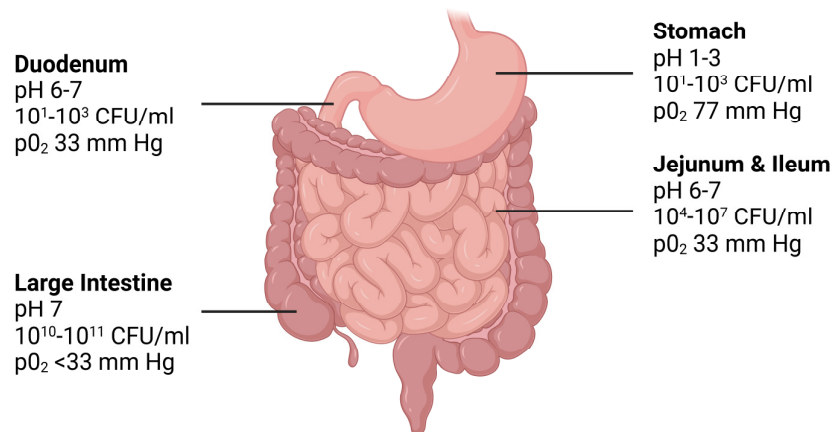


Figure 2: Differential chemical properties along the gastrointestinal tract favour the growth of specialized bacteria. The pH value and the amount of colony forming units (CFU) per mL increases from stomach to colon, while the oxygen partial pressure (pO<sub>2</sub>) is decreasing from stomach to colon. Adapted from Clarke et al., 2019<sup>13</sup>.

Multiple investigations of the human core gut microbiota using 16s rRNA gene amplicon sequencing and shotgun metagenomics approaches revealed that a human individual typically harbours at least 160 different bacterial species, of which >95 % are members of the phyla *Firmicutes*, *Bacteroidetes*, *Actinobacteria*, and *Proteobacteria*<sup>14,15</sup>. While the composition of the gut microbiota varies inter-individually from a pool of more than 1000 possible species, the diversity of microbial gene categories, known as the microbiome, is largely homogeneous, providing evidence for a shared functionality<sup>15</sup>. These functions are primarily attributed to energy, cell growth, and reproductive metabolism<sup>15</sup>, with each bacterial species having different requirements for physico-chemical environmental conditions and nutrients<sup>8</sup>. Breakdown of primary nutrients by specific members of the microbial community enables mutual cross-feeding<sup>16</sup>, giving the notion of individual microbial cells merging into a functional collective organ. These consumed and secreted metabolites permit microbe-microbe, as well as microbe-host-interactions, in a complexity that is currently far from understood<sup>16</sup>. A well-studied example of the mutualistic cross-species interplay is the production of short-chain fatty acids (SCFAs) acetate, butyrate, and propionate (and other<sup>17</sup>) by gut bacteria. Following fibre ingestion by the host, members of the gut microbiota depolymerize indigestible complex carbohydrates into monosaccharides, lactate and acetate, which other members then ferment to SCFAs, enabling absorption by colonic epithelial cells<sup>18,19</sup>. Upon absorption, SCFAs were found to influence (epi-)genetical regulation, thereby playing an important role in apoptosis, immunological and neuroendocrine signalling and thus the host's health<sup>20</sup>. For example, butyrate is known to limit oxygen diffusion into the gut lumen by activating colonocyte mitochondrial  $\beta$ -oxidation and the nuclear receptor peroxisome proliferator-activated

receptor gamma (PPAR $\gamma$ ), as well as repressing gene expression of the inducible nitric oxid synthase (iNOS). This not only regulates colonocyte health, but also directly influences oxygen and nitrate levels at the luminal side and thus selection of gut microbes attached to the epithelium<sup>19</sup>. Furthermore, SCFA-mediated induction of retinoic acid synthesis by intestinal epithelial cells indirectly regulates the composition of the gut microbiota by affecting host immunity<sup>21</sup>. The host immune system is in close contact with the gut microbiota especially via pattern recognition receptors (PRRs) that signal a defense response upon specific antigen encounter. PRRs are expressed on a variety of somatic and immune cells, such as enterocytes, macrophages, baso-, neutro- and eosinophils, and dendritic cells<sup>19</sup>. The latter are known to sample bacterial cells in an M-cell-dependent and –independent manner and also cross-present viral antigen captured from infected epithelial cells<sup>22</sup>. In a healthy steady-state, intestinal resident and lymphatic conventional DCs (cDCs) are inducing the differentiation of naïve T cells towards a gut-homing regulatory T cell (T<sub>reg</sub>) phenotype via p38 MAPK-, interleukin (IL)10-, transforming growth factor-beta (TGF $\beta$ )- and retinoic acid-signalling<sup>23,24</sup>. T<sub>regs</sub> in turn regulate quantity and quality of B-cell derived IgA that are secreted into the epithelial mucus layer, resulting in a selective immunotolerance of commensal microbiota<sup>25,26</sup>.

The interactions between microbes and their host are tightly regulated and various disturbances can cause sensitive damage to intestinal homeostasis. The change in oxygen availability on the apical side of the intestinal epithelium is of particular importance here. Butyrate producers, mainly belonging to the phylum *Firmicutes* such as *Coprococcus* or *Faecalibacterium*, are primarily strictly anaerobic bacteria, which are displaced by facultatively anaerobic microbes such as *Proteobacteria* when the local oxygen concentration increases<sup>27,28</sup>. This may lead to a decrease in mitochondrial  $\beta$ -oxidation in enterocytes due to the lack of butyrate levels, which in turn further drives up the luminal oxygen concentration due to low O<sub>2</sub> consumption<sup>29</sup>. The decrease in butyrate producers is frequently caused by antibiotic use, competing pathogenic microorganisms, imbalanced inflammatory responses, or defective host metabolism. For example, an excessive or chronic inflammatory response of the intestinal mucosa may carry a potential for dysbiosis. Inflammation-associated increased gene activity of inducible nitric oxid synthase (*iNOS*) gene in infiltrating immune cells may lead to a local increase in nitrate, which in turn favours nitrate consumers such as the facultative anaerobic *Escherichia coli*<sup>30</sup>. Also, the increased presence of undifferentiated colonocytes due to repeated intestinal tissue damage and repair mechanisms outside the Lieberkühn crypts is microbiota-modulating, as they have normoxic levels at their surface in contrast to hypoxic differentiated cells<sup>31</sup>.

Furthermore, a breakdown of intestinal barrier integrity can affect the intestinal homeostasis. Sensing of pathogen-associated microbial patterns (PAMPs) together with IgA-immune complexes within the lamina propria via dendrite PRRs, such as Toll-like receptor (TLR), NOD-like receptor (NLR), or C-type lectin receptor (CLR)<sup>32,33</sup>, can directly affect the development of myeloid cells in the bone marrow<sup>34</sup> or lead to inflammation-associated infiltration of DC-like monocyte-derived pro-inflammatory cells<sup>35</sup>. This results in a higher secretion of the pro-inflammatory cytokines IL12-23p40 and IL6 that exceeds the unaltered levels of anti-inflammatory IL10, resulting in a shift from a T<sub>reg</sub>-driven environment to a pro-inflammatory effector response mediated by T helper cells 17 (T<sub>H</sub>17) and 1 (T<sub>H</sub>1)<sup>24</sup>. Overly active PRRs



or the inability to downregulate an inflammatory response can ultimately increase the risk of chronic inflammatory diseases and autoimmune disorders<sup>19</sup>.

### 1.3. Inflammatory bowel disease – Complexity of a multihit disorder

Emphasizing the importance of the gut microbiota in health and disease, compositional changes have been associated with various intestinal and other diseases. One of the best-studied examples is inflammatory bowel disease (IBD), with its two main subtypes Crohn's disease (CD) and ulcerative colitis (UC), which is an as yet incurable burden, with incidence and prevalence increasing worldwide<sup>36</sup>. Crohn's Disease (CD) is characterised by transmural inflammation that can affect any part of the gastrointestinal tract and associated with various complications, such as granuloma formation, abscesses, fistulas, and strictures<sup>37</sup>. The terminal ileum and the proximal colon are the most commonly but not exclusively affected areas of the gastrointestinal tract, often in a non-continuous ("skip lesions") pattern<sup>37</sup>. In contrast, UC is distinguished by superficial mucosal inflammation that is limited to parts of or the whole colon (pancolitis) in a continuous pattern<sup>37</sup>. IBD patients frequently suffer from abdominal pain, bloody diarrhea, and weight loss as a result of chronic recurrent episodes of intestinal tissue inflammation, resulting in low quality of life. The high prevalence in certain groups, particularly but not exclusively in economically developed Western societies<sup>38</sup>, indicates environmental, cultural and genetic components in the disease aetiology. To date, genome-wide association studies (GWAS) have identified over 230 single nucleotide polymorphisms (SNPs) that are associated with IBD<sup>39</sup>. These SNPs are known to affect various pathways responsible for the regulation of innate or adaptive immunity, such as mutations in the *XIAP* or *NOD2* genes, as well as autophagy and microbial defense, such as mutations in *ATG16L1*. Additionally, these genetic malfunctions impact biological processes that affect barrier function, epithelial restitution, reactive oxygen species generation, and endoplasmic or mitochondrial stress pathways<sup>40,41</sup>. The altered processes influence microbiota-host interactions to favour a less diverse and dysbiotic gut microbiota, which is considered a key mechanism for IBD development and progression<sup>41-44</sup>. Environmental changes such as diet, medication, or lifestyle have been proposed as an alternative route of providing initial triggers of pro-inflammatory processes that modify the gut microbiota, and in turn potentially favour dysregulated host responses, giving rise to the notion of a multi-hit model for IBD aetiology<sup>45-47</sup> (Figure 3).

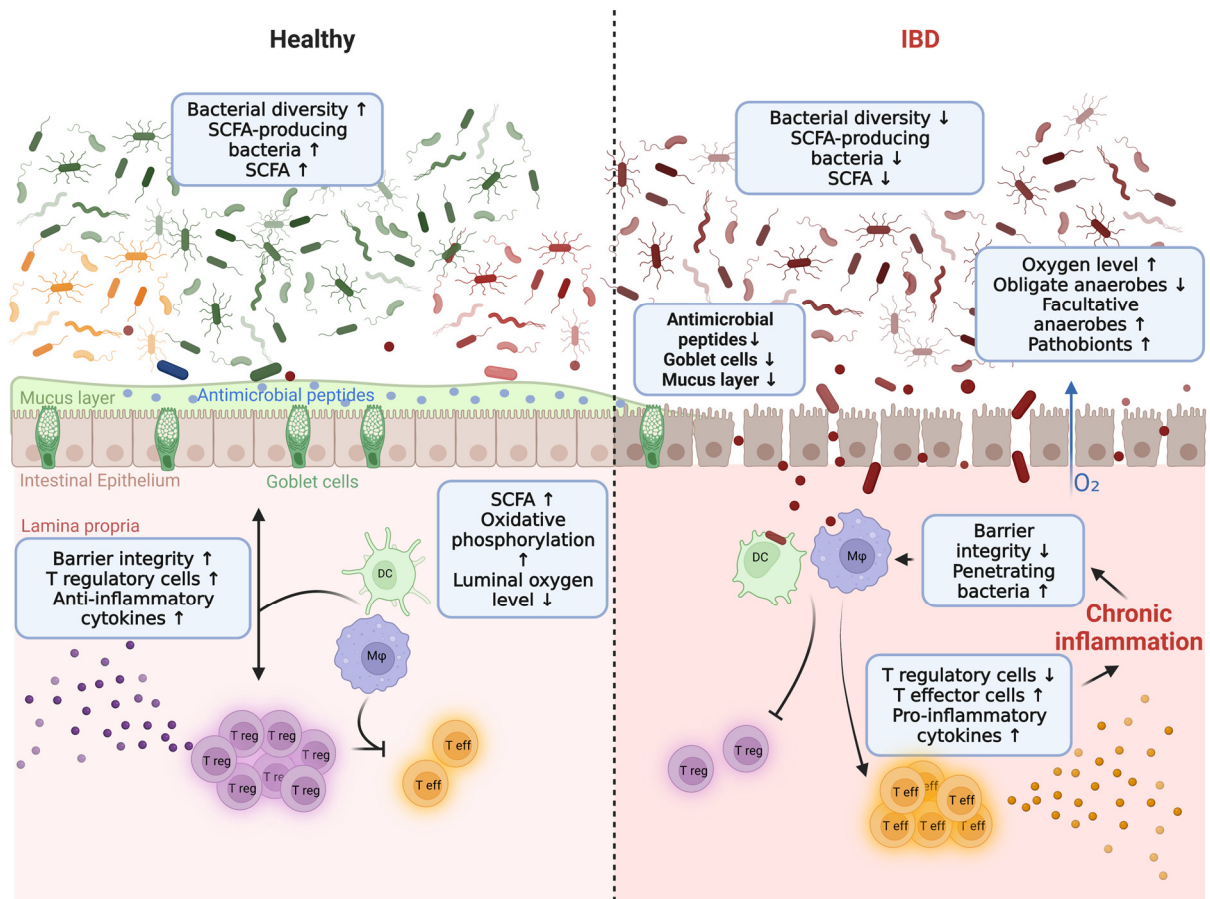


Figure 3: Microbe-Host-Interactions in health and inflammatory bowel disease. In a healthy state, a diverse bacterial population that includes short chain-fatty acids (SCFA)-producing bacteria helps to maintain homeostasis between pro- and anti-inflammatory host responses. This balance is mediated by members of both the innate (such as dendritic cells (DCs) or macrophages (Mφs)) and adaptive immunity (such as T regulatory ( $T_{reg}$ ) or T effector cells ( $T_{eff}$ )), which in turn support the growth of these microorganisms. On the other hand, a dysbiotic state - which may be a cause or consequence of IBD - is characterised by a reduction in bacterial diversity and loss of often obligate facultative SCFA-producers. Dysbiosis fuels chronic pro-inflammatory processes that ultimately lead to impaired barrier integrity and dysfunctional intestinal tissue function. Adapted from "Compare and Contrast Layout - Healthy and Inflamed Epithelium" by BioRender (2023).

Human IBD is characterised by a reduction in intestinal gut biodiversity, which leads to a concomitant loss of essential functions required for maintaining intestinal barrier integrity and regulating host immunity<sup>48</sup>. Additionally, increased numbers of facultative anaerobes at the expense of obligate anaerobes are frequently observed, namely, decreased abundance of *Bacteroides*, *Firmicutes*, *Clostridia*, *Lactobacillus*, *Ruminococcaceae*, and an increase of *Gammaproteobacteria* and *Enterobacteriaceae*<sup>11,49</sup>. In particular, SCFA-producers such as *Faecalibacterium prausnitzii* were decreased in IBD patients while sulfate-reducing bacteria that mediate intestinal barrier damage and mucosal inflammation such as *Desulfovibrio* were increased<sup>40</sup> (Figure 3). However, the search for disease-modulating taxa is still in its infancy. So far, only a limited number of individual microorganisms have been associated with disease severity in mouse models of IBD. One such example is the group of segmented filamentous bacteria (SFB) (*Candidatus Arthromitus*), that adhere closely to the absorbing epithelial cells in the ileum and the cells overlying the Peyer's patches. This colonization normally does not lead to pathology but protects the host from pathogens by upregulating host innate

defence genes, inducing a strong and broad IgA response and stimulating the T cell compartment<sup>50</sup>. In mouse models of ileal inflammation, mono-colonization with SFBs was found to initiate gut immune responses and disease, while ileitis in germ-free (GF) mice was completely absent<sup>42</sup>. However, the causal role of SFBs in human pathology is still highly debated<sup>51</sup>. Studies on faecal microbiota transplantation (FMT) in GF disease models have shown that clinical symptoms of certain diseases can be reversed under GF conditions<sup>42,48,52,53</sup>, thereby providing compelling evidence for a functional role of the microbiota in shaping host-intestinal diseases.

#### 1.4. The *TNF*<sup>ΔARE/+</sup> mouse and other models of IBD

The widespread use of rodent models of IBD in preclinical research has greatly contributed to the understanding of the underlying molecular mechanisms, identification of new therapeutics, and characterization of specific metabolic and microbial signatures<sup>54</sup>. These models include mice that are chemically induced, spontaneous, and genetically modified (GM), such as those treated with oxazolone, 2,4,6-trinitrobenzene sulfonic acid (TNBS), or dextran sulfate sodium (DSS), as well as *IL10*<sup>-/-</sup>, *CASP8*<sup>IECKO</sup>, *XBP1*<sup>IECKO</sup>, *XIAP*<sup>-/-</sup> mutant, and CD4<sup>+</sup> T cell transfer mice<sup>54-57</sup>. So far, research has mainly focused on mouse models with colitis, as a large number of inducible and spontaneous colitis models are available and there are only a few models for ileitis. It is important to note that findings from these models cannot be generalized to all IBD subtypes, as there are topological and molecular variations between UC and CD. This highlights the necessity for further development of models specific to Crohn's Disease<sup>54</sup>. One of the best studied currently available disease models of CD-like ileitis is the *TNF*<sup>ΔARE</sup> mouse, which was genetically modified to overexpress *TNF-alpha* (*TNF*) by deleting the transcript-destabilizing type II Adenosine-Uracil-rich element (ARE) within its 3' untranslated region (UTR)<sup>58</sup>.

##### 1.4.1. TNF as a central mediator of immunology and cell death control

*TNF*, is present in two forms: the 26 kDa type II transmembrane (tmTNF) and the 17 kDa soluble (sTNF) protein<sup>59,60</sup>. The expression of *TNF* is upregulated through LPS and other microbial antigens, enterotoxins, and cytokines, including TNF itself<sup>61</sup>. It is a central mediator in the immunologic processes of infection control, autoimmunity, allergic disease, and anti-neoplastic activity<sup>62</sup>. In the gut, TNF induces the production of chemokines that recruit proinflammatory myeloid cells to the intestinal mucosa<sup>63</sup> and controls tissue barrier functions by regulating apoptosis of intestinal epithelial cells (IECs), expression of tight junction proteins and mucus secretion<sup>64-66</sup>. TNF exhibits these pleiotropic functions mainly via interacting with its two functionally diverging main receptors TNFRI and TNFRII<sup>62</sup>.

TNFRI is a death domain receptor (DD-receptor) that is near to ubiquitously expressed and is activated through binding of mTNF or sTNF<sup>67</sup>. Upon ligand recognition, TNFRI-trimerization occurs which allows to recruit the TNFR1-associated DD (TRADD)<sup>68</sup>. In turn, this leads to the assembly of the TNFRI-signalling complex consisting of TNFR-associated factor (TRAF) 2 or 5, receptor-interacting serine/threonine-protein kinase 1 (RIPK1), and cellular inhibitor of apoptosis protein (cIAP) 1 and 2<sup>69,70</sup>.

This signalling complex is able to induce either NFκB-, JUN NH<sub>2</sub>-terminal kinase (JNK)- and p38-mediated pro-inflammatory pathways via the formation of complex I<sup>71</sup>, Caspase 8-mediated apoptosis via the formation of complex IIa or IIb<sup>72</sup>, or RIPK1/3-mediated necroptosis via complex IIc, depending on the ubiquitination status of RIPK1 and the availability of de-ubiquitinases and caspases. Complex I-formation is depending on sufficient ubiquitination of RIPK1<sup>71</sup>, while ubiquitin chain-disruption results in the formation of complex IIa, IIb or IIc<sup>73,74</sup>. The formation of complex I results in canonical NFκB activation that leads to the NFκB essential modulator (NEMO)-dependent activation of the inhibitor of κB kinase (Iκκ)-complex, which enables the translocation of the RelA/p52 heterodimer to the nucleus and the activation of multiple transcription factors for pro-inflammatory and survival downstream signalling<sup>62</sup>. Whether complex IIa or IIb is formed depends on which de-ubiquitinase processes RIPK1. However, both complexes lead to the activation of caspase 8, which in turn degrades RIPK1 and RIPK3, initiating cell apoptosis<sup>67</sup>. The absence or reduced availability of caspase 8 or of the Fas-associated DD (FADD), e.g. due to high concentrations of the large form of FLICE-like inhibitory protein (cFLIP<sub>L</sub>) or its short form cFLIP<sub>S</sub>, lead to insufficient RIPK1 and RIPK3 degradation and a phenotypically distinct mixed lineage kinase domain-like (MLKL)-dependent cell death, which is known as necroptosis<sup>74</sup>. Of note, necroptosis was shown to be inducible via the presence of viral cFLIP<sub>S</sub>-mimetics<sup>75</sup> or via TLR-3 and -4 signalling<sup>76</sup>, interconnecting the faith of cells with the microbiome. In apoptosis, cells disintegrate into apoptotic bodies that are removed by resident phagocytic cells, and surrounding cells are not "alerted" but instead produce signals that prevent inflammation. In contrast, in necroptosis, cells die by rupture of the plasma membrane, and cell contents, including damage-associated molecular patterns (DAMPs), pro-inflammatory cytokines, and other alarmins, are released into the microenvironment, and surrounding cells respond pro-inflammatorily (Figure 4). Thus, apoptosis is generally anti-inflammatory, whereas necroptosis locally exacerbates inflammation<sup>62</sup>. At first glance, it may seem paradoxical that microorganisms would trigger a robust immune response in their environment, effectively priming their own demise. However, this phenomenon may represent an evolutionary arms race between eukaryotic hosts and prokaryotic pathogens. There is an ongoing debate if necroptosis serves as a mechanism to rapidly shut down the potentially harmful effects of robust TLR-mediated immune responses, which could otherwise result in long-term inflammation and cytokine release<sup>77</sup>. This delicate balance between immune activation and regulation may be beneficial for both the microorganism community and the host, as it can help prevent life-threatening cytokine storms in certain situations.

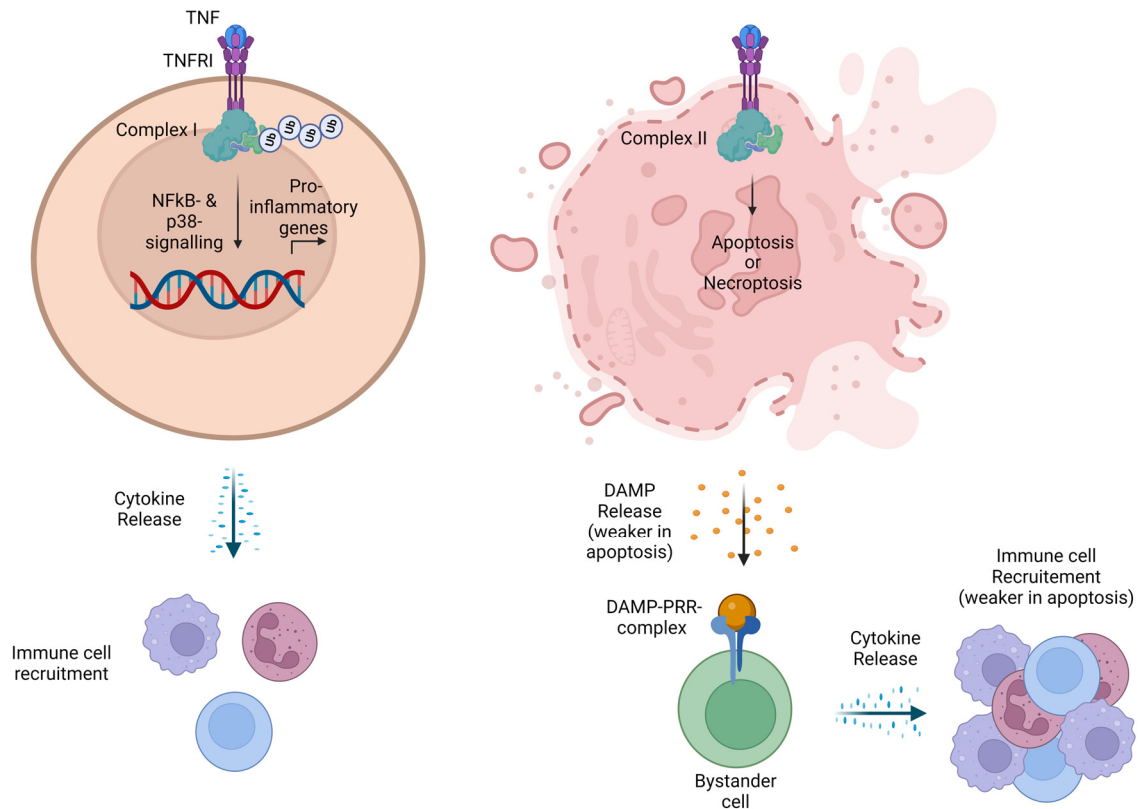


Figure 4: TNF-mediated pleiotropic function in cell proliferation, cell death and the recruitment of immune cells. (Left) TNF receptor I (TNFR1) binding directly enhances inflammation by activating pro-inflammatory signalling pathways NFκB and p38, which result in the transcriptional upregulation of genes encoding proinflammatory mediators such as cytokines and chemokines. (Right) TNFR1 activation also indirectly causes inflammation by inducing cell death. Damage-associated molecular patterns (DAMPs) are released by lytic forms of cell death such as apoptosis, necroptosis (or pyroptosis), which stimulate proinflammatory gene expression in bystander cells. Pattern recognition receptor, PRR. Adapted from van Loo et al., 2022<sup>78</sup>.

TNFR2 in turn is primarily expressed by endothelial cells, fibroblasts, and certain T- and B-lymphocytes<sup>79</sup>. The receptor is mainly but not exclusively activated by binding through tmTNF<sup>80</sup>. Upon binding of its ligand, TNFR2 trimerization occurs, which enables the recruitment of TRAF1/2 and cIAP1/2 or TRAF3. This leads to the disruption of a NFκB-inducing kinase (NIK)-inhibiting complex, thereby allowing NIK to recruit components of the IκB-complex, which finally results in nuclear translocation of the NFκB RelB/p52 heterodimer<sup>81</sup>. Thus, TNFR2-signalling activates NFκB-signalling in a non-canonical way, thereby promoting proliferative and survival signalling. It was further shown that the expression of RelB and the precursor of p52, p100, is induced by TNFR1-signalling, while TNFR2-activity promotes the formation of complexes IIa, IIb and IIc in a receptor-ratio-dependent manner<sup>62</sup>, providing evidence for cell-death activity of this receptor pathway. Interestingly, several studies examining the differential roles of TNFR1 and TNFR2 in microbial infections have shown that the latter contributes to protective immune responses but, unlike TNFR1, is not essential for clearing infections<sup>82,83</sup>. In addition, while most described TNF-mediated pro-inflammatory functions are predominantly mediated via TNFR1, TNFR2-mediated non-canonical NFκB-activity was found to be

particularly enhanced in the suppressive arms of the adaptive immunity<sup>80</sup>, providing a hint for the pleiotropic functionality of *TNF* in the fine-tuning of immune responses.

#### 1.4.2. Post-transcriptional control through AU-rich element-binding factors

In *TNF<sup>ΔARE</sup>* mice, the deletion of the ARE in the 3'UTR of *TNF* leads to overexpression of TNF protein (Figure 5).

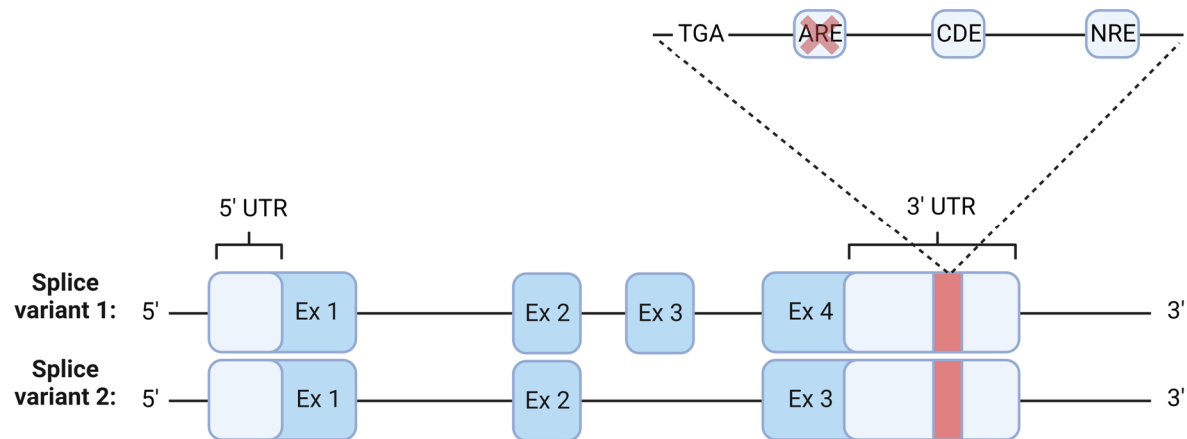


Figure 5: Schematic view of the two splice variants of the murine *Tnf* gene. Dark blue boxes represent exons, light blue boxes mark 5' and 3' untranslated regions (UTRs). The red marking highlights the deletion of the ARE sequence. The extension shows the stop codon (TGA), as well as the AU-rich element (ARE), constitutive decay element (CDE), and the new regulatory element (NRE). The deletion of the ARE sequence is indicated by a red cross. Black lines between the exons represent introns.

AREs are known to play a critical role in regulating mRNA stability and translation<sup>84</sup>. The AREs are recognized by specific RNA-binding proteins (RBPs), such as T-cell intracellular antigen-1 (TIA-1), -related protein (TIAR), AU-rich element binding protein 1 (AUF1), members of the human antigen (Hu)-family, and tristetraprolin (TTP), which influence *TNF* expression post-transcriptionally. These motifs are categorized into three types based on the quantity and distribution of AUUUA pentamers: Class I AREs are distinguished by the presence of one to three pentamers scattered throughout a considerable portion of the 3' UTR of transcripts, as well as surrounding U-rich areas. Class II AREs, to which the *TNF*-ARE belongs, have at least two overlapping copies of the nonamer UUAUUU(U/A)(U/A)U and are located in a U-rich area. Class III AREs lack pentamers but contain U-rich regions<sup>85</sup>. Of note, it has been shown that class II AREs are dominant instability determinants of transcripts, and thus often are found within the 3' UTR of highly regulated molecules such as cytokines, whereas class I AREs do not necessarily induce mRNA instability and can even be bound by mRNA stabilizers<sup>86</sup>. Binding of these motifs by RBPs is mostly independent of inflammatory stimuli and involve all ARE classes. Members of the TTP family, which includes ZFP36L1 and ZFP36L2, preferentially bind type II AREs upon stimulation with LPS and act as transcript destabilizers<sup>85,87</sup>. The destabilizing activity of TTP is largely dependent on NFκB and p38-induced pathways and even regulate the nuclear translocation of NFκB, providing

direct and indirect feedback loops for pro-inflammatory stimuli<sup>88,89</sup>. During a non-inflammatory state, translation of spliced *TNF* mRNA appears to be repressed in most cell types via an ARE-dependent mechanism<sup>90</sup>. TTP was shown to co-localize with poly-A-mRNAs, including the type II ARE-containing mRNAs, in discrete cytoplasmic loci known as stress granules (SGs)<sup>91</sup>. In SGs, TTP binds to its targets, leading to deadenylation and subsequent 3'-5'-exosomal degradation<sup>92</sup>. Inflammation-associated p38 signalling results in the phosphorylation of TTP through MAPK-activated protein kinase 2 (MK2), allowing it to form complexes with 14-3-3 proteins. 14-3-3 proteins are a group of highly conserved binding partners of phosphorylated proteins that regulate their function, transport, and interaction with other molecules. Binding to 14-3-3 proteins excludes TTPs from SGs, which in turn prevents the degradation of mRNAs containing a type II ARE within their 3' UTR<sup>91</sup>. Of note, p38 MAPK-activity also induces the expression of dual-specificity phosphatases (DUSPs), which are known to dephosphorylate MK2. DUSPs and TTP<sup>93</sup> contain type II AREs themselves, which results in a concentration-dependent bi-phased regulation of the TTP-mediated post-transcriptional inflammatory response in an ARE-dependent manner<sup>94</sup>.

The *TNF<sup>ΔARE</sup>* mice exhibit abrogation of transcriptional repression of *TNF*, resulting in increased *TNF* mRNA half-life and enhanced *TNF* protein expression. This is also true for non-hematopoietic cells, which lack *TNF* expression in wild-type mice<sup>58</sup>. The elevated *TNF* expression was associated with an exaggerated pro-inflammatory response to microbial triggers, resulting in mucosal inflammation at 6-8 weeks of age in around 50 % of heterozygous mutants and very early onset of disease in homozygous mice<sup>58</sup>. With disease progression, intestinal inflammation became chronic and extended to the submucosa and muscularis propria<sup>58</sup>. The histopathological examination showed that the *TNF<sup>ΔARE</sup>* mice resembled major characteristic of human CD including villous blunting, formation of granulomas, and development of tertiary lymphoid structures (TLOs) with active germinal centers in the inflamed LP<sup>58</sup>. Various forms of cell death in the gut were observed, which were proposed to result in massive intestinal epithelial cell shedding, subsequently followed by villous shortening and diarrhea<sup>58,78</sup>. Of note, the phenotype was absent in GF mutant animals<sup>42</sup> and crossing *TNF<sup>ΔARE</sup>* with *TNFR1<sup>-/-</sup>* mice ameliorated the pro-inflammatory phenotype, while crossing with *TNFR2<sup>-/-</sup>* mice resulted in exacerbation in some but not all tissues<sup>58</sup>. The underlying complexity of this phenotype, including host cellular, immunity, and intestinal microbiota interactions, has been investigated in numerous studies using mouse models<sup>41,42,78,95,96</sup>.

## 1.5. Benefits of large animal models: Understanding their necessity

Mouse models are of limited utility for evaluating human-scale technology and treatments, and in certain situations are less appropriate as disease models than animals that are genetically, physiologically, and anatomically closer to humans. Studies investigating nutritional strategies for disease treatment including the use of pre- and probiotics on IBD mouse models have repeatedly failed to translate their findings to the human clinic<sup>97-99</sup>. More promising results were observed when using wild mice with a more natural gut microbiome<sup>100,101</sup>. Nevertheless, while mice have been extensively used as research models to study the gut microbiota, other animal models such as rats, dogs, non-human primates

(NHPs) and pigs could provide alternatives for the scientific community. Rats resemble gut bacterial communities of humans more closely compared to murine models<sup>102</sup>, which is why this species was extensively used in investigating disease and treatment-associated shifts of the bacteriome<sup>103–105</sup>. However, due to a more comparable body and organ size to humans, large animals, such as dogs, primates, and pigs, provide a more relevant platform to study the role of gut microbiota in health and disease<sup>106</sup>. Various reports find that the canine gut microbiome is highly similar to that of humans, with the exception of *Fusobacteria* as a more dominant genus in the dog gastrointestinal tract<sup>107</sup>. Changes of the gut microbiota due to nutritional interventions and enteropathies are well conserved between the two species<sup>108,109</sup>. Dogs and NHPs tend to suffer from idiopathic inflammatory bowel diseases, making them a valuable tool for the research community<sup>110</sup>. However, using dogs for research has significant obstacles, such as a high mortality rate due to their sensitivity to intestinal ischemia and an increasing societal resistance to canine animal testing<sup>106</sup>. These hurdles can significantly impede research progress and limit the number of experimental animals. The latter also applies to working with NHPs, such as macaques, marmosets or chimpanzees, where additionally the risk for zoonotic disease transmissions, low litter sizes and comparatively high costs have to be considered<sup>106</sup>.

Pigs are valuable animal model for investigating the gut microbiota because of the similarities in anatomy, physiology, immunology, and nutritional requirements to human<sup>111–115</sup>. This allows for safe dosage testing of novel therapeutics to treat human diseases or the assessment of prototypic human-relevant diagnostic procedures<sup>114</sup>. Because of the pigs' role in food production, there is generally less societal resistance of using pig models in translational disease research. Compared to other large animals, pigs have comparatively short reproduction times and large litters<sup>114</sup>. In addition, pigs can be fed a human diet, and faecal microbiota transfer from people to pigs results in a gut microbiota that is very similar to the donor's<sup>116,117</sup>. To functionally study the role of certain bacterial strains in various contexts, pig bacterial libraries have recently been established<sup>118</sup>. Pigs have minimum nutrient requirements comparable to those of humans and possess similar nutrient tasting receptor repertoires. Moreover, pigs have human-like digesta transit times and nutrient absorption processes due to their colon acting as the primary fermentation site for fibrous dietary components, which differs from rodent models<sup>111,114</sup>. Thus, porcine models have been extensively utilized to study the impact of human diet on metabolic disorders, obesity, and food allergies<sup>111,114</sup>. A recent study of a large pig population examined the influence of host genotype on the composition of the intestinal microbiota, showing the acceptance within the microbiome research community<sup>119</sup>.

## 1.6. Porcine biotechnology

Particularly due to their importance for xenotransplantation and human disease research, genome editing tools such as the site-specific nucleases zinc finger nucleases (ZFNs), transcription activator-like effector nucleases (TALENs) or CRISPR/Cas9 have been established for use in swine biotechnology. To date, genetically modified pig models were generated for a variety of human diseases, including Alzheimer's or Huntington's disease, breast, bone, lung and colorectal cancer, cardiovascular diseases, cystic fibrosis, diabetes and retinitis pigmentosa<sup>114,120–125</sup>.



### 1.6.1. DNA repair mechanisms for double-strand breaks

Gene editing is a process that involves creating targeted double-strand breaks (DSBs) in specific locations within the genome. The purpose of inducing these breaks is to activate the cellular DNA repair machinery, which can result in genetic modifications. In diploid organisms that are in the S/G2-mitotic phase and have closely located sister chromatid, homology-directed repair (HDR) is activated. The invasion of the 3' end of the damaged strand into the homologous template results in the formation of double holiday junctions, which are then cleaved to facilitate the recombination of donor and damaged strands. This process can be exploited to introduce foreign DNA sequences into the genome by flanking the modified sequence with homology arms in close proximity to the DSB<sup>126</sup>. This allows knock-ins of transgenes or desired mutations, but has the disadvantage of lower efficiency compared to other repair mechanisms<sup>127</sup>.

After S/G2-phase or when no homologous sequence is close to the DSB, the error-prone non-homologous end-joining (NHEJ) is activated. Even during phases of close sister chromatid-proximity, DSB-repair by NHEJ is more frequently activated. During NHEJ, Ku protein binds to DNA-ends, thus forming a Ku:DNA-complex. This complex then recruits DNA repair units, such as DNA-nucleases, -polymerases and ligases, thereby causing insertions and deletions (InDel-mutations) in a randomised manner<sup>128</sup>. In detail, each resected DNA end is bound by one heterodimeric, toroidal Ku-protein, which enables independent recruitment of nucleases, polymerases and ligases in any possible order<sup>129</sup>. The recruited enzymes for DSB-repair, Artemis-nuclease, Mu- and lambda-polymerases, as well as DNA-Ligase IV are each among the most flexible members within their enzyme family, being able to delete, expand or ligate DNA sequences of manifold chemical condition<sup>129</sup>. Following the recruitment of repair units, it is likely that several rounds of action occur, resulting in the joining of varying DNA strands, each generated by iterative processes with multiple routes and various outcomes. Lower affinity of Ku towards finally ligated DNA strands leads to complex dissociation<sup>129</sup>. The error-prone nature of NHEJ is exploited for the introduction of mutations in coding sequences, with the aim to achieve open reading frame (ORF) shifts and thus knock-outs (Figure 6). Furthermore, the simultaneous introduction of multiple DSBs can result in the deletion of larger DNA fragments.

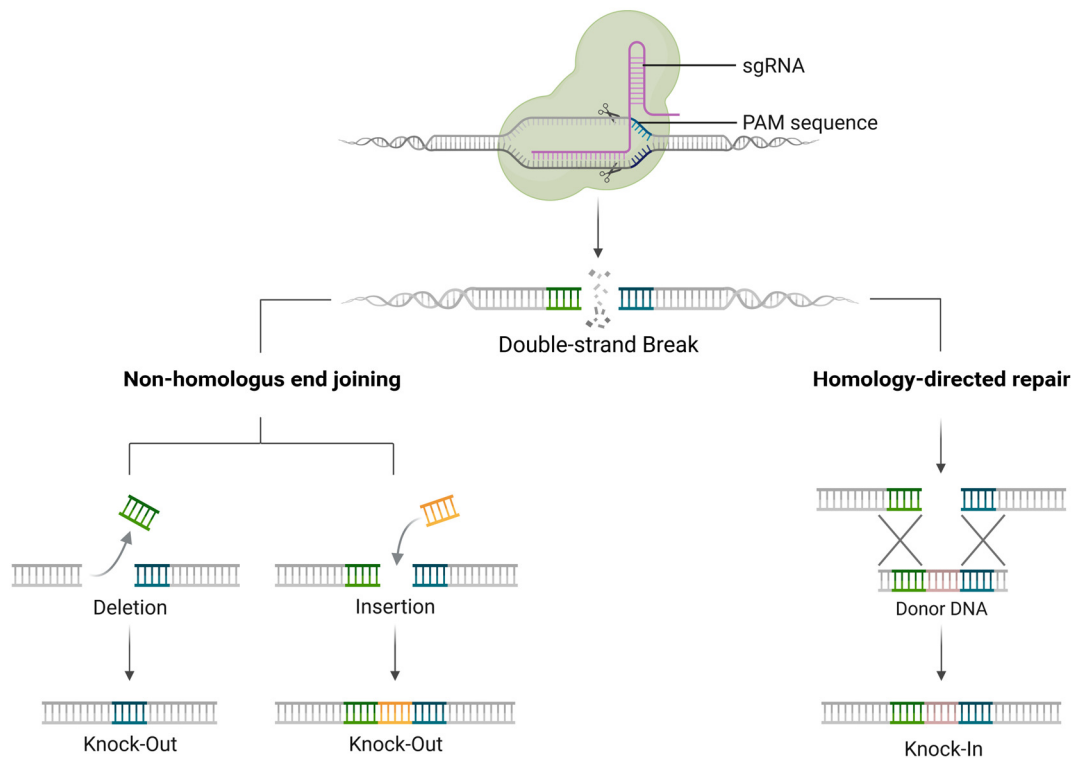


Figure 6: SpCRISPR/Cas9-mediated double-strand break (DSB) results in the activation of two DNA repair pathways, Non-homologous end-joining (NHEJ) and Homology-directed repair (HDR). NHEJ is a highly error-prone repair mechanism, that frequently results in InDel formations. HDR results in homologous template-based repair of disrupted DNA strands, which enables targeted mutations and knock-in of transgenes. Adapted from Esmée Dragt<sup>130</sup>.

### 1.6.2. Precision gene editing: Site-specific nucleases in Biotechnology

Several methods for gene editing were successfully exploited for the targeted disruption of coding or non-coding genes, the knock-in of transgenes or the modification of gene expression<sup>131,132</sup>. Following pioneering work involving reprogrammed meganuclease Sce-I, ZFNs and TALENs became widely used tools for gene editing<sup>133</sup>. Here, DNA binding domains of transcription factors were fused to FokI monomers that exhibit endonuclease activity upon dimerization<sup>134,135</sup>. ZFN's DNA binding domain contains a tandem array of Cys2-His2, being able to each recognise approximately three base pairs of DNA. A single zinc atom is bound by approximately 30 amino acids, leading to a finger-like appearance of each subunit<sup>136</sup>. By using four arrays of fingers, one ZFN can target a DNA sequence of 12 base pairs, whereas dimerization leads to recognition of 24 base pairs for targeted induction of a DSB. For the generation of suitable ZFNs, a strategy termed modular assembly has been applied for several purposes. Here, finger array sequences corresponding to specific triplet-arrays are integrated into a composite sequence before evaluation and optimisation by protein engineering is performed<sup>134</sup>.

TALENs are similar to ZFNs, only differing in their type of DNA binding-domain. Here, this domain is composed of transcription activator-like effector (TALE)-derived, highly conserved repeats that are proteins secreted by *Xanthomonas spp.* bacteria<sup>135</sup>. 33-35 amino acid repeats, that are flanked by additional TALE-derived domains at the N- and C-terminal ends of the array, bind DNA, while two

hypervariable residues, at position 12 and 13 of the repeat, determine single base-recognition<sup>137</sup>. TALE repeat arrays containing the hypervariable residues NN, NI, HD and NG were found to specifically recognise guanine, adenine, cytosine, and thymine. Compared to ZFNs, TALENs induce less off-target DSBs due to their ability of single base pair recognition<sup>138</sup>.

However, the interaction of amino acids and nucleotides, the complex nature, unpredictable function and labour-intensive production of protein engineered ZFNs and TALENs impeded high-throughput applications<sup>133</sup>. In 2012, clustered regularly interspaced short palindromic repeats (CRISPR)/CRISPR-associated protein (Cas), derived from bacterial and archaeal RNA-mediated adaptive defence systems<sup>139</sup>, was recognized as a versatile tool for high-throughput induction of DSBs for gene targeting approaches<sup>140</sup>. In the original setting, in bacteria and archaea harbouring CRISPR array-loci consisting of specific genome-targeting sequences (spacers) interspersed with identical repeats, CRISPR/Cas mediated immunity is started by integrating short fragments of foreign source (protospacers), such as viral and plasmid nucleic acids, into the bacterial genome, proximal to the CRISPR array. Protospacers are then transcribed into the precursor CRISPR RNA (pre-crRNA), which is subsequently cleaved by Cas proteins and host factors to become mature crRNA. In case of foreign nucleic acid recurrence, crRNA binds its respective target DNA sequence via Watson-Crick base pairing. Target recognition further directs a Cas protein to foreign DNA, which results in target sequence silencing<sup>141</sup>. In type II CRISPR/Cas-systems, including the *Streptococcus pyogenes*-derived CRISPR-Cas9 system (*Sp*CRISPR/Cas9), trans-activating crRNA (tracrRNA) guides the Cas9 protein to crRNA, resulting in the degradation of double-stranded DNA sequences bound by crRNA<sup>140</sup>. Cas9 protein itself was described as analogous to a bilobed jaw in shape and contains one recognition (REC) and one nuclease (NUC) lobe<sup>142</sup>. The REC domain, containing REC1 and REC2, connected via a helix bridge motif, is the DNA target recognition site, whereas the endonucleolytically active NUC domain is comprised of RuvC, HNH and P1<sup>143</sup>. Cleavage of the DNA strand complementary to the guide RNA is catalysed by the HNH domain, while cleavage of the non-complementary strand is performed by RuvC<sup>142</sup>. In many CRISPR systems, including the *Sp*CRISPR/Cas9 system, target sequence degradation is dependent on the presence of protospacer adjacent motifs (PAMs), that are adjacent to the crRNA recognition site (NGG in the case of *Sp*Cas9)<sup>144</sup>.

In the years following the groundbreaking studies of CRISPR<sup>145</sup>, numerous research teams have successfully adopted this adaptive immunity for the application as a gene editing tool in mammalian cells<sup>146</sup>. It was shown that for type II CRISPR-systems, a tracrRNA:crRNA-heteroduplex can be designed to form a single guide RNA (gRNA) being capable of leading Cas9 protein to the crRNA binding site, when adjacent to a PAM<sup>140</sup>. Nowadays, single plasmids bearing a specific gRNA together with Cas9 rationally engineered orthologs are widely used for high-throughput gene targeting applications<sup>146</sup>. In addition, the use of gRNA-Cas9-ribonucleoprotein complexes (RnPs) enables an alternative approach with reduced cytotoxicity, less off-targets and enhanced timing possibilities<sup>147,148</sup>.

### 1.6.3. The generation of Genetically Modified Pigs

In contrast to the mouse, true pluripotent embryonic stem cells that would allow the use of robust methods for generating GM pigs have not been found to date<sup>149</sup>. Therefore, the introduction of genetic modifications in pigs relies on alternative methods, such as somatic cell nuclear transfer (SCNT) or microinjection of gene editing tools directly into the pronucleus of zygotes. In the case of SCNT, somatic cells are first genetically modified in culture, allowing for pre-analysis of correct gene editing or insertion of transgenes at a pre-determined position. The genetically edited somatic cells are then transferred into enucleated, *in vitro* matured oocytes before embryo transfer<sup>123</sup> (Figure 7). This approach reduces the proportion of non-correctly targeted animals considerably and is superior to microinjection for challenging attempts, such as multiplexed genome editing and knock-in strategies. However, it is more labour-intensive, and cloned offspring often suffer from developmental defects caused by abnormal epigenetic imprinting<sup>150</sup>.

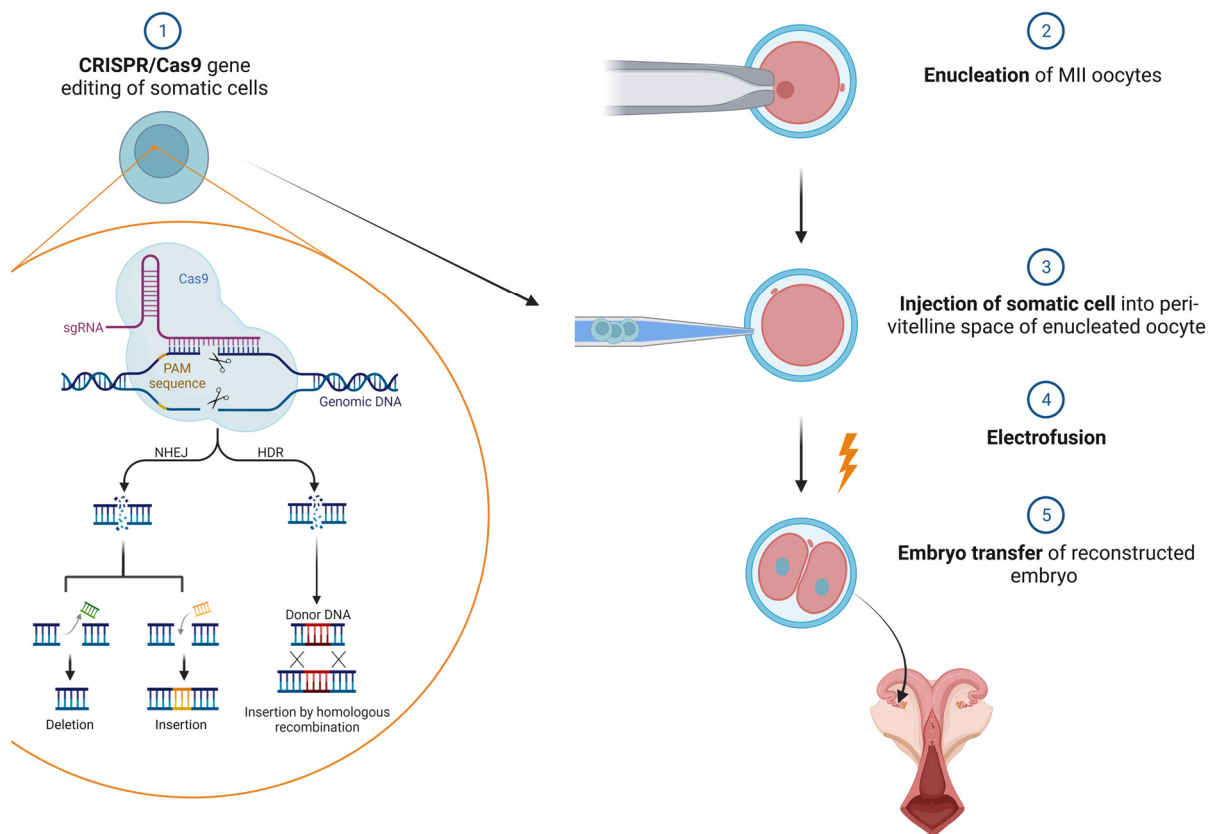


*Figure 7: Somatic cell nuclear transfer is a cloning technique that involves the transfer of the nucleus from a somatic cell into an enucleated oocyte. The somatic cells are first genetically modified and selected based on the desired modification. Next, single cells are inserted into the perivitelline space of enucleated oocytes in metaphase II (MII)-phase. Electrofusion leads to the transfer of the somatic cell nucleus into the enucleated oocyte and the start of cell division. These reconstructed embryos can then be transferred to a surrogate mother to develop into a cloned offspring with the desired genetic characteristics.*

On the other hand, microinjection is the method of choice for the rapid generation of GM pigs as it does not require prior cultivation and gene editing of somatic cells. Gene editing tools are physically

introduced into, or near to the pronuclei of fertilised oocytes, followed by embryo transfer of GM embryos into a recipient sow (Figure 8)<sup>125</sup>. The disadvantage is a high probability of mosaicism in the progeny, making it essential to evaluate the most appropriate method for each project's production of genetically modified pigs<sup>125</sup>.

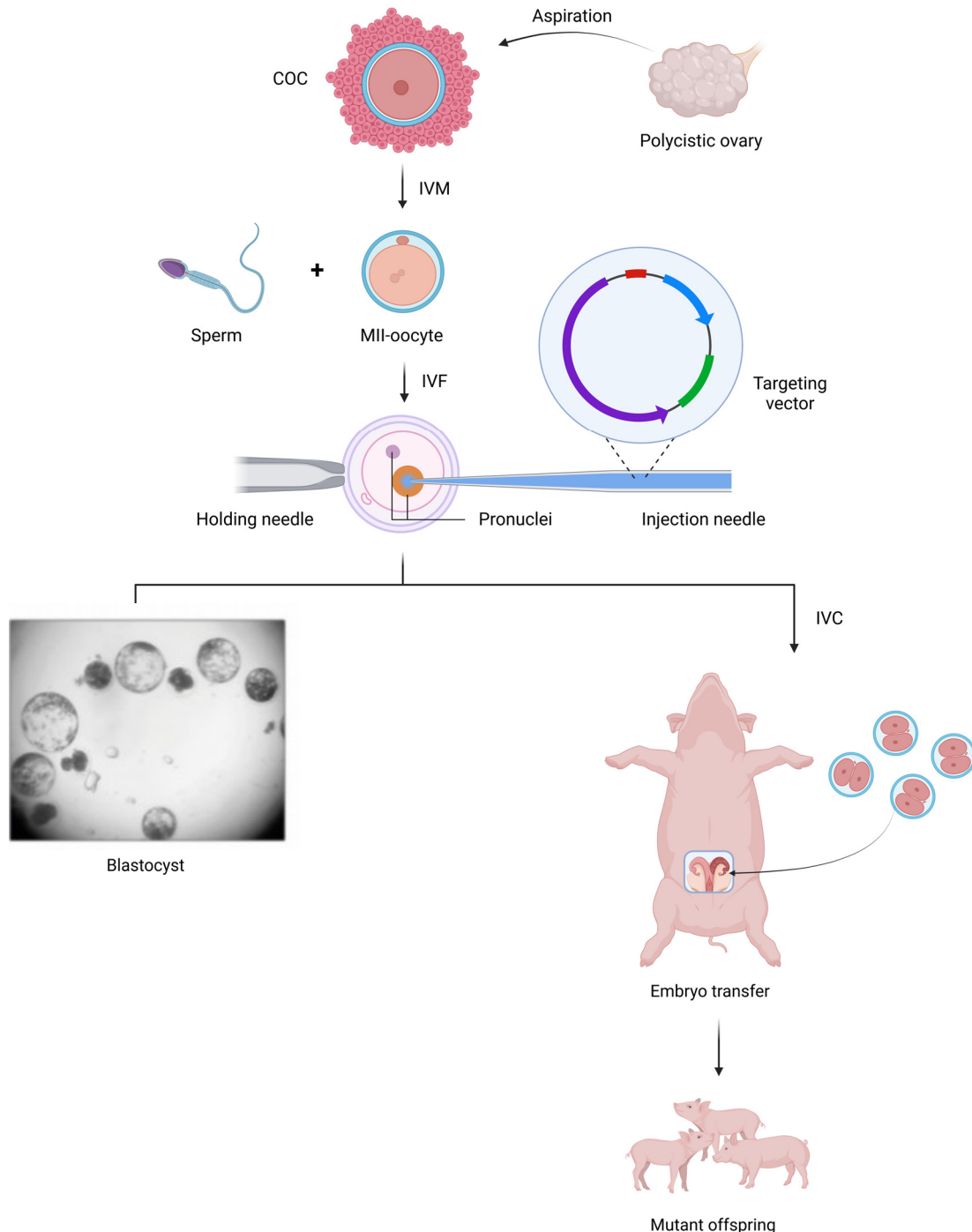


Figure 8: Microinjection of gene editing vectors into porcine zygotes at the pronuclear stage. First, cumulus-oocyte-complexes (COCs) are aspirated from polycystic ovaries derived from slaughterhouse material. COCs are then in vitro matured (IVM) to the metaphase II (MII)-phase, indicated by polar body extrusion. Next, in vitro fertilisation (IVF) is performed, and zygotes are obtained (7-10 hours post IVF). Subsequently, the vector is microinjected into the cytoplasm in close proximity to the pronuclei, followed by in vitro cultivation (IVC). Microinjected embryos can either be cultured in vitro until the blastocyst stage (7 days) for genotyping and genotoxicity analyses or until the 2-cell stage (1-2 days) for embryo transfer into a surrogate mother to produce mutant offspring.

## 1.7. Aims of this thesis

This thesis aims to develop a porcine model that closely mimics human IBD pathology and immune response. To achieve this aim, several research questions will be addressed. The first objective is to investigate whether the introduction of mutations, such as the deletion of the *TNF ARE*, can induce IBD in pigs, as has been observed in mice. A second aim is to characterise the viability and phenotype of the mutant pigs in terms of physiology and morphology. The third research question relates to the analysis of the underlying molecular mechanisms and immune responses in the mutant pig model. Finally, the fourth objective of this work relates to the changes in the gut microbiome of the mutant pigs. Therefore, a reference pig microbiome will be created to compare with the mutation-induced changes, to find possible microbial triggers of intestinal inflammation and to determine how well the pig model mimics the human gut microbiome in IBD.

The overall aim of this thesis is to provide a preclinical platform for investigating the pathogenesis of inflammatory bowel disease and testing novel human-relevant therapies and diagnostic procedures. By answering the research questions outlined above, this thesis will contribute to advancing our understanding of inflammatory bowel diseases and provide a basis for developing new treatments and diagnostic tools.

## 2. Materials and methods

### 2.1. Materials

#### 2.1.1. Laboratory equipment

Table 1: Laboratory equipment

Name	Manufacturer
Accu-jet pro	Brand, Dietenhofen, GER
Cauter	HBH Medizintechnik, Tuttlingen, GER
Cooling unit: Freezer -20 °C	Liebherr international, Bulle, CHE
Cooling unit: Freezer -80 °C	Thermo Electron GmbH, Dreieich, GER
Cooling unit: Refrigerator 4 °C	Siemens AG, Munich, GER
Countess automated cell counter	Thermo Fisher Scientific, Waltham, Massachusetts, USA
Countess cell counting chamber slides	Thermo Fisher Scientific, Waltham, Massachusetts, USA
Cryo Freezing aid "Mr. Frosty"	Sigma-Aldrich Chemie GmbH, Steinheim, GER
Cryotome: CryoStar NX70	Thermo Fisher Scientific, Waltham, Massachusetts, USA
FACS: AttuneNxT Auto Sampler	Thermo Fisher Scientific, Waltham, Massachusetts, USA
Fluorescence microscope: Zeiss Axiovert 200M	Carl Zeiss AG, Oberkochen, GER
Foam Pads for Mini Trans-Blot cell	Bio-Rad Laboratories, Hercules, USA
Gel documentation system: Quantum Vilber Lourmat	Vilber Lourmat Deutschland GmbH, Eberhardzell, GER
Gel electrophoresis: Chamber	Bio-Rad Laboratories GmbH, Munich, GER
Gel electrophoresis: Power supply unit	Bio-Rad Laboratories GmbH, Munich, GER
Heating Cabinet model ED 23	Binder GmbH, Tuttlingen, GER
Homogenizer: SpeedMill Plus	AnalytikJena AG, Jena, GER
Hybridization oven Shake'n'Stack	Thermo Fisher Scientific, Waltham, Massachusetts, USA
iBind Flex Cards	Thermo Fisher Scientific, Waltham, Massachusetts, USA
iBind Flex western blot device	Thermo Fisher Scientific, Waltham, Massachusetts, USA
Ice maker	Eurfrigor, Lainate, ITA
Incubator: BD	Binder GmbH, Tuttlingen, GER
Incubator: Steri-cycle CO <sub>2</sub>	Thermo Fisher Scientific, Waltham, Massachusetts, USA
Intensifying Screen SC400 24x30	Rego GmbH, Augsburg, GER
M920 – StainTray staining system	Simport, Quebec, CA
Microinjector: CellTram Vario	Eppendorf AG, Hamburg, GER
Micromanipulator: TransferMan NK2	Eppendorf AG, Hamburg, GER
Microscope: Axiovert 40 CFL	Carl Zeiss Jena GmbH, Jena, GER
Microtome: MICROM HM355 S2 with COOL-CUT	Thermo Fisher Scientific, Waltham, Massachusetts, USA

Microwave	Ok., Imtron GmbH, Ingolstadt, GER
Mini-PROTEAN Tetra Handcast system for Western Blot Handcasting	Bio-Rad Laboratories, Hercules, USA
Multichannel pipette: Rainin pipet-lite (100-1200 µL, 50-100 µL, 2-20 µL)	Mettler Toledo, Gießen, GER
NanoDrop lite Spectrophotometer	Thermo Fisher Scientific, Waltham, Massachusetts, USA
PCR Cycler: PeqStar	Peqlab Biotechnologie GmbH, Erlangen, GER
PCR Tube Centrifuge	Nippon Genetics Europe GmbH, Düren, GER
pH meter: CyberScan 510	Eutech Instruments, NL
Pipettes: Gilson Pipetman (2, 20, 200, 1000 µl)	Gilson Incorporated, Middleton, WI, USA
Pipettes: Rainin Pipeto lite (2, 20, 200, 1000 µl)	Mettler Toledo, Gießen, GER
Plate Reader: FLUOstar OMEGA	BMG Labtech, Ortenberg, GER
Pressure cooker	Prestige Medical Ltd., Northridge, USA
proBLUEVIEW Transilluminator	Cleaver Scientific Ltd., Colchester, UK
qPCR device: QuantStudio 5 Real-Time-PCR	Thermo Fisher Scientific, Waltham, Massachusetts, USA
Safety hood Hera safe Class 2 Type H	Heraeus Instruments, München, GER
Scale	Denver Instrument, Göttingen, GER
Scale KERN EMB 2200-0	Kern & Sohn GmbH, GER
Shaker: KH500	Noctua GmbH Labor-, Umwelt-, Fertigungstechnik, Melle, GER
Table centrifuge	Serva Electrophoresis GmbH, Heidelberg, GER
Table centrifuge: 1-14	Sigma-Aldrich Chemie GmbH, Steinheim, GER
Table centrifuge: 1-15 K	Sigma-Aldrich Chemie GmbH, Steinheim, GER
Table centrifuge: 4-16KS	Sigma-Aldrich Chemie GmbH, Steinheim, GER
Table centrifuge: 4-K15	Sigma-Aldrich Chemie GmbH, Steinheim, GER
Table centrifuge: Mini Plate Spinner	Labnet, Dülmen, GER
Table centrifuge: miniSpin	Eppendorf AG, Hamburg, GER
Tea can for ovary transport	Alfi GmbH, Wertheim-Bestenheid, GER
Thermostat: Labline 26005 Slide warmer	Thermo Fisher Scientific, Waltham, Massachusetts, USA
Transportable Incubator	Minitüb GmbH, Tiefenbach, GER
Unitwist 3-D rocker-shaker	Uniequip GmbH, Ostring, GER
Vacuum Pump: Jun-Air	Jun-Air, Redditch, UK
Vacuum pump: Jun-Air	Jun-Air, Redditch, UK
Vortex Mixer	Scientific industries, Bohemia, NY, USA
Vortex Mixer	Velp Scientifica, Mailand, IT
Water bath	GFL mbH, Burgwedel, GER



## 2.1.2. Consumables

Table 2: Consumables

<b>Name</b>	<b>Manufacturer</b>
12- Well Cell culture plate	Corning Inc., New York, USA
15 ml and 50 ml Falcons	Sarstedt AG, Sevelen, CHE
15 ml and 50 mL Falcons	Greiner Bio-One International GmbH, Kremsmünster, AUT
18g Blunt Fill Needle	Becton Dickinson, Franklin Lakes, USA
Catheter "Careflow 5F", 300 mm	Merit Medical, Jordan, USA
Cell culture flask T175	Corning Inc., New York, USA
Cell culture plate 35 mm x 10 mm	Corning Inc., New York, USA
Cell Scraper S	TPP AG, Trasadingen, CHE
Cellulose swabs	B. Braun AG, Melsungen, GER
Cloning rings	Greiner Bio-One, Frickenhausen, GER
Cover slips	Superior Marienfeld, Lauda-Königshofen, GER
Cryotubes	Corning Inc., New York, USA
Disposable Razor	B. Braun AG, Melsungen, GER
Disposable Scalpels	Swann-Morton, Sheffield, UK
Electroporation Cuvettes (2mm/4mm)	PeqLab Biotechnology, Erlangen, GER
F96 Maxisorp Nunc-Immuno Plate	Thermo Fisher Scientific, Waltham, Massachusetts, USA
Glass pipettes	Marienfeld GmbH, Landa, GER
Histology Biopsy Cassette	Simport, Quebec, CA
IVF 4-well plates (nunclon-treated surface)	Thermo Fisher Scientific, Waltham, Massachusetts, USA
Lysing Matrix B Tubes	MPbio, Santa Ana, USA
Lysing Matrix B tubes	MP Biomedicals, Norwood, USA
Lysis Tube P	Innuscreen GmbH, Kronberg, GER
MicroAmp Fast Optical 96-Well Reaction Plate with Barcode	Life Technologies Holdings Pte Ltd, Marsiling, SGP
Needle Holder, Matthieu, 20 cm	Omega Medical, Winnenden, GER
Object slide SuperFrost Plus	VWR International, Radnor, USA
Occult test Haemocult	Beckman Coulter, Brea, USA
Optical Adhesive Covers	Life Technologies Holdings Pte Ltd, Marsiling, SGP
PCR plate sealer: PX1	Bio-Rad Laboratories GmbH, Munich, GER
Petri Dishes	Greiner Bio-One, Frickenhause, GER
Pipette tips (1000 µL)	Axon Labortechnik, Kaiserslautern, GER
Pipette tips (2-20 µL, 20-200 µL)	Mettler Toledo, Gießen, GER

Pipette tips (2-20 $\mu$ L, 20-200 $\mu$ L, 1000 $\mu$ L): FisherBrand SureOne	Thermo Fisher Scientific, Waltham, Massachusetts, USA
Reaction containers ("Eppis") (1.5 and 2 ml)	Brand GmbH & Co. KG, Wertheim, GER
Reagent reservoir 25 mL	Biotix Inc., San Diego, USA
S Monovette 9 mL K3EDTA	Sarstedt AG, Sevelen, CHE
Seditainer glass columns with Na-Citrate	Becton, Dickinson and Company; Plymouth, UK
Serological Pipette: Stripette (5, 10, 25, 50 mL)	Corning Inc., New York, USA
Sterile Syringe Filter	Berrytec, Grünwald, GER
Surgical disposable scalpels	B. Braun AG, Melsungen, GER
Surgical drape	B. Braun AG, Melsungen, GER
Surgical gloves, Peha-taft latex	Omega Medical, Winnenden, GER
Surgicryl Monofilament DS 24, 3.0 (2/0) 75cm	Omega Medical, Winnenden, GER
Surgicryl, 910 HS, 5 (2), 90 cm	Omega Medical, Winnenden, GER
Syringes	BD Biosciences, Le Pont de Claix, FR
Syringes Omnifix 10 mL	B. Braun AG, Melsungen, GER
White cap Falcon	Greiner Bio-One International GmbH, Kremsmünster, AUT
White cap falcon	Greiner Bio-One, Frickenhausen, GER

### 2.1.3. Chemicals

Table 3: Chemicals

Name	Manufacturer
1x TMB Solution	Thermo Fisher Scientific, Waltham, Massachusetts, USA
3,3' Diaminobenzidin (DAB) Solution	Sigma-Aldrich, St. Louis, USA
4x Laemmli Buffer	Bio-Rad Inc., Hercules, USA
Accutase	Sigma-Aldrich Chemie GmbH, Steinheim, D
Actinomycin D	Calbiochem, San Diego, USA
Advanced DMEM/F12	Thermo Fisher Scientific, Waltham, Massachusetts, USA
Advanced Protein Assay Reagent	Cytoskeleton, Tempe, USA
Agarose	Sigma-Aldrich, St. Louis, USA
Alcian Blue	Sigma-Aldrich, St. Louis, USA

Altrenogest (Regumate)	MSD-Tiergesundheit, Unterschleißheim, GER
Amphotericin B	Sigma-Aldrich, St. Louis, USA
AndroStar Plus Semen extender	Minitube GmbH, Tiefenbach, GER
Androstar Plus sperm dilution medium	Minitube, Tiefenbach, GER
Antibiotics: Amphotericin B solution	Sigma-Aldrich Chemie GmbH, Steinheim, D
Antibiotics: Penicillin Streptomycin	Sigma-Aldrich Chemie GmbH, Steinheim, D
Attune 1X Focusing Fluid	Thermo Fisher Scientific, Waltham, MA, USA
Attune Debubble Solution	Thermo Fisher Scientific, Waltham, MA, USA
Attune NxT Flow Cell Cleaning Solution	Thermo Fisher Scientific, Waltham, MA, USA
Attune performance tracking beads	Thermo Fisher Scientific, Waltham, MA, USA
Attune Shut Down Solution	Thermo Fisher Scientific, Waltham, MA, USA
Attune Wash Solution	Thermo Fisher Scientific, Waltham, MA, USA
Azaperone	Elanco GmbH, Bad Homburg, GER
Blocking Reagent	Roche, Basel, CH
Bovine serum albumin fraction V	Roche, Basel, CH
Brefeldin A	Biolegend, San Diego, USA
Calcium chloride	Sigma-Aldrich Chemie GmbH, Steinheim, D
Calciumchloride Dihydrate	Sigma-Aldrich, St. Louis, USA
Cetyltrimethylammonium ammonium bromide (CETAB)	Sigma-Aldrich, St. Louis, USA
Cetyltrimethylammoniumbromide (CETAB)	Sigma-Aldrich Chemie GmbH, Steinheim, D
Chloroform	Applichem GmbH, Walldorf, GER
Citric Acid	Sigma-Aldrich, St. Louis, USA
Cycloheximide	Sigma-Aldrich, St. Louis, USA
Cysteine	Sigma-Aldrich, St. Louis, USA
Dimethyl-sulfoxide (DMSO)	Sigma-Aldrich, St. Louis, USA
Dithiothreitol (DTT) 2M	Carl-Roth GmbH + Co. KG, Karslsruhe, GER
DNA stool stabilization buffer	Invitek Molecular, Berlin, GER
Dulbecco's Modified Eagle's Medium - High Glucose	Sigma-Aldrich Chemie GmbH, Steinheim, D

Dulbecco's Modified Eagle's Medium (DMEM) – High Glucose	Sigma-Aldrich Chemie GmbH, Steinheim, D
Dulbecco's phosphate buffered saline	Sigma-Aldrich Chemie GmbH, Steinheim, D
Dulbecco's phosphate buffered saline (dPBS)	Sigma-Aldrich, St. Louis, USA
EDTA	Sigma-Aldrich, St. Louis, USA
Eosin Solution (2 %)	Waldeck GmbH, Münster, GER
Epidermal Growth Factor (EGF)	Sigma-Aldrich, St. Louis, USA
Equine chorion gonadotropin (ECG) - Intergonan	MSS-Tiergesundheit, Unterschleißheim, GER
Ethanol (EtOH) absolute	Fisher Scientific, Loughborough, GBR
Ethanol (EtOH) denatured	CLN GmbH, Niederhummel, GER
Eukitt quick-hardening mounting medium	Sigma-Aldrich, St. Louis, USA
Fetal Calf Serum	PAA Laboratories, Pasching, AUT
Fibroblast Growth Factor 2 (FGF2)	Sigma-Aldrich, St. Louis, USA
Formaldehyde solution (30 %)	Sigma-Aldrich, St. Louis, USA
Formaldehyde Solution 37 % (CH <sub>2</sub> O)	Sigma-Aldrich, St. Louis, USA
Gel loading dye, purple (6x)	New England BioLabs, Ipswich, USA
Glacial acetic acid	Applichem GmbH, Walldorf, GER
Glucose	Carl-Roth GmbH + Co. KG, Karlsruhe, GER
GlutaMAX™	Invitrogen GmbH, Darmstadt, D
Glycine	Carl-Roth GmbH + Co. KG, Karlsruhe, GER
Haemalaun solution (Mayer)	Carl Roth GmbH, Karlsruhe, GER
Hank's balanced Salt Solution (HBSS)	Sigma-Aldrich, St. Louis, USA
HEPES	Sigma-Aldrich, St. Louis, USA
Human chorion gonadotropin (HCG) - Ovogest	MSS-Tiergesundheit, Unterschleißheim, GER
Human M-CSF	PeproTech Inc., Rockyhill, USA
Hydrogen peroxide (H <sub>2</sub> O <sub>2</sub> )	Sigma-Aldrich, St. Louis, USA
Insuline-like Growth Factor 1 (IGF1)	Peprtech, Brookvale, AUS
Intesticult Organoid Growth Medium	Stemcell Technologies Inc., Vancouver, CAN
Ketanest	Elanco GmbH, Bad Homburg, GER

L-Alanine-L-Glutamine	Sigma-Aldrich, St. Louis, USA
Leukemia-inhibitory Factor (LIF)	MiliporeSigma, Darmstadt, GER
Lipofectamine 2000	Jena Analytic, Jena, GER
Lipopolysaccharide Solution	Invivogen, San Diego, USA
Lymphocyte separation medium 1.077 g/mL	Lonza Group AG, Basel, CHE
Lymphocyte Separation Medium, 1.077 g/mL	Lonza Group AG, Basel, CHE
MagicMark XP Western Protein Standard	Thermo Fisher Scientific, Waltham, MA, USA
Magnesium sulfate	Sigma-Aldrich Chemie GmbH, Steinheim, D
Mannitol	Sigma-Aldrich Chemie GmbH, Steinheim, D
Medium 199 (HEPES-modified)	Gibco, Paisley, UK
MEM NEAA Non-essential Amino Acid Solution (100x)	Sigma-Aldrich Chemie GmbH, Steinheim, D
Methanol (CH <sub>3</sub> OH)	Sigma-Aldrich, St. Louis, USA
Milk Powder, blocking grade	Carl Roth, Karlsruhe, GER
Mineral oil	Sigma-Aldrich, St. Louis, USA
Mineral oil	Sigma-Aldrich Chemie GmbH, Steinheim, D
Monopotassium phosphate	Sigma-Aldrich, St. Louis, USA
Non-essential amino acids (NEAA)	Sigma-Aldrich, St. Louis, USA
Normal Donkey Serum	Sigma-Aldrich, St. Louis, USA
Normal Goat serum	Sigma-Aldrich, St. Louis, USA
Normal Rabbit Serum	Biorbyt, Nottingham, UK
Opti-MEM	Gibco, Paisley, UK
Opti-Mem I	Thermo Fisher Scientific, Waltham, Massachusetts, USA
Osteosoft	Merck, Darmstadt, GER
Penicillin G	Sigma-Aldrich Chemie GmbH, Steinheim, D
Penicillin-Streptomycin	Sigma-Aldrich, St. Louis, USA
PeqGREEN dye	VWR International, Ismaning, GER
Periodic Acid 1 % - Accustain	Sigma-Aldrich, St. Louis, USA
Phenol red	Sigma-Aldrich, St. Louis, USA

Phytohemagglutinin	Sigma-Aldrich, St. Louis, USA
Pierce ECL Plus western blotting substrate	Thermo Fisher Scientific, Waltham, MA, USA
Polyacrylamide 40 %	Carl-Roth GmbH + Co. KG, Karslsruhe, GER
Polyvinyl alcohol (C <sub>2</sub> H <sub>4</sub> O)	Sigma-Aldrich, St. Louis, USA
Polyvinyl alcohol (PVA) (0.1 % w/v)	Sigma-Aldrich Chemie GmbH, Steinheim, D
Ponceau S	Sigma-Aldrich, St. Louis, USA
Porcine fertilization medium (PFM)	Fujihira Industry, JAP
Porcine fertilization medium (PFM)	Fujihira Industry, Tokyo, Japan
Porcine zygote medium (PZM)-5	Fujihira Industry, Tokyo, Japan
Porcine zygote medium 5 (PZM5)	Fujihira Industry, JAP
Potassium chloride	Sigma-Aldrich, St. Louis, USA
Proteinase inhibitor cocktail (PIC), cOmplete tablets, Mini EASY pack	Roche Diagnostics, Mannheim, GER
Puromycin	Invivogen, San Diego, USA
Recombinant porcine GM-CSF	R&D Systems, Minneapolis, USA
Roti® Histokitt	Carl-Roth GmbH + Co. KG, Karlsruhe, GER
Roti®Histol	Carl Roth GmbH, Karlsruhe, GER
Roti®-Liquid Barrier Marker	Carl-Roth GmbH + Co. KG, Karlsruhe, GER
RPMI-1640 Medium	Sigma-Aldrich Chemie GmbH, Steinheim, D
Schiff's Reagent - Accustain	Sigma-Aldrich, St. Louis, USA
Sodium Carbonate	Sigma-Aldrich, St. Louis, USA
Sodium dodecyl sulfate	Carl-Roth GmbH + Co. KG, Karlsruhe, GER
Sodium pyruvate	Sigma-Aldrich, St. Louis, USA
Sodium pyruvate (100 mM)	Sigma-Aldrich Chemie GmbH, Steinheim, D
Streptomycin sulfate	Sigma-Aldrich Chemie GmbH, Steinheim, D
Sulfuric Acid	Sigma-Aldrich, St. Louis, USA
Tetramethylethylenediamine (TEMED)	Carl-Roth GmbH + Co. KG, Karslsruhe, GER
Thiazovivin	Sigma-Aldrich Chemie GmbH, Steinheim, D
Tissue culture medium (TCM) 199	Gibco, Paisley, UK
Tissue Tek O.C.T.™ Compound	Sakura Finetek, Alphen aan den Rijn, NL

TMB Substrate	Moss Inc., Pasadena, USA
Tris	Sigma Aldrich Chemie GmbH, Steinheim, GER
Tris-HCL	Sigma-Aldrich, St. Louis, USA
Triton X-100	OMNILAB Laborzentrum, Bremen, GER
Trypan Blue	Thermo Fisher Scientific, Waltham, Massachusetts, USA
Trypan Blue, 0.4 %	Thermo Fisher Scientific, Waltham, Massachusetts, USA
Trypsin-EDTA	Sigma-Aldrich Chemie GmbH, Steinheim, D
Tween20	Promega Corporation, Madison, USA
Vectashield mounting medium with DAPI	Vector Labs, Burlingame, USA
Vectashield Mounting Medium with DAPI	Vector Laboratories Inc., Burlingame, USA
Water sterile-filtered, BioReagent, suitable for cell culture	Sigma-Aldrich, St. Louis, USA
X-ray developer T32	Calbe Chemie GmbH, Calbe, GER
X-ray fixing solution Superfix 25	Tetenal Europe, Norderstedt, GER

#### 2.1.4. Enzymes and enzyme buffers

Table 4: Enzymes and enzyme buffers

<b>Name</b>	<b>Manufacturer</b>
5x Green GoTaq reaction buffer	Promega, Mannheim, GER
5x Q5 reaction buffer	New England BioLabs, Ipswich, USA
BbsI restriction endonuclease	New England BioLabs, Ipswich, USA
CutSmart Buffer	New England BioLabs, Ipswich, USA
GoTaq G2 DNA polymerase	Promega, Mannheim, GER
Hyaluronidase	Sigma-Aldrich, St. Louis, USA
Proteinase K (20 mg/ml)	Sigma-Aldrich, St. Louis, USA
Q5 high-fidelity DNA polymerase	New England BioLabs, Ipswich, USA
qPCRBIO SyGreen Mix Lo-ROX	PCR Biosystems Ltd., London, UK
RiboLock RNase Inhibitor	Thermo Fisher Scientific, Waltham, Massachusetts, USA

T4 DNA ligase	New England BioLabs, Ipswich, USA
T4 DNA Ligase	New England BioLabs, Ipswich, USA
T4 DNA ligase buffer (10x)	New England BioLabs, Ipswich, USA

## 2.1.5. Antibodies

Table 5: Antibodies

Name	Isotype	Dilution	Manufacturer	Used for
Anti-Bovine IFN $\gamma$ -AF647 (MCA-1783)	Mouse	1:4	Bio-Rad Inc., Hercules, USA	FACS
Anti-Dog ZO-1 (61-7300)	Rabbit	1:50	Thermo Fisher Scientific, Waltham, Massachusetts, USA	WB, LCMS
Anti-Human CD14-RPE-AF647 (MCA1568P647)	Mouse	1:20	Bio-Rad Inc., Hercules, USA	FACS
Anti-Human GATA3-PE (12-9966-42)	Rat	1:20	Thermo Fisher Scientific, Waltham, Massachusetts, USA	FACS
Anti-Human IL17A-APC-eFluor780 (47-7179-42)	Mouse	1:4	Thermo Fisher Scientific, Waltham, Massachusetts, USA	FACS
Anti-human MPO (DLN-012930)	Rabbit	1:300	Dianova GmbH, Hamburg, Deutschland	IHC
Anti-Human Occludin (LS-B5737-50)	Rabbit	1:100	LSbio, Seattle, USA	WB, LCMS
Anti-Human ROR $\gamma$ t-PE (12-6988-82)	Rat	1:4	Thermo Fisher Scientific, Waltham, Massachusetts, USA	FACS
Anti-Human T-bet-eFluor660 (50-5825-82)	Mouse	1:20	Thermo Fisher Scientific, Waltham, Massachusetts, USA	FACS
Anti-Human TNF $\alpha$ -PE-Cy7 (25-7349-82)	Mouse	1:4	Thermo Fisher Scientific, Waltham, Massachusetts, USA	FACS
Anti-mouse CD4-FITC (74-12-4)	Goat	1:20	Thermo Fisher Scientific, Waltham, Massachusetts, USA	FACS
Anti-mouse FOXP3-PE (12-5773-82)	Rat	1:6.67	Thermo Fisher Scientific, Waltham, Massachusetts, USA	FACS
Anti-Mouse IgG1-BV421 (406615)	Rat	1:40	Biolegend, San Diego, USA	FACS



Anti-mouse IgG <sub>k</sub> BP-B (DLN-012930)	Recombinant	1:100	Santa Cruz Biotechnology, Dallas, USA	IHC
Anti-Mouse TNF $\alpha$ (14-7321-85)	Rat	1:1000	Thermo Fisher Scientific, Waltham, Massachusetts, USA	WB
Anti-Pig CD172a-PE (561499)	Mouse	1:20	BD Biosciences, San Jose, USA	FACS
Anti-Pig CD25/IL2-R $\alpha$ -chain-AF647 (MCA1736A647)	Mouse	1:8	Bio-Rad Inc., Hercules, USA	FACS
Anti-pig CD3 (4511-01)	Mouse	1:100	Southern Biotech Inc, Birmingham, USA	IHC
Anti-Pig CD3-PE (561485)	Mouse	1:40	BD Biosciences, San Jose, USA	FACS
Anti-Pig CD3-PerCP-Cy5.5 (561478)	Mouse	1:40	BD Biosciences, San Jose, USA	FACS
Anti-Pig CD8 $\beta$ -PE (561484)	Mouse	1:20	BD Biosciences, San Jose, USA	FACS
Anti-Pig CD8 $\alpha$ -FITC (551303)	Mouse	1:20	BD Biosciences, San Jose, USA	FACS
Anti-Pig TCR $\gamma\delta$ (unconjugated) (WS0621S-100)	Mouse	1:20	Kingfisher Biotech Inc., Saint Paul, USA	FACS
Anti-rabbit IBA1 (019-19741)	Goat	1:2000	FUJIFILM Wako Pure Chemical Corporation, Osaka, Japan	IHC
Anti-rabbit IgG (H+L)-Biotin (BA-1000)	Goat	1:400	Vector Laboratories, Burlingame, USA	IHC
Anti-rabbit IgG-HRP (SC-2780)	Goat	1:400	Cell Signaling, Beverly, USA	IHC, WB
Anti-rabbit Ki67 (DiagKi681C002)	Goat	1:300	Thermo Fisher Scientific, Waltham, Massachusetts, USA	IHC
Fixable viability dye eFluor 506 (65-0866-18)	-	1:1000	Thermo Fisher Scientific, Waltham, Massachusetts, USA	FACS
Goat anti-mouse IgG2a (STAR-133P)	Goat	1:400	Santa Cruz Biotechnology, Dallas, USA	IHC

## 2.1.6. Kits

Table 6: Kits

<b>Name</b>	<b>Manufacturer</b>
AllPrep DNA/RNA Micro Kit	Qiagen, Hilden, GER
Attune Fix & Perm Cell Permeabilisation Kit	Thermo Fisher Scientific, Waltham, Massachusetts, USA
Avidin/ Biotin Blocking Kit	Vector Laboratories Inc., Burlingham, USA
DAB Peroxidase Substrat Kit = Vector DAB plus Ni-Substrate Kit	Vector Laboratories Inc., Burlingham, USA
DNeasy Blood and Tissue Kit	Quiagen GmbH, Hilden, GER
EZ DNA Methylation-Direct Kit	Zymo Research, Irvine, USA
GenElute Mammalian Genomic DNA Kit	Sigma-Aldrich, St. Louis, USA
iBind Solution Kit	Thermo Fisher Scientific, Waltham, Massachusetts, USA
Lipofectamine 2000	Jena Analytic, Jena, GER
LunaScript RT Master Mix Kit (primer-free)	New England BioLabs, Ipswich, USA
Mix2Seq Kit	Eurofins, Ebersberg, GER
Monarch DNA Gel Extraction Kit	New England BioLabs, Ipswich, USA
Monarch Total RNA Miniprep Kit	New England BioLabs, Ipswich, USA
NucleBond Xtra Midi Kit	Macherey-Nagel, Düren, GER
pGEM T-Easy Cloning Kit	Promega, Madison, USA
pGEM-T Easy Kit	Promega
Pig Calprotectin (CALP) ELISA Kit (CSB-EQ013485PI)	Cusabio, Cambridge, USA
Vectastain Elite Peroxidase ABC Kit	Vector Laboratories Inc., Burlingham, USA
Wizard SV gel and PCR clean-up system	Promega, Mannheim, GER

## 2.2. Cells

### 2.2.1. Prokaryotic cells

Table 7: Prokaryotic cells

Name	Genotype	Source
<i>E. coli</i> ElectroMAX DH10B	F-mcrA $\Delta$ (mrr-hsdRMS-mcrBC)	Thermo Fisher Scientific, Waltham, MA, USA

### 2.2.2. Eukaryotic cells

Table 8: Eukaryotic cells

Cell type	Genotype	Breed	Gender	Source
Porcine earclip epithelial cells	Wild-type, <i>TNF</i> <sup><math>\Delta</math>ARE/+</sup> , <i>TNF</i> <sup><math>\Delta</math>ARE/<math>\Delta</math>ARE</sup>	GL x Pietrain	Various	Chair of Livestock Biotechnology, Freising, GER
Porcine enteroids	Wild-type, <i>TNF</i> <sup><math>\Delta</math>ARE/+</sup> , <i>TNF</i> <sup><math>\Delta</math>ARE/<math>\Delta</math>ARE</sup> , <i>APC</i> <sup>1311/+</sup>	GL x Pietrain	Various	Chair of Livestock Biotechnology, Freising, GER
Porcine intestinal crypts	Wild-type, <i>TNF</i> <sup><math>\Delta</math>ARE/+</sup> , <i>TNF</i> <sup><math>\Delta</math>ARE/<math>\Delta</math>ARE</sup> , <i>APC</i> <sup>1311/+</sup>	GL x Pietrain	Various	Chair of Livestock Biotechnology, Freising, GER
Porcine kidney fibroblasts	Wild-type, <i>TNF</i> <sup><math>\Delta</math>ARE/+</sup> , <i>TNF</i> <sup><math>\Delta</math>ARE/<math>\Delta</math>ARE</sup> , <i>IL10</i> <sup>+/-</sup> , <i>IL10</i> <sup>-/-</sup>	Various	Various	Chair of Livestock Biotechnology, Freising, GER
Porcine oocytes	Wild-type	German Landrace (GL)	Female	Vion SBL food GmbH, Landshut, GER
Porcine sperm "Mayuko"	Wild-type	Pietrain	Male	Bayerngenetik GmbH, Altenbach, GER

## 2.3. Nucleotides

### 2.3.1. Primers

Table 9: Primers

Name	Sequence 5' à 3'
Cas9 3' LR F1	GCAGATCAGCGAGTTCTCCA
GAPDH_S.Scrofa F	TTCCACGGCACAGTCAAGGC
GAPDH_S.Scrofa R	GCAGGTCAGGTCCACAAC
IL10_IsoformCheck_F1	CCTCTAAAGCTTCCTCCCCA
IL10_IsoformCheck_F2	CTGTCTCTAAAGCTTCCTCC
IL10_IsoformCheck_R1	ACGGCCTTGCTCTTGTTTTTC
IL10_IsoformCheck_R2	AGAAATTGATGACAGCGCCG
IL10_Check_F2	GGCCTCACTGAACCCACAAT
IL10_Check_R1	CCAACCACGTCCAACCTTG
IL-6_qPCR_F1	TCTGCAATGAGAAAGGAGATGTG
IL-6_qPCR_F2	AGGTTTCAGGTTGTTTTCTGCC
IL-8_qPCR_F1	CTGTGAGGCTGCAGTTCTG
IL-8_qPCR_R1	GTGATTGAGAGTGGACCCCA
NFkB_p50_qPCR_F1	AGATGTGAAGATGCTGCTGG
NFkB_p50_qPCR_R1	CCAAGTGCAAGGGTGTCTG
Offtarget 3' - Hit 1_Rev 1	TTTTGTCGTTTTAGGGCCGC
OffTarget 3*-VCPIP_Rev 2	CCGTCAATGCTCCATCTTCC
OffTarget 3'-Hit 1_Fwd 1	ACAGCAACACCGGATCCTTA
OffTarget 3'-Hit 1_Fwd 2	CTGCTTTGCCTAAACTGCCT
OffTarget 3'-Hit 1_Rev 1	TCATCGTCTTCAGCTCCCTC
OffTarget 3'-Hit 2_Fwd 1	TGGAACACAAACTTGGCATGT
OffTarget 3'-Hit 2_Fwd 2	CTGGAAACTTCAGTACACCCC
OffTarget 3'-Hit 2_Rev 2	GGCTTCTCTGGCTCACTGTA
OffTarget 3'-Hit 3_Fwd 1	TGGCACTTCCCATGATCCAT
OffTarget 3'-Hit 3_Fwd 2	GTGTGTGTGTGTGTGTGTGT
OffTarget 3'-Hit 3_Rev 1	TAGTTGGGCCCTCAAAGCAA
OffTarget 3'-Hit 3_Rev 2	TCACCAGGAGAGAGCATTGA
OffTarget 3'-Hit 4_Fwd 1	CAATGAAGCCCAAGTCCAGG
OffTarget 3'-Hit 4_Fwd 2	GCCCAAGAGCAGACATTCT
OffTarget 3'-Hit 4_Rev 1	GTGTCTCCAGCTGTGTTGTC
OffTarget 3'-Hit 4_Rev 2	TTTTCCCTGGTGCCTTGAAG
OffTarget 3'-Hit 5_Fwd 1	TTCACAAGTCTCCCCACACA

OffTarget 3'-Hit 5_Fwd 2	GGGGAGTTGGTGGTTTTTCAG
OffTarget 3'-Hit 5_Rev 1	ACGAAAGAGCCTGAACAAGC
OffTarget 3'-Hit 5_Rev 2	GGCAAACCCAGCTTTCTAG
OffTarget 3'-VCPIP_Fwd 1	AGGAGGATGGTGGTTGTGTT
OffTarget 3'-VCPIP_Fwd 2	TAGGGACCCAGCAAGCATAAC
OffTarget 3'-VCPIP_Rev 1	AATCCACAACCACACTTGCC
OffTarget 5*-Hit 3_Fwd 1	GCTCGGTGGCATGGAATTTA
OffTarget 5*-Hit 3_Rev 2	TAGAATTCAGGGCTGGGAGG
OffTarget 5'-Hit 1_Fwd 2	GGAAGCCACCACCAAGTCTA
OffTarget 5'-Hit 1_Rev 1	GCATGAGTGGTATGAGTTGCA
OffTarget 5'-Hit 1_Rev 2	TGGGCATGCTGACTATTTGC
OffTarget 5'-Hit 2_Fwd 1	TCAGACAGACTTGGGTTCCA
OffTarget 5'-Hit 2_Fwd 2	ATGGATGAGACTGTTGCCCT
OffTarget 5'-Hit 2_Rev 1	GGGCCCTCAAAGCAATGTTT
OffTarget 5'-Hit 2_Rev 2	TCGGAGAAATTCTAGGTCTGC
OffTarget 5'-Hit 3_Fwd 2	TGTAAGCCAAGCCTGCCTAT
OffTarget 5'-Hit 3_Rev 1	CCCATCTCCTCTGACCCTTC
OffTarget 5'-Hit 4_Fwd 1	ATTTCTTTGGGCCACTTCCG
OffTarget 5'-Hit 4_Fwd 2	TTATCTGTGGGGAAGTGGCA
OffTarget 5'-Hit 4_Rev 1	TTCCTGGTCTTCGTCCTGAC
OffTarget 5'-Hit 4_Rev 2	GGGCAAAGTTTGGGAGACTGG
OffTarget 5'-Hit 5_Fwd 1	AGTGGAAGGCTGAGTGTGAG
OffTarget 5'-Hit 5_Fwd 2	CCTCCCAGCTCAGTAAACCA
OffTarget 5'-Hit 5_Rev 1	GGCTTCTCTGGCTCACTGTA
OffTarget 5'-Hit 5_Rev 2	TTGAGCCAGTGTGCAGTAGA
OffTarget-Hit 1_Rev 2	AGAATTGATGAAGGGAGCATGC
Rosa26 BGH R1	GGGAGGGGCAAACAACAGAT
RSP28_qPCR_F1	GTTACCAAGTTCTGGGCAG
RSP28_qPCR_R1	CAGATATCCAGGACCCAGCC
TNF_qPCR_F1	TTCTGCCTACTGCACTTCGA
TNF_qPCR_R1	GGGCTTATCTGAGGTTTGAG
TNF $\alpha$ check_F2	GGCCCCAGAAGGAAGAGTT
TNF $\alpha$ check_R2	ATGCGGCTGATGGTGTGAGT

### 2.3.2. gRNA oligonucleotides

Table 10: gRNA oligonucleotides

Name	Sequence 5' à 3'	gRNA target site
IL10 g1/1	CCACCCCTGCCAGGAAGATC AGG	IL10 Ex 1
IL10 g2/1	GCTGTTCTCAGACTTAATGC TGG	IL10 Ex 1
IL10 g3/1	TCGGAGTTCCCGGAGCATGC TGG	IL10 Ex 1
IL10 g4/1	CAATAGAGCAGTGCTGAGCT GGG	IL10 Ex 1
IL10 g5/1	ATTGCCTGATCTTCCTGGCA GG	IL10 Ex 1
IL10 g6/1	TATTGCCTGATCTTCCTGGC AGG	IL10 Ex 1
IL10 g7/1	GCAATAGAGCAGTGCTGAGC TGG	IL10 Ex 1
TNF $\alpha$ _g4 (3' gRNA)	TGTATTTATTCAGGAGGGCG PAM: AGG	TNF ARE/CDE1 3'
TNF $\alpha$ _g5 (5' gRNA)	TAAGAGGGAGCTGGCCCTGT PAM: GGG	TNF ARE/CDE1 5'

### 2.3.3. Molecular cloning vectors and DNA constructs

Table 11: Molecular cloning vectors and DNA constructs

Name	Source
pX330-U6-Chimeric_BB-CBh-hSpCas9-T2A-puro_MCS (Amp_R, Puro_R) (plasmid #841) ("px330")	Daniela Huber, Chair of Livestock Biotechnology, TUM, Freising, GER
px330 TNF $\Delta$ ARE_5' gRNA + 3' gRNA	Alessandro Grodziecki, Chair of Livestock Biotechnology, TUM, Freising, GER
px330 IL10 $^{-/-}$ _g1	Generated during thesis
px330 IL10 $^{-/-}$ _g2	Generated during thesis
px330 IL10 $^{-/-}$ _g3	Generated during thesis
px330 IL10 $^{-/-}$ _g4	Generated during thesis
px330 IL10 $^{-/-}$ _g5	Generated during thesis
px330 IL10 $^{-/-}$ _g6	Generated during thesis
px330 IL10 $^{-/-}$ _g7	Generated during thesis

## 2.4. Software and Webtools

Table 12: Software and webtools

Name	Manufacturer
Adobe Illustrator 2019	<a href="https://www.adobe.com/ch_de/products/illustrator.html">https://www.adobe.com/ch_de/products/illustrator.html</a>
Benchling	<a href="https://www.benchling.com/">https://www.benchling.com/</a>
Biorender	<a href="https://biorender.com/">https://biorender.com/</a> (Figures were created using Biorender)
CRISPOR	<a href="http://crispor.tefor.net/">http://crispor.tefor.net/</a>
EMBOSS Needle Pairwise Alignment	<a href="https://www.ebi.ac.uk/Tools/psa/emboss_needle/nucleotide.html">https://www.ebi.ac.uk/Tools/psa/emboss_needle/nucleotide.html</a>
Ensembl database	<a href="https://www.ensembl.org/index.html">https://www.ensembl.org/index.html</a>
Finch TV Chromatogram viewer	<a href="https://digitalworldbiology.com/FinchTV">https://digitalworldbiology.com/FinchTV</a>
Gel documentation software Vision-capt Vilber Lourmat	Vilber Lourmat Deutschland GmbH, Eberhardzell, D
Inference of CRISPR edits (ICE) analysis tool	<a href="https://ice.synthego.com/#/">https://ice.synthego.com/#/</a>
Integrated Microbial Next Generation Sequencing pipeline (IMNGS)	<a href="https://www.imngs.org/">https://www.imngs.org/</a>
Molecular Evolutionary Genetics Analysis (MegaX)	<a href="https://www.megasoftware.net/">https://www.megasoftware.net/</a>
NAMCO Microbiome explorer	<a href="https://exbio.wzw.tum.de/namco/">https://exbio.wzw.tum.de/namco/</a>
NCBI database	<a href="https://www.ncbi.nlm.nih.gov/gene/">https://www.ncbi.nlm.nih.gov/gene/</a>
Phylogenetic visualization management (EvoView) Tree an tool	<a href="https://www.evolgenius.info/evolview">https://www.evolgenius.info/evolview</a>
PRIMER 3	<a href="https://primer3.ut.ee">https://primer3.ut.ee</a>
Prism Version 8	<a href="https://www.graphpad.com/scientific-software/prism/">https://www.graphpad.com/scientific-software/prism/</a>
QuantaSoft™ Software	<a href="http://www.bio-rad.com/de-de/sku/1864011-quantasoft-software-regulatory-edition?ID=1864011">http://www.bio-rad.com/de-de/sku/1864011-quantasoft-software-regulatory-edition?ID=1864011</a>
Reverse complement	<a href="https://www.bioinformatics.org/sms/rev_comp.html">https://www.bioinformatics.org/sms/rev_comp.html</a>
Rhea pipeline	Ilias Lagkourdos et al. <sup>151</sup>
RStudio 2022.07.1+554	<a href="https://www.rstudio.com">https://www.rstudio.com</a>
SILVA database	<a href="https://www.arb-silva.de/">https://www.arb-silva.de/</a>
STAMP bioinformatics software	<a href="https://beikolab.cs.dal.ca/software/STAMP">https://beikolab.cs.dal.ca/software/STAMP</a>

## 2.5. Length and molecular weight standards

Table 13: Length and molecular weight standards

Name	Manufacturer
2-Log DNA Ladder	New England Biolabs GmbH, Frankfurt, D
Low Molecular Weight DNA Ladder	New England Biolabs GmbH, Frankfurt, D
MagicMark XP Western Protein Standard	Thermo Fisher Scientific, Waltham, Massachusetts, USA

## 2.6. Buffers and solutions

Table 14: Buffers and solutions

Name	Components	Quantity
0.5 M Tri – HCl, pH 6.8	Tris ddH <sub>2</sub> O HCl ddH <sub>2</sub> O	15.14 g 125 ml Set pH to 6.8 Ad 250 ml
10x Running Buffer (Western Blot)	Tris Glycine SDS ddH <sub>2</sub> O	30 g 144 g 10 g Ad 1 l
10x SDS	SDS ddH <sub>2</sub> O	10 g Ad 100 ml
10x TAE-Buffer	Tris-HCL 0,5 M EDTA pH 8,0 ddH <sub>2</sub> O	158 mg 29 mg Ad 100 ml
10x TBE-Buffer	Tris H <sub>3</sub> BO <sub>4</sub> 0,5 M EDTA pH 8,0 ddH <sub>2</sub> O	545 g 276 g 200 mL Ad 5 L
10x TBS	Tris Tween 20 ddH <sub>2</sub> O	24.2 g 80 g Ad 1 l
12 % Polyacrylamide-SDS gel	40 % Polyacrylamide 1 M Tris-HCl, pH 8.8 10 % SDS	4.62 ml 5.8 ml 154 µl



	ddH <sub>2</sub> O 10 % APS TEMED	4.7 ml 154 µl 6.2 µl
1M Tris – HCl, pH 8.8	Tris-HCL ddH <sub>2</sub> O HCl ddH <sub>2</sub> O	39.4 g 125 ml Set pH to 8.8 Ad 250 ml
1x Laemmli Buffer	4x Laemmli Buffer DTT 1M	90 % v/v 10 % v/v
1x Semi-Dry Blotting Buffer	Tris Glycine Methanol ddH <sub>2</sub> O	3.03 g 14.4 g 200 ml Ad 1 l
1x TBST	10x TBS Tween 20 ddH <sub>2</sub> O	100 ml 1 ml Ad 1 l
5 % Polyacrylamide-SDS gel	40 % Polyacrylamide 0.5 M Tris-HCl, pH 6.8 10 % SDS ddH <sub>2</sub> O 10 % APS TEMED	1.1 ml 2.2 ml 88 µl 5.3 ml 88 µl 8.8 µl
APS 10 %	(NH <sub>4</sub> ) <sub>2</sub> S <sub>2</sub> O <sub>8</sub> ddH <sub>2</sub> O	1g Ad 10 ml
Blocking Buffer (IHC)	D-PBS Animal Serum	98 ml 2 ml
Blocking Buffer (Western Blot)	Milk powder 1x TBST	5 g Ad 100 ml
Embryo working medium	HEPES-buffered TCM 199 FCS Penicillin-Streptomycin-Solution	44.5 ml 5 ml 0.5 ml
Erythrocyte lysis buffer	NH <sub>4</sub> Cl KHCO <sub>3</sub> 0,5 M EDTA pH 8,0 ddH <sub>2</sub> O	8.3 g 1.1 g 100 mg Ad 1 l
Intestinal crypt basic medium	Advanced DMEM/F12 GlutaMAX 0.5 M HEPES 0.5 M N-Acetylcysteine (in ddH <sub>2</sub> O)	500 ml 5 ml 5 ml 1 ml

Intestinal crypt freezing medium	FCS DMSO Thiazovivin	9.5 ml 0.5 ml 10 µl
Intestinal crypt isolation buffer	D-PBS 0.5 M EDTA  2 M DTT	28 ml 1.8 mL (colon) 0.9 ml (ileum) 150 µl
LB-Medium	Yeast Extract NaCl Tryptone/Peptone ddH <sub>2</sub> O	5 g 10 g 10 g Ad 1 l
Na-Citrate buffer (IHC)	Tri-Sodium Citrate (Dihydrate) ddH <sub>2</sub> O HCl	2,94 g Ad 1000 mL Set pH to 6.0
NP-40 buffer	NaCl Triton X-100 Tris-HCL, pH 8.0 ddH <sub>2</sub> O	150 mM 0.1 % 50 mM
Oocyte <i>in vitro</i> maturation buffer (FLI medium)	TCM 199 Glucose Na-Pyruvate Cysteine EGF LH FSH PVA LIF IGF1 FGF2	Ad to desired vol. 3.05 mM 0.91 mM 0.57 mM 10 ng/ml 0.5 µg/ml 10 ng/ml 1.1 % w/v 20 ng/ml 20 ng/ml 40 ng/ml
Oocyte Transport Solution	dPBS Penicillin-Streptomycin-Solution Amphotericin B	500 ml 5 ml 5 ml
Permeabilization solution (IHC)	D-PBS Animal Serum Triton X-100	98.6 ml 1 ml 0.4 ml
Tissue culture freezing medium	FCS Tissue culture medium for pKDNFs (non-primary cells)	70 % v/v 20 % v/v

	DMSO	10 % v/v
Tissue culture medium for M1-macrophages	RPMI 1640 FCS GlutaMAX From day 6: poGM-CSF1	500 ml 50 ml 6 ml 10 <sup>4</sup> U/ml
Tissue culture medium for pKDNFs (non-primary cells)	DMEM NEAA Na-Pyruvate GlutaMAX FCS	500 ml 5.6 ml 5.6 ml 6 ml 50 ml
Tissue culture medium for pKDNFs (primary cells)	DMEM NEAA Na-Pyruvate GlutaMAX FCS	500 ml 5.6 ml 5.6 ml 6 ml 100 ml
TTE-Buffer	Tris Triton-X-100 0,5 M EDTA pH 8,0 ddH <sub>2</sub> O	242 mg 1 ml 584 mg Ad 100 ml

### 3. Methods

#### 3.1. Reference gene annotations

Gene annotation was performed using currently available porcine reference genome sequence (Pig: NCBI GCF\_000003025.6, Sscrofa 11.1) and compared to the human genome (NCBI NC\_060925.1, HGNC:5962) by using Benchling.

#### 3.2. Plasmid construction

##### 3.2.1. Oligonucleotide annealing

Respective forward and reverse oligonucleotides encoding selected gRNA candidates were diluted in TE-Buffer and mixed at a final concentration of 10 ng/ $\mu$ l. For hybridization, the oligonucleotide-mix was heated to 100 °C for 5 min, followed by ambient cooling to room temperature.

##### 3.2.2. Restriction digest

Backbone-plasmids for cloning were digested with the respective endonuclease for linearization or to confirm correct insert integration (Table 15).

*Table 15: Components for restriction digest*

Component	Quantity
Plasmid DNA	1-15 $\mu$ g
Restriction endonuclease (e.g. BbsI)	3 U/ $\mu$ g
10x NEB Buffer	5 $\mu$ l
ddH <sub>2</sub> O	Ad 50 $\mu$ l

##### 3.2.3. Ligation

T4 Ligase was used to ligate vector backbones to DNA fragments according to the manufacturer's instructions. The ligation components were mixed and incubated for 2 h at room temperature and stored at 4 °C overnight (Table 16).

Table 16: Components for DNA ligation

Component	Quantity
Insert DNA	1:5 molar ratio Insert:Backbone
Backbone DNA	4:5 molar ratio Insert:Backbone
T4 DNA Ligase	27 U/ml
10x T4 DNA Ligase Buffer	3 $\mu$ l
ddH <sub>2</sub> O	Ad 30 $\mu$ l

### 3.2.4. Electroporation of prokaryotes

50  $\mu$ l of electrocompetent ElectroMAX® DH10B-cells were thawed on ice. 3  $\mu$ l of the overnight ligated plasmid were added before transferring the mixture into electroporation cuvettes. A single pulse with a voltage of 2.5 kV for 5 ms was applied. Cells were transferred into 0.5 ml LB-medium for 30 minutes for regeneration. Following transformation, cells were plated on agar plates containing antibiotics for selection of successfully electroporated prokaryotic cells.

### 3.2.5. Polymerase chain reaction

Polymerase chain reaction (PCR) was performed using GoTaq chemistry according to the protocol shown in tables 17 and 18.

Table 17: Pipetting scheme for GoTaq-PCR. Shown is the pipetting scheme for a single reaction.

Component	Volume
ddH <sub>2</sub> O	16.35 $\mu$ l
GoTaq 5x-Buffer	5 $\mu$ l
dNTPs (10 $\mu$ m)	0.5 $\mu$ l
Forward-Primer (10 $\mu$ m)	0.5 $\mu$ l
Reverse-Primer (10 $\mu$ m)	0.5 $\mu$ l
GoTaq-Polymerase	0.15 $\mu$ l
Template DNA	2 $\mu$ l
TOTAL	25 $\mu$ l

Table 18: GoTaq-PCR program. Duration of denaturation within the cycle is determined by the origin of template DNA, 30" for plasmids and 45" for genomic DNA. Duration of elongation within the cycle is determined by template DNA size.

Step	Temperature	Duration
Heat lid	110 °C	
Initial Denaturation	95 °C	2 min.
Cycle start (35 times):		
➤ Denaturation	95 °C	30 " Plasmid/45 " gDNA
➤ Annealing	60 °C	45 "
➤ Elongation	72 °C	1 kB/1 min.
Final Elongation	72 °C	5 min.
Storage	8 °C	∞

### 3.2.6. Colony PCR

To identify *E. coli* colonies containing correct plasmid constructs, colony PCR was performed. Primers (e.g. IL10\_Check F2/R1) were selected to amplify a segment that spanned the vector backbone and the insert. Single cell colonies were streaked on a backup-agar plate and then resuspended in 30 ml TTE buffer using a sterilized toothpick. The backup-agar plate was stored at 37 °C until further use. The lysis of bacteria was achieved by heating the TTE buffer-bacteria mixture in 95°C for 5 minutes. Afterwards, 2 µl of the mixture was used as a DNA template for PCR.

### 3.2.7. Agarose gel-electrophoresis

PCR products were separated on a 1 % TBE or TAE agarose gel with 0.4 µl/l PeqGreen-staining for electrophoresis. 2log DNA ladder was used for determination of band lengths. PeqGreen fluorescent dye was added to sample, and the products were visualised using a transilluminator.

For cloning, PCR products of desired size were separated on a TAE agarose gel electrophoresis, cut out with a scalpel and purified with the DNA Gel Extraction Kit according to the manufacturer's instructions.

### 3.2.8. PCR Amplicon sequencing

To analyse the DNA sequence, purified amplicons were sent to Eurofins Genomics for Sanger sequencing using a forward or reverse primer at the concentration recommended by the manufacturer (Table 19).

Table 19: Pipetting scheme for Eurofinngenomics-sequence samples.

Component	Volume
ddH <sub>2</sub> O	16 µl
Primer	2 µl
PCR product	1 µl

Sequencing results were analysed using Finch TV chromatogram viewer, Benchling and/or Inference of CRISPR edits (ICE).

### 3.2.9. Plasmid Midiprep and freezing of prokaryotic cells

Bacterial cells harbouring intermediate or final plasmid constructs were picked from the backup-agarose plate and transferred to 100 ml of LB-medium with the appropriate antibiotics for overnight selection at 37 °C in a lab shaker. The next day, 500 µl of the overnight culture was mixed with 1 ml glycerol in a cryotube and frozen at -80 °C for long-term storage. The remaining volume was lysed, and the plasmid purified with the NucleoBond® Xtra Midi kit according to the manufacturer's instructions. The plasmid was dissolved in 100 µl TE buffer and stored at 4 °C for use within a few weeks or at -20 °C for long-term storage.

### 3.2.10. Measurement of DNA-concentration

DNA concentration was determined using Nanodrop UV/VIS spectrophotometry. For this purpose, 1 µl DNA sample was applied to a calibrated nanodrop spectrophotometer. Interfering absorptions caused by proteins in solution are considered through assessing the optical density ratio  $OD_{260}/OD_{280}$ , whereby protein-free solutions achieve values between 1.8 and 2.0<sup>152</sup>.

## 3.3. Eukaryotic cell culture

### 3.3.1. Isolation of primary cells

To establish a primary cell culture from porcine kidneys, ear clips or intestinal crypts, fresh organ samples were obtained and transported in D-PBS (supplemented with Penicillin and Streptomycin) at 4 °C, and quickly processed. The tissue samples were washed three times with ice-cold D-PBS to remove any contaminants, then minced into small pieces using sterile scissors and scalpels. The minced tissue was transferred into a sterile centrifuge tube.

For kidney and ear clip tissue, minced pieces were digested with collagenase type IA to release cells from the extracellular matrix. The collagenase digestion was performed by adding 10 mg/ml collagenase type IA to the tissue suspension and incubating it at 37 °C for 30 mins with gentle agitation. An equal volume of D-PBS was added to stop the reaction through dilution and the suspension was centrifuged

at 300x g for 5 min. The supernatant was removed, and the cell pellet was either resuspended in a suitable cell culture medium or frozen in eukaryotic cell culture freezing medium at -80 °C.

For the isolation of intestinal crypts, minced pieces were transferred to a 15 mL conical tube. The tissue fragments were allowed to settle by gravity and the supernatant was aspirated. Crypt isolation buffer was added to the tube and incubated at 4 °C on a rocking platform for 30 minutes. In the meantime, intestinal crypt freezing medium and Thiazovivin was added to prevent anoikis. After 30 minutes, the tube was centrifuged, the supernatant was aspirated, and intestinal crypt basic medium was added. Crypts were scraped out of the lamina propria using 18 G needles. The number of crypts was determined by counting them in a 100 µl aliquot of the sample using an inverted microscope. The sample was centrifuged again, and the supernatant was aspirated except for 100 µl. Crypts were frozen using intestinal crypt freezing medium.

### 3.3.2. Thawing of eukaryotic cells

For thawing, corresponding freezing vials containing eukaryotic cells were placed in a water bath at 37 °C for 2-3 minutes. Due to the cryoprotectant (DMSO)-induced cytotoxicity above 4 °C, rapid dilution of thawed cell suspensions was necessary. Thus, cells were transferred into 5 ml pre-warmed supplemented DMEM, followed by centrifugation at 300 x g for 5 minutes. Supernatant was discarded, cells were resuspended in supplemented DMEM and transferred on a T150 cell culture flask for further cultivation.

### 3.3.3. Culture of porcine kidney fibroblasts

pKDNFs and ear clip fibroblasts were cultured at 37 °C, 5 % CO<sub>2</sub> in a humidified environment. High degree of sterility was achieved using HEPA-filters (high efficiency particulate air filters) in incubators and sterile class II laminar flow hoods for culture work. Fresh media was added every 2-3 days.

### 3.3.4. Passaging of eukaryotic cells

Subcultivation of finite eukaryotic cell culture took place before 90 % of confluence. Detachment was achieved using the peptidase Accutase in combination with ethylenediaminetetraacetic acid (EDTA). Generally, present peptidases digest cell-matrix-interactions, whereas EDTA as Ca<sup>2+</sup>-chelator disbands cell-cell-interactions (e.g. Cadherine-interactions)<sup>153</sup>.

When cells reached 80-95% confluence, the medium was removed using a vacuum pump, followed by a washing step with D-PBS. To detach, the cells were incubated for 10-20 min with Accutase. To stop the Accutase-catalyzed reaction, serum-containing medium was added. The resulting cell-medium solution was then split into appropriate cell culture flasks, frozen, or used for DNA isolation.



### 3.3.5. Lipofection of eukaryotic cells

For the lipofection of eukaryotic cells, 30-50 % confluent cells (T150 cell culture flask) were diluted 1:30, split up onto an adequate amount of 10 cm-dishes and incubated overnight at 37 °C, 5 % CO<sub>2</sub>.

The following day, 300 µl Opti-MEM was mixed with 6 µl Lipofectamine 2000 per dish and incubated for 5 minutes. 300 µl Opti-MEM was then mixed with 5 µg of plasmid DNA and incubated for 5 minutes. Opti-MEM-Lipofectamine 2000- and Opti-MEM-DNA-mixtures were then mixed and incubated for 25 minutes. During this time, cells were washed with D-PBS and covered with 4 ml Opti-MEM. 600 µl of the Opti-MEM-Lipofectamine 2000-DNA-mixture was added to each 10 cm-dish. Cells were incubated for 4-6 hours in the incubator for lipofection. After incubation, 6 mL of supplemented DMEM was added to cell culture. Cells were incubated overnight in the incubator.

The following day, medium was changed to 10 mL supplemented DMEM with 0.15 mg/ml Puromycin for selection of puromycin resistance cassette-bearing cells that were cultivated for SCNT. For the screening of selected gRNA candidates and analysis of editing efficiencies via ICE, cells were immediately harvested the next day without prior selection.

### 3.3.6. Selection of transfected cells

Cells bearing the puromycin resistance gene *pac*, encoding for the puromycin N-acetyl transferase (PAC), were selected using 0.15 mg/ml puromycin in supplemented DMEM for two days.

### 3.3.7. Separation of single cell clones

After the selection of successfully transfected cells, clones were transferred to several other cell culture dishes in a low cell number which enabled isolated growth of single cell colonies. 1200 cells were seeded onto a 15 cm cell culture dish. To spread a defined number of cells, Countess™ automated cell counting was used. According to the manufacturer's instructions, 10 µl of 1 ml cells resuspended in D-PBS were mixed with 10 µl of trypan blue stain (0.4 %). From this mixture, 10 µl were pipetted into a Countess™ counting chamber for counting.

Large clones were identified under a microscope and circled using a lab marker. For picking single cell clones, sterilised cloning rings were first dipped in sterile silicone grease and then placed over marked colonies. 50 µl Accutase was used to detach cells, followed by stopping the reaction using 100 µl of supplemented DMEM. These suspensions were then transferred into wells of a 12-well plate containing 2 ml supplemented DMEM.

### 3.3.8. Upscaling of single cell clones

80-95 % confluent cells in a 12-well plate, were passaged onto a 6-well plate. Confluent cell clones were then passaged onto four wells of a 6-well plate, followed by a passage onto a T75 cell culture-flask. Confluent cells of a T75 flask finally were frozen and stored at -80 °C.

### 3.3.9. DNA-Isolation from porcine kidney cells

For isolation of genomic DNA, cell clones were detached using Accutase and centrifuged at 300 x g for 5 minutes. The pellet was resuspended in 30 µl Quick Extract, followed by a PCR-cycler protocol for DNA extraction: 68 °C for 10 minutes for optimal proteinase K-activity, followed by 95 °C for 8 minutes for deactivation of proteinase K. The supernatant was used for PCR.

### 3.3.10. Assessment of gRNA targeting efficiencies in eukaryotic somatic cell culture

pKDNFs that were subject to lipofection using various single or multiple plasmids encoding a respective gRNA and Cas9 were lysed and DNA was isolated. The genetic region of interest was amplified and PCR products were sent for Sanger sequencing. Sequencing results were uploaded for ICE analysis to assess the ratio of introduced insertions or deletions, and to identify the contribution of DNA variants to the total amplicon population.

## 3.4. *In vitro* embryo culture

### 3.4.1. Collection of ovaries and *in vitro*-maturation of oocytes

Ovaries from prepubertal gilts were collected at a local slaughterhouse (VION SBL, Landshut) in a tea can filled with 500 ml of pre-warmed PBS and 1x penicillin-streptomycin pre-warmed to 38.5 °C. Following arrival to the lab, ovaries were washed several times with pre-warmed PBS (+1 % CETAB) and subsequent washing with pre-warmed PBS only. Ovaries were stored in PBS, placed on a heating plate at 38.5 °C and follicular fluid was carefully aspirated using an 18G-needle attached to 10 ml disposable syringes to collect oocytes. As the meiotic and thus maturation state of oocytes directly correlates with the size and state of the follicle, only non-bloody graafian follicles with a diameter of 3-5 mm were aspirated. Aspirated follicular fluid was stored in 15 mL tubes in a 38.5 °C incubator until all follicles were aspirated. Cumulus-oocyte-complexes (COCs) were sedimenting as a visible pellet. The supernatant was discarded and the pellet was mixed with 7 mL of embryonic working solution. For selection of high-quality oocytes, the suspension was then pipetted onto a 10 cm bacteriological petri dish that has been subdivided into equal parts by indentations. COCs were scored from A to D according to the amount of surrounding cumulus cells, with D being oocytes with no surrounding cumulus cells and A being oocytes with more than 5 surrounding layers<sup>125</sup>. A- to B-graded COCs with several layers of surrounding cumulus cells and dark, evenly distributed cytoplasm were selected and transferred to

an embryo working medium for washing. Consideration was given to transferring as little adjacent debris as possible to reduce the risk of contamination and increase the success rate of maturation. COCs were washed and then stored in a NUNC 4-well plate filled with 500 µl per well of previously equilibrated FLI-*in vitro* maturation medium. Cells were incubated for 46 hours at 38.5 °C in a triple-gas incubator (5 % CO<sub>2</sub>, 90 % N<sub>2</sub>) for *in vitro* maturation.

### 3.4.2. *In vitro*-fertilization

The day prior to *in vitro*-fertilization (IVF), two NUNC 4-well plates per 100 COCs were prepared. The wells of the first plate were each filled with 500 µl of porcine fertilization medium (PFM). The wells of the second plate were each filled with 500 µl porcine zygote medium (PZM-5), covered with a thin layer of embryonic grade mineral oil. Both plates were stored in a triple-gas incubator overnight for gas equilibration. On the day of IVF, successful maturation of COCs was determined by visual assessment of evenly granulated cytoplasm, polar body extrusion and cumulus cell expansion. COCs were washed in embryo working medium and subsequently stored in PFM until IVF. A deep-frozen straw filled with sperm of a breeding boar was thawed in water pre-warmed to 38.5 °C for 30 seconds. Sperm was diluted with pre-warmed sperm diluent and subsequently spun down at 1000 rcf for five minutes. The supernatant was discarded and a second round of diluting, spinning down and discarding supernatant was performed. Sperm was resuspended in 500 µl of previously equilibrated PFM and 20 µl or 10 µl for sperm counting and sperm viability assessment were removed, respectively. Residual sperm suspension was stored in a triple-gas incubator at 38.5 °C until further use. Sperm viability was assessed by pipetting 10 µl of sperm suspension on a pre-heated glass slide for microscopic evaluation of mass and single sperm motility, as well as sperm morphology<sup>125</sup>. Sperm count was determined by diluting 20 µl of sperm suspension with 180 µl of tap water and counting using a Neubauer improved counting chamber. An optimized sperm count (~7500 sperm per 50 COCs) was transferred to the COCs in PFM and incubated in a triple-gas incubator at 38.5 °C for 7 hours. Cumulus cells and attached were subsequently removed by forcedly pipetting zygotes up and down in embryo working medium containing 1 mg/ml hyaluronidase. Cumulus cell- and spermatozoa-free zygotes were washed twice in embryo working medium and selected for the presence of two polar bodies indicating successful fertilization. Fertilized embryos were transferred to embryo working medium and covered with embryonic grade mineral oil for subsequent microinjection of CRISPR/Cas9 constructs.

### 3.4.3. Microinjection

The injection solution containing 5 ng/µl of the CRISPR/Cas9 plasmid or ribonucleoprotein complexes (RNPs) in low Tris-EDTA was stored on ice. An empty microinjection needle was placed into the solution for filling by capillary forces. After assembly of the micromanipulation holding pipette and filled injection needle to the micromanipulator, the tip of the injection needle was gently opened by repeated tapping against the holding pipette. Groups of 20-30 zygotes were transferred into a 4 µl drop of embryo working medium covered by embryonic grade mineral oil. Zygotes were fixed to the holding pipette by applying

negative pressure, taking care to position the extruded polar bodies in a 6 o'clock position. The injection needle was gently inserted into the zygote's cytoplasm close to the polar body extrusion and ~10  $\mu$ l of injection solution was injected. Successful injection was verified visually by observing the movement of intracellular lipid droplets caused by the influx of the injection solution. The injected zygotes were located in the lower part of the 4- $\mu$ l droplet, separated from the non-injected zygotes, which were located in the upper part of the droplet. Sham-injected or non-injected zygotes served as control. Zygotes were then rinsed with PZM5 and placed in groups of 50 oocytes in each well of the NUNC 4-well plate previously filled with PZM5. Embryos were cultivated in a triple gas incubator for 12-16 hours until 2-cell stage for embryo transfer or for seven days until blastocyst development for the assessment of targeting efficiency and genotoxicity.

#### 3.4.4. Assessment of plasmid genotoxicity and targeting efficiency in blastocysts

The ratio of viable injected blastocysts to incompletely developed embryos was assessed in comparison to a sham- and non-injected group to determine the degree of plasmid genotoxicity. To analyse the efficiency of different targeting approaches, blastocysts were transferred to a PCR tube containing 10  $\mu$ l of lysis buffer and incubated at 65 °C for one hour, followed by 95 °C for ten minutes. The lysate was used as a template for genotyping and ICE analysis.

#### 3.4.5. Embryo Transfer

The day prior to embryo transfer, the transportable incubator was pre-warmed to 38.5 °C. Additionally, 15 ml HEPES-free TCM-199 medium in a 15 ml tube without lid (Tube 1) as well as 2 ml HEPES-free TCM-199 medium in a Polystyrene Round-Bottom Tube with a gas-permeable lid (Tube 2) were stored in the triple gas-incubator for equilibration of gases. On the day of embryo transfer, embryos were rinsed in working medium and transferred into the Polystyrene Round-Bottom Tube. Embryos were transported to the pig facility in tube 2 using the transportable incubator. At the pig facility, three 35 mm corning dishes were placed on a heating plate set to 38.5 °C and filled with HEPES-free TCM-199 medium from tube 1:

- Dish A contained 2 ml medium
- Dish B contained 1.5 ml medium
- Dish C contained no medium

Embryos were transferred to dish C using an unmodified glass pipette connected to a suction bulb. Tube 2 was rinsed with medium from dish B to avoid loss of embryos. Embryos were washed by transferring them into dish B and subsequently into dish C using a mouth pipette. Embryos were collected in the smallest possible volume (approx. 1 mL) into a sterile catheter, followed by 0.2 ml air and 0.2 ml HEPES-free TCM-199 medium. This segmentation facilitated the assessment of successful

subsequent embryo transfer. The filled catheter was transported to the surgery room on a sterile, pre-warmed 15 cm glass plate and stored on a heating plate at 38.5 °C until embryo transfer.

Simultaneously with the embryo preparations described, a 12-hour-fasted synchronized surrogate mother sow was anesthetized with intravenous (i.v.) application of Ketamine Hydrochloride (1.2 mg/10 kg) and Xylazine (0.5 ml/10 kg). 0.4 mg/kg bodyweight meloxicam and 15 mg/kg bodyweight Amoxicillin were applied intramuscularly (i.m.) peri-operative. Synchronization of recipient surrogate mother sows was achieved by supplementing feed of young adult sows with Altrenogest (Regumate) for 15 days. 24 h after the last Regumate administration, 750 IU equine chorion gonadotropin (ECG) were injected intramuscularly. 750 IU of human chorion gonadotropin (HCG) were injected intramuscularly 80 h after ECG injection. One to two days after HCG administration, embryo transfer was performed. The abdominal area was cleaned with warm water and soap, shaved, and disinfected using iodine solution. The recipient was fixed on a surgery table at 30 °C head down position. Self-adhesive surgery drape was placed at the abdomen, and a skin incision at height of the second to last pair teats following the Linea Alba was carried out by a trained veterinarian (Dr. Bernhard Klinger). Correct ovulation state visually assessed by inspecting the presence of fresh ovulation sites and antral follicles.

The catheter was inserted into the oviduct and 70-400 embryos were released while gently withdrawing the catheter. The abdomen was closed in three layers using single stiches for muscle and subcutaneous tissue and running stitches for skin.

Surrogate mother sows were regularly screened for pregnancy using ultrasound detection.

### 3.5. Housing and animal husbandry

#### 3.5.1. Animal housing and termination criteria

Wild-type and *TNF<sup>ΔARE</sup>* pigs were co-housed in a pig facility at the Technical University of Munich (TUM). Animals were euthanized when they met termination criteria or at intended time points, along with a control animal. All pigs were vaccinated against *Lawsonia intracellularis*, PPV, PRRS, Influenza, mycoplasma, and PCV2. No antidiarrheal medications were used. The animals received the same diet consisting of HEMO U 134 pellets (LikraWest, Germany) with 16.5% crude protein, 3% crude fat, 4% crude fiber, 5% crude ash, 0.75% calcium, 0.42% phosphorus, 0.18% sodium, 1% lysine, 0.28% methionine, and additives. Water was provided ad libitum.

#### 3.5.2. Gross phenotyping

The weight of of subset of piglets was determined every two weeks using a scale. The external appearance as well as the possible fulfillment of termination criteria were examined daily. To this end, nutritional status, general condition and behavior in the group, respiration, defecation, neurological disorders, and signs of hierarchical fighting were examined daily, as described in table 20 below.

Table 20: Clinical parameters for severity scoring for pigs predisposed to IBD.

Clinical parameter	Observation	Severity
Nutritional status	Weight identical to control group	0
	<10 % weight loss	5
	10-20 % weight loss	15
	>20 % weight loss	45
General condition / behavior in the group	Attentive behaviour of the animal, mobility	0
	Unphysiological posture, reduced movement, restlessness, reluctance to eat	5
	Curved up back, drawn up abdominal wall	15
	Apathy, isolation from the group	45
Breathing	Breathing rate unremarkable according to age	0
	Respiratory rate slightly increased	5
	Increased respiratory rate, mildly increased abdominal breathing	15
	Respiratory rate increased, moderate increased abdominal breathing	45
Defecation	No visible deviations from the control group	0
	Feces abnormal in amount, color, consistency; mild diarrhea; hard feces (Bristol stool score 1-2).	5
	Watery diarrhea, bloody feces, pieces of intestinal tissue in feces, constipation.	15
	Sunken eyes, rectal prolapse, persistent watery and/or bloody diarrhea.	45
Neurological disorders	No impairments	0
	Clamp gait, reduced vision	5
	Head tilting, stilted gait, tremors, balance disorders	15
	Coordination disorders, falling over	45

If the total score was between 5 and 15 points, interventions such as analgesia or subcutaneous fluid substitution were carried out as necessary. If the total score was between 15 and 45 points, a veterinarian was consulted and interventions were implemented. If the total score exceeded 45 points, the experiment was terminated and the animals were humanely euthanized by an authorized individual.

### 3.6. Sample isolation

#### 3.6.1. Sampling procedure

Faecal samples were collected regularly by digital sampling. Sterilized cotton swabs were used to collect samples from newborn piglets. Bristol stool score was determined during sampling. Intestinal contents and tissues were collected after death. Samples were taken from rectum, distal, medial and

proximal colon, caecum, distal ileum, medial jejunum and proximal duodenum for 16s ribosomal RNA gene amplicon sequencing. These and samples from various other organs were collected according to the tissue sampling guide for porcine biomedical models<sup>154</sup> for molecular analysis and histological examination, respectively. Blood samples were collected in appropriate monovettes and sent to an external service provider (Tiergesundheitsdienst Bayern e.V.) for a complete blood count or directly processed for PBMC isolation. Tissue for the isolation of intestinal crypts was washed with and stored in ice-cold PBS with antibiotics.

Samples (~100 mg aliquots) for 16s ribosomal RNA gene amplicon sequencing were collected in Lysing Matrix B tubes filled with 500 µl Stool DNA Stabilizer. Control samples of ambient air, as well as of the buffer used, were collected. Samples for molecular analysis were collected in cryovials. All samples were immediately placed on dry ice and stored at -80 °C until processing. Specimens for histological examination were fixed in 4% formalin for at least 2 days, followed by embedding in paraffin.

During necropsy, gross examination of tensile strength, vascularization and coloration was performed. Sizes of lymph nodes and gut length were recorded. Pictures were taken from suspicious samples using a smartphone camera (Xiaomi Redmi Note 8 Pro).

### 3.6.2. Isolation of mammalian genomic DNA from ear clip biopsies

Genomic DNA was isolated from ear biopsy using the GenElute Mammalian Genomic DNA Kit according to the manufacturer's protocol. DNA was eluted in 50 µl elution buffer and stored at -20 °C until further processed.

### 3.6.3. PBMC isolation

EDTA anti-coagulated blood was collected from anaesthetized pigs of the same litter by intravenous (i. v.) puncture of the vena jugularis. Peripheral blood mononuclear cells (PBMCs) were isolated from 15ml of fresh EDTA-blood by Ficoll-density gradient centrifugation with lymphocyte separation medium (MP Biomedicals) at 920xg for 30 min at RT with slow start and brake. Erythrocytes were lysed and 5 x 10<sup>6</sup> PBMCs per vial were frozen in 70 % FCS, 20 % DMEM and 10 % DMSO until further use or directly cultured in appropriate culture medium.

### 3.6.4. Isolation of RNA from macrophage and intestinal organoid culture

RNA was isolated from scraped off and frozen macrophage using the Allprep DNA/RNA Micro Kit according to the manufacturer's instructions. RNA was eluted in 10 µl elution buffer and stored at -80 °C until further processing.

### 3.6.5. Isolation of RNA from tissue biopsies

RNA was isolated from frozen tissue biopsies. For this purpose, small amounts of tissue (< 30 mg) were homogenized in a Lysis Tube P and a SpeedMill Plus Homogenizer before using the Monarch Total RNA Miniprep Kit with an integrated DNase digestion step according to the manufacturer's instructions. The RNA was eluted in 30 µl elution buffer and stored at -80 °C until further processing.

### 3.6.6. Isolation of proteins from tissue biopsies

Proteins were isolated from frozen tissue biopsies by homogenizing small amounts of tissue (< 30 mg) in a Lysis Tube P, that contained ice-cold 200 µl of NP-40 Buffer supplemented with 1 tab of c0mplete proteinase inhibitor per ml, and a SpeedMill Plus Homogenizer. Samples were homogenized for 30 sec, and placed on ice for 20 min. A second homogenization step was performed, again for 30 sec before samples were centrifuged for 10 min at 4 °C at full speed. The supernatants were transferred to a new eppi and stored at -80 °C until further use.

### 3.6.7. Isolation of proteins from feces

Faecal water was isolated by diluting 50 mg of feces in 400 l PBS and vortexing thoroughly. After centrifuging homogenates at 500g for 5 minutes, the supernatant was collected for a second round of centrifugation at 6000g for 5 minutes. For protein measurement, the supernatant was diluted 5-fold with 1x assay reagent.

## 3.7. Macrophage culture and LPS challenge

PBMCs were cultured in 10 ml RPMI 1640, supplemented with 10 % FCS, 1 % GlutaMax (Sigma), 1 % Pen-Strep/Amphotericin B and 10<sup>4</sup> U/ml recombinant porcine granulocyte-macrophage colony-stimulating factor (poGM-CSF) on a bacteriological plate for seven days without medium change. Equal cell numbers of derived macrophages were split on 6-well plates and cultured overnight. Since macrophages cannot easily be detached by Accutase treatment, trypsin-EDTA in combination with cell scrapers were used for this purpose.

Macrophages were divided into four groups: (1) no supplements (2) supplemented with 0.1 µg/ml LPS (3) with LPS and 150 µg/ml Polymyxin B (4) with LPS and after 45 min additionally with 10 µg/ml Actinomycin D. Supernatants and cells were harvested at timepoints 0, 45 and 90 min and frozen at -80 °C until further processing.



### 3.8. Transcript analyses

#### 3.8.1. cDNA synthesis

200 ng of total RNA was reverse-transcribed from using the LunaScript RT Master Mix Kit according to the manufacturer's instructions.

#### 3.8.2. Real-time quantitative polymerase chain reaction

To measure relative gene expression, real-time quantitative PCR (RT-qPCR) was performed using SYBR green I dye chemistry-based approach (Table 21). The RT-qPCR was carried out on a 96-well plate using QuantaStudio 5 software according to the manufacturer's instructions. All default settings were used, except for the reaction volume, which was adjusted to 10 µl, and the "fast" setting, which was used for all experiments. To test the efficiency of qPCR primers, a standard curve was generated by performing a qPCR with a dilution series of at least five dilutions of a pool of cDNA and the primers in question. The dilution series ranged from undiluted cDNA to a 1:10000 dilution of the cDNA pool. Each sample was run in duplicate, and the average Ct value of each dilution was plotted against the dilution. The slope of the regression between the dilution and the average Ct values was displayed on the graph. The primer efficiency was then calculated using the following formula:

$$Efficiency (\%) = \left(10^{\frac{1}{Slope}} - 1\right) \times 100$$

The primer efficiency was calculated to ensure the correct interpretation of results. When using the delta-delta Ct method to calculate relative gene expression, a comparable primer efficiency of both the target primers and the housekeeping gene primers was assumed. Acceptable primer efficiencies lie between (90 – 110%).

Table 21: Pipetting scheme for qPCR.

Component	Quantity
2x SYBR Green qPCR Mix	5 µl
Primer Forward	0.4 µl
Primer Reverse	0.4 µl
ddH <sub>2</sub> O	3.2 µl
cDNA	1 µl
TOTAL	10 µl

#### 3.8.3. Determination of housekeeping genes

The most stable housekeeper was determined using cDNA pools derived from small and large intestinal tissue of three animals per genotype. Optimal housekeeping genes were evaluated using the overlapping results of analyses with BestKeeper and Normfinder. In Bestkeeper, an optimal

housekeeper has a standard deviation  $<1$  ( $\pm$  CP) and  $<2$  ( $\pm$  x-fold), as well as coefficient of correlation  $\sim 1$ , while in Normfinder, small values are advantageous for both stability value and standard error.

#### 3.8.4. Prediction of RNA structures

RNAfold<sup>155</sup> was used to accomplish comparative transcript structure prediction across wild-type and mutant sequences. The introns were removed from the input sequences. The resulting sequences were then passed into RNAfold to determine structure. RNAfold employs a thermodynamic model of RNA folding that considers base pair stability as well as the energetic cost of loop structures. Based on the minimal free energy (MFE) concept, the algorithm estimates the most stable structure for a given RNA sequence. The structures were then compared, which allowed the identification of structural variations that were unique to individual sequences.

### 3.9. Protein analyses

#### 3.9.1. Measurement of protein concentrations

Protein concentrations were determined using advanced protein assay reagent. 2  $\mu$ l protein isolate was mixed with 998  $\mu$ l advanced protein assay reagent and the absorption at 600 nm was measured in triplicate. A BSA dilution series served as standard. Protein concentrations in mg/ml were calculated by multiplying the average blank-subtracted optical density (OD)-values by 30, according to the manufacturer's instructions.

#### 3.9.2. Determination of protein abundance via Western Blot

Ileal and colonic proteins were obtained by homogenizing tissue in NP-40 Buffer with cOmplete Mini Protease Inhibitor Cocktail. The protein concentrations were determined using the Bradford Assay. Protein lysates (15-40  $\mu$ l) were being focused on a 5% polyacrylamide-SDS gel at 80 V for 30 min and then separated on the underlying 12% polyacrylamide-SDS gel at 140 V for 60 min. Blotting was being performed on a methanol-activated blotting membrane in a semi-dry buffer at 80 V and 4 °C for 1 h. The blot was being blocked overnight in blocking buffer containing 5% milk powder at 4 °C. The following day, incubation with primary and secondary antibodies was taking place using the iBind flex apparatus. Blots were being developed using Pierce ECL Plus Western Blotting Substrate at optimized incubation time periods.

#### 3.9.3. Determination of protein abundance via ELISA

Faecal calprotectin protein concentrations were measured using faecal water and a commercially available poCalprotectin ELISA kit according to the manufacturer's protocol.

### 3.10. Guaiac resin-based faecal occult blood test

Chronic inflammatory bowel disease causes damage to the intestine, often resulting in blood entering the intestinal lumen and thus the stool. This occult blood can be detected using the guaiac resin method. Guaiac resin is extracted from trees of the yoke-leaf family and contains phenolic guaiac acid. This is converted from a colourless to a blue colour product by oxidation with the developing solution, which is added in the form of hydrogen peroxide. This reaction is catalysed by the pseudoperoxidase haemoglobin. Thus, the test is only positive if there are erythrocytes in the stool that have released haemoglobin. Stool from different pigs was tested according to the manufacturer's instructions.

### 3.11. Immunohistochemistry and Pas/AB-staining

Immunohistochemical (IHC) stainings were conducted using 3.5 µm formalin-fixed-paraffin-embedded (FFPE) tissue sections on SuperFrost Plus slides. Deparaffinization was accomplished by incubating the sections in descending alcohol concentrations (100%, 95%, 70%, 50%, and ddH<sub>2</sub>O). Antigen retrieval was achieved by subjecting deparaffinized slides to microwaving in Na-citrate-buffer and a pressure cooker for 23 min. To block endogenous peroxidase activity, slides were incubated in 3% H<sub>2</sub>O<sub>2</sub> in Methanol for 5 min. Tissue was made permeable by incubating slides in permeabilization solution for 5 min. Non-specific binding sites were blocked by incubating slides in 5% animal serum (species of secondary antibody) in PBS with 1% BSA for 1 h. Primary antibody incubation was performed at 4°C overnight, followed by washing with PBS. The sections were subsequently incubated with the secondary antibody, and chromogen development was accomplished using 3,3'-diaminobenzidine (DAB). For staining with low signal intensity, ABC-kits were utilized, and suitable blocking steps were taken to block endogenous biotin. Counterstaining was carried out by incubating slides in hematoxylin for 30 seconds. Negative control slides were incubated with secondary antibody only, and no staining was detected.

To stain mucus-containing cells, Periodic acid-Schiff-Alcian blue (Pas/AB) staining was performed. Deparaffinization was carried out on 3.5 µm FFPE tissue sections, followed by incubation in 1% Alcian blue solution for 3 minutes, and washing with running tap water for 3 minutes. The sections were then incubated in 1% periodic acid solution for 10 minutes to oxidize glycol groups, followed by washing with running tap water for 10 minutes. Schiff's reagent was then used to stain the formed aldehyde groups magenta for 10 minutes, followed by washing with running hot tap water for 5 minutes. Counterstaining with hematoxylin was carried out.

The stained sections were scanned using a M8 Slide Scanner (Precipoint) and analysed with Viewpoint (Precipoint). Quantification of lamina propria CD3<sup>+</sup>, IBA1<sup>+</sup>, and Ki67<sup>+</sup> cells was carried out by randomly selecting areas and calculating the ratio of positive to negative cells. Additionally, Pas/AB<sup>+</sup> and crypt Ki67<sup>+</sup> cells were quantified by counting positive cells per area within well-oriented crypts.

Immunofluorescence staining was carried out on 3.5 µm FFPE colonic sections using the following primary antibodies: anti-ZO1, ThermoScientific (61-7300) at a dilution of 1:50, and anti-occludin, LSBio (LS-B5737) at a dilution of 1:100. Goat-anti-rabbit-Alexa Fluor Plus 594, Invitrogen (A11012), was used

as the secondary antibody at a dilution of 1:100. Confocal laser scanning microscopy was performed with an Olympus FV 3000 confocal microscope equipped with a 60x/NA1.2/WD0.28 UPLSAPO60XS2 objective and water immersion. The Olympus four-channel TruSpectral detection system and the Olympus FV 3000 Imaging Software, Cells Desktop Version 1 of the Center for Advanced Light Microscopy (CALM, Technical University of Munich, Germany), were used for image acquisition and analysis.

### 3.12. Microbiomics

#### 3.12.1. High-throughput sequencing of 16s rRNA gene amplicons

Metagenomic DNA was extracted by the ZIEL Core facility as previously described<sup>156</sup>. Briefly, cells were mechanically lysed in DNA stabilization buffer and phenol/chloroform/isoamyl alcohol (25:24:1, by vol.) using a FastPrep®-24 bead beater (3 x 30 sec at maximum speed). After treatment with heat (95°C, 5 min) and centrifugation (15000 x g/5 min/4 °C), the supernatants were subjected to RNase treatment (0.1 µg/µl; Amresco) for 30 min at 37°C. Metagenomic DNA was purified using gDNA columns (Macherey-Nagel) according to the manufacturer's instructions. The concentrations and purity of the DNA samples were assessed using a NanoDrop® (Thermo Scientific) spectrophotometer. Samples were stored at 4°C during library preparation and at -20°C for longer storage. To amplify the V3/V4 region of 16S rRNA genes, a 2-step procedure was followed to limit amplification bias. Bacteria-specific primers 341F and 785R were used to amplify 12 ng of metagenomic DNA for 25 cycles. The resulting amplicons were purified using the AMPure XP system (Beckmann) and pooled in an equimolar amount before being sequenced in paired-end mode (PE275) using a MiSeq system (Illumina Inc.)<sup>157</sup>.

#### 3.12.2. 16s rRNA amplicon processing

The Integrated Microbial Next Generation Sequencing (IMNGS) pipeline<sup>158</sup> and the R shiny application Namco<sup>159</sup> were utilized for pre-processing of raw 16s rRNA amplicon reads. Trimming of five nucleotides on the 5' end and 3' end was performed for the R1 and R2 read (trim score 5) with an expected error rate of 1. Detected chimeric sequences were eliminated using UCHIME<sup>160</sup>. Sequences with relative abundance <0.25% and <300 and >600 nucleotides were excluded from analysis. Clustering of zero-radius operational taxonomic units or amplicon sequence variants (OTUs/ASVs) was done at 97% sequence similarity before filtering. Taxonomic distribution in sample groups for specific levels was carried out using the SILVA project for ribosomal RNA gene database<sup>161</sup>. To normalize the samples, rarefaction was performed by subsampling all samples to an equal depth. This allowed for an unbiased comparison of the microbial communities between samples. Downstream analysis was conducted using either Rhea<sup>151</sup> or NAMCO.

### 3.12.3. 16s rRNA amplicon sequence analyses

Alpha-Diversity analysis was performed using the Shannon effective entropy and richness index of diversity within a sample. Statistical significance of differences in alpha-diversity between sample groups was assessed using pairwise Wilcoxon test. Beta-diversity analysis was used to evaluate differences between sample groups using generalized UniFrac distances. Statistical evaluation of beta-diversity was performed by permutational multivariate analysis of variance (PERMANOVA). The Benjamin-Hochberg false-discovery rate was employed for correction of multiple testing. For the identification of shared zOTUs among sample groups, combined metadata and corresponding relative abundances of zOTUs were filtered for zOTUs which were present in at least one sample. Per group, a .tsv file was generated in which the remaining zOTUs were listed in a column "zOTUs". The amount of zOTUs was counted and intersects were generated using the list command in RStudio. Plots were generated using the plot command. Taxonomic binning based on sequence similarity was used to compare the relative abundances of taxa between sample groups. The resulting binning information was used to identify taxa that were differentially abundant between the sample groups. To identify age-related shifts in phylum abundancies, time series analysis of taxa abundances was conducted. Co-occurrence analysis of zOTUs/ASVs was performed to identify pairs of taxa that were more likely to co-occur or to identify differentially occurring nodes in various phenotype severities. In addition, analysis of confounders and explained variation was conducted to identify factors that may have affected the microbial composition in the samples, such as differences in litter group, tissue type, age, or other environmental factors. This analysis also aimed to identify factors that explained the variation in the abundance of taxa between samples. Phylogenetic analyses were performed by generating maximum-likelihood trees using FastTree based on MUSCLE alignments in MegaX<sup>162</sup>. The Wilcoxon test with Bonferroni correction for multiple testing was performed to identify statistically significant difference in the abundance of taxa between groups. In addition, linear discriminant analysis Effect Size (LEfSe) analysis was performed. This is a multivariate method that uses linear discriminant analysis (LDA) to identify features that are differentially abundant between two or more groups. It differs from the Wilcoxon test with Bonferroni correction in that it considers not only the statistical significance but also the biological relevance of the features. LEfSE identifies features that are not only statistically different between groups but also have a significant impact on distinguishing the groups. It then calculates the effect size of each feature and ranks them according to their impact on group differentiation.

### 3.12.4. Absolute quantitation of SFBs in samples

Residual metagenomic DNA extracted for amplicon sequencing of the 16s rRNA gene was used for absolute quantification of segmented filamentous bacteria (SFB) in different samples by RT-qPCR. Porcine SFB-specific primers (Grzeskowiak et al., 2021) were tested for specificity and efficiency, and a  $C_T$  value of less than 35 was considered SFB positive.

### 3.13. Flow cytometry

PBMCs were analysed for the subtypes of immune cells using flow cytometry in collaboration with Evelina Stastna from Statens Serum Institut, Denmark. The cryopreserved PBMCs were rapidly thawed in a water bath and then washed twice with RPMI1640 + 20% FCS. The cells were then incubated overnight in a V-bottom 96-well plate with RPMI1640 + 10% FCS at 37 °C and 5% CO<sub>2</sub>. The next day, cells were either stimulated with 2 µg/ml phytohemagglutinin-1 (PHA) for 6 h or left as unstimulated control. To inhibit the secretion of cytokines and thus facilitate the discrimination of subtypes via cytokine expression profiles, 10 µg/ml Brefeldin A was added for the last 4 h of stimulation. Cells were pelleted at 700 x g for 1 min, and the supernatant was discarded. 100 µl FACS wash solution was added per well and the well was centrifuged. Cells were incubated with live/dead staining solution for 30 min, washed twice with FACS wash solution, and then surface marker staining was performed with 20 µl of the appropriate antibody mix in FACS buffer for 30 min at 4 °C. After washing the cells twice, they were permeabilized and fixed by incubating with Cytotfix/Cytoperm solution for 20 min at 4 °C, followed by staining of intracellular markers with 20 µl of the appropriate antibody mix in FACS-buffer for 30 min at 4 °C. In all staining procedures, a non-staining and a fluorescence-minus-one (FMO) control were included. The samples were acquired using an AttuneNxT Auto Sampler (ThermoFisher) flow cytometer, and the PMT voltages were adjusted based on the non-staining control. Outputs were analysed using FlowJo Data Analysis Software Version 10. The analysis was performed on viable, single cells, and a minimum of 30,000 cells were recorded for each analysis.

### 3.14. Statistical analysis

Statistical comparison of differential transcript and immune cell population abundancies was performed using GraphPad Prism 8 (GraphPad 8). For group comparisons, one-way analysis of variance followed by Tukey test for multiple comparisons was computed. Pearson tests were conducted to analyse correlations. Data are presented as boxes ranging from the 25th to the 75th percentile, with whiskers leading to the lowest and highest values, and median values. P values less than 0.05 were considered statistically significant. Statistical significances differed for P values <0.05 (\*), <0.01 (\*\*), <0.001 (\*\*\*), and <0.0001 (\*\*\*\*).

## 4. Results

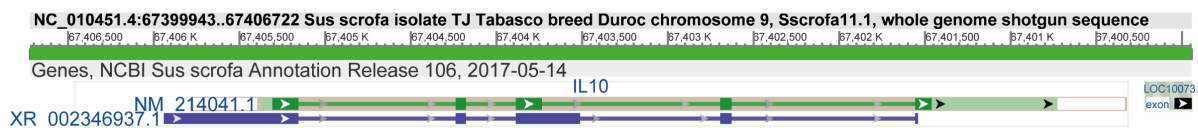
### 4.1. gRNA design and vector cloning

To generate porcine models for inflammatory bowel disease, two approaches were initially pursued, the knockout of the immunoregulator *IL10*, and the overexpression of the pro-inflammatory *TNF* by deleting mRNA-destabilizing elements in its 3' UTR. For this purpose, the target genes were first annotated, and possible protein isoforms were identified. Next, gRNAs were designed and cloned into the px330-U6-Chimeric\_BB-CBh-hSpCas9 vector. The positively tested gRNAs were used to generate IBD pigs. The generation of TNF plasmids was a part of another work and will not be described here.

#### 4.1.1. Annotation and identification of protein isoforms of the porcine *IL10* gene

For the annotation and identification of alternative variants of the porcine *IL10* gene, the corresponding entries in NCBI and Ensemble (Sscrofa11.1) databases were analysed. A major gene variant consisting of 5 exons was found in both databases. In NCBI, an additional transcript variant containing a larger exon 1, larger exon 3 and shorter exon 5 was deposited, indicating alternative splicing events (Figure 9).

A



B

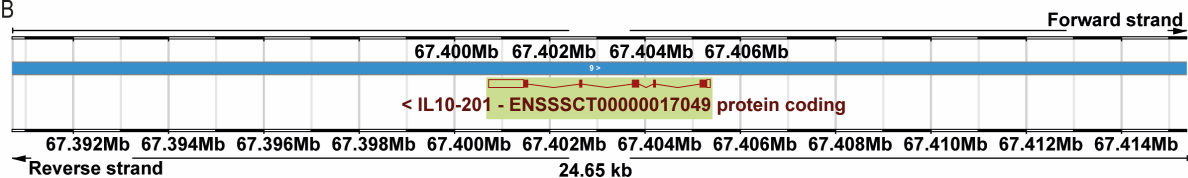


Figure 9: Porcine *IL10* gene and transcript annotation deposits found in NCBI (A) and Ensemble (B) databases. The *IL10* gene was found on porcine chromosome 9 on the reverse strand at position 67,405,777 bp to 67,405,372 bp. In NCBI, dark green boxes represent coding sequences, dark green lines represent introns, light green boxes represent untranslated regions, purple boxes represent exons found within transcripts and purple lines represent introns found within pre-mature transcripts. In Ensemble, red boxes represent coding sequences, red lines represent introns and empty red boxes represent untranslated regions.

However, since database entries of porcine genes are computationally predicted and often contain incomplete information, a comparison with the human *IL10* sequence was also used to identify possible splice variants. Two human *IL10* isoforms were found in NCBI, the first consisting of 5 exons similar to the porcine homolog, while the second consists of the last three exons. In addition, alternative splice variants with exon 3 and 4 were identified (Figure 10).

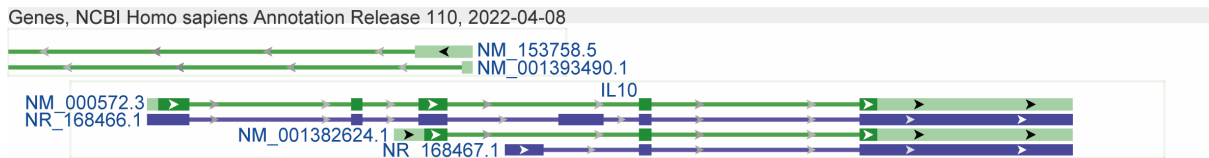


Figure 10: Human IL10 gene and transcript annotation deposits found in NCBI database. The IL10 splice variants were found on human chromosome 1 on the reverse strand at position 206,767,602 bp to 206,772,494 bp (isoform #1) and at position 206,767,602 bp to 206,771,189 bp (isoform #2), respectively. Dark green boxes represent coding sequences, dark green lines represent introns, light green boxes represent untranslated regions, purple boxes represent exons found within transcripts and purple lines represent introns found within pre-mature transcripts.

A cDNA pool was generated from bulk RNA isolates obtained from various porcine tissues, including PBMCs, liver, kidney, muscle, heart, bone, lung, colon, caecum, ileum, jejunum, and duodenum. Qualitative RT-PCR was used to screen for the presence of the second splice variant in porcine tissue, using three primer combinations. The forward primers were designed to bind within the predicted 5' UTR of exon 3 (NM\_001382624), without binding to the known splice variant. The reverse primers for each combination bind within exons 3 and 4. The primer combinations used were Check\_1 (IL10\_IsoformCheck\_Fwd1 + IL10\_IsoformCheck\_Rev1), Check\_2 (IL10\_IsoformCheck\_Fwd2 + IL10\_IsoformCheck\_Rev2), and Check\_3 (IL10\_IsoformCheck\_Fwd1 + IL10\_IsoformCheck\_Rev2) (Figure 11).

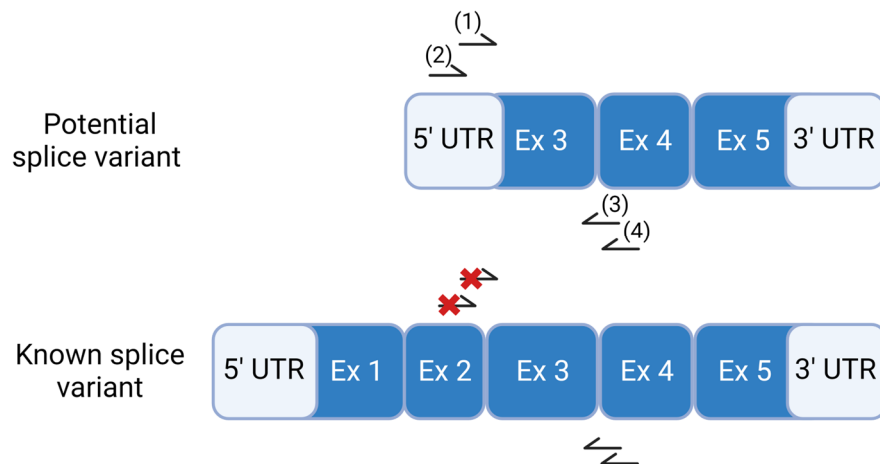


Figure 11: Schematic representation of the potential (top) and known (bottom) splice variants of the porcine IL10 transcript. Shown are coding exons (Ex), the untranslated regions (UTRs) and selected primers for the qualitative assessment of the potential second splice variant. The potential second splice variant consists of exons 3-5 of the known splice variant. The primers were selected to amplify the sequence from the novel 5'-UTR in a potential splice variant but not in the known splice variant. Primers: (1) IL10\_IsoformCheck\_Fwd1, (2) IL10\_IsoformCheck\_Fwd2, (3) IL10\_IsoformCheck\_Rev1 and (4) IL10\_IsoformCheck\_Rev2.

ACTN gene served as an internal control. No RT-PCR amplicons were generated with the primer combinations Check\_1 and Check\_2, and a larger-than-expected amplicon was generated with the primer combination Check\_3, which was identified as a nonspecific amplicon by sequencing. Actin RT-PCR generated the expected fragment (Figure 12). Thus, it was concluded that no alternative transcript is present in the porcine IL10.



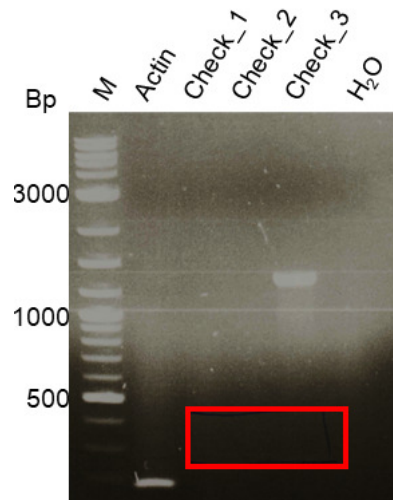


Figure 12: Qualitative RT-PCR for the identification of a porcine alternative *IL10* isoform using a cDNA pool derived from various porcine bulk RNA isolates.. Three primer combinations *Check\_1*, *Check\_2* and *Check\_3* were used to amplify a potential isoform.  $H_2O$  served as negative control, while the amplification of the *actin* gene served as positive control. (*M*) Log2-Marker indicates band sizes.

As the preferential target sequence for genome editing should be at or near the start of translation to ensure gene inactivation, exon 1 of the *IL10* gene was sequenced from five randomly selected pigs to determine if there were any SNPs deviating from the reference sequence. A deletion 47 bp upstream of the start codon was found, within the coding region no deviation was present (Figure S1).

#### 4.1.2. gRNA candidate selection

To ensure disruption of protein function with minimal off-target effects, suitable target sites and gRNAs were selected using CRISPOR. The target sites were chosen within the CDS, close to the start codon, and processable by SpCas9. The DSB repair via faulty NHEJ should lead to an open reading frame (ORF)-shift, ideally resulting in a premature stop codon or amino acid sequence alteration, disrupting protein function. The simultaneous use of multiple gRNAs was also considered, as this would increase the likelihood of DSB formation, possibly leading to the deletion of a larger gene fragment and thus also resulting in gene knockout. The selection of gRNAs also depended on specificity, efficiency, and potential off-targets. For *IL10*, suitable gRNAs were selected within the coding region of exon, with high specificity and low off-targets (Figure 13).

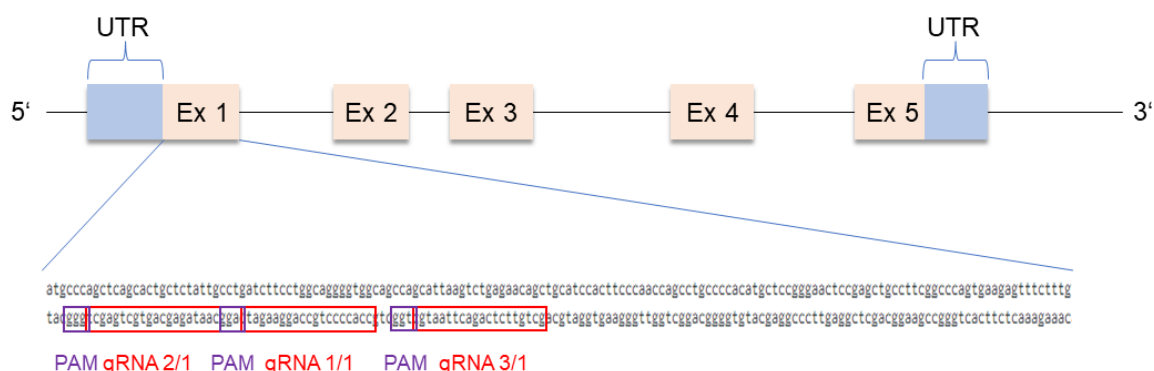


Figure 13: Schematic view of the porcine *IL10* gene and selected gRNA candidates. Shown are the 3' and 5' untranslated regions (UTR) and exons (Ex) 1-5 represented as boxes. The expanded view shows the base pair sequence of exon 1. Selected gRNA candidate target sequences are marked in red with their respective PAM site marked in purple.

Table 22 lists the selected candidates, as well as their specificity scores and predicted off-targets for the respective exons.

Table 22: Extended information for selected gRNA candidates.

gRNA no./Exon no.	gRNA sequence + PAM (strand)	Specificity score (MIT/CFD)	Off-targets for 0-1-2-3-4 mismatches (+ next to PAM)
1/1	CCACCCCTGCCAGGAAGATC AGG (Reverse)	59/80	0-1-3-35-255 (0-0-0-3-0)
2/1	GCTGTTCTCAGACTTAATGC TGG (Reverse)	87/93	0-0-2-7-95 (0-0-0-0-0)
3/1	TCGGAGTTCCCGGAGCATGC TGG (Reverse)	66/94	0-1-0-2-51 (0-0-0-1-1)

#### 4.1.3. Generation and preliminary testing of CRISPR/Cas9 targeting vectors

The corresponding gRNA candidate oligos (table 22) with overhang for digestion by a BbsI restriction enzyme were ordered, annealed, and assembled via golden gate assembly into a px330-U6-Chimeric\_BB-CBh-hSpCas9 vector ("px330 vector"). Correct integration of the gRNA oligo was validated by qualitative PCR. For the analysis of gRNA efficiencies, vectors were subsequently transfected into pKDNFs by lipofection. After selection for successfully transfected cells genomic DNA of the transfected and control pKDNFs was isolated, amplified, and sequenced. Inference of CRISPR edits (ICE) analysis was used to determine the efficiency of gene editing events. InDels were identified

in 3%, 51%, and 36% of sequencing for gRNAs 1/1, 2/1, and 3/1, respectively. Accordingly, gRNAs 2/1 and 3/1 were selected for the knockout of the *IL10* gene. Simultaneous transfection of both gRNAs into pKDNFs had a cumulative InDel efficiency of 95%, with deletion of a 47 bp sequence located between the target sequences in 44% and an insertion of a thymine molecule at position +8 bp relative to the start codon in 41 % of analysed sequences (Figure 14).

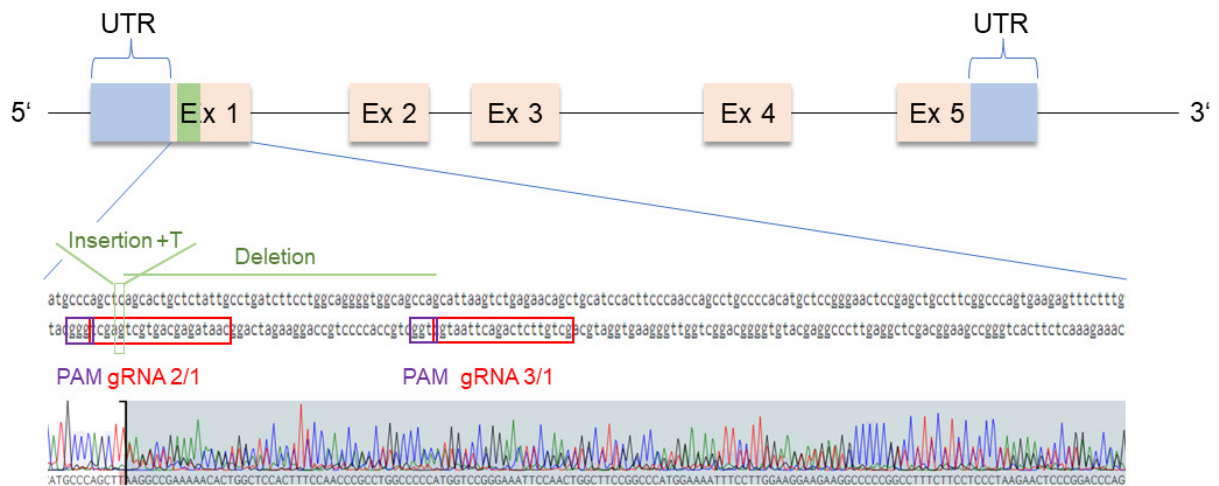


Figure 14: Schematic view of the porcine *IL10* gene and selected gRNAs. Shown are the 3' and 5' untranslated regions (UTR), exons (Ex) 1-5 represented as pink boxes and the excised sequence represented as green box. The expanded view shows the base pair sequence of exon 1. Selected gRNA target sequences are marked in red with their respective PAM site marked in purple. The insertion of a thymidine molecule (Insertion +T) and the deleted sequence are marked in green. The Sanger sequencing result is shown at the bottom. A mismatch to the reference genome is highlighted by a darker coloration.

The deletion resulted in a frame shift inducing premature stop codon at amino acid position 31, thus potentially resulting in a functional knockout of *IL10* (Figure 15).

WT

```

atgccagctcagcactgctctattgctgatcttctctggcaggggtggcagccagcattaagctctgagaacagctgcatccacttcccaaccagcctgccccacatgctccgggaactccgagctgccttcgcccagtgaaagatttctttg
tacgggtcgagctgtagcagagataacggactagaaggaccgtccccaccgtcggtcgaattcagactcttctgacgtaggtagaagggttggtcggacgggggtgacgagggccttgaggctcgacgggaagccgggtcacttctcaagaaac
M P S S A L L Y C L I F L A G V A A S I K S E N S C I H F P T S L P H M L R E L R A A F G P V K S F F
IL10 CDS: Region 1

```

$\Delta$ gRNA\_2/1 + gRNA\_3/1

```

atgccagcttaagctctgagaacagctgcatccacttcccaaccagcctgccccacatgctccgggaactccgagctgccttcgcccagtgaaagatttctttg
tacgggtcgaaattcagactcttctgacgtaggtagaagggttggtcggacgggggtgacgagggccttgaggctcgacgggaagccgggtcacttctcaagaaac
M P S L S L R T A A S T S Q P A C P T C S G N S E L P S A Q * R V S F
IL10 CDS: Region 1

```

Figure 15: Wild-type (WT, top) and mutant ( $\Delta$ gRNA\_2/1 + gRNA\_3/1, bottom) versions of the base pair and amino acid sequences of exon 1 of the *IL10* gene. An asterisk shows the premature stop codon in the mutant sequence.

## 4.2. *In vitro* analysis of vector genotoxicity and gene editing efficiency

### 4.2.1. *IL10* knockout

For the *in vitro* analysis of *IL10* knockout vector genotoxicity and gene editing efficiency in porcine embryos, ribonucleoprotein (RnP) complexes consisting of gRNAs 2/1 and 3/1, as well as the SpCas9 protein were microinjected into porcine fertilized oocytes. In contrast to the microinjection of plasmid vectors, RnP complex-injection increases InDel efficiency, reduces mosaicism and avoids random integration of backbone elements of the CRISPR/Cas9 vector. 53% (7/13) of sham-injected zygotes developed into blastocysts compared to 24% (8/33) of cells injected with gRNA 2/1 + 3/1 RnP complexes. 50% (4/8) of blastocysts injected with the gRNA 2/1 showed a deletion in exon 1 of the *IL10* gene. Two had a homozygous deletion (#1 and #6) and two were heterozygous (#3 and #8) (Figure 16).

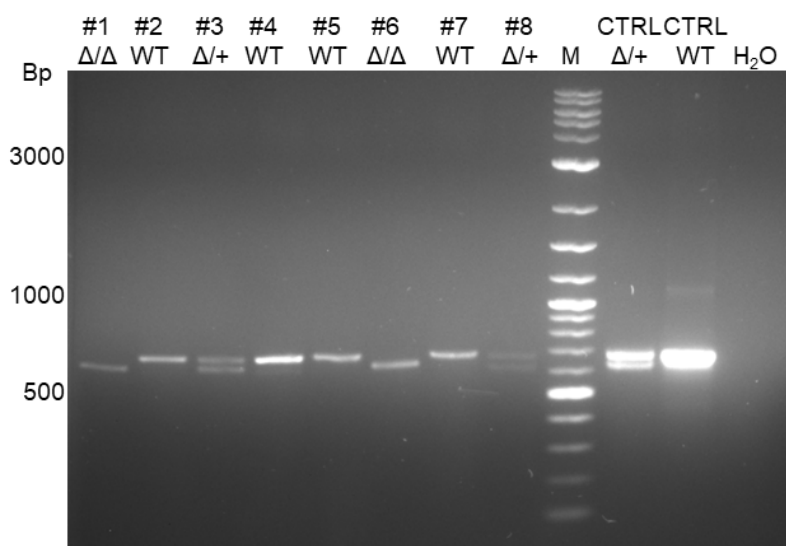


Figure 16: Genotyping PCR using primers *IL10\_Check\_F2* and *IL10\_Check\_R1* of genome edited and wild-type blastocysts following sham-microinjection and microinjection of gRNA 2/1 + 3/1 RnP complexes into *in vitro* derived zygotes. Expected size for the amplified wild-type *IL10* fragment 674 bp, for *IL10*<sup>Δ</sup> 627 bp. M, size marker. CTRL, control template. Genotypes are annotated below the respective blastocyst number.

### 4.2.2. *TNF ARE/CDE1* deletion

The CRISPR/Cas9 vector for deletion of the *TNF ARE/CDE1* sequence was also based on px330. Two separate U6-gRNA constructs, coding for gRNA 5' and gRNA3', were cloned into the vector as part of a different PhD thesis ("*TNF*  $\Delta$ A px330 vector") (Figure 17).

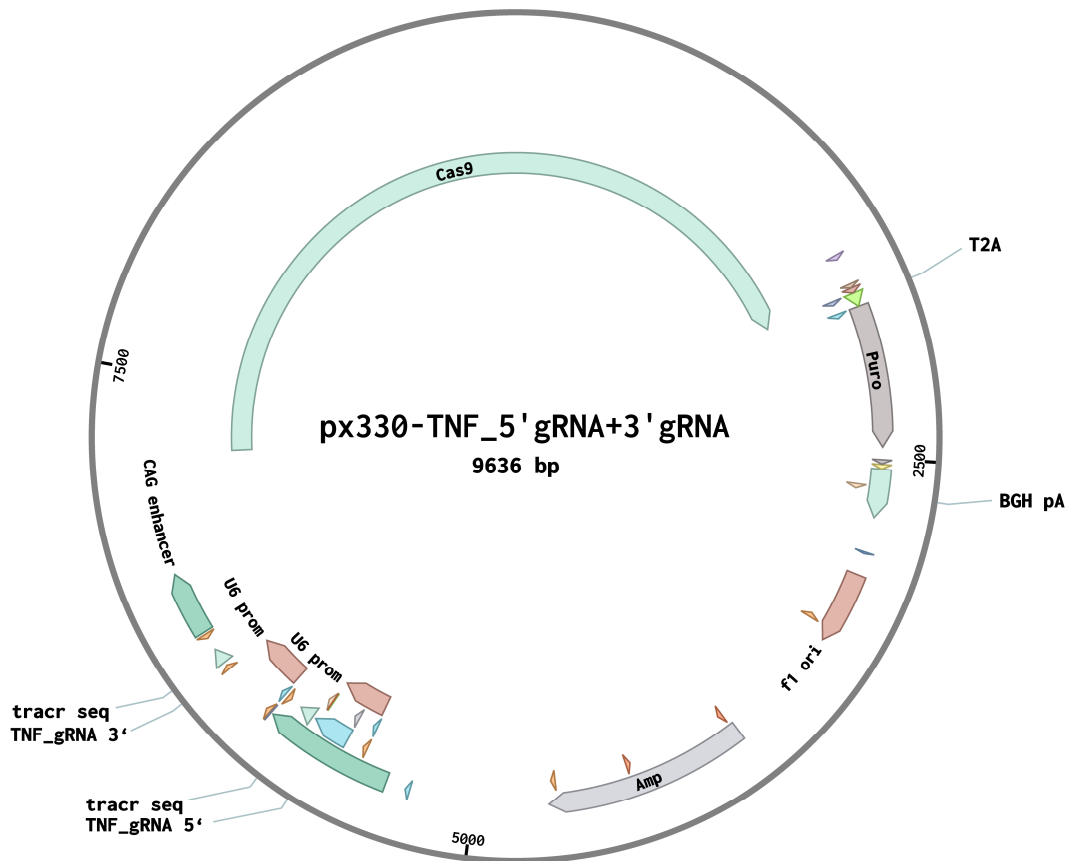


Figure 17: Plasmid map of the CRISPR/Cas9 vector used for the generation of  $TNF^{ARE}$  pigs. The plasmid is encoding two gRNAs, gRNA 5' and gRNA 3', each under the control of a separate U6 promoter (U6 prom) and the Cas9 protein under the control of a CAG promoter (CAG enhancer). The plasmid additionally encodes puromycin N-acetyltransferase (Puro), which is co-expressed with Cas9 through T2A-mediated ribosome skipping and enables selection of eukaryotic cells with puromycin, and a beta-lactamase (Amp), which enables selection of prokaryotic cells with ampicillin.

The two gRNAs recognize target sites up- or downstream of the ARE/CDE1-sequence. Introduction of DSBs at the target sites resulted in the deletion of the 96 bp ARE/CDE1 sequence ( $\Delta$ ) (Figure 18).

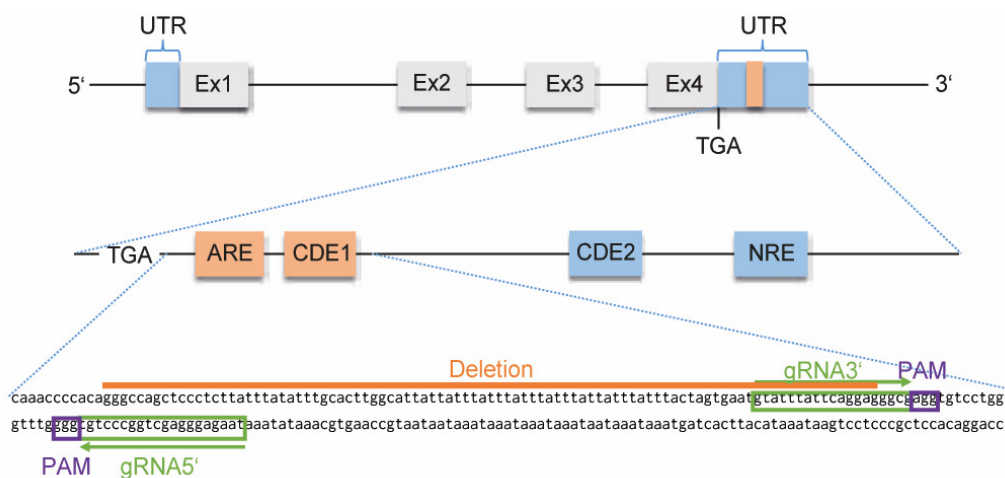


Figure 18: Strategy for the deletion of ARE and CDE1 in TNF by CRISPR/Cas9-based gene editing. The 3' UTR and the deleted sequence with the gRNA binding sites (marked in green) are shown in the enlarged view. The excised sequence (93 bp) is highlighted in orange, and the ARE, CDE, and NRE elements are displayed as boxes. Adapted from Winogrodzki et al.<sup>163</sup>.

To test the genotoxicity and editing efficiency, the *TNF*  $\Delta$ A px330 vector was microinjected into 250 *in vitro*-derived zygotes (together with Dr. Bernhard Klinger and Wei Liang, TUM). A total of 8 blastocysts were obtained and DNA was isolated. PCR amplification using primers TNF\_check\_F2/TNF\_check\_R2 followed by gel electrophoresis showed the presence of a lower band (431 bp) in 2/8 (25 %) blastocysts indicating successful excision of the ARE/CDE1 sequence (Figure 19).

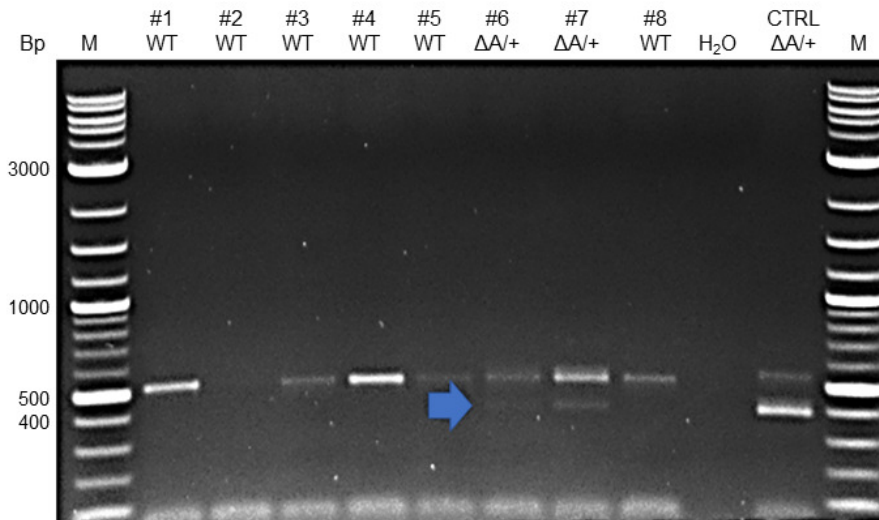


Figure 19: Genotyping PCR using primers TNF\_Check\_F2 and TNF\_Check\_R2 of genome edited and wild-type blastocysts. Expected size for the amplified wild-type *TNF* fragment 524 bp, for the mutated *TNF* <sup>$\Delta$ ARE</sup> sequence 431 bp. M, size marker. CTRL, control. Genotypes are annotated below the respective blastocyst number.

Successful deletion of the ARE/CDE1-sequence was confirmed by Sanger sequencing (Figure 20).

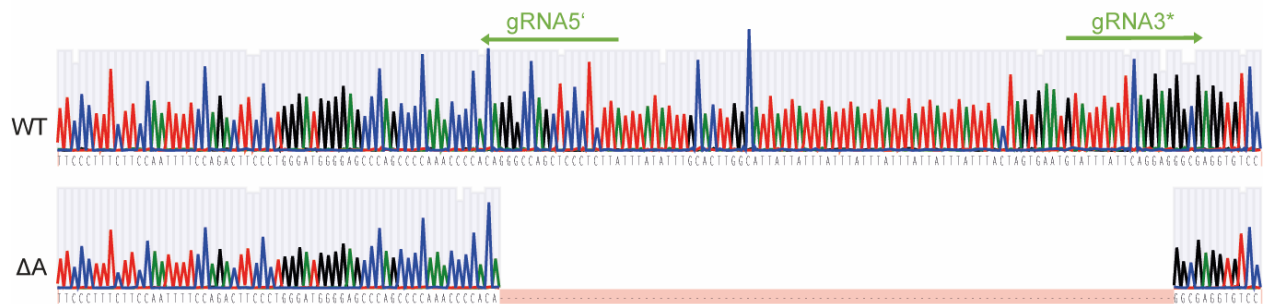


Figure 20: Sanger sequencing showing the wild-type and mutated ARE/CDE1 sequence. gRNA binding sites are marked in green. Adapted from Winogrodzki et al.<sup>163</sup>.

### 4.3. Generation of *TNF* <sup>$\Delta$ ARE</sup> pigs

For the generation of *TNF* <sup>$\Delta$ ARE</sup> pigs, 1178 *in vitro*-derived zygotes were subject to microinjection with the *TNF*  $\Delta$ A px330 vector over the course of three experiments. A total of five embryo transfers were performed, which resulted in two pregnancies and ten piglets born.



## 4.4. Genetic analyses and establishment of the pig line

### 4.4.1. Genotyping

Of the piglets born, five showed a monoallelic deletion ( $TNF^{\Delta ARE/+}$ ; pigs #1688, #1690, #1693, #1530, #1532) and two a biallelic deletion ( $TNF^{\Delta ARE/\Delta ARE}$ ; pigs #1689 and #1692) (Figure 21).

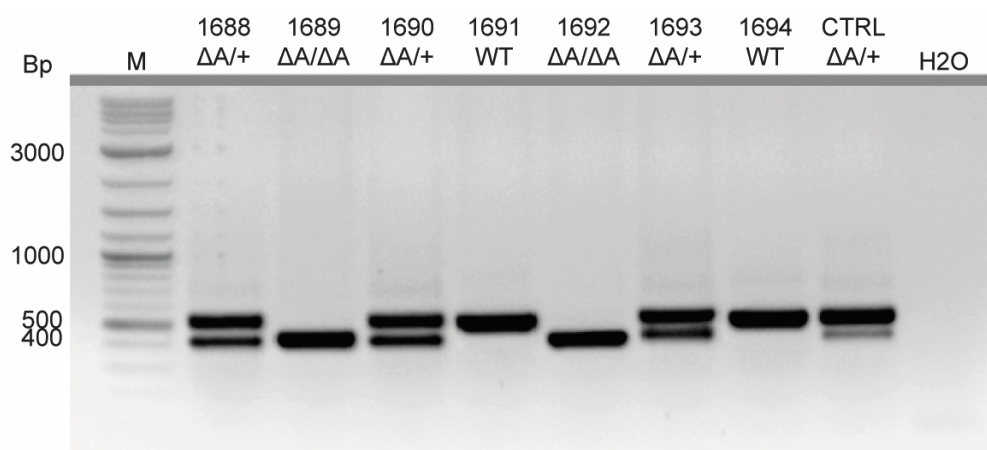


Figure 21: Genotyping PCR of genome edited founder piglets (Pigs# 1688-1694 from 1 of 2 founding litters born). M, size marker, predicts a size of 524 bp for the amplified wild-type TNF fragment and 431 bp for  $TNF^{\Delta ARE}$ . CTRL, Control. The genotypes are indicated below the respective animal number. Adapted from Winogrodzki et al.<sup>163</sup>.

The wild-type and mutant alleles were excised from the gel, purified and sequenced using the primer TNF\_check\_F2. Sequencing and ICE analysis revealed that mosaicism was present in two of the  $TNF^{\Delta ARE/+}$  animals, as shown by a high diversity of SNPs found by ICE CRISPR editing data analysis. Additionally, an insertion in the wild-type allele (+G, 3 bp upstream of the 3' gRNA PAM site) was found in one mosaic animal (#1688). The mutant allele of the other genetically modified pigs and progeny showed an identical 96 bp deletion of the ARE/CDE1 sequence. In the F<sub>0</sub> and F<sub>1</sub> generation the InDel mutation occurred in 44.14 %, 43.43 % or 32.86 % ( $R^2 > 0.9$ ) of analysed sequences when only the 5' gRNA, the 3' gRNA or both gRNAs were considered, respectively.

### 4.4.2. Comparative structural analysis of transcripts

The ability of RNA strands to fold back on themselves and form stable three-dimensional structures is fundamental to RNA transcription, splicing, translation, localization, and turnover. Accordingly, the centroid structure of the wild-type allele, the mutant allele containing the +G 3 bp upstream of the 3' gRNA PAM site and the  $TNF^{\Delta ARE}$  allele were predicted using RNAfold. The centroid structure predicts the secondary structure with minimal base pair distance to all other secondary structures in the Boltzmann ensemble and thus comes with less prediction errors compared to minimal free energy prediction models<sup>164</sup>. Comparison of secondary structures shows that the SNP in the wild-type allele of #1688 has minimal effect on the centroid structure in contrast to the  $TNF^{\Delta ARE}$  mutation, resulting in a more severe alteration (Figure 22). Thus, the effect of the SNP was expected to be neglectable.

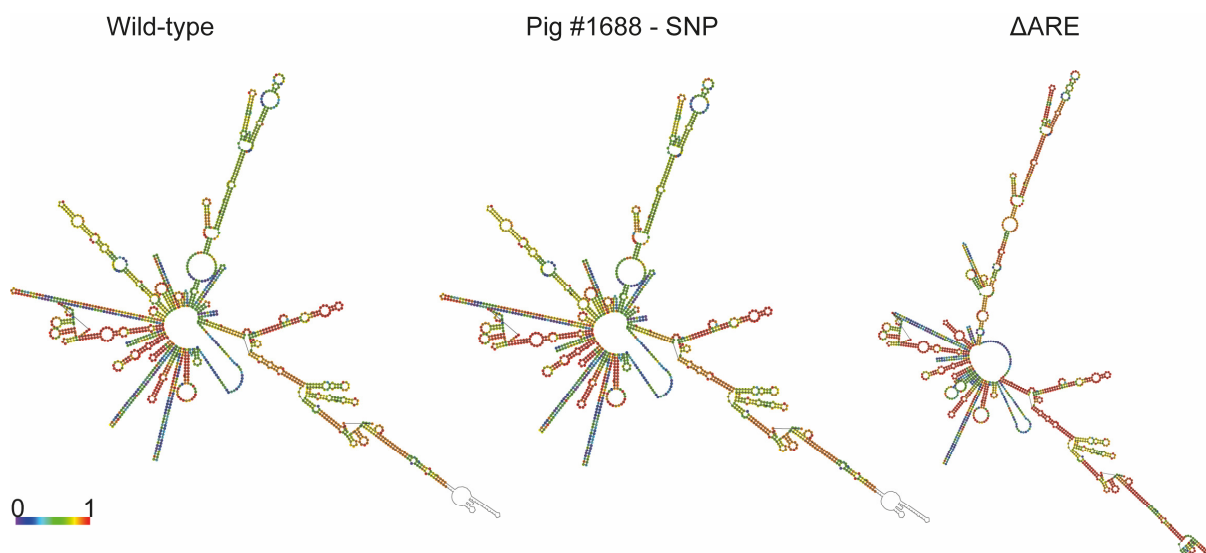


Figure 22: Wild-type, SNP- and  $\Delta$ ARE sequence and RNAfold-predicted RNA structure of the TNF transcript. Color scale shows calculated base-pair probabilities.

#### 4.4.3. Analysis of off-target and random integration events

To identify potential off-target events, the five most probable sites predicted by CRISPOR were sequenced using DNA isolated from ear clip biopsies of all founder animals. In addition, predicted off-targets within exons were sequenced if they were listed among the ten most likely off-target sites. No mutations were found in the analysed sequence (Table 23).

Table 23: Highest ranked predicted off-targets of TNF 5' gRNA (top) and 3' gRNA (bottom)

Predicted off-target 5' gRNA
2:intergenic:ENSSSCG00000015687-CXCR4
4:intergenic:CADPS-SYNPR
4:intergenic:TSHZ3-ZNF507
4:intergenic:DAXX-ENSSSCG00000001510
4:intergenic:MYC-FAM84B

Predicted off-target 3' gRNA
4:intergenic:5S_rRNA-CU463271.1
4:intron:CDH7
4:intergenic:CDCP1-ENSSSCG000000026521
4:intron:SARDH
4:intergenic:URI1-ZNF536
4:exon:VCPIP1



The possibility of a random integration event of the gene encoding puromycin-N-acetyltransferase from the injected plasmid (px330) was verified by qualitative PCR. Previously generated primers Cas9 3'LR F1 and Rosa26 BGH R1 (does not bind to the porcine Rosa26 locus), which bind up- and downstream of the puromycin-N-acetyltransferase gene and possess no binding sites within the porcine genome, were used for amplification of potentially integrated plasmid DNA. While amplification of control plasmid px330 resulted in a strong band no signal could be detected in DNA from founder animals, confirming that no random integration of the plasmid-derived gene has occurred (Figure 23).

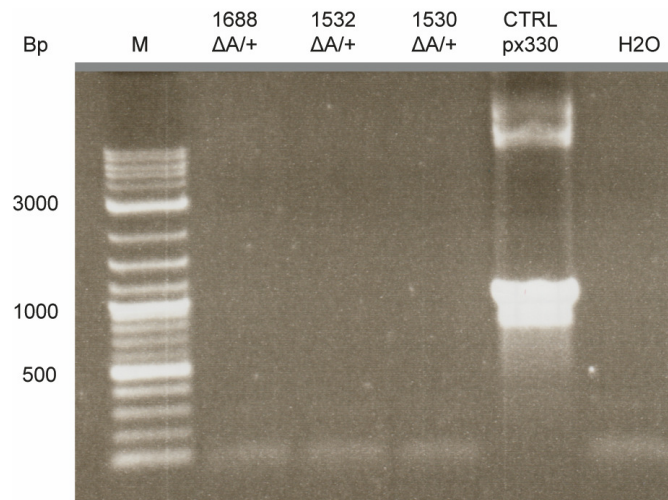


Figure 23: Qualitative PCR for the assessment of potential random integration of the puromycin-N-acetyltransferase gene into the porcine genome. M, size marker. CTRL, control.

#### 4.4.4. SNP identification in the *TNF* gene

To identify breed-specific SNPs, the *TNF* gene was sequenced in *TNF<sup>ΔARE</sup>* (n = 8) and wild-type (n = 2) pigs. The obtained sequences were compared to the publicly available pig reference genome (NCBI GCF\_000003025.6, Sscrofa 11.1). Three SNPs were identified: 548 bp downstream (intron 1), 1401 bp downstream (intron 3) and 1827 bp downstream (exon 4) of the CDS start odon (Figure 24).

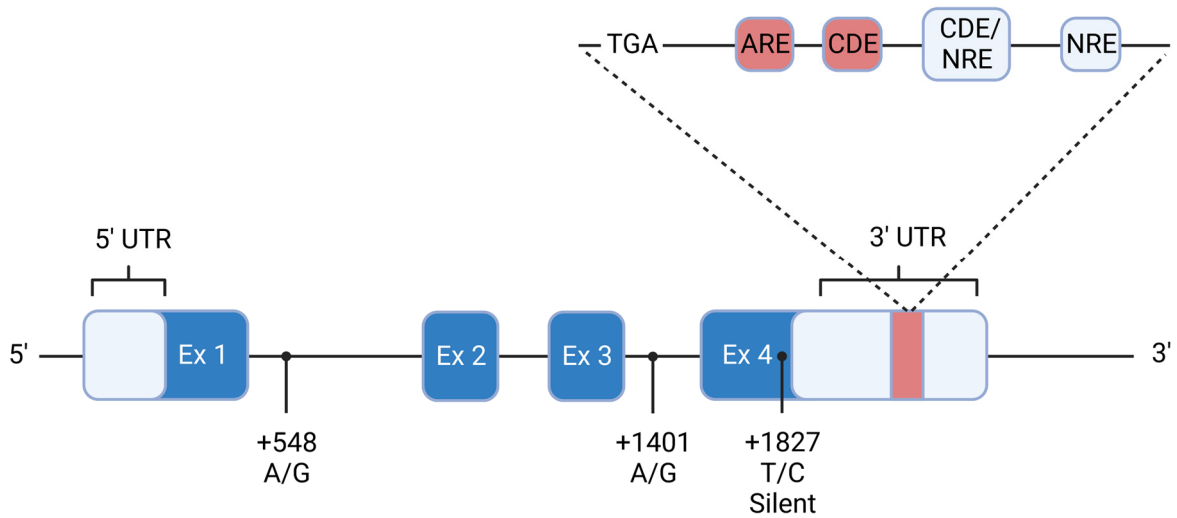


Figure 24: Overview of identified SNPs in the *TNF* gene. Dark blue boxes represent exons, light blue boxes mark 5' and 3' untranslated region (UTR). The ARE/CDE1 sequence is marked in red. The extension shows the stop codon (TGA), and the ARE, CDE1, CDE2, ADE and NRE elements. Black lines between the exons are representing introns. The position and type of SNPs are indicated.

#### 4.4.5. Breeding strategy of *TNF<sup>ΔARE</sup>* pigs

For the breeding, *TNF* pigs were selected based on several factors and mated accordingly: (1) presence of mosaicism, (2) presence of an InDel mutation, (3) severity of phenotype, (4) size matching of breeding partners, (5) age of the animals. *TNF<sup>ΔARE/+</sup>* pigs that did not exhibit mosaicism and had an intact wild-type allele were preferably mated with genotype- and age-matched pigs of a different litter. To exclude the possible effect of the mosaicism and the SNP found in the second allele (indel) on the phenotype in mutant offspring, mosaic *TNF<sup>ΔARE/indel</sup>* pigs were mated with wild-type animals. Progeny were screened by sequencing to confirm correct excision of the ARE/CDE1, or the presence of the indel allele. 25 % (2/8) F<sub>1</sub> offspring inherited the indel mutation close to the 3' gRNA PAM site (*TNF<sup>indel/+</sup>*, Figure 25), indicating mosaicism of the InDel. However, these pigs did not show phenotypes differing from wild-type controls.

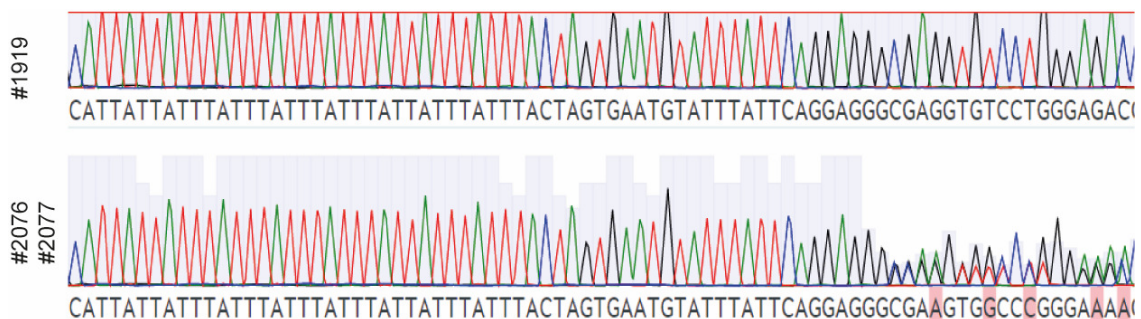


Figure 25: Representative sanger sequencing result of offspring without (top) and with (bottom) inherited mutations in close proximity to the ARE/CDE region. Mutations are highlighted in red.

#### 4.4.6. Influence of sex on genotype and phenotype

Eleven  $TNF^{\Delta ARE/+}$  and two  $TNF^{\Delta ARE/\Delta ARE}$  animals were born in the F<sub>1</sub> generation, seven  $TNF^{\Delta ARE/+}$  and four  $TNF^{\Delta ARE/\Delta ARE}$  animals in the F<sub>2</sub> generation, and 4  $TNF^{\Delta ARE/+}$  and one  $TNF^{\Delta ARE/\Delta ARE}$  animal in the F<sub>3</sub> generation. In total, 30 male (9 wild-type, 18  $TNF^{\Delta ARE/+}$ , 3  $TNF^{\Delta ARE/\Delta ARE}$ ) and 25 female animals (10 wild-type, 12  $TNF^{\Delta ARE/+}$ , 3  $TNF^{\Delta ARE/\Delta ARE}$ ) were born. The low number of homozygous mutants is most likely due to the fact that it was difficult to obtain heterozygous females of reproductive age for mating, which hindered breeding success. Fisher's exact test was used to determine sex dependency of the disease manifestation time point for  $TNF^{\Delta ARE/+}$  pigs (early onset < 12 months, late or no onset > 12 months), no significant correlation was found ( $\alpha = 0.05$ ,  $p = 1$ ).  $\chi^2$  test was used to determine sex dependence of the genotype (mutants contain at least one  $TNF^{\Delta ARE}$  allele), no significant correlation was found ( $\alpha = 0.05$ ,  $\chi^2 = 0.6031$ ,  $p = .437409$ ) (Figure 26).

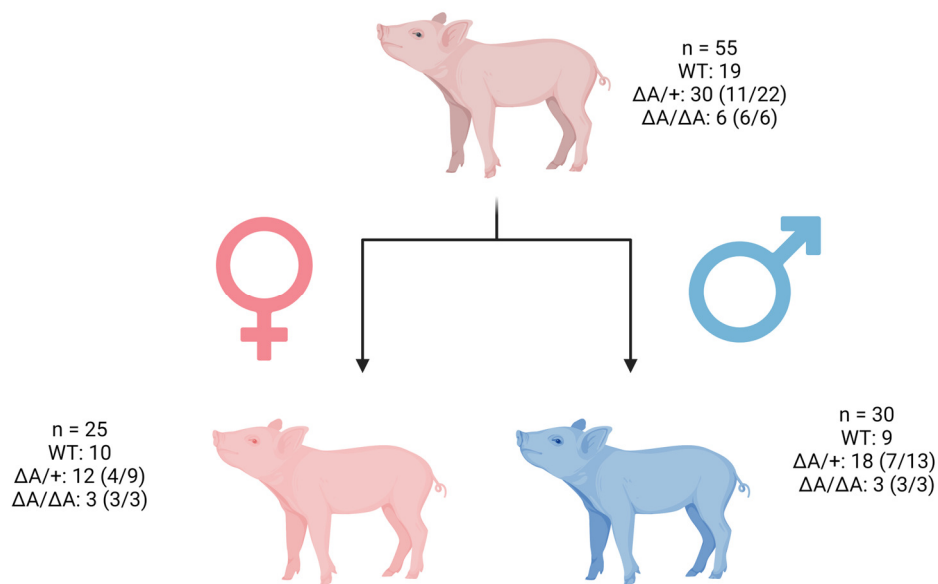


Figure 26: Sex distribution of genotypes. Shown are the total number of pigs  $n$  (top), the number of wild-types (WT),  $TNF^{\Delta ARE/+}$  ( $\Delta A/+$ ) and  $TNF^{\Delta ARE/\Delta ARE}$  pigs ( $\Delta A/\Delta A$ ), regardless of further mutations (e.g. including  $APC^{1311/+} \times TNF^{\Delta ARE/+}$ ). The numbers of pigs showing an early disease onset per pigs with the same genotype are shown in brackets, only  $TNF^{\Delta ARE/+}$  or  $TNF^{\Delta ARE/\Delta ARE}$  pigs were considered (e.g. excluding  $TNF^{\Delta ARE/+} \times APC^{1311/+}$ ).

The phylogenetic tree visualization of representative litters clearly shows that the pathophenotype is present in all homozygous offspring. In contrast, the pathophenotype in heterozygotes occurs independently of the sex and phenotype of the parents, indicating that both genetic and environmental factors may contribute to the disease's etiology (Figure 27). The inheritance patterns observed in the matings only partially conform to Mendelian inheritance patterns. In a mating between a heterozygote and a wild-type, a 1:1 ratio of genotypes would be expected, but a 6:1 or 9:4 ratio was observed, respectively. Similarly, in a mating between two heterozygotes, a 1:2:1 ratio of wild-type:heterozygote:homozygote would be expected, but a 3:4:4 ratio was observed. However, due to the small sample size, these deviations may be attributed to chance. It should be noted that the

observed inheritance patterns were accompanied by variations in disease penetrance and expressivity, which may also indicate the involvement of non-Mendelian factors.

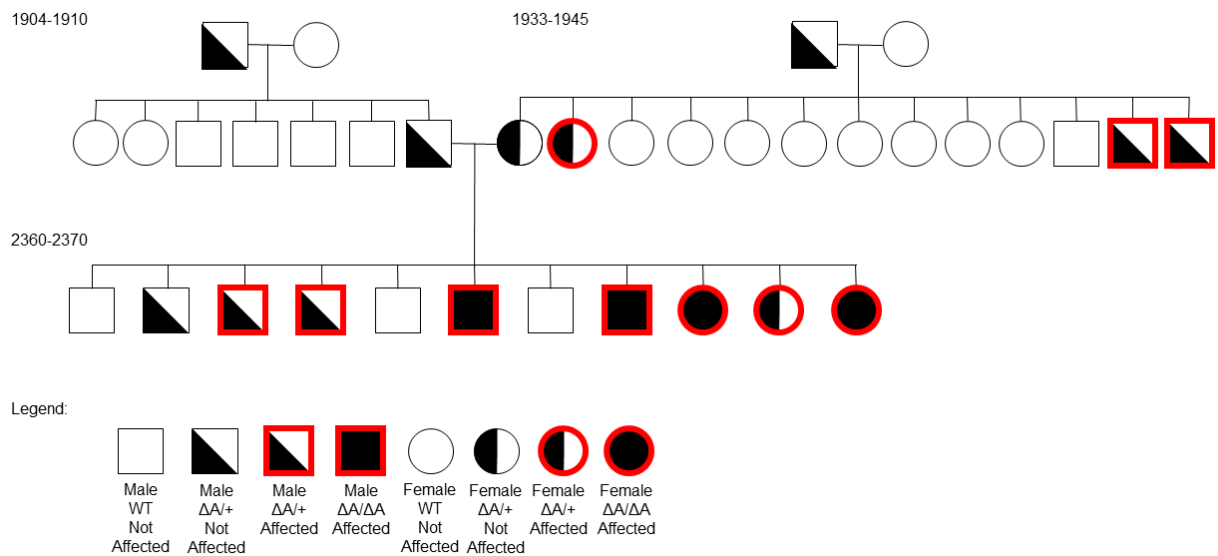


Figure 27: Phylogenetic tree visualizing sex, geno- and phenotype distribution for representative litters 1904-1910, 1933-1945 and 2360-2370.

#### 4.5. Phenotypic characterization of the $TNF^{\Delta ARE}$ pig model

Based on the pig sampling guide by Albl et al.<sup>154</sup> and the score sheets submitted with the animal experiment application, an evaluation score sheet was established for the classification of phenotype. The animals' health status was evaluated on a regular basis. Health-relevant data such as weight and stool consistency were recorded. Upon reaching a termination criterion, the diseased animals were euthanized, and samples collected. Wild-type littermates were used as control animals. The primary focus of sampling was the gastrointestinal region, although other tissues such as pancreas, lung, liver, heart, skin, brain, fat, trachea, oesophagus, kidney and muscle were also examined.

##### 4.5.1. Phenotyping

Average weight gain was determined for three wild-type, four  $TNF^{\Delta ARE/+}$ , and three  $TNF^{\Delta ARE/\Delta ARE}$  pigs of the same litter (pigs #2360-2370). In the first 39 days, weight did not differ statistically significantly between groups, with  $TNF^{\Delta ARE/\Delta ARE}$  pigs tending to weigh the least and wild-type pigs the most (Figure 28). An average weight gain for this period was 0.15 kg/day (wild-type), 0.16 kg/day ( $TNF^{\Delta ARE/+}$ ), and 0.12 kg/day ( $TNF^{\Delta ARE/\Delta ARE}$ ), respectively.

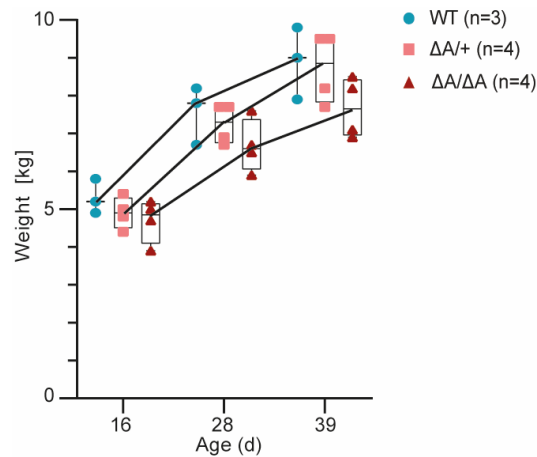


Figure 28: Wild-type, heterozygous, and homozygous  $TNF^{\Delta ARE}$  siblings' weight [kg] ranged from 16 to 39 days. Adapted from Winogrodzki et al.<sup>163</sup>.

A common deterioration in the health status of  $TNF^{\Delta ARE}$  pigs was observed shortly after weaning (after 35 days). After weaning, all  $TNF^{\Delta ARE/\Delta ARE}$  pigs and 11/22 (50 %) of  $TNF^{\Delta ARE/+}$  pigs showed chronic diarrhea. The persistent diarrhoea was accompanied by a failure to gain weight and, in severe cases, a gradual loss of body weight and increasing apathy. Weight gain of non-diseased mutant animals did not show statistically significant differences in comparison to wild-type pigs. The mean time to reach termination criteria was 68.7 days (median 68 days) for  $TNF^{\Delta ARE/\Delta ARE}$  pigs and 192.7 days (median 104.5 days) for  $TNF^{\Delta ARE/+}$  pigs (Figure 29).

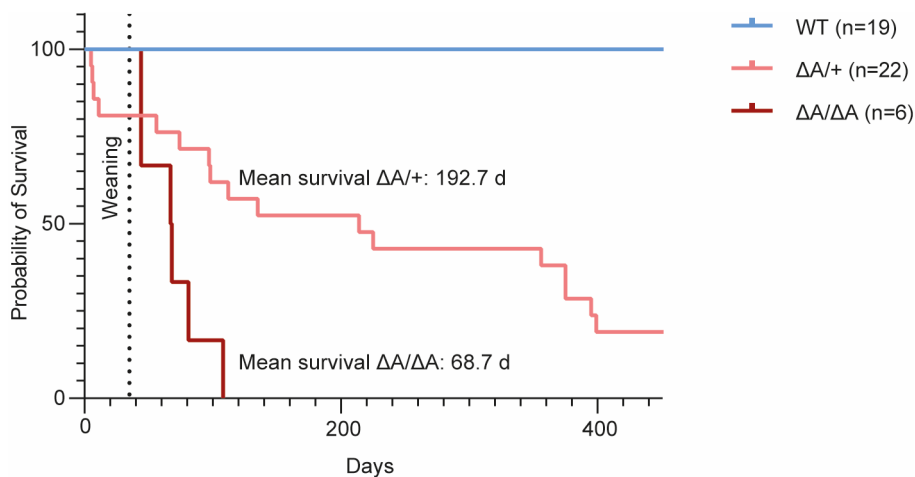


Figure 29: Kaplan-Meier diagram showing the time at which the animals were killed due to their declining health status. Indicated are the mean survival times for  $TNF^{\Delta ARE/+}$  and  $TNF^{\Delta ARE/\Delta ARE}$  pigs that had to be killed. The time point of weaning is indicated at 35 days. Adapted from Winogrodzki et al.<sup>163</sup>.

The intestinal tissue of  $TNF^{\Delta ARE}$  pigs was generally fatter with frequently observed “creeping” fat patches that are believed to be a harmful plug of leaky intestinal segments<sup>165</sup>. The intestine of diseased  $TNF^{\Delta ARE}$  pigs was easily ruptured, exhibited greatly increased vascularization, and showed discolouration due to hemorrhagic and necrotic processes. In addition, the mesenteric lymph nodes

were swollen up to fourfold in size and in some animals stricturing of the small intestine occurred, resulting from fibrotic tissue segments (Figure 30).

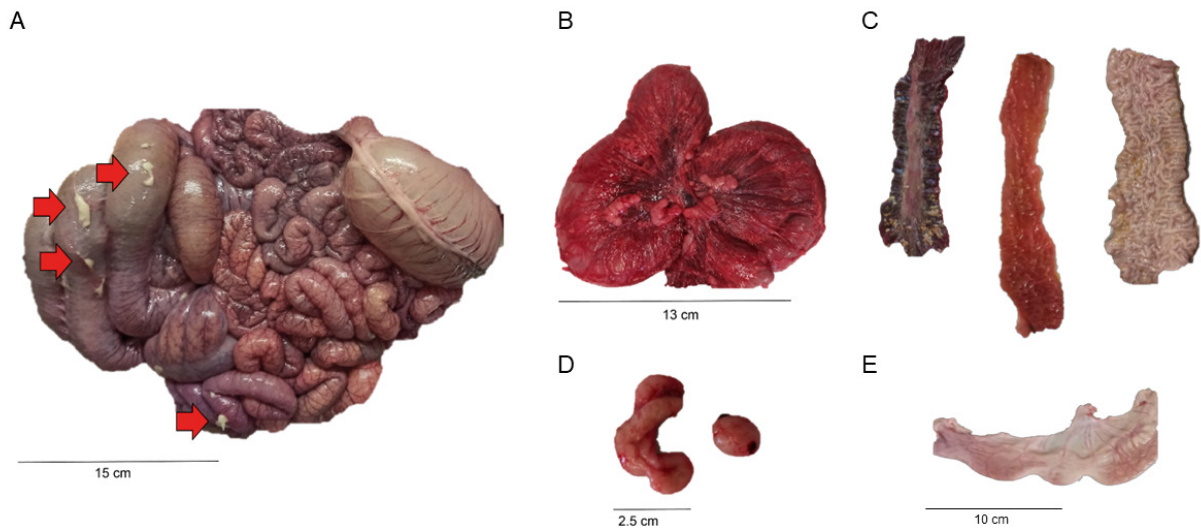


Figure 30: Frequent macroscopic gastrointestinal findings in diseased  $TNF^{\Delta ARE}$  pigs. (A) Colonic "creeping" fat patches and (B) a generally more vascularized phenotype were observed frequently. (C) Intestinal mucosal tissue was found to be highly (left) or intermediate (middle) inflamed compared to wild-type tissue (right). (D) Mesenteric lymph nodes were found to be swollen (left) compared to wild-type lymph nodes (right). (E) Stricturing of the small intestine was frequently observed. Size bars are shown.

Biopsies of the intestinal mucosa were taken from the rectum, distal, medial, and proximal colon, caecum, distal ileum, medial jejunum, and proximal duodenum for histological and molecular analyses, as well as intestinal content for 16s rRNA gene amplicon sequencing, metabolomics and culture of intestinal bacteria. The intestinal contents had a Bristol stool score of 3-4 in wild-type controls, 5-6 in mildly diseased animals in the ileocolitic region and a Bristol stool score of higher than 6 in severely diseased animals throughout the intestine. An admixture of blood and intestinal mucosa was evident in severely diseased animals, a positive faecal occult test result was found for two severely inflamed individuals (Figure 31). In the proximal duodenum of diseased swine, green staining of the intestinal contents was frequently observed. The intensity of faecal odour correlated with the disease severity, especially in the ceacal compartment.



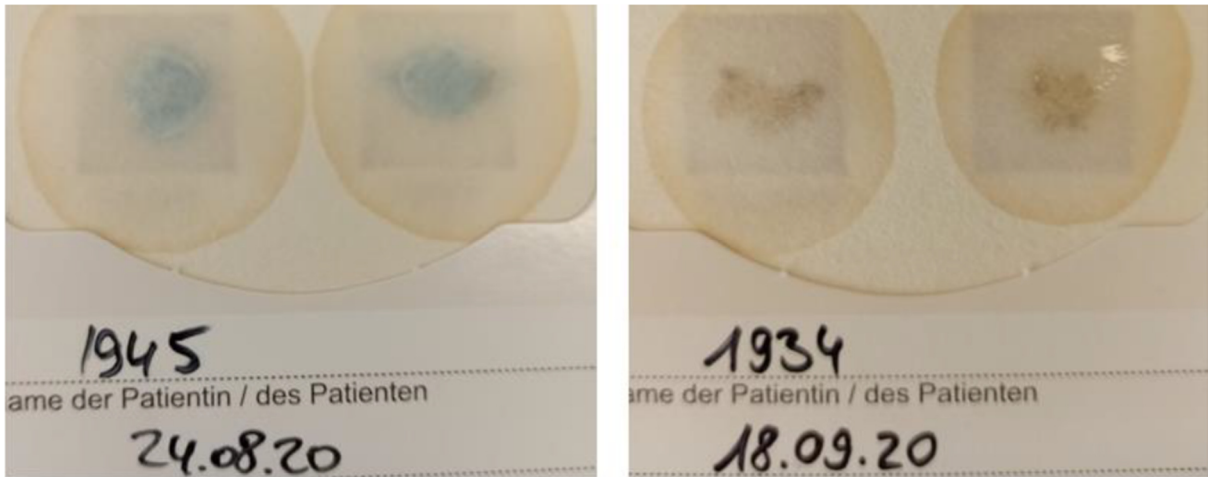


Figure 31: Representative results from a (left) positive and (right) negative occult test using faecal samples. The presence of blood in the sample leads to a colour change from colourless to blue.

The intestine was opened, cleaned, and macroscopically examined for aberrant mucosal coloration, stricturing, loss of mucosal folds and crusting. Diseased  $TNF^{\Delta ARE}$  pigs frequently showed intestinal edema and hemorrhage throughout the colon and segmentally in the small intestine (Figures 32 and 33).

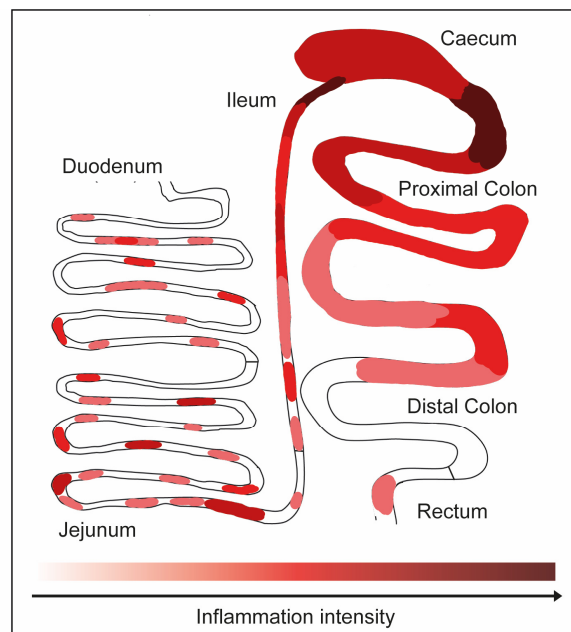


Figure 32: Illustration of the intestinal tract and areas of inflammation. Increased inflammation is indicated by darker red coloring. Adapted from Winogrodzki et al.<sup>163</sup>.

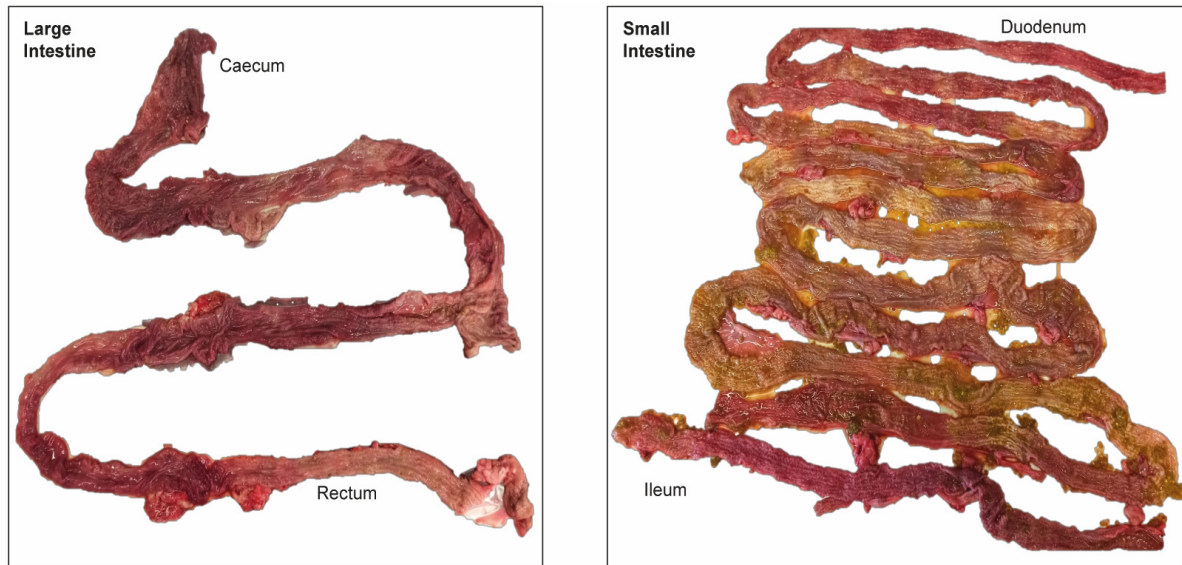


Figure 33: Images showing the inflamed large and small bowel. In the large intestine, there were continuous macroscopically visible symptoms of inflammation; in the small intestine, these signs were segmental. Adapted from Winogrodzki et al.<sup>163</sup>.

Anal prolapse was not observed. Caecal hemorrhage and accumulation of fibrinous exudates were observed in  $TNF^{\Delta ARE/\Delta ARE}$  (2/5) and  $TNF^{\Delta ARE/+}$  (2/18) pigs. The strongest observable modification in  $TNF^{\Delta ARE/\Delta ARE}$  pigs was an ulcerative enteritis, which was occasionally coated with diphtheritic membranes in the caecum (Figure 34).



Figure 34: Crust formation in the caecum of a  $TNF^{\Delta ARE/\Delta ARE}$  pig. The crust was found to consist of diphtheritic membranes. Adapted from Winogrodzki et al.<sup>163</sup>.

Whole body examination was carried out by a veterinarian pathologist from the TGD Bayern e. V. on  $TNF^{\Delta ARE/+}$  animal (#2079) and control wild-type littermate (#2077). It showed focal adhesions of the pleura pulmonalis to the pleura costalis in pig #2079 that were detachable only with loss of substance.



A cranioventral condensed atelectatic lung with suspected fibrinoid necrosis, as well as fibrosis of the tissue, was also observed. Pig #2079 showed the presence of neutrophils, macrophages, and single multinucleated syncytia in the lungs with little fibrin in the air-bearing pathways. In addition, marked bronchus-associated lymphoid tissue (BALT) hyperplasia was noted, as well as mononuclear infiltrates perivascularly and septally, and pleural fibrosis. Overall, the  $TNF^{\Delta ARE/+}$  animal was found to have moderate, partly fibrinous, partly bronchointerstitial, cranioventral pneumonia, with positive results when tested for *P. Multocida* and *M. Hyopneumoniae*.

The knee joints of both examined animals (#2079, #2077) showed increased filling with markedly reddened and shaggy synovium. However, there were no increased signs of rheumatoid arthritis for mutant pigs in contrast to what was found in the corresponding mouse model<sup>58</sup>. Villous hypertrophy of the synovial membrane was observed in the joint, as well as little fibrin on it. In addition, lymphocytes with follicular formation and granulocytes were observed. Low-grade fibroblastic pleuritis and moderate hypertrophic and mixed-cell synovitis of the right knee joint were found. However, regardless of genotype, all individuals in this litter suffered from a paw malformation from birth, as did their sire. Accordingly, the control animal was also found to suffer from low-grade hypertrophic synovitis of the right stifle joint.

Moreover, stiff lung tissue in pig #2079 indicating pulmonary fibrosis, reduction of the neck fat volume indicating emaciation and nutrient malabsorption, as well as diphteric membrane covers in the stomach were found frequently. It is worth noting that  $TNF^{\Delta ARE/+}$  animal (#2079) showed several pathological findings, such as cranioventral pneumonia and pulmonary fibrosis, which may be related to the  $TNF^{\Delta ARE}$  genotype. However, other pathological findings, such as paw malformation and hypertrophic synovitis, were found in both  $TNF^{\Delta ARE/+}$  animal and control wild-type littermate, indicating that they may not be related to the mutation.

As IBD patients are known to frequently suffer from ankylosing spondylitis<sup>166</sup>, the spine and ribs were macroscopically examined by the author of this dissertation for vertebral body fusion and regarding mobility. No abnormalities of the spine or ribs indicative of ankylosing spondylitis were found in the two examined severely diseased  $TNF^{\Delta ARE/\Delta ARE}$  animals (Figure 35).



Figure 35: Image of a spinal cord of a severely diseased  $TNF^{\Delta ARE/\Delta ARE}$  animal that has been freed from muscle and fat tissue, and ribs. Size bar displays reference size.

#### 4.5.2. Microscopic findings

H&E-stained gut sections were sent for the histopathological evaluation by a certified pathologist with experience in human pathologies (Dr. Katja Steiger, TUM). 67% (4/6) of the  $TNF^{ARE/+}$  animals displayed ileitis and/or colitis with mixed lamina propria infiltrations that frequently extended into the tela submucosa, along with a (fibrino-)suppurative serositis and GALT activation. One of these animals showed regular herniation of crypts through the lamina muscularis mucosae and widespread development of crypt abscesses (Figure 36).

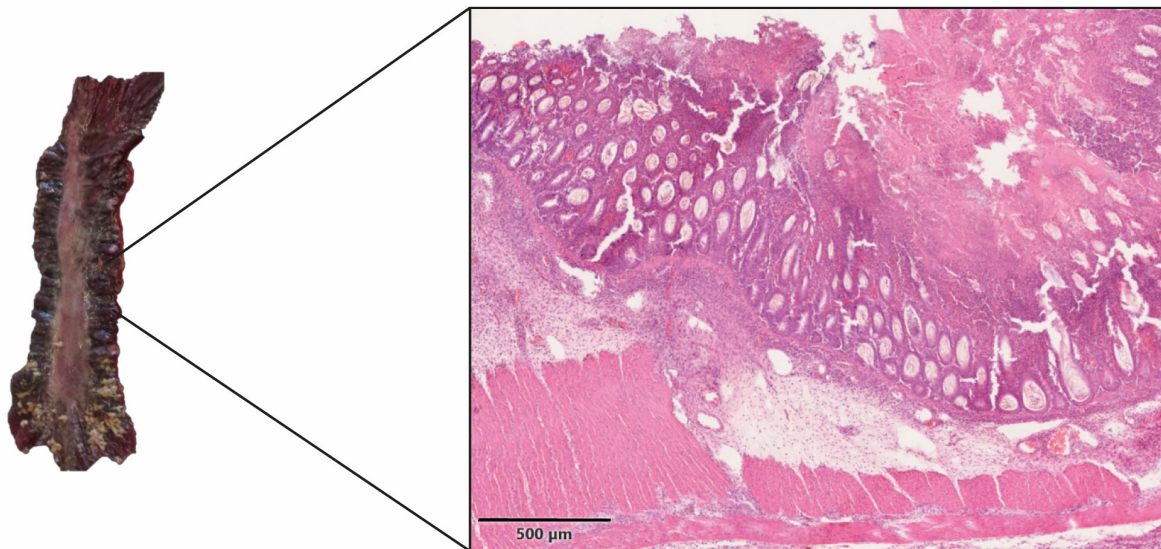


Figure 36: Necrotic colonic mucosal tissue specimen of a severely diseased  $TNF^{\Delta ARE/+}$  animal. Corresponding H&E-stained tissue section is shown. Herniation of crypts and fibrinous exudates are shown in this tissue section.

Ulceration of the lamina propria mucosae with mixed infiltration and development of a fibroangioblastic granulation tissue was also observed in one of the  $TNF^{\Delta ARE/+}$  animals. The  $TNF^{\Delta ARE/\Delta ARE}$  pigs showed more severe intestinal alterations than the  $TNF^{\Delta ARE/+}$  littermates, up to severe ulcerative inflammation with crust formation (Figure 37).

The pathologist identified impaired intestinal barrier function in a  $TNF^{\Delta ARE/\Delta ARE}$  pig, as evidenced by the invasion of *Balantidium Coli* into the mucosa (Figure 38).



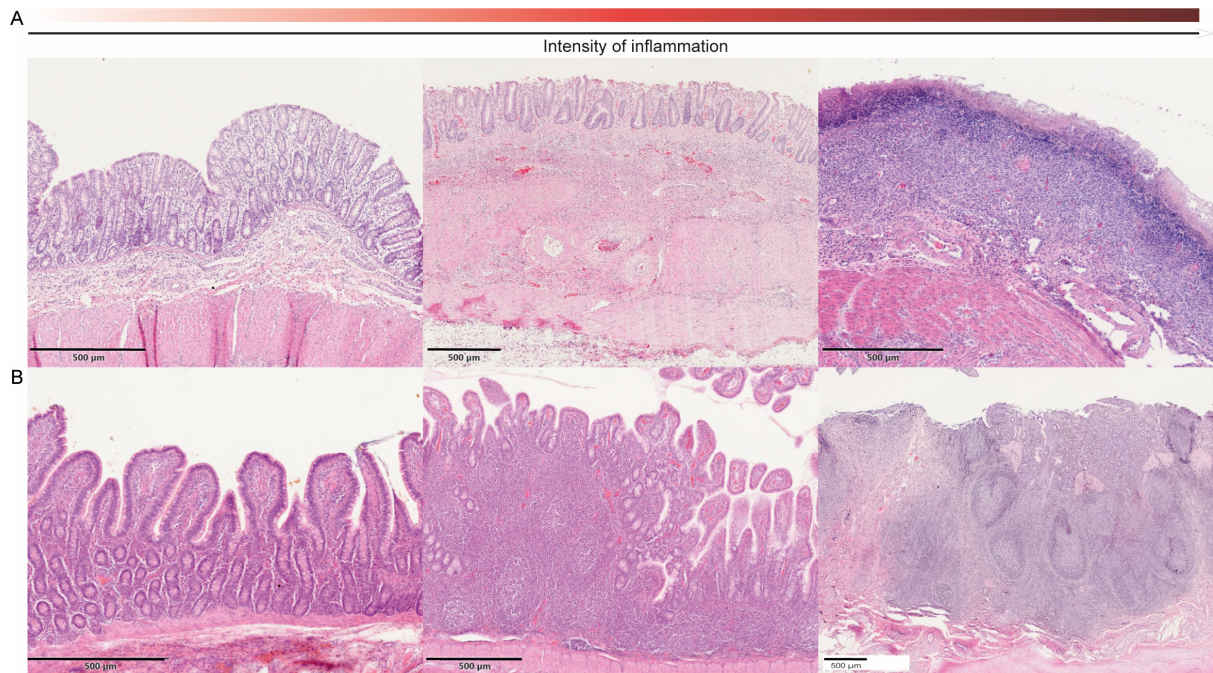


Figure 37: Representative images of H&E-stained colonic and ileal gut sections. Shown are non-inflamed (left), mildly (middle) and highly inflamed (right) tissue sections of the colon (top) and ileum (bottom). Bars indicate 500 µm.

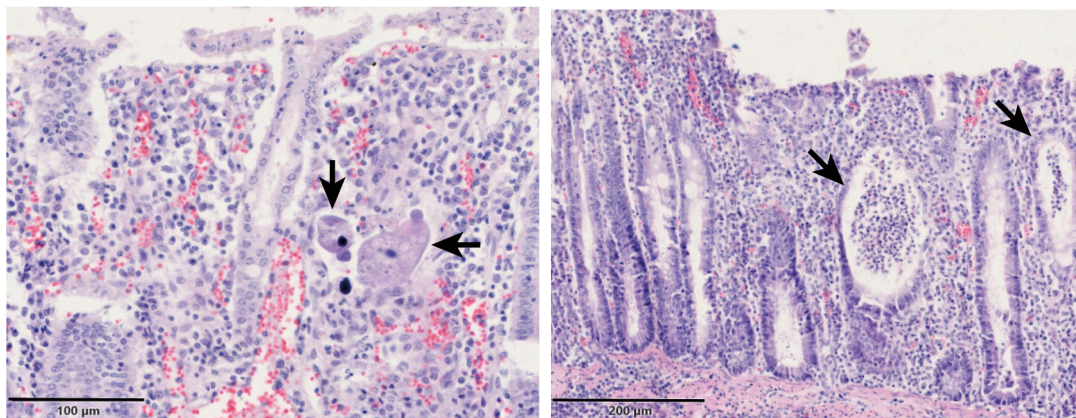


Figure 38: Image of H&E-stained colonic tissue section with invasive *Balantidium Coli*. Arrows show bacterial localization. Size bars display reference size. Evaluation was performed by Dr. Katja Steiger. Adapted from Winogrodzki et al.<sup>163</sup>.

To further investigate a potentially impaired barrier integrity, tight junction (TJ) analysis and the abundance of zona occludens-1 (ZO-1) and occludin (OCLN) proteins was investigated in inflamed colonic tissue from *TNF<sup>ΔARE</sup>* and healthy wild-type pigs. Western Blots showed considerably lower protein levels in most (5 out of 6) mutant pigs compared to wild-types (Figures 39 and S2).



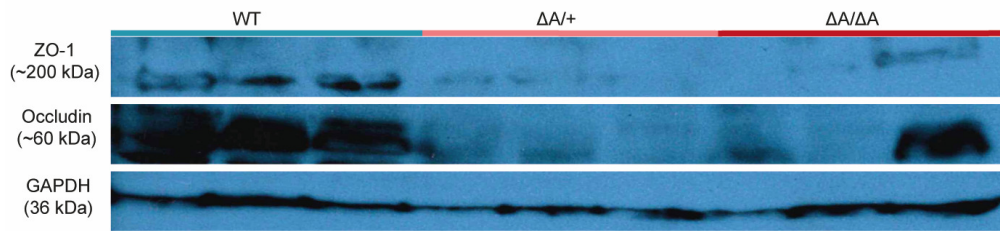


Figure 39: Western Blot sections displaying band intensities for ZO-1 (top), Occludin (middle) and GAPDH (bottom) for colonic tissue isolates from three wild-type, three  $TNF^{\Delta ARE/+}$  and  $TNF^{\Delta ARE/\Delta ARE}$  swine. Adapted from Winogrodzki et al.<sup>163</sup>.

To further confirm the disruption of the intestinal barrier integrity, confocal laser scanning microscopy was performed. A clear localization and strong signal for TJ proteins at the cell membrane of wild-type colon tissue was found, while diffuse localization and weak signal intensity was observed in inflamed tissue. Noteworthy, diffuse localization occurred in highly inflamed tissue areas only (Figure 40).

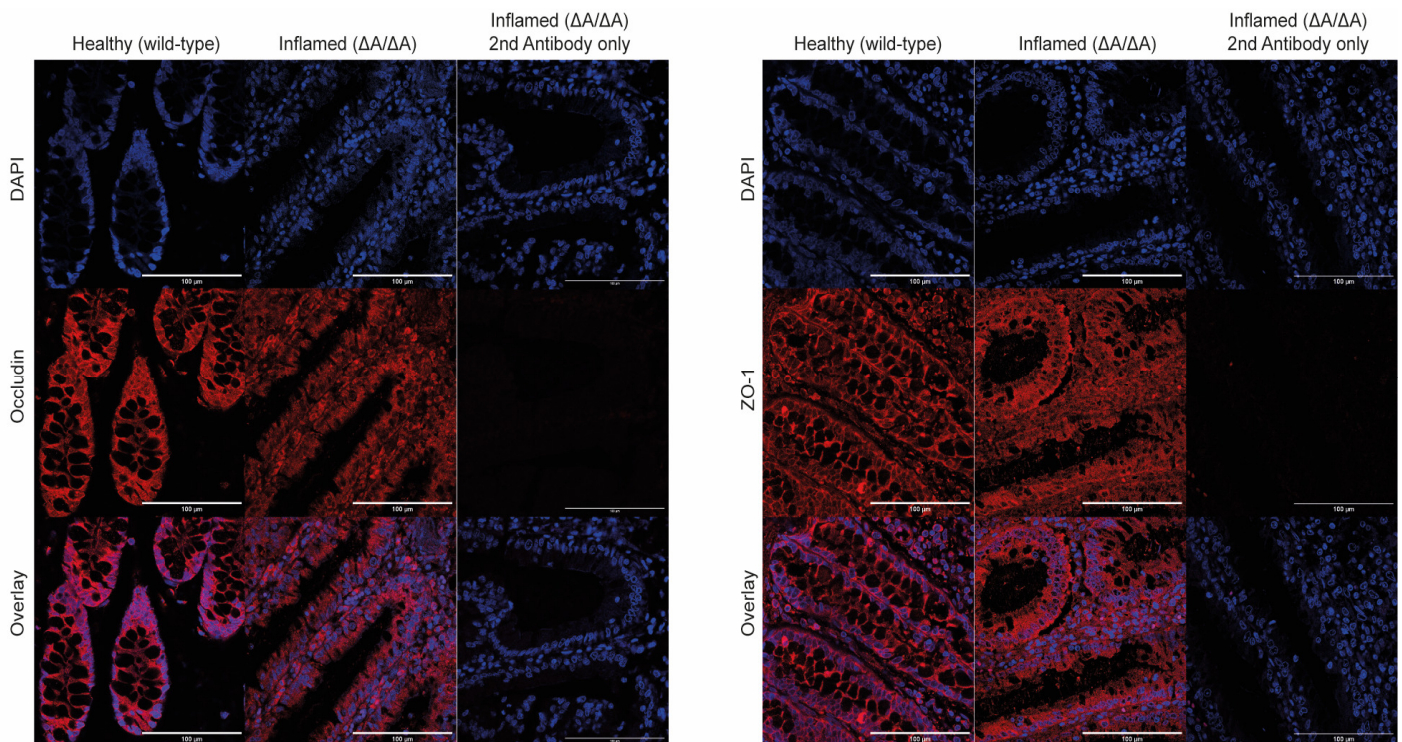


Figure 40: (Top) Confocal laser scanning microscopy images of occludin and (bottom) ZO-1 immunofluorescence stainings (red) of healthy and highly inflamed colonic tissue, additionally stained with DAPI (blue). Scale bars indicate 100  $\mu m$ . Original signal intensities were adjusted for clear visualization of defined or diffuse antigen localization. Signals captured from tissue sections stained with secondary antibodies and DAPI only served as control. Adapted from Winogrodzki et al.<sup>163</sup>.

Immunohistochemical staining of  $Ki67^{+/-}$ ,  $MPO^{+/-}$ ,  $CD3^{+/-}$ , and  $IBA1^{+/-}$ -cells was performed on gut sections derived from pigs at the age of 2-4 months. Staining of acidic and neutral mucin-containing cells was performed by Pas/AB-staining. In general, an increase in  $Ki67^{+/-}$ ,  $CD3^{+/-}$  and  $IBA1^{+/-}$ -cells and a decrease in  $Pas/AB^{+/-}$ -cells was observed in  $TNF^{\Delta ARE}$  swine compared to wild-type littermates (Figure 41 and S3).



The decrease in Pas/AB<sup>+</sup>-cells was most prominent in ileal tissue sections. No differences in the number of MPO<sup>+</sup>-cells were observed. It must be noted that statistical evaluation was not possible for the most inflamed tissue sections due to the absence of an intact tissue structure.

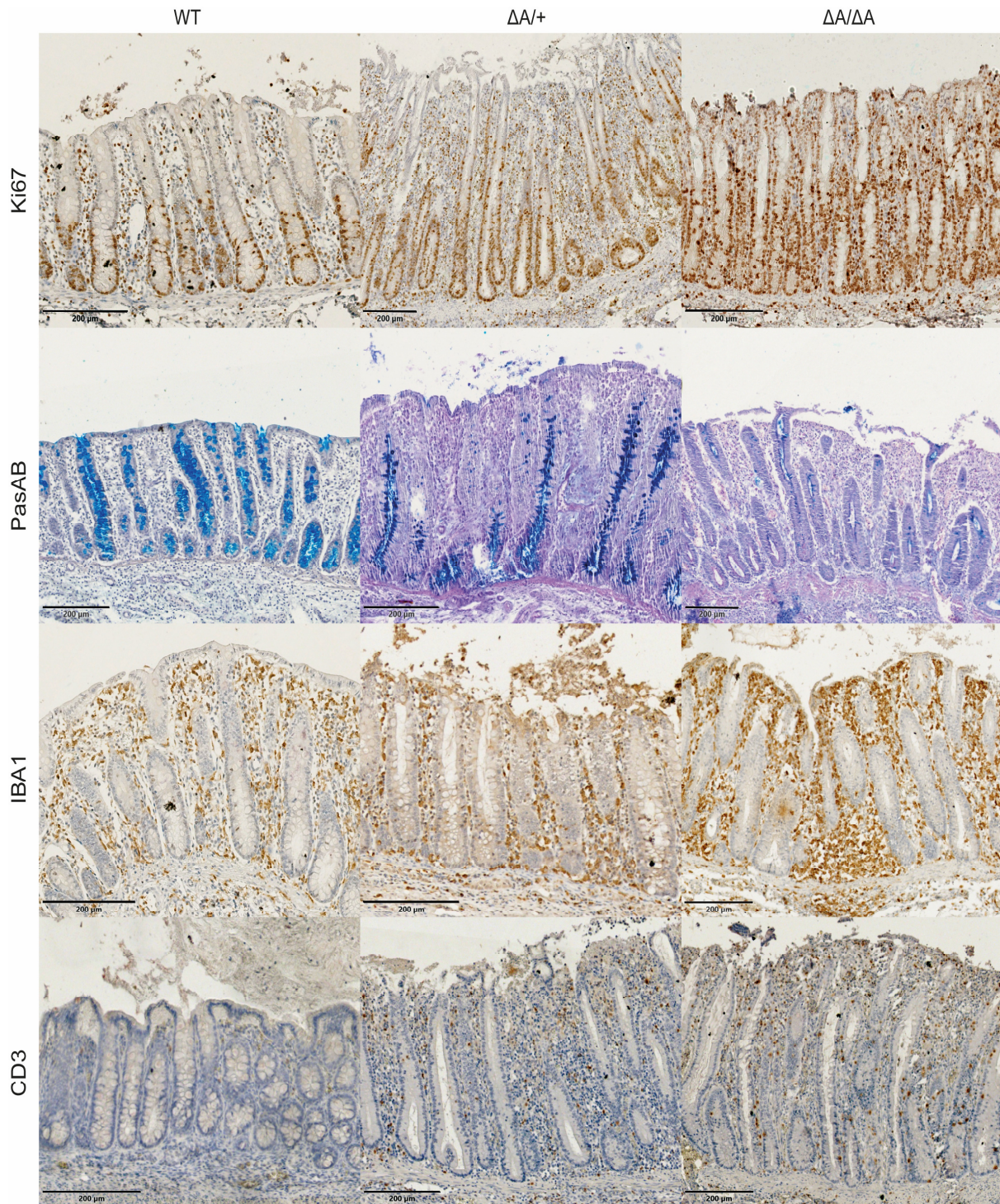


Figure 41: Representative images of immune-histological stainings of wild-type,  $TNF^{\Delta ARE/+}$  and  $TNF^{\Delta ARE/\Delta ARE}$  colonic tissue sections. Scale bars indicate 200  $\mu m$ . Adapted from Winogrodzki et al.<sup>163</sup>.

The thickness of mucosa, measured from muscularis mucosa to the epithelium, was 597.7  $\mu m$  in wild-type ( $\pm 118.5 \mu m$ ; n=3), 408.73  $\mu m$  in  $TNF^{\Delta ARE/+}$  ( $\pm 100.1 \mu m$ ; n=3), and 359.2  $\mu m$  in  $TNF^{\Delta ARE/\Delta ARE}$  ( $\pm 68.37$

$\mu\text{m}$ ;  $n=3$ ) in the small intestine and  $389.2 \mu\text{m}$  in wild-type ( $\pm 79.1 \mu\text{m}$ ;  $n=3$ ),  $377.8 \mu\text{m}$  in  $TNF^{\Delta ARE/+}$  ( $\pm 99.46 \mu\text{m}$ ;  $n=3$ ), and  $387.2 \mu\text{m}$  in  $TNF^{\Delta ARE/\Delta ARE}$  ( $\pm 91.92 \mu\text{m}$ ;  $n=4$ ) in the large intestine. This finding suggests mucosal thickening in the proximal colon and villus atrophy in the small intestine, which was more pronounced in the proximal part of the small intestine (Figure 42).

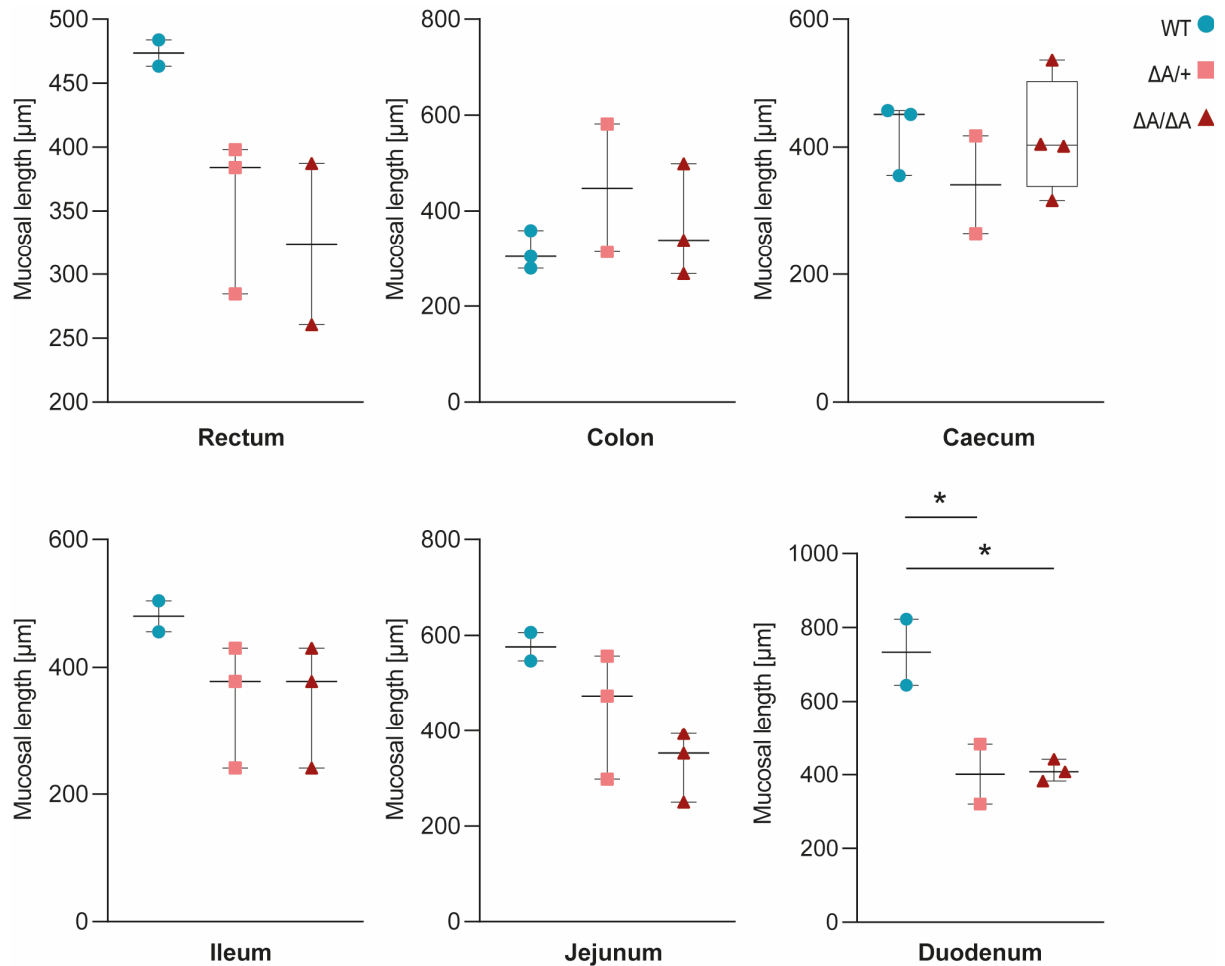


Figure 42: Statistical evaluation of mucosal thickness layer measured from muscularis mucosa to the epithelium for various tissue sections from wild-type,  $TNF^{\Delta ARE/+}$  and  $TNF^{\Delta ARE/\Delta ARE}$  swine.

#### 4.5.3. Complete blood count and qualitative pathobiont analysis

Whole blood samples were collected from pigs of the same litter (#2360-2370, excluding the already deceased  $TNF^{\Delta ARE/\Delta ARE}$  #2367) at day 36. Whole blood results showed increased monocyte count without significant change in leukocytes, an increased urea-to-creatinine ratio, an elevated copper-to-zinc ratio, hypoalbuminemia and basophilia. In addition, blood samples of a group of severely inflamed animals were tested for the ileitis-inducing pathogen *Lawsonia Intracellularis*, no tested animal was found to be positive (Figure 43 and Table S1).



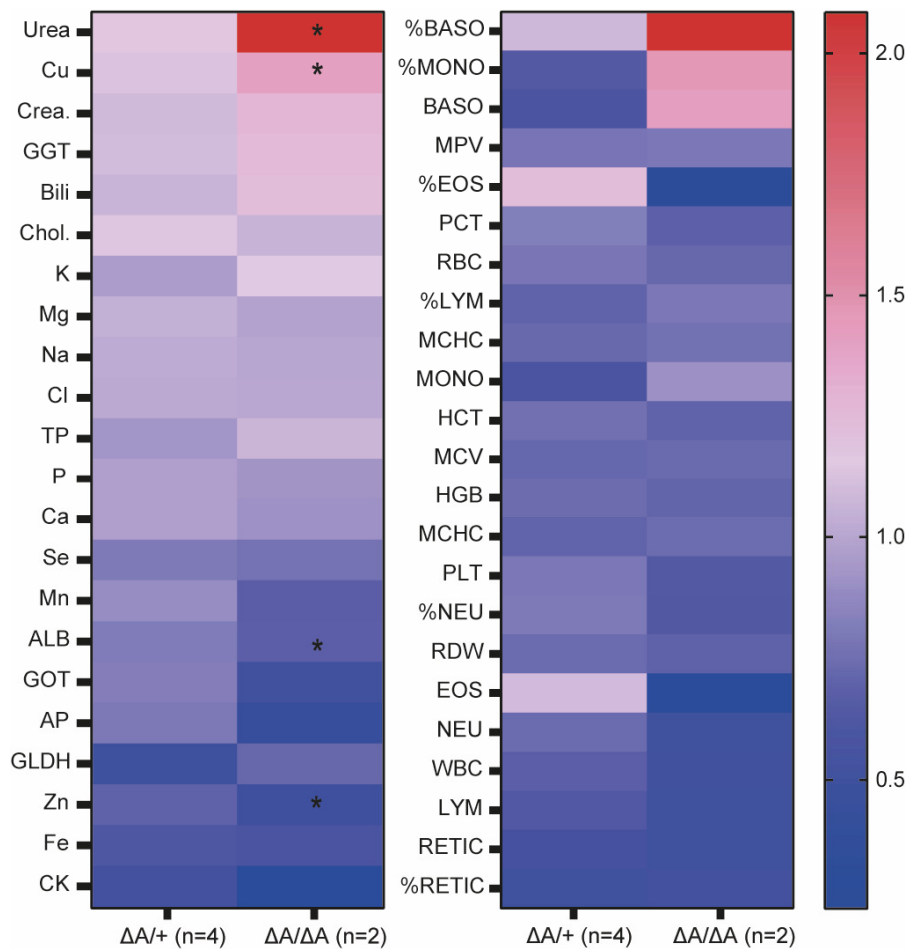


Figure 43: Heatmap of the complete blood count of  $TNF^{\Delta ARE/+}$  and  $TNF^{\Delta ARE/\Delta ARE}$  pigs in comparison to wild-type siblings (n=3). GOT: glutamate-oxalacetate-transaminase; GLDH: glutamate-dehydrogenase; GGT:  $\gamma$ -Glutamyl-Transferase; Bili: Bilirubin; AP: alkaline phosphatase; Chol.: cholesterol; TP: total protein; ALB: albumin; RBC: red blood cells; HCT: haematocrit; HGB: haemoglobin; MCV: mean corpuscular volume; MCHC: Mean corpuscular haemoglobin concentration; RDW: red cell distribution; RETIC: reticulocyte; WBC: white blood cell; NEU: neutrophils; LYM: lymphocytes; MONO: monocytes; EOS: eosinophils; BASO: basophils; PLT: platelets; MPV: mean platelet volume; PCT: procalcitonin. \*, significant difference. Adapted from Winogrodzki et al.<sup>163</sup>.

## 4.6. Molecular analyses

### 4.6.1. Selection of housekeeping genes for RT-qPCR

To be able to make reliable statements about differentially abundant transcripts of wild-type and mutant tissue, expression of several housekeeping genes: *ACTN*, *B2M*, *HMBS*, *HPRT*, *RPL4*, *RPL19*, *HSPCB*, *RPL32* and *RSP28* in both genotypes was determined using Bestkeeper<sup>167</sup> and Normfinder<sup>168</sup> (Tables 24 and 25). Bestkeeper and Normfinder analyses indicated that all tested genes but *B2M* are suitable for use as reference genes in this study. *RSP28* was selected and used for qPCR analysis.

Table 24: Values for standard deviation and coefficient of correlation (coeff. of corr.) for selected housekeeper candidates calculated using Bestkeeper. Values are based on qPCR results using cDNA pools from three each of wild-type,  $TNF^{\Delta ARE/+}$  and  $TNF^{\Delta ARE/\Delta ARE}$  animals.

Gene name	ACTN	B2M	HMBS	HPRT	RPL4	RPL19	HSPCB	RPL32	RPS28
Standard Deviation [± CP]	0.23	1.55	0.20	0.65	0.29	0.28	0.33	0.56	0.60
Standard Deviation [± x-fold]	1.18	3.08	1.15	1.60	1.24	1.22	1.27	1.51	1.55
Coeff. of corr. [r]	0.997	0.970	0.822	0.980	0.817	0.993	0.999	0.991	0.999

Table 25: Values for stability value and standard error for selected housekeeper candidates calculated using Normfinder. Values are based on qPCR results using cDNA pools from three each of wild-type,  $TNF^{\Delta ARE/+}$  and  $TNF^{\Delta ARE/\Delta ARE}$  animals.

Gene name	Stability value	Standard error
β-Actin	0.006	0.011
B2M	0.081	0.041
HMBS	0.017	0.012
HPRT	0.002	0.024
RPL4	0.012	0.010
RPL19	0.001	0.043
HSPCB	0.001	0.043
RPL32	0.002	0.024
RSP28	0.007	0.011

#### 4.6.2. *TNF* transcript half-life assessment in macrophages

*TNF* is expressed by a variety of cell types, with monocytic lineage cells such as macrophages showing the highest levels of expression<sup>169</sup>. Consequently, macrophage (mΦ) cultures derived from PBMCs were established to determine the impact of the ARE/CDE1 deletion on *TNF* mRNA half-life (Figure 44). To this end, blood from pigs #2360-2370 at the age of 36 days was analysed.



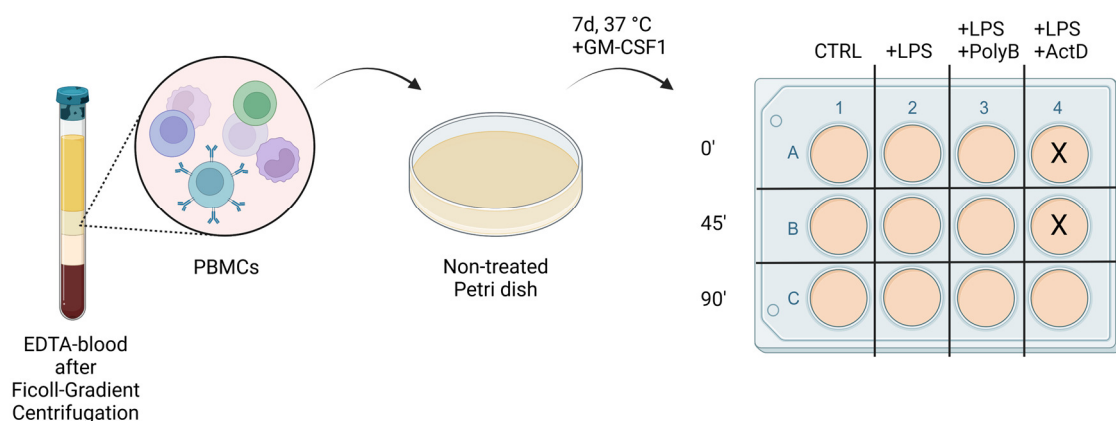


Figure 44: Workflow and pipetting scheme for the analysis of *TNF* transcript half-lives. EDTA-blood was isolated from the vena jugularis, followed by ficoll-gradient centrifugation to isolate PBMCs. PBMCs were cultured for seven days at 37 °C on a bacteriological petri dish in the presence of poGM-CSF1 before cells were transferred onto a 12-well culture plate in equal cell numbers. Cells were incubated with LPS alone, LPS+Polymyxin B or LPS+Actinomycin D for 0, 45 or 90 minutes. X, wells not used.

Before addition of 0.1 µg/ml LPS, mutant mθs were found to have 1.23-fold (±0.29-fold) *TNF* transcript levels of wild-type mθs in *TNF<sup>ΔARE/+</sup>* and 1.96-fold (±0.73-fold) in *TNF<sup>ΔARE/ΔARE</sup>* cells. After 45 minutes of LPS incubation, *TNF* transcript levels increased to 174.5-fold (±13.72-fold) of start values in wild-type, 119.5-fold (±54-fold) in *TNF<sup>ΔARE/+</sup>* and 86.6-fold (±82.33-fold) in *TNF<sup>ΔARE/ΔARE</sup>* cells. After 90 minutes of LPS incubation, *TNF* transcript levels were found to be 126.7-fold (±29.53-fold) of starting values in wild-type, 216.8-fold (±92.38-fold;  $p_{\text{adj}} = 0.0267$  for control vs. LPS 90') in *TNF<sup>ΔARE/+</sup>* and 227-fold (±162.63-fold;  $p_{\text{adj}} = 0.0126$  for control vs. LPS 90') in *TNF<sup>ΔARE/ΔARE</sup>* mθs. There was no significant difference between the genotypes for *TNF* transcript levels after 90 min of incubation with LPS ( $p_{\text{adj}} = 0.0559$  for LPS 90' wild-type vs. LPS 90' *TNF<sup>ΔARE/ΔARE</sup>*).

In comparison, addition of 10 µg/ml Actinomycin D after 45 minutes of LPS incubation resulted in 33.5- (±12.83-fold) increase in transcript levels for wild-type, 52.2- (±22.63-fold) for *TNF<sup>ΔARE/+</sup>* and 89.5-fold (±69.26-fold) for *TNF<sup>ΔARE/ΔARE</sup>* cells. It must be noted that mθs derived from pig #2367 (*TNF<sup>ΔARE/ΔARE</sup>*) were not considered for this comparison as transcript levels following treatment with LPS for 90 min and Actinomycin D for 45 min were found to be higher than transcript levels after LPS treatment for 45 min. Therefore, treatment with Actinomycin D was considered to have failed for this group of cells (82.9-fold (±57.32-fold) increase compared to transcript levels at start time point for *TNF<sup>ΔARE/ΔARE</sup>* mθs when including this value). Actinomycin D treatment resulted in 70.4 % (±14.4 %) reduction of transcript levels when compared to treatment with LPS alone in wild-type, 74.9 % (±10 %) in *TNF<sup>ΔARE/+</sup>*, and 63 % (±1.1 %) in *TNF<sup>ΔARE/ΔARE</sup>* mθs (no significant difference between genotypes). Transcript levels following 90 minutes of LPS and 45 minutes of Actinomycin D treatment were 19.4 % (±8 %) of transcript levels after 45 min of LPS treatment in wild-type, 45.3 % (±18.2 %) in *TNF<sup>ΔARE/+</sup>*, and 73.7 % (±4.4 %) in *TNF<sup>ΔARE/ΔARE</sup>* ( $p_{\text{adj}} = 0.0236$  for wild-type vs. *TNF<sup>ΔARE/ΔARE</sup>*) cells (Figure 45). This is equal to a half-life of ~19 min in

wild-type, ~58 min in  $TNF^{\Delta ARE/+}$ , and ~708 min in  $TNF^{\Delta ARE/\Delta ARE}$  mOs, if it is assumed that transcription was completely and directly silenced from the time of Actinomycin D addition.

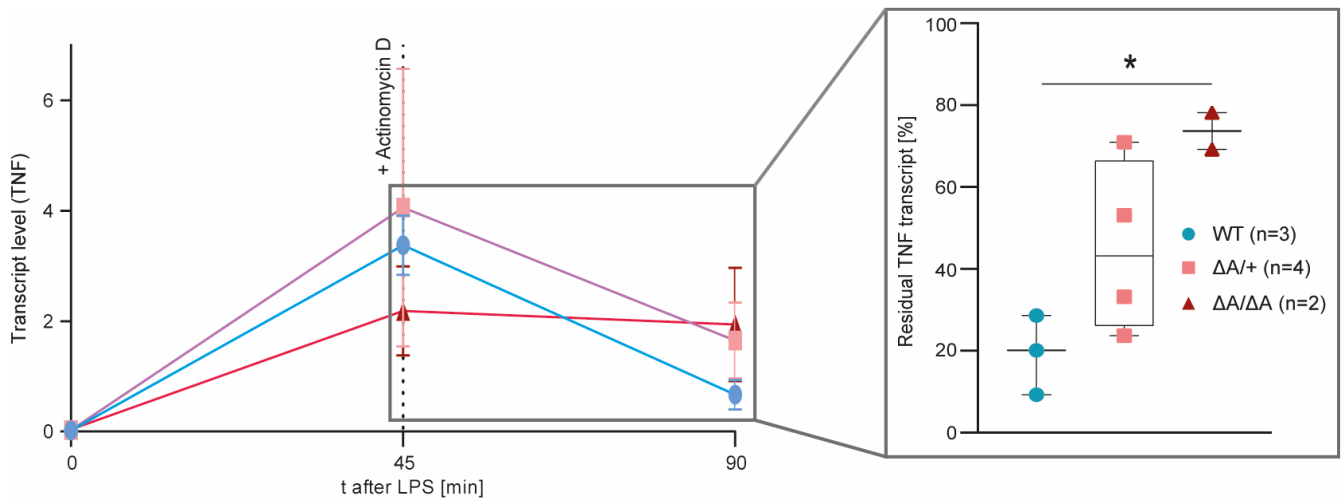


Figure 45: Determination of  $TNF$  mRNA levels and half-lives in macrophages from  $TNF^{\Delta ARE}$  and wild-type pigs. Macrophages were subject to LPS challenge, followed by co-incubation with the global transcription inhibitor actinomycin D. Extended view shows percentage of  $TNF$  transcript levels at time points 90 minutes (after 45 min of co-incubation with actinomycin D) and 45 minutes (before the addition of actinomycin D). Adapted from Winogrodzki et al.<sup>163</sup>.

To exclude external effects on  $TNF$  transcription, 10  $\mu\text{g/ml}$  LPS-inhibitor Polymyxin B was added together with LPS on an additional group of mOs derived from pig #2366 (wild-type). Polymyxin B acts through binding to lipid A, the toxic component of LPS, thereby preventing LPS from binding to its receptors<sup>170</sup>. After 45 min, 29.6-fold increase and after 90 min, 10-fold increase in  $TNF$  transcript levels compared to the starting point were found (Figure S4). Therefore, Polymyxin B reduces  $TNF$  transcript levels by 81.5% (after 45 minutes) and 92.5% (after 90 minutes), and it can be concluded that LPS is the main trigger for the increase in  $TNF$  transcripts.

$NF\kappa B$  (p50) transcript levels were compared between genotypes in untreated mOs and after 90 mins of LPS treatment to identify possible differences in inflammatory processes preceding  $TNF$  expression. In the untreated controls,  $NF\kappa B$  transcript levels were 1.61-fold ( $\pm 0.74$ -fold) higher in  $TNF^{\Delta ARE/+}$  and 1.34-fold ( $\pm 0.26$ -fold) in  $TNF^{\Delta ARE/\Delta ARE}$  cells, compared to wild-type. After 90 min of LPS treatment,  $NF\kappa B$  transcript levels increased to 4.7-fold ( $\pm 1.42$ -fold) of start points in wild-type, 7.3- ( $\pm 4.81$ -fold) in  $TNF^{\Delta ARE/+}$  and 6.13-fold ( $\pm 5.13$ -fold) in  $TNF^{\Delta ARE/\Delta ARE}$  mOs and were not significantly differing between genotypes for both time points ( $p_{\text{adj}} = 0.6138$  for LPS 90' wild-type vs. LPS 90'  $TNF^{\Delta ARE/+}$  and  $p_{\text{adj}} = 0.8944$  for LPS 90' wild-type vs. LPS 90'  $TNF^{\Delta ARE/\Delta ARE}$ ) (Figure S5). Thus, it can be concluded that no unexpected differential regulation of  $NF\kappa B$  occurred between wild-type,  $TNF^{\Delta ARE/+}$  and  $TNF^{\Delta ARE/\Delta ARE}$  mOs.

#### 4.6.3. Transcript and protein quantification in biopsy samples

The  $TNF$  transcription in intestinal tissue was higher in  $TNF^{\Delta ARE}$  pigs in comparison to wild-type littermates. Specifically, the proximal colon of  $TNF^{\Delta ARE/\Delta ARE}$  pigs showed a 8.4-fold higher expression

( $\pm 2.78$ ;  $p_{\text{adj}}=0.0027$ ) compared to wild-types, while 3.5-fold ( $\pm 3.12$ ;  $p_{\text{adj}}=0.343$ ) higher expression was found in the same tissue in  $TNF^{\Delta ARE/+}$  pigs. Noteworthy,  $TNF$  mRNA levels within the same animal and gut section were higher in highly hemorrhagic or fibrinous tissue. Activation of the classical TNFR1-mediated pathway of the sTNF form was assessed via RT-qPCR of NF $\kappa$ B downstream targets  $IL-6$  and  $IL-8$ . Transcript levels of the pro-inflammatory  $IL-6$  were consistently higher throughout the intestine of  $TNF^{\Delta ARE}$  pigs, while the transcript levels of the neutrophil chemoattractant  $IL-8$  were higher in the ileocolonic region, indicating biological consequences of altered  $TNF$  transcript properties (Figure 46). Elevated  $TNF$  transcript level in heart, kidney, stomach and lung  $TNF^{\Delta ARE}$  were found (Figure S6).

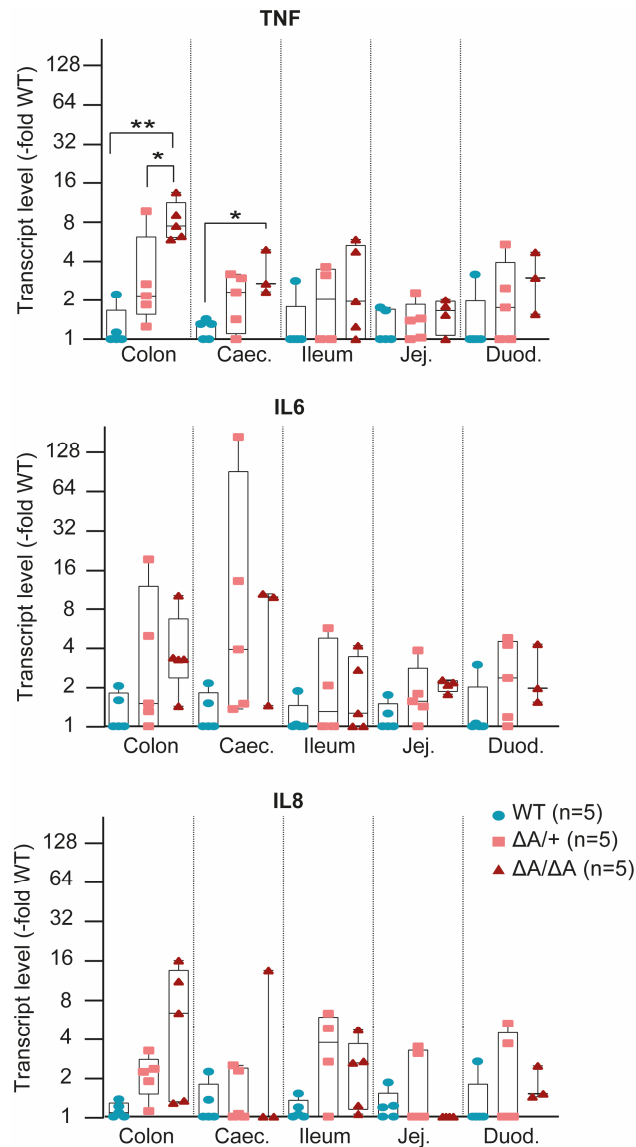


Figure 46:  $TNF$ ,  $IL-6$ , and  $IL-8$  mRNA levels in intestinal tissue samples shown as log<sub>2</sub> multiples of the average wild-type value. Caec., Caecum; Duod., Duodenum; Jej., Jejunum. Adapted from Winogrodzki et al.<sup>163</sup>.

Western blot revealed higher  $TNF$  protein levels in ileocolonic tissue. Of note, mainly a 26 kDa protein band was detected (Figure 47).

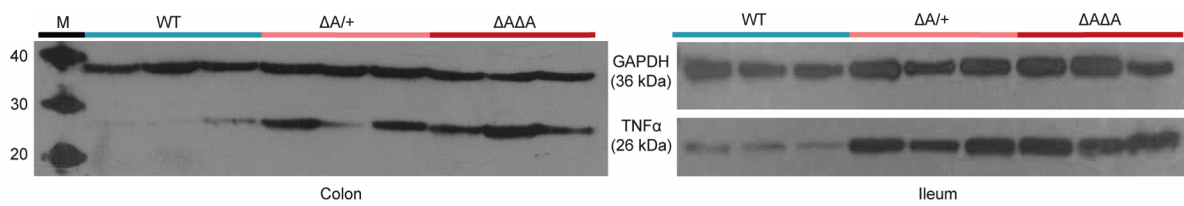


Figure 47: Expression of TNF and GAPDH proteins in ileal (bottom) and colonic (top) samples from 3 wild-type, 3  $TNF^{\Delta ARE/+}$ , and 3  $TNF^{\Delta ARE/\Delta ARE}$  pigs, respectively. M, size marker. Adapted from Winogrodzki et al.<sup>163</sup>.

#### 4.7. Flow cytometric analysis of peripheral immune cells

An exaggerated pro-inflammatory immune response has been suggested as one of the major drivers of IBD<sup>171</sup>. Therefore, pro-inflammatory immune cell populations from isolated PBMCs were quantified by flow cytometry in three wild-type, three  $TNF^{\Delta ARE/+}$ , and two  $TNF^{\Delta ARE/\Delta ARE}$  pigs. For the  $TNF^{\Delta ARE/+}$  genotype, pigs showing different disease severity were selected.

All cells were gated for live, single cells. The forward scatter (FSC)-A/side scatter (SSC)-A-ratio was used to select cell types based on their unique light scattering properties. Fluorophore-labelled antibodies targeting characteristic epitopes on specific cell subsets enabled further differentiation between functionally distinct cell populations, such as CD3<sup>+</sup> cells (Figure 48).

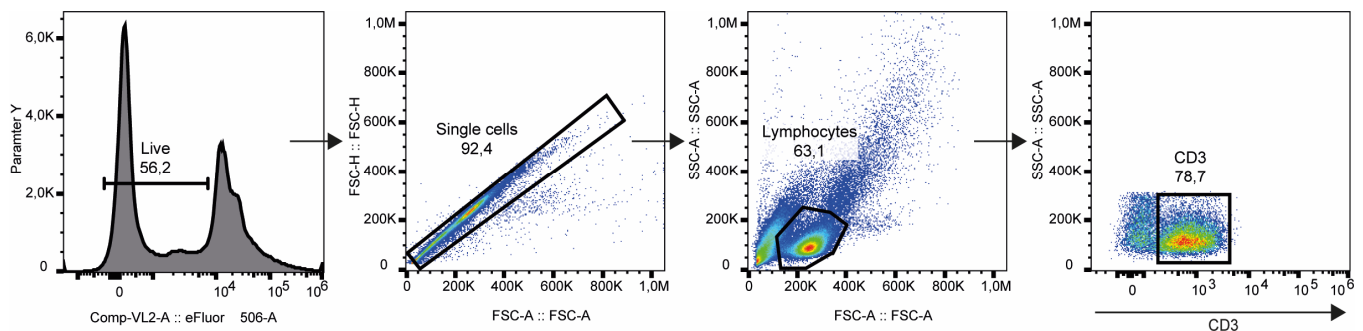


Figure 48: Gating strategy for flow cytometry analysis of CD3<sup>+</sup> cell subsets. (From left to right) Viable cells were selected based on low viability dye signal that incorporates into dead cells. Viable cells were further gated based on equal FSC-H/FSC-A-ratio to select single cells. The lymphocyte cell population was selected from viable, single cells based on a characteristic SSC-A/FSC-A-ratio. CD3<sup>+</sup> cells were selected from viable, single lymphocytes based on a high CD3 signal intensity.

Flow cytometric analysis revealed that the proportion of cells gated in  $FSC^{Med}/SSC^{low}$  was lower, while the  $FSC^{high}/SSC^{high}$  population was higher in mutant pigs compared to wild-type animals (Figure 49).

Subsequent analysis of the CD3<sup>+</sup>-to-CD14<sup>-</sup> and CD3<sup>+</sup>-to-CD172a<sup>+</sup>-ratios based on gating for all non-debris-signals, validated considerable decrease of T-lymphocytes and an increase of monocytic phagocytes in  $TNF^{\Delta ARE}$  pigs. The ratios tended to be lower in severely diseased mutant animals (Figure S7).

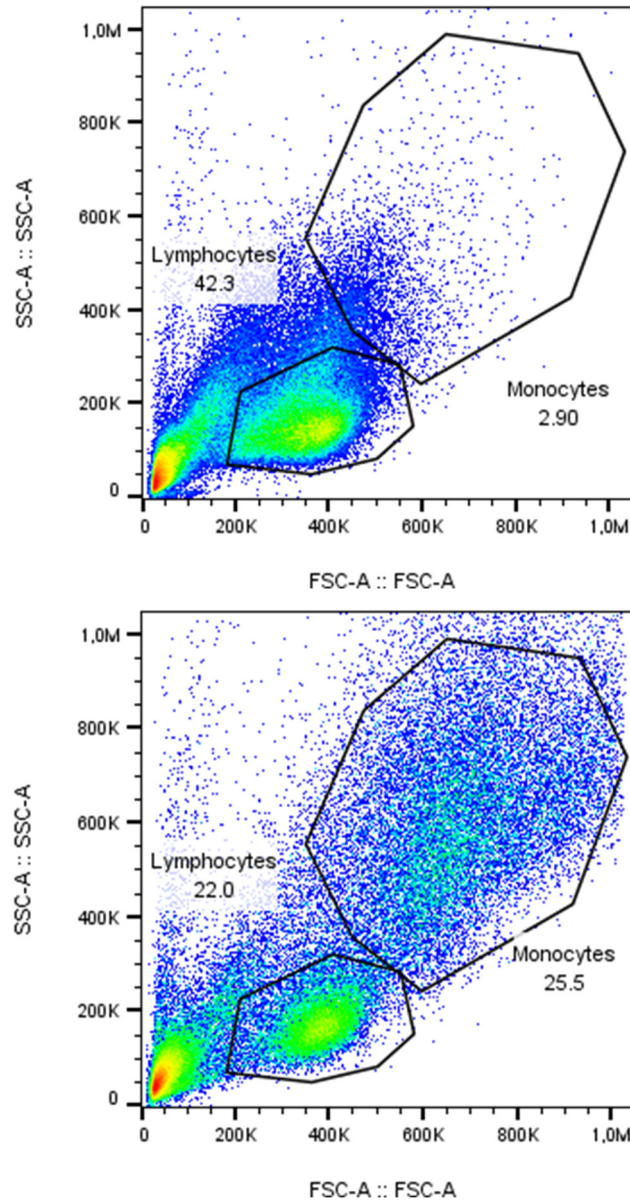


Figure 49: Viable, single lymphocyte and monocyte cell populations in (top) wild-type and (bottom) inflamed  $TNF^{\Delta ARE}$  pigs. Gates and cell ratios of the gate are shown.

To determine the extent to which the ARE/CDE1 deletion is responsible for this observation and affects immune cells in general, the number of  $TNF^+$  cells in different immune cell subsets was analysed.  $TNF^{\Delta ARE/+}$  monocytes, as gated on viable single  $FSC^{high}/SSC^{high}$  cells, showed 1.8-fold ( $\pm 0.57$ ;  $p_{adj} = 0.3302$ ) and  $TNF^{\Delta ARE/\Delta ARE}$  a 2.7-fold ( $\pm 0.43$ ;  $p_{adj} = 0.0631$ ) increase compared to wild-type cells. In the group of  $CD3^+$ -cells, the subpopulation of  $TNF^+$  cells was 3- ( $\pm 0.45$ ;  $p_{adj} = 0.0604$ ) or 23.6-fold ( $\pm 11.55$ ;  $p_{adj} = 0.0437$ ) increased in  $TNF^{\Delta ARE/+}$  or  $TNF^{\Delta ARE/\Delta ARE}$  cells compared to wild-types (Figure 50).

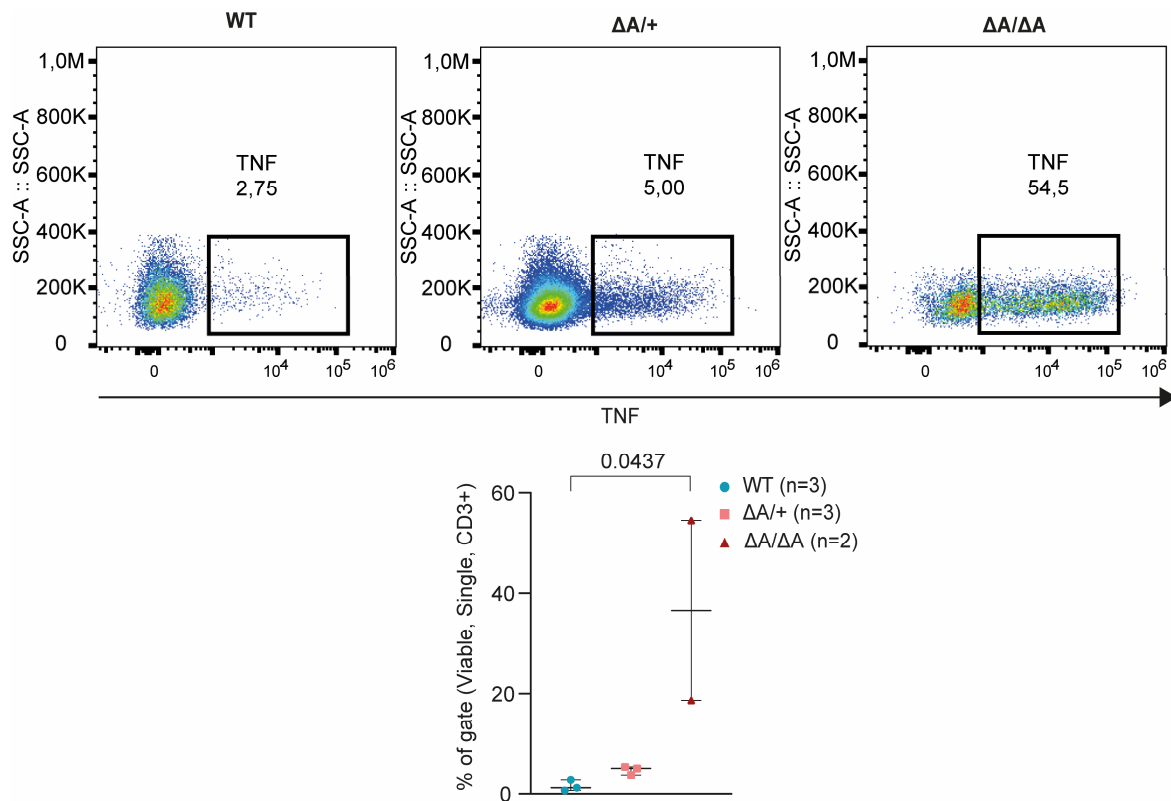


Figure 50: Gating strategy for flow cytometry analysis of  $TNF^+CD3^+$  viable single lymphocytes of PBMCs derived from 3 wild-type, 3  $TNF^{\Delta ARE/+}$ , and 3  $TNF^{\Delta ARE/\Delta ARE}$  swine (top) and statistical analysis (bottom).

All cells that expressed CD4 or high amounts of CD8 and co-expressed CD3 are, by definition, T cells after leaving the thymus<sup>172</sup>. Therefore, cell subsets that either expressed high amounts of CD4 or CD8 were further analysed for  $TNF$  expression levels. Additionally, the  $CD3^+/CD4^+/CD8^+$  and  $CD3^+/CD4^-/CD8^-$  pig T-cell subsets were evaluated.  $CD4^+/CD8^-$  cell ratio relative to the  $CD3^+$  population was found to be slightly increased 1.19-fold in  $TNF^{\Delta ARE/+}$  ( $\pm 0.263$ -fold; n.s.) and 1.71-fold in  $TNF^{\Delta ARE/\Delta ARE}$  pigs ( $\pm 0.11$ -fold; n.s.), no differences to the relative amount of  $CD4^-/CD8^+$  cell ratio was found. Double positive cell subsets were increased 1.96-fold in  $TNF^{\Delta ARE/+}$  ( $\pm 0.86$ -fold; n.s.) and 2.54-fold in  $TNF^{\Delta ARE/\Delta ARE}$  pigs ( $\pm 1$ -fold; n.s.), while the relative amount of double negative cells was decreased to 0.84-fold in  $TNF^{\Delta ARE/+}$  ( $\pm 0.321$ -fold; n.s.) and to 0.365-fold in  $TNF^{\Delta ARE/\Delta ARE}$  pigs ( $\pm 0.029$ -fold; n.s.) (Figure 51).

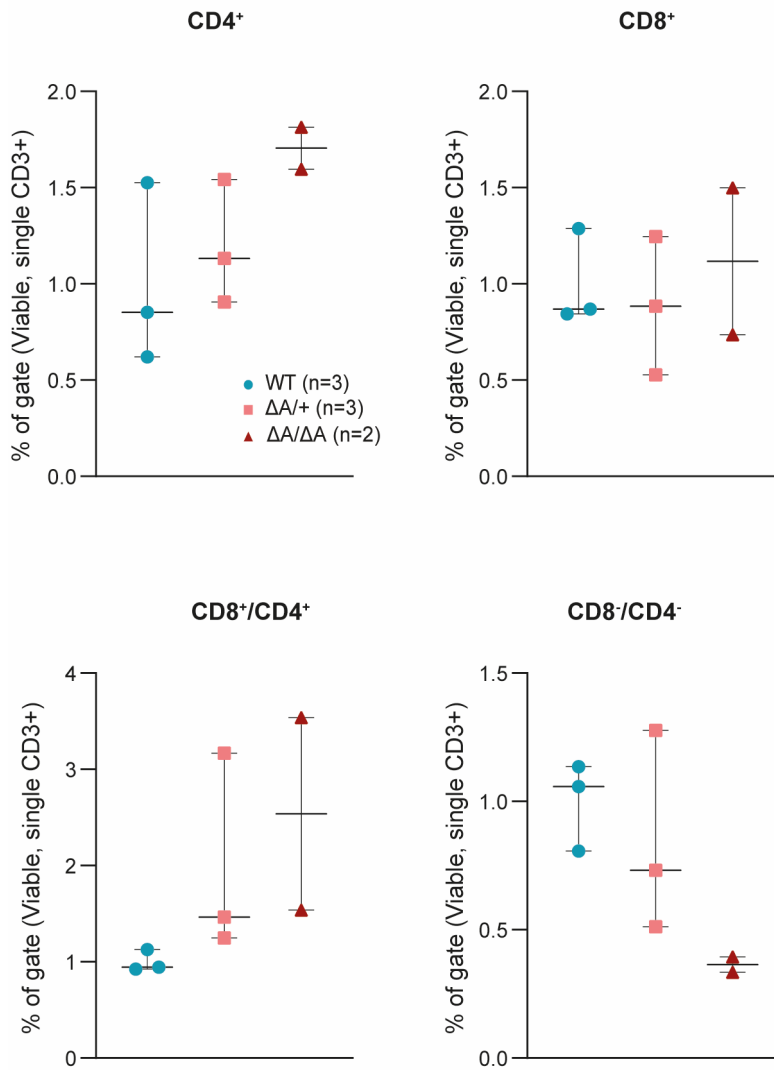


Figure 51: Statistical analysis of CD3<sup>+</sup>/CD4<sup>+</sup>/CD8<sup>-</sup> (top left), CD3<sup>+</sup>/CD4<sup>-</sup>/CD8<sup>+</sup> (top right), CD3<sup>+</sup>/CD4<sup>+</sup>/CD8<sup>+</sup> (bottom left), CD3<sup>+</sup>/CD4<sup>-</sup>/CD8<sup>-</sup> (bottom right) cell subsets derived from 3 wild-type, 3  $TNF^{\Delta ARE/+}$ , and 2  $TNF^{\Delta ARE/\Delta ARE}$  swine.

All analysed subsets of CD3<sup>+</sup> cells showed a larger TNF<sup>+</sup> subpopulation in  $TNF^{\Delta ARE}$  swine. Specifically, CD4<sup>+</sup>/CD8<sup>+</sup> ( $p_{adj} = 0.0085$ ;  $TNF^{\Delta ARE/\Delta ARE}$ ), CD8<sup>+</sup> ( $p_{adj} = 0.0439$ ;  $TNF^{\Delta ARE/\Delta ARE}$ ), and CD4<sup>-</sup>/CD8<sup>-</sup> ( $p_{adj} = 0.0458$ ;  $TNF^{\Delta ARE/\Delta ARE}$ ) cell subsets were significantly increased (Figure 52 and S8).



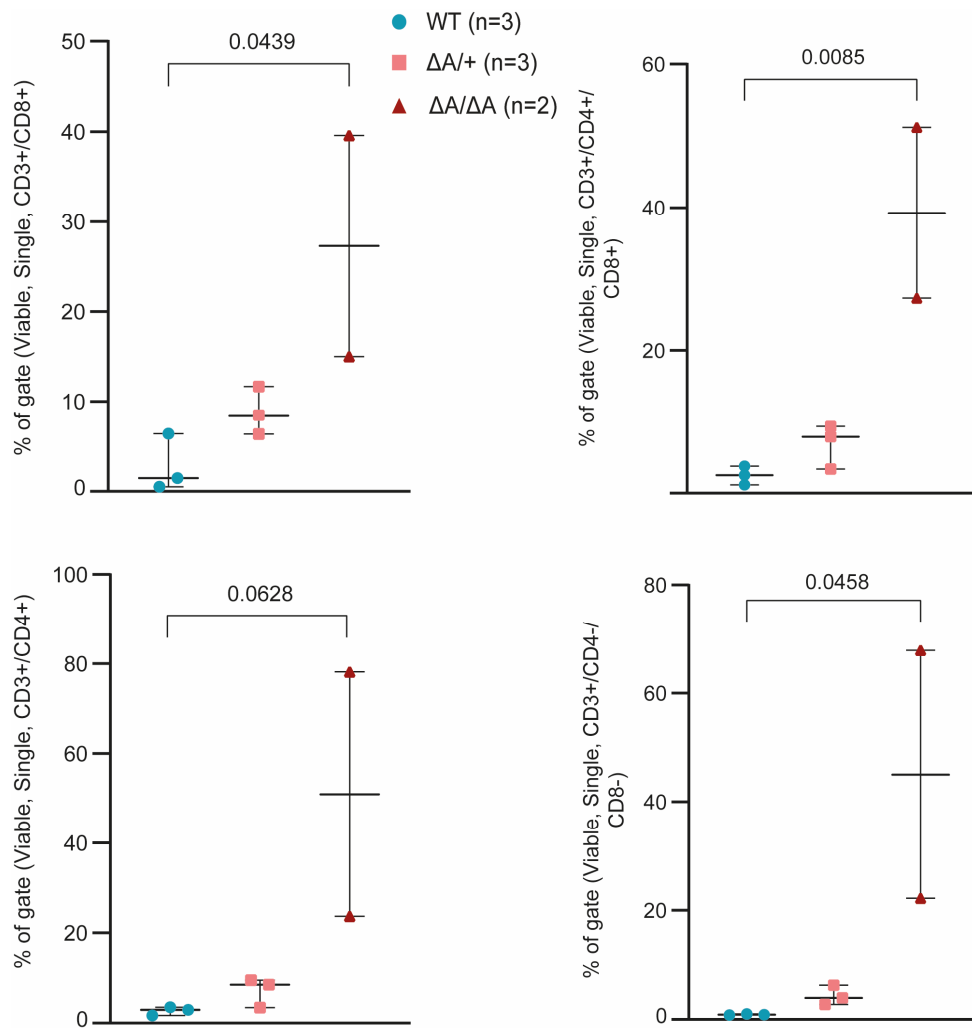


Figure 52: Statistical analysis of  $TNF^+CD4^+CD8^+$ ,  $TNF^+CD4^-CD8^+$ ,  $TNF^+CD4^+CD8^-$ , and  $TNF^+CD4^-CD8^-$  viable single lymphocytes derived from 3 wild-type, 3  $TNF^{\Delta ARE/+}$ , and 2  $TNF^{\Delta ARE/\Delta ARE}$  swine.

The observation of an increased  $CD4^+/CD8^-$  cell subset in inflamed mutant pigs prompted further examination of the T-helper ( $T_H$ ) cell population. To precisely quantify the presence of T-regulatory cells ( $T_{regs}$ ), T-helper 1 cells ( $T_{H1}$ ), T-helper 2 cells ( $T_{H2}$ ), and  $\gamma\delta^+$  T-cells, a detailed analysis was performed. Within the  $CD3^+/CD4^+$  cell subset, the populations were defined using  $CD25^+/FOXP3^+$  gating for  $T_{regs}$ ,  $Tbet^+$  gating for  $T_{H1}$  cells,  $GATA3^+$  gating for  $T_{H2}$  cells, and  $TCR1\delta^+$  gating for  $\gamma\delta^+$  T-cells.

The proportion of  $CD3^+/CD4^+/CD25^+/FOXP3^+$  cells decreased in  $TNF^{\Delta ARE}$  pigs ( $p_{adj} = 0.0432$ ;  $TNF^{\Delta ARE/\Delta ARE}$ ), most likely due to homing into the intestinal mucosal tissue<sup>173</sup>. Differences in the proportion of  $TNF^+$  cells could not be analyzed with confidence as the number of gated cells was too low (2-115 cells) (Figure 53).



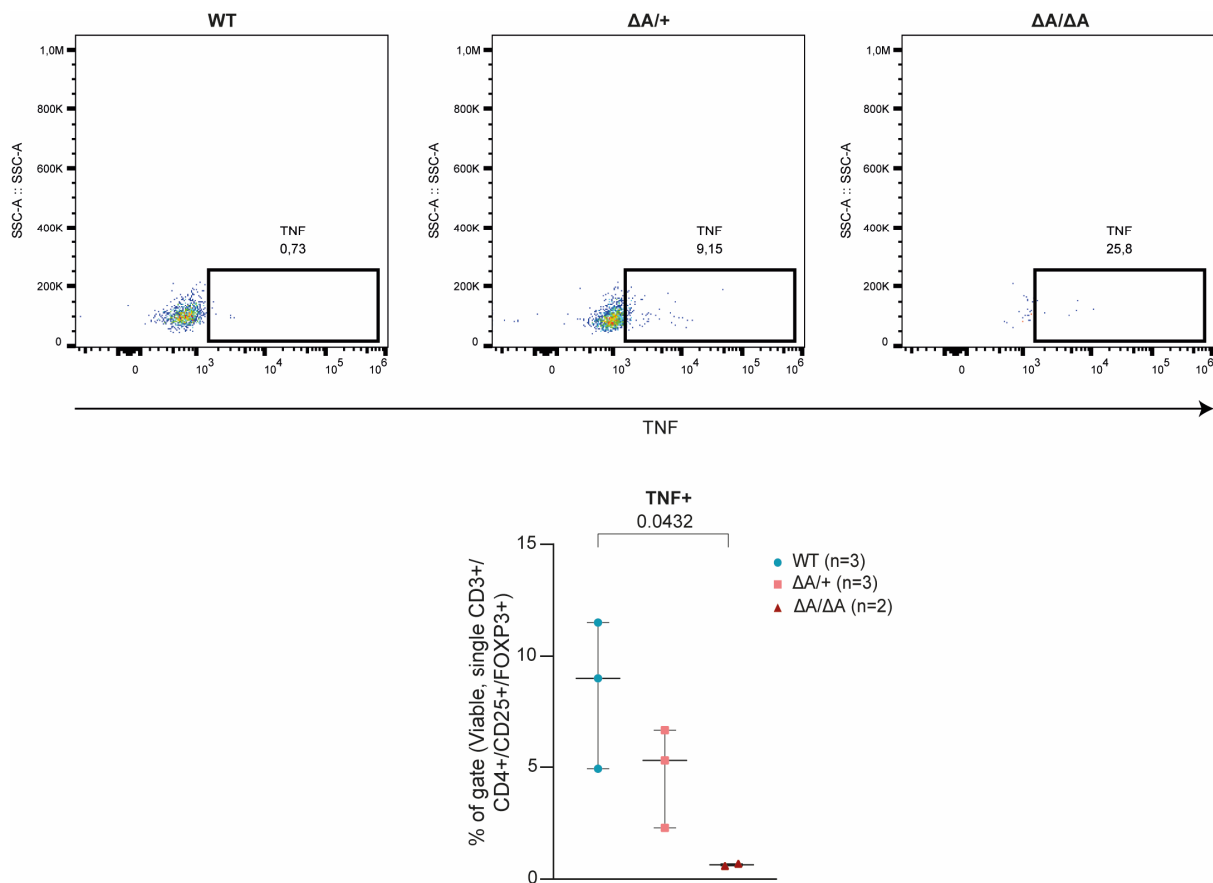


Figure 53: Gating strategy for flow cytometry analysis of  $TNF^+/CD3^+/CD4^+/CD25^+/FOXP3^+$  viable, single lymphocytes of PBMCs derived from 3 wild-type, 3  $TNF^{\Delta A/RE/+}$ , and 2  $TNF^{\Delta A/RE/\Delta A/RE}$  swine (top) and statistical analysis (bottom).

The  $T_H1$  subpopulation tended to be 3.63-fold (n.s.) and 1.72-fold (n.s.) increased in  $TNF^{\Delta A/RE/+}$  and  $TNF^{\Delta A/RE/\Delta A/RE}$  pigs, respectively. Noteworthy, non- treated immune cells derived from  $TNF^{\Delta A/RE/\Delta A/RE}$  and highly inflamed  $TNF^{\Delta A/RE/+}$  pigs showed a 1.95-fold increase in T-bet<sup>+</sup> cell ratio compared to PHA-treated controls, which was an effect not observed in other immune cell subsets (Figure S9).

The  $T_H2$  cell population was decreased to a 0.42-fold (n.s.) and 0.78-fold (n.s.) of the wild-types in  $TNF^{\Delta A/RE/+}$  and  $TNF^{\Delta A/RE/\Delta A/RE}$  pigs, respectively. The proportion of  $T_H17$  cells was initially identified to be increased by measuring the amount of  $CD3^+/CD4^+/IL17^+/ROR\gamma^+$  cells. However, this finding could not be reproduced due to barely detectable  $IL17^+$  and  $ROR\gamma^+$  fluorescence intensities in the replication studies (Figure 54).

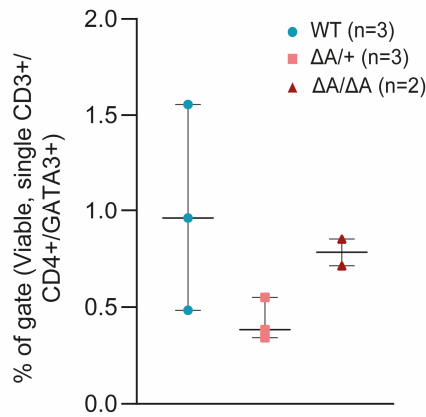


Figure 54: Statistical evaluation of for flow cytometry analysis of  $TNF^+/CD3^+/CD4^+/Tbet^+$  viable, single lymphocytes of PBMCs derived from 3 wild-type, 3  $TNF^{\Delta ARE/+}$ , and 2  $TNF^{\Delta ARE/\Delta A}$  swine.

In contrast to findings in human IBD patients<sup>174</sup>, the subset of  $\gamma\delta^+$  cells was decreased in the circulation of  $TNF^{\Delta ARE/+}$  ( $p_{adj} = 0.1531$ ) and  $TNF^{\Delta ARE/\Delta A}$  pigs ( $p_{adj} = 0.1724$ ) (Figure 55), highlighting the need for further research on the quickly responding  $\gamma\delta^+$  cell subsets in  $\gamma\delta^{high}$  species such as the pig<sup>175</sup>.

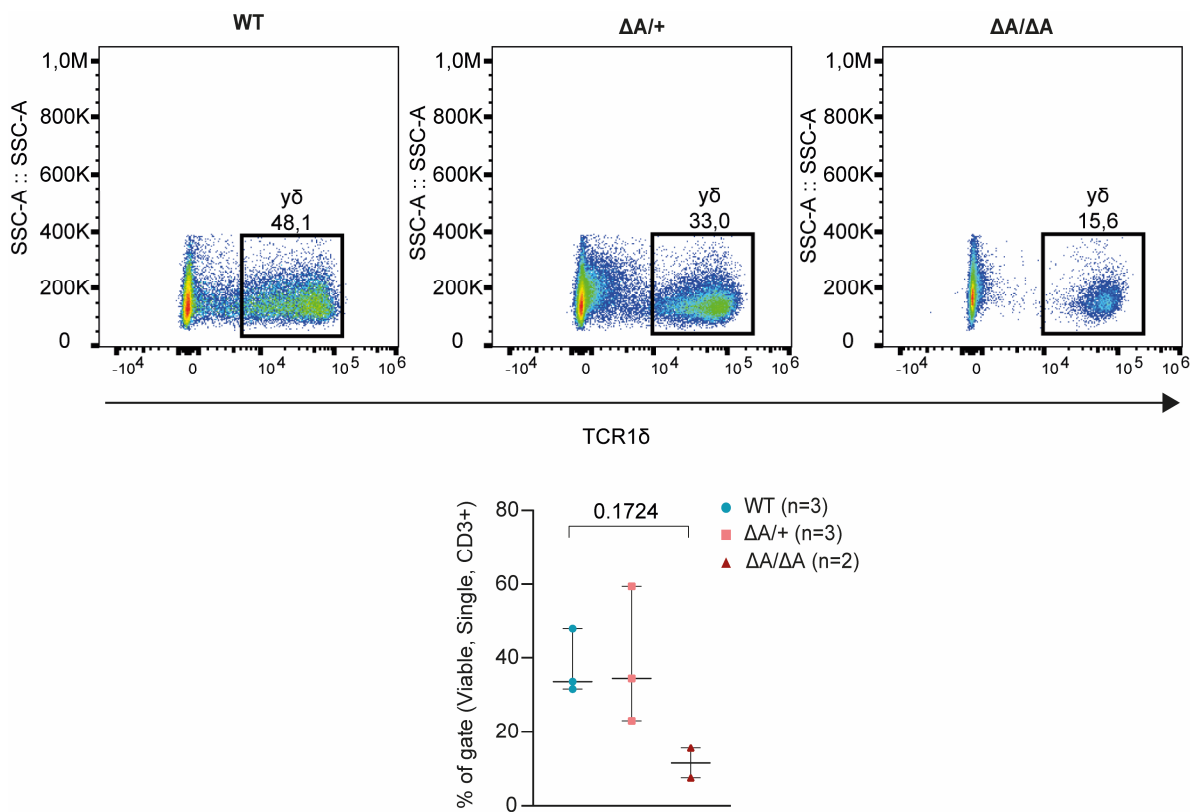


Figure 55: Gating strategy for flow cytometry analysis of  $TNF^+/CD3^+/TCR15^+$  viable, single lymphocytes of PBMCs derived from 3 wild-type, 3  $TNF^{\Delta ARE/+}$ , and 2  $TNF^{\Delta ARE/\Delta A}$  swine (top) and statistical analysis (bottom).

While in most analysed cell subsets, the proportion of  $IFN\gamma^+$  cells was consistent between groups,  $TNF^{\Delta ARE/+}$  ( $p_{adj} = 0.0015$ ) and  $TNF^{\Delta ARE/\Delta A}$  ( $p_{adj} = 0.2481$ )  $CD4^+/CD8^+$  cells showed an increased  $IFN\gamma^+$

subpopulation. The effect was stronger in the heterozygous mutant PBMCs, indicating a complex dosage-dependent relationship between TNF and IFN $\gamma$  in these cells (Figure 56).

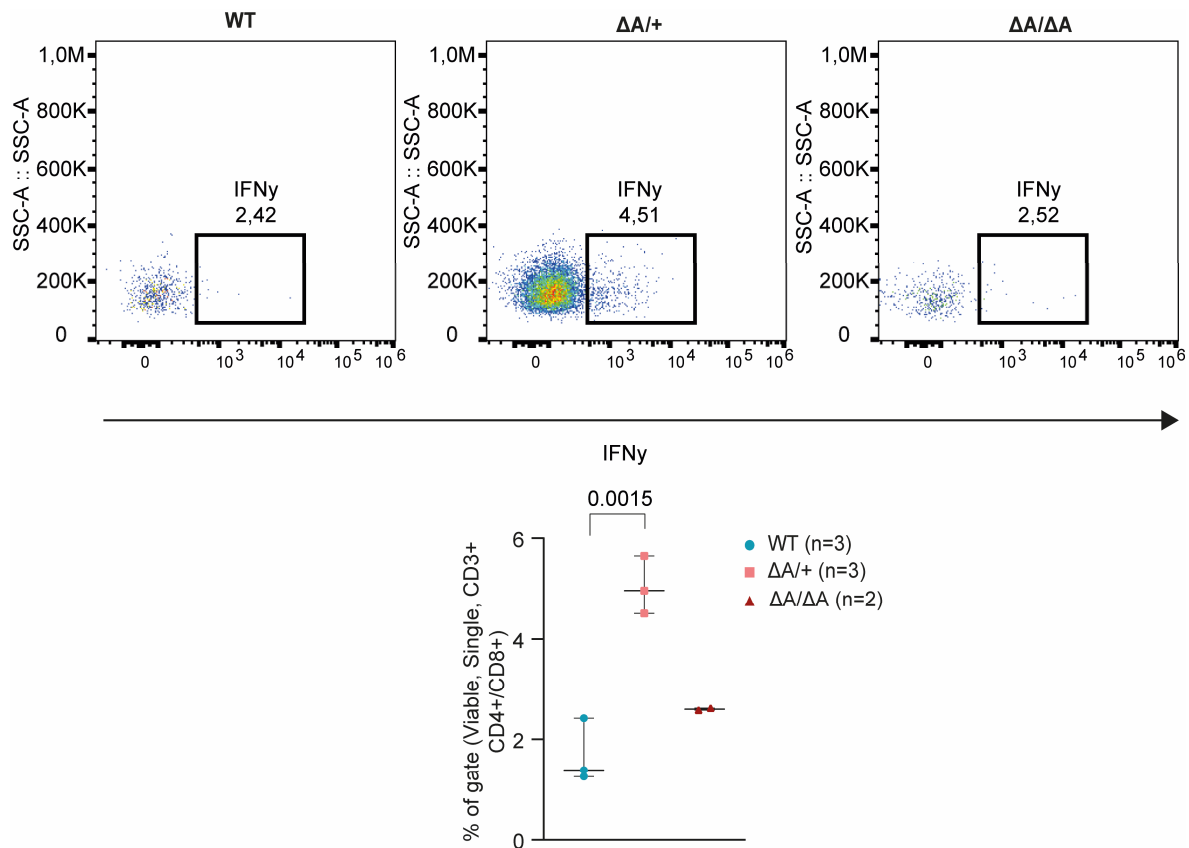


Figure 56: Gating strategy for flow cytometry analysis of TNF $^+$ /CD3 $^+$ /CD4 $^+$ /CD8 $^+$ /IFN $\gamma$  $^+$  viable, single lymphocytes of PBMCs derived from 3 wild-type, 3 TNF $\Delta ARE/+$ , and 2 TNF $\Delta ARE/\Delta ARE$  swine (top) and statistical analysis (bottom).

In summary, all analysed subsets showed increased ratios of TNF $^+$  cell subsets in TNF $\Delta ARE$  pigs compared to wild-type controls. Furthermore, the previously mentioned increase in monocytes (Figure 43) was supported by an observed increase in absolute macrophage-to-lymphocyte ratio in diseased animals.

Table 26 summarizes the results of this chapter.

Table 26: Summary of findings from flow cytometric analyses of PBMCs. Upward (↑) and downward (↓) arrows indicate increase and decrease, respectively, relative to the wild-type group (n=3).

Cell type	Marker profile	<i>TNF<sup>ΔARE/+</sup></i> (n=3)	<i>TNF<sup>ΔARE/ΔARE</sup></i> (n=2)
Lymphocytes	FSC <sup>med</sup> /SSC <sup>low</sup>	↓	↓↓
Monocytes and granulocytes	FSC <sup>high</sup> /SSC <sup>high</sup>	↑	↑↑
Monocytes	CD14 <sup>+</sup>	↑	↑↑
	CD172a <sup>+</sup>	↑	↑↑
Lymphocytes	CD3 <sup>+</sup>	↓	↓↓
	CD3 <sup>+</sup> /TNF <sup>+</sup>	↑	↑↑
T-Lymphocyte subsets	CD3 <sup>+</sup> /CD4 <sup>+</sup>	↑	↑↑
	CD3 <sup>+</sup> /CD4 <sup>+</sup> /TNF <sup>+</sup>	↑	↑↑
	CD3 <sup>+</sup> /CD8 <sup>+</sup>	-	-
	CD3 <sup>+</sup> /CD8 <sup>+</sup> /TNF <sup>+</sup>	↑	↑↑
	CD3 <sup>+</sup> /CD8 <sup>+</sup> /CD4 <sup>+</sup>	↑	↑↑
	CD3 <sup>+</sup> /CD8 <sup>+</sup> /CD4 <sup>+</sup> /TNF <sup>+</sup>	↑	↑↑
	CD3 <sup>+</sup> /CD8 <sup>+</sup> /CD4 <sup>+</sup> /IFN $\gamma$ <sup>+</sup>	↑↑	-
	CD3 <sup>+</sup> /CD8 <sup>-</sup> /CD4 <sup>-</sup>	↓	↓↓
	CD3 <sup>+</sup> /CD8 <sup>-</sup> /CD4 <sup>-</sup> /TNF <sup>+</sup>	↑	↑↑
T-helper cell subsets	CD3 <sup>+</sup> /CD4 <sup>+</sup> /CD25 <sup>+</sup> /FOXP3 <sup>+</sup>	↓	↓↓
	CD3 <sup>+</sup> /CD4 <sup>+</sup> /Tbet <sup>+</sup>	↑↑	↑
	CD3 <sup>+</sup> /CD4 <sup>+</sup> /GATA3 <sup>+</sup>	↓	↓
$\gamma\delta$ -T-cells	CD3 <sup>+</sup> /TCR1 $\delta$ <sup>+</sup>	-	↓↓

#### 4.8. Analysis of the gut microbial composition

The relevance of dysbiotic microbial communities in initiating CD-like inflammation in *TNF<sup>ΔARE</sup>* mice, was previously shown. Under GF conditions, the mice are completely disease-free and only upon the transfer of disease-associated gut microbial communities, *TNF<sup>ΔARE/+</sup>* mice developed intestinal inflammation<sup>42</sup>.

To characterise the changes in intestinal microbiota composition in *TNF<sup>ΔARE</sup>* pigs 16s ribosomal RNA gene sequencing (V3-V4) was performed and compared with wild-type controls. In total 122 mucosal

tissue biopsies, 44 luminal and 61 stool samples derived from 23 pigs were analysed. The sequencing results were then also compared to publicly available data derived from *TNF<sup>ΔARE</sup>* mice (98 stool samples from 53 mice) and a human CD patient cohort (133 stool samples from 29 CD patients) (Figure 57).

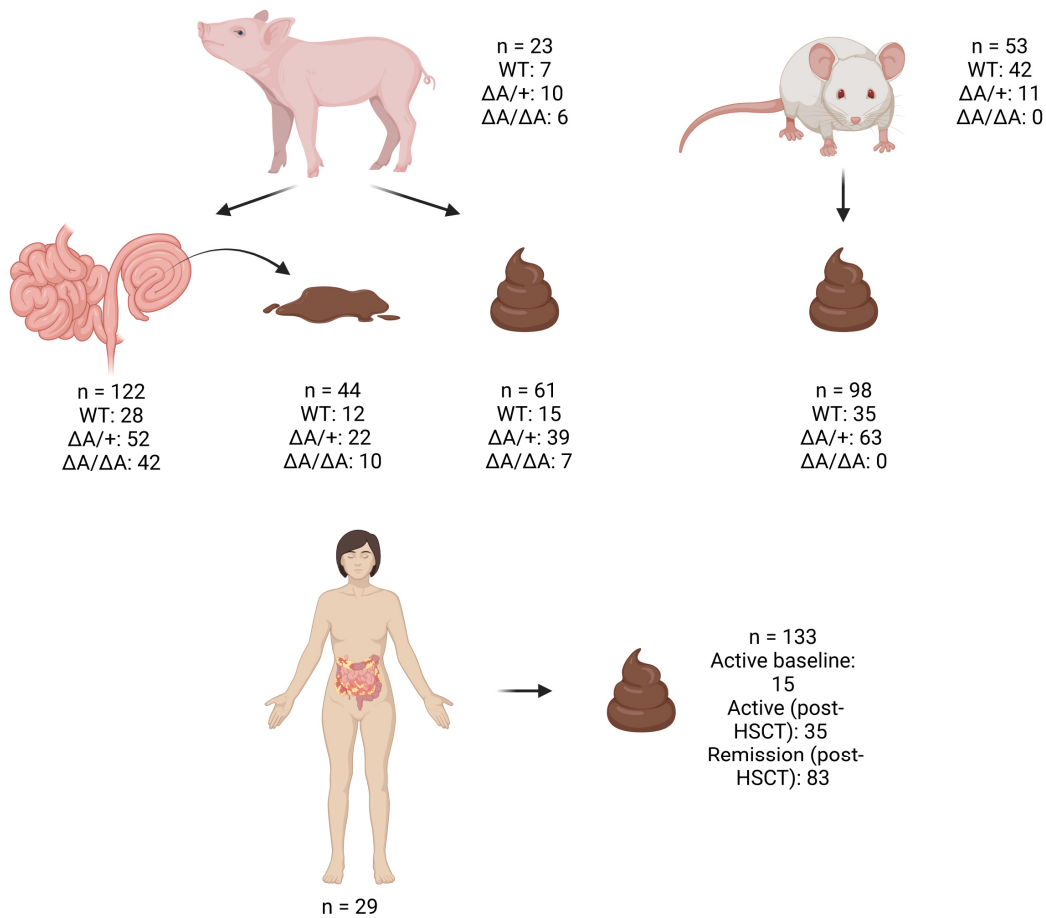


Figure 57: Overview of analysed porcine, murine and human samples for microbiome analysis.

#### 4.8.1. Testing for sample contaminations

In the collection of samples for microbiome analysis, unintended contaminations often occur due to contaminated buffers, washing solutions, or collection devices. Microorganisms in the surrounding air frequently can lead to sample contamination making collection controls essential. To exclude contaminations of analysed samples, air, washing solution, and buffer controls were collected during each sampling.

Comparison of controls with five randomly selected luminal, tissue, stool, and polyp samples showed a significantly reduced alpha-diversity, and most zOTUs approaching values close to or reaching the value zero after normalization via rarefaction in control samples (Figure 58), indicating that mostly background noise was observed and thus no contamination was to be expected.

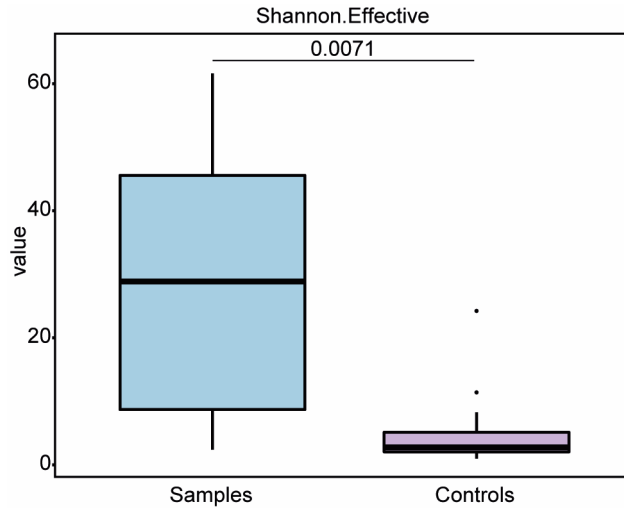


Figure 58: Alpha-Diversity analysis (Shannon effective) of five randomly selected luminal, tissue, stool, and polyp samples with ambient air, buffer, and washing solution controls.

#### 4.8.2. Defining a wild-type reference microbial signature

Prior to conducting a comprehensive analysis of the mutation-induced alterations in the IBD model generated, it was necessary to establish a reference microbial signature.

The luminal samples collected from the rectum, colon, and caecum of wild-type pigs were primarily dominated by *Firmicutes* and *Bacteroidota*. In contrast, the ileum and jejunum were dominated by *Firmicutes* and *Proteobacteria*. From rectum to distal colon, an increase in the relative abundance of *Bacteroidota* and a decrease of *Spirochaetota* was observed (Figure 59).

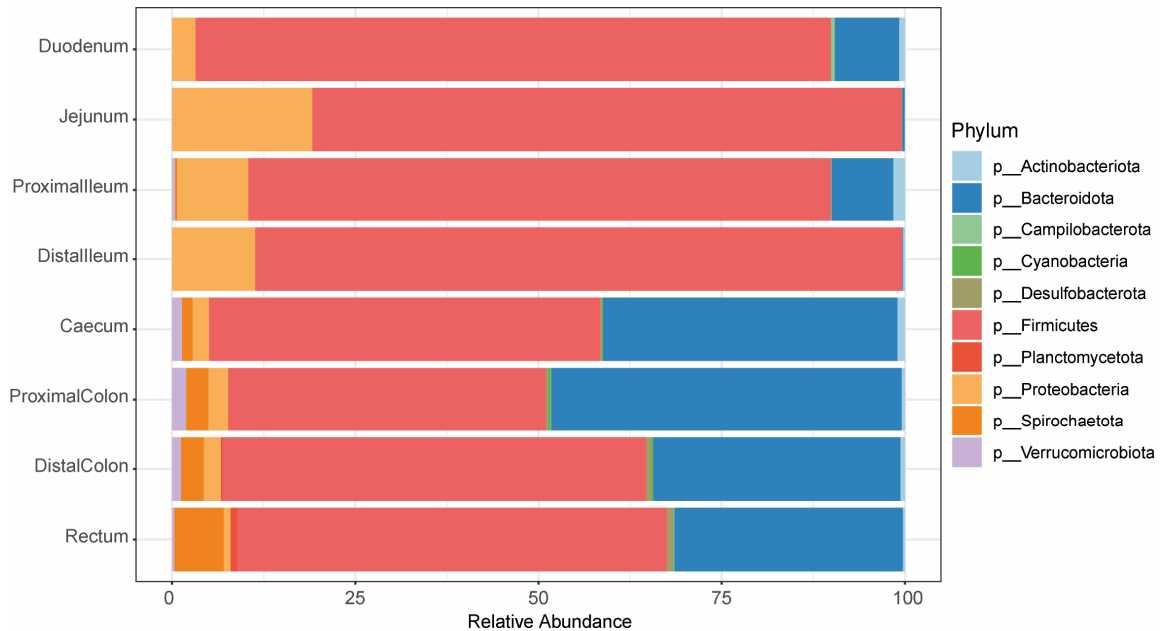


Figure 59: Taxonomic binning of phyla showing taxonomic differences between luminal samples derived from various intestinal sections.

Shannon effective diversity, as a weighted measure of both diversity and evenness of the gut microbiota, was 3-fold higher in the large intestine than in the small intestine (Figure 60).

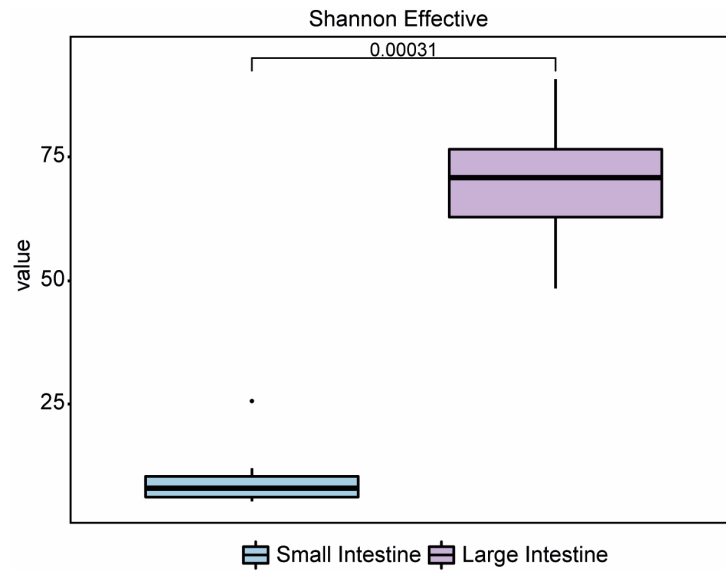


Figure 60: Shannon effective number of small and large intestinal luminal samples derived from wild-type pigs.

The luminal microbial profiles of large intestine and small intestine clustered separately in wild-type pigs when stratified based on sample section (Figure 61).

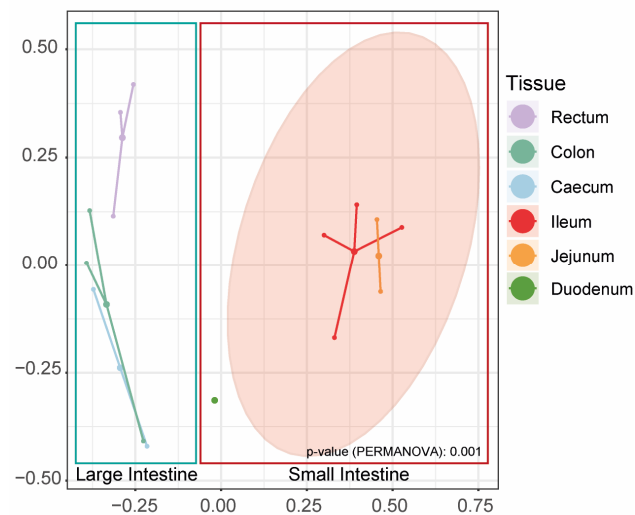


Figure 61: PCoA plot of microbial profiles derived from luminal rectal, colonic, caecal, ileal, jejunal and duodenal samples stratified by tissue sections. The separation of luminal colon and small intestine samples is highlighted by framing the respective samples.

In contrast, no clear separation of microbial profiles in mucosal biopsies of wild-type samples was found ( $p_{\text{adj}} = 0.122$ ) (Figure 62).

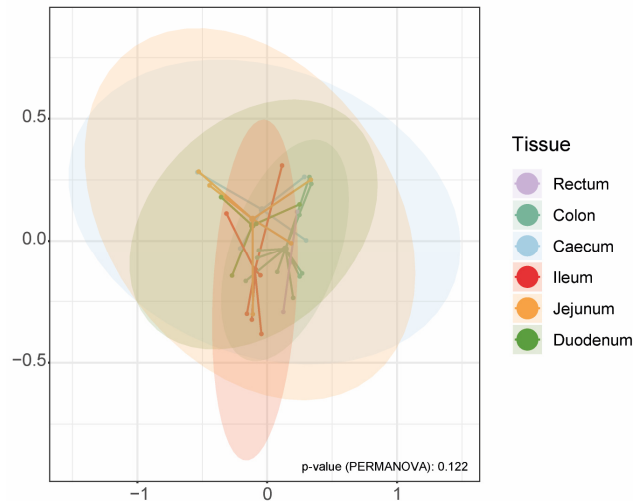


Figure 62: PCoA plot of microbial profiles derived from tissue rectal, colonic, caecal, ileal, jejunal and duodenal samples stratified by tissue sections.

Comparison of relative tissue-associated microbial abundances revealed, that the duodenum, jejunum, and ileum were dominated by the two major phyla *Firmicutes*, and *Proteobacteria* in contrast to large intestinal microbiota, which was dominated by *Firmicutes* and *Bacteroidota*, including *Proteobacteria* for caecal tissue biopsies (Figure 63).

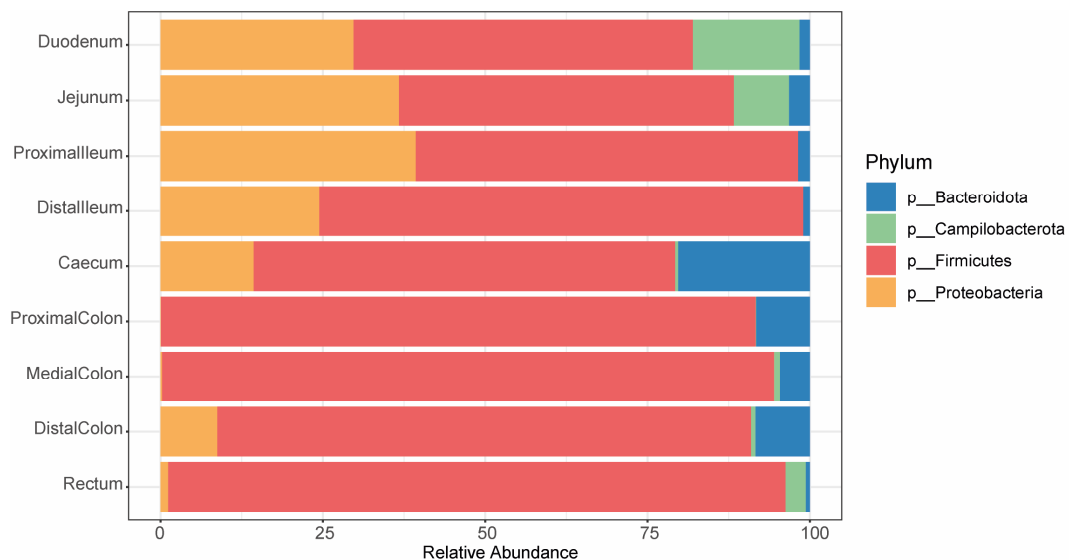


Figure 63: Taxonomic binning of phyla showing taxonomic differences between tissue samples derived from various intestinal sections.

Comparison of the bacterial microbiota composition from tissue with luminal samples revealed that 87 % of zOTUs were shared (Figure 64). Tissue-exclusive zOTUs were mainly members of the genera *Helicobacter*, *Candidatus Arthromitus*, *Clostridium sensu stricto 1*, and to lesser extent members of the genus *Pseudomonas* and of *Selenomonadaceae* and *Lachnospiraceae*. On the other hand, lumen-



exclusive zOTUs were mainly consisting of members of the genera *Sarcina* and *Escherichia-Shigella*, with one zOTUs matching members of the genus *Actinobacillus*.

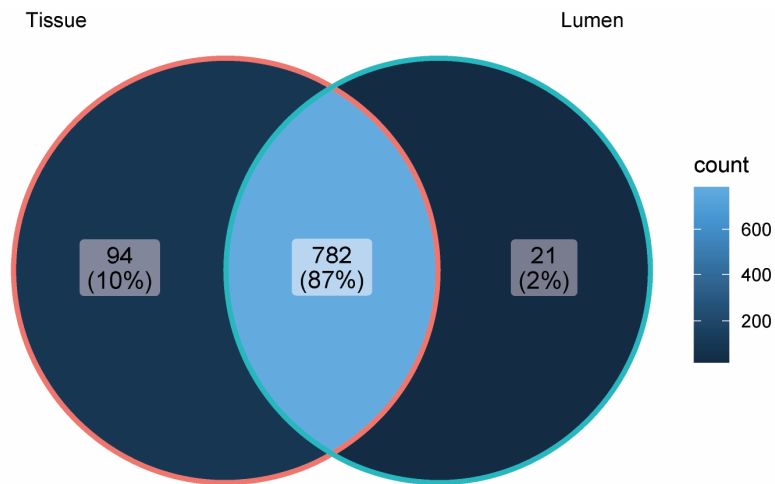


Figure 64: Venn Diagram showing the absolute amount of shared and exclusive zOTUs between luminal and tissue samples.

Linear discriminant analysis Effect Size (LEfSe) analysis identified, among others, *Lactobacillus*, *Turicibacter*, *Alloprevotella* to be present mainly in biopsy tissue, while *Actinobacillus* was identified to be present in mainly luminal sample (Figure 65).

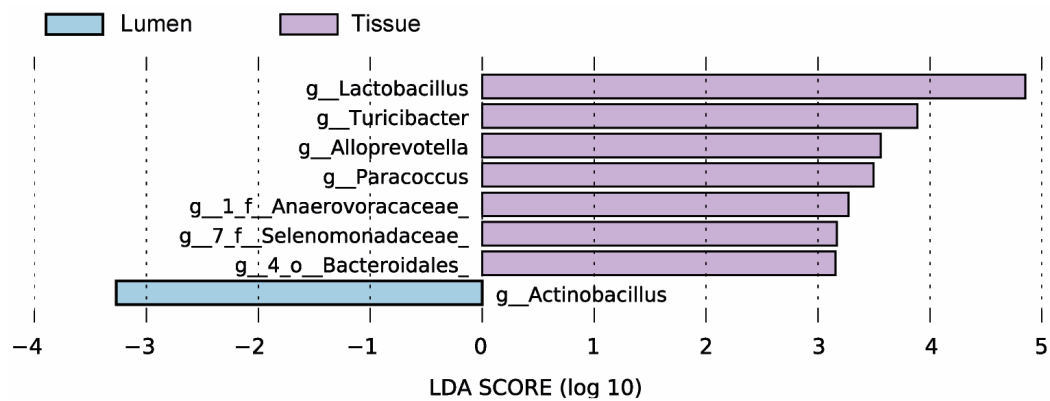


Figure 65: LEfSe analysis of luminal and tissue microbiomes from wild-type samples. The bar lengths illustrate logarithmic fold-changes of differentially abundant genera. The respective LDA linear discriminant analysis score is shown.

No considerable difference in bacterial profile clustering was found between luminal and tissue biopsy sample types when stratified based solely on tissue type or when additionally stratified based on gut section (Figure S10).

Comparison of taxonomic binning between luminal and tissue samples of the same tissue section revealed a relative increase in *Proteobacteria* in duodenal and ileal tissue, of *Campilobacterota* in duodenal, jejunal and rectal tissue and a relative decrease in *Proteobacteria* in jejunal, colonic and rectal tissue (Figure 66).

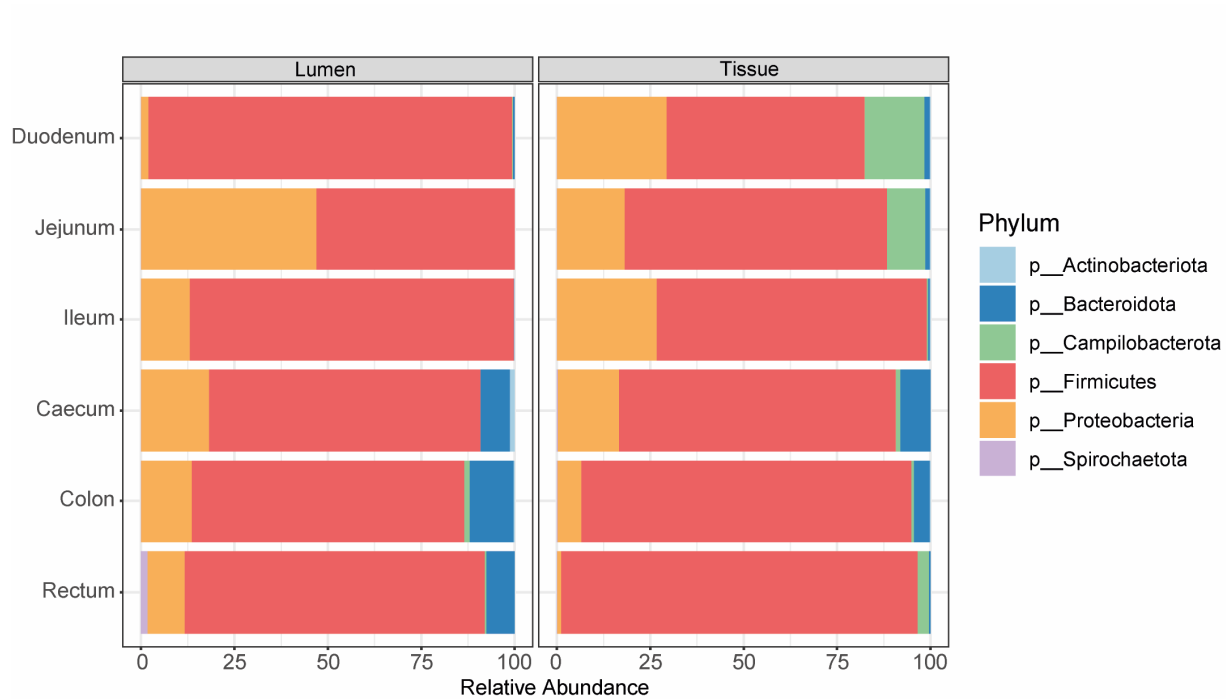


Figure 66: Taxonomic binning of phyla showing taxonomic differences between luminal and tissue samples derived from various intestinal sections.

The most minimally invasive approach for examining genotype- and treatment-induced alterations in the microbial community is through the collection and analysis of faecal samples. To further assess the divergence between the tissue-associated and luminal microbiota, comparative analysis was conducted using end-point faecal samples collected from the same subjects. During the sampling of control animals for comparison with a diseased mutant pig, faecal samples were not consistently collected from all individual animals. As a result, the number of animals sampled for faecal analysis was reduced to three pigs compared to the sampling of diseased mutant pigs. A decreasing trend in microbial diversity and evenness from tissue to luminal to faecal samples was observed (Figure 67).

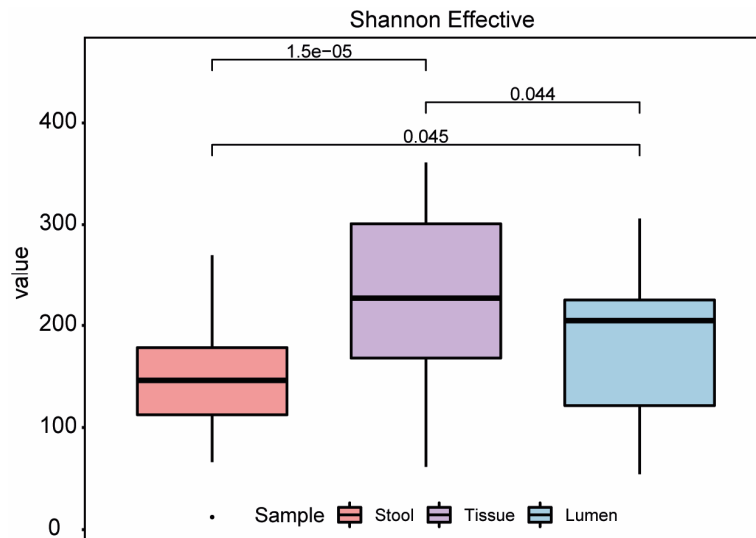


Figure 67: Shannon effective numbers of stool, intestinal tissue-associated and luminal bacteria derived from wild-type pigs.

Luminal and tissue biopsy samples were found to cluster closer together compared to faecal samples, indicating a more similar bacterial profile (Figure 68).

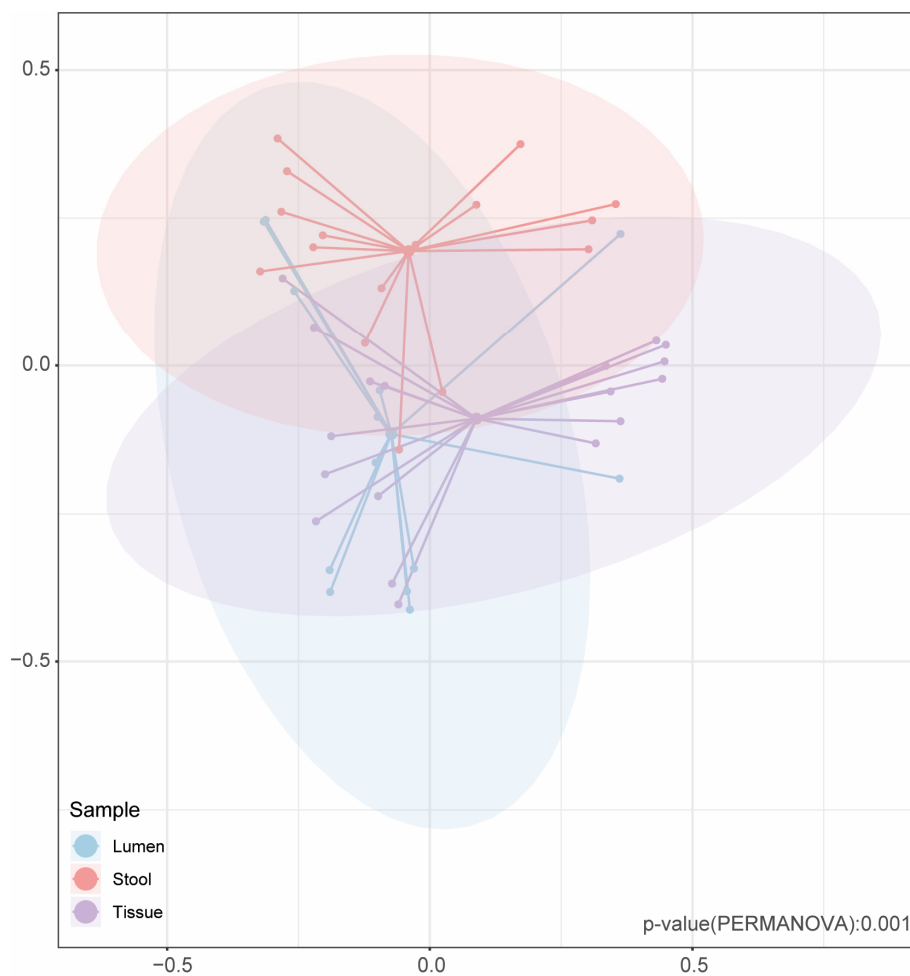


Figure 68: PCoA plot of microbial profiles derived from stool, tissue and luminal samples stratified by sample type.

Analysis of exclusively occurring zOTUs revealed that stool samples shared more exclusive zOTUs with tissue samples compared to luminal samples (Figure S11). Discrimination of luminal and tissue samples according to their intestinal section (large or small intestine) further identifies a stronger overlap of stool with large intestinal samples in general (Figure 69). It also becomes clear that within the small intestine, a larger overlap between tissue-associated and luminal zOTUs occurs compared to large intestinal samples. These findings indicate that stool analysis reflects microbiome alterations in the colon.

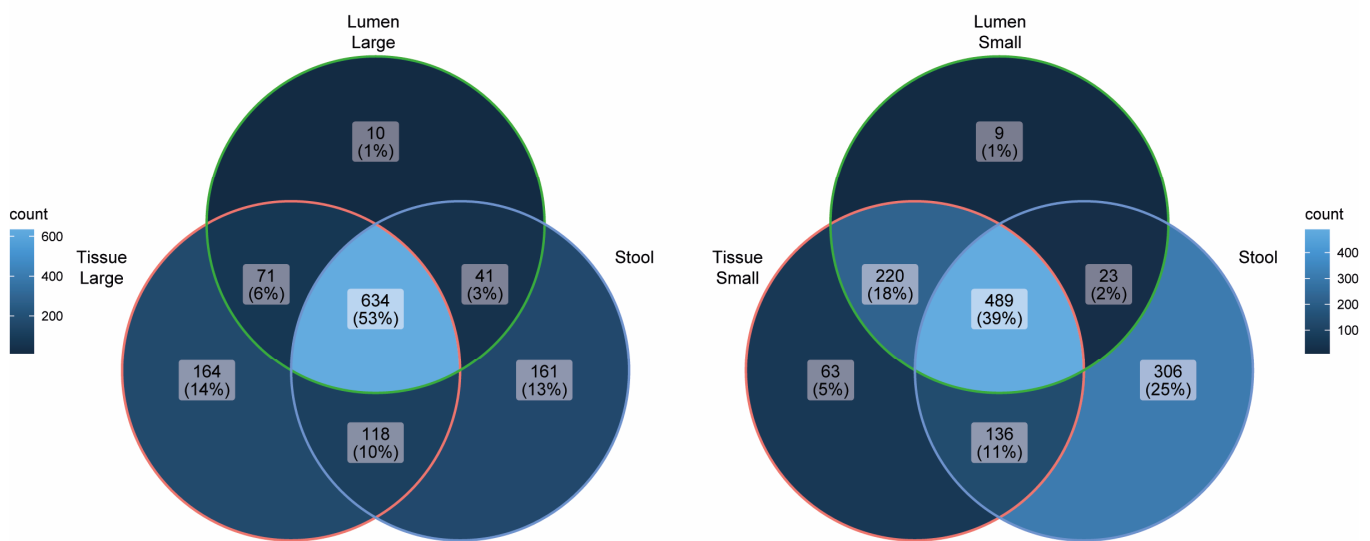


Figure 69: Venn Diagram showing the absolute amount of shared and exclusive zOTUs between stool, and large intestinal (rectum, colon, caecum) or small intestinal (ileum, jejunum, duodenum) luminal and tissue samples derived from wild-type pigs. A brighter color indicates a larger overlap.

LEfSe analysis revealed that members of the genus *Bacillus* were associated with luminal samples, while members of the genus *Bacteroides* were associated with faecal samples (Figure S12). However, as this statistical tool is more conservative and focuses on identifying taxa that are specifically associated with a particular group, rather than identifying over- or underrepresented taxa between groups, a less sensitive statistical evaluation, Wilcoxon test with Bonferroni correction was utilized. Among others, Wilcoxon test with Bonferroni correction for multiple testing identified several *Bacteroidetes* (*g\_7 Muribaculaceae*, *Prevotellaceae UCG-001*, *g\_Prevotella*, and *Bacteroides*), and *Spirochaetes* (*Treponema*) to be over-, and several *Firmicutes* (*Bacillus*, *g\_Clostridium sensu stricto 1*, *Romboutsia*, *Streptococcus*, *Terrisporobacter*, and *Turicibacter*) to be underrepresented in stool compared to luminal or tissue samples (Figure S13).

In addition to the obvious influence of tissue type and intestinal region on the composition of the associated microbiota, it was possible that other factors (metadata) might have had a significant impact on microbiota differences. Thus, it was necessary to understand important influences on the baseline microbiome composition to accurately assess the impact of the ARE/CDE1 mutation on the microbiome.

To this end, as an important first step, a confounder analysis was performed. This analysis helps to control for variables that may affect the observed relationships between the microbiome and other variables, ensuring that the conclusions drawn from the study are reliable and accurate. The intestinal section together with the sample type (e.g. Colon\_Lumen, "Tissue.Sample"), only the sample type (e.g. Lumen, "Sample"), only the intestinal sample location (e.g. colon or ileum, "Gut.Section"), a more detailed intestinal sample location (e.g. distal or proximal colon, "Gut.section.detail"), the individual pig (e.g. #1945, "Pig"), the mother sow (e.g. #1532, "Mother"), the father boar (e.g. #1933, "Father"), the litter group (e.g. Litter A, "Litter"), the gender (e.g. male, "Gender") and the individual's age at time of sampling in days (e.g. 35, "Age.d") were evaluated to determine if they had an effect on other variables. No significantly confounding variables were found. Although not significant, the strongest influence on other variables was found for metadata describing the intestinal location, sample type and litter group indicating that these variables are expected to have potential distorting effects on the microbiota compositions (Figure 70).

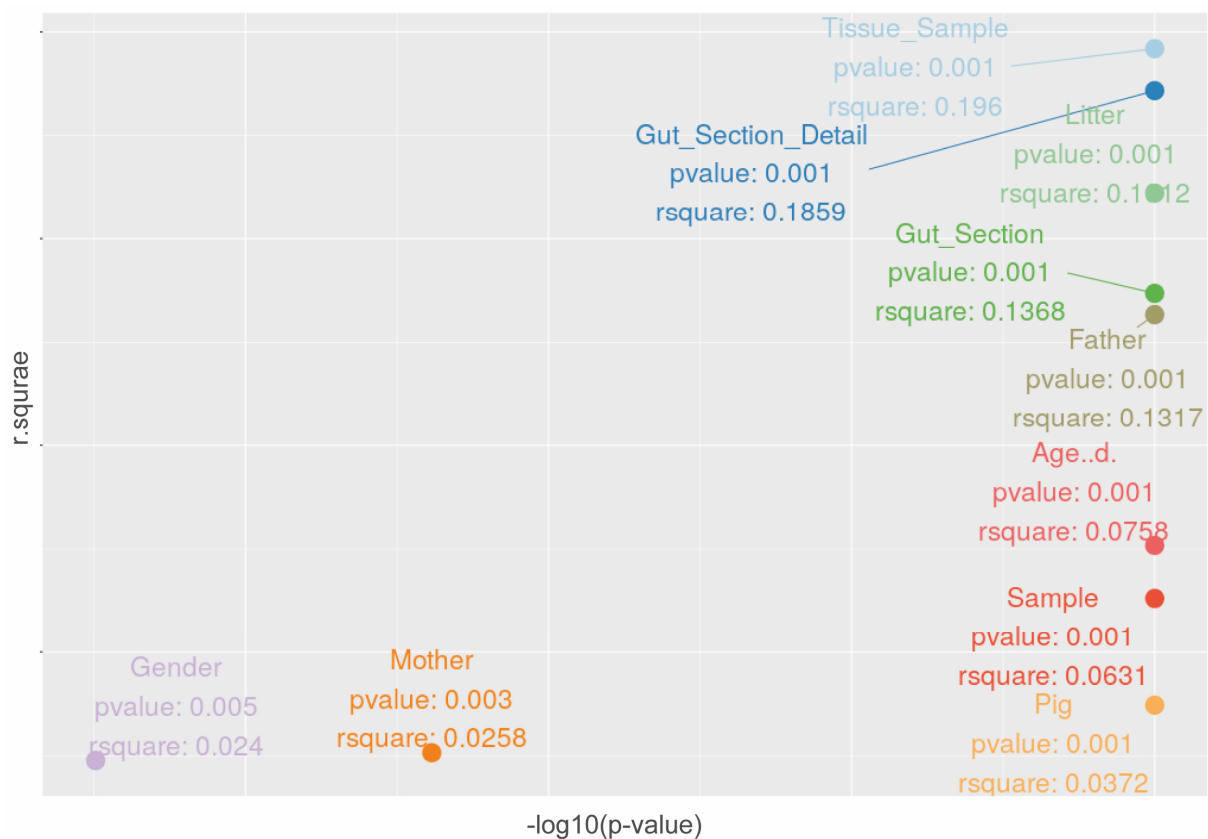


Figure 70: Explained variation plot representing individual groups that are plotted over their negative log 10 p-value and R<sup>2</sup> value derived from a confounding analysis. P-values and R<sup>2</sup> values are shown.

Above mentioned findings have indicated an important role of weaning in disease penetration (Figure 29). In order to verify these findings, detailed confounding analysis was performed.

To this end, mucosal or faecal bacterial profiles stratified by sex ( $n_{\text{mucosal-male}} = 12$  samples from 3 animals;  $n_{\text{mucosal-female}} = 18$  samples from 3 animals;  $n_{\text{stool-male}} = 20$  samples from 6 animals;  $n_{\text{stool-female}} = 29$  samples from 4 animals) or age ( $\text{mean}_{\text{mucosal-male}} = 79.5 \pm 10.5$  days;  $\text{mean}_{\text{mucosal-female}} = 235.78 \pm 162.88$  days;  $\text{mean}_{\text{stool-male}} = 120.8 \pm 48.31$  days;  $\text{mean}_{\text{stool-female}} = 167.45 \pm 102.322$  days) were compared. Differing bacterial profiles of samples derived from pigs of different gender and age were observed. Only weak differences were found for bacterial  $\alpha$ -diversity, although pigs between 0-4 months of age were harbouring the most diverse bacterial ecosystem. Here, a trend towards a lower standard deviation between samples was observed for old (>12 months) pigs, indicating a more stable microbiome in adult swine (fed the same diet). To a lesser extent, this was also reflected in stool, again highlighting the limitations that come with this sample type and providing an explanation on why confounding effects might have been masked (Figure S14). In sows, a higher abundance of members of the genera *Streptococcus*, *Rikenellaceae RC9\_gut group* and *Cellulosilyticum* was found among others, while members of the genera *g\_4 (f\_Peptostreptococcaceae)*, *Phascolarctobacterium* and *Sarcina*, were more abundant in boars (Figure S15 and S16). There was no overlap of significantly differentially abundant genera between mucosal biopsy and stool samples. Analysis of luminal samples was not performed, as all sample sequencing data available was derived from female pigs only.

#### 4.8.3. Assessment of genotype-associated shifts in microbial communities

The investigation of the effects of the  $\Delta\text{ARE}$  mutation on the microbiota composition involved comparing genotype-specific taxonomic binning, as well as alpha- and beta-diversity, with a focus on analysing tissue and stool samples. Tissue samples also provided insights into inflammation status, and stool samples allowed for longitudinal analysis. It was found that observed macro- and microscopic differences in  $TNF^{\Delta\text{ARE}}$  pigs to wild-type pigs were reflected in the microbiota composition, along with inter-individual variations (Figure 71).

### Taxonomic classification (Phyla level)

- Actinobacteriota
- Bacteroidota
- Campylobacterota
- Fibrobacterota
- Firmicutes
- Fusobacteriota
- Proteobacteria
- Verrucomicrobiota

### Biopsy location \*

- Upper GIT
- Lower GIT + Stool

### Genotype \*\*

- Wild-type
- $\Delta A/+$
- $\Delta A/\Delta A$

### Pig number \*\*\*

- |  |   |   |   |
|--|---|---|---|
| <span style="color: #800080;">■</span> P#1 | <span style="color: #8B0000;">■</span> P#7  | <span style="color: #E91E63;">■</span> P#13 | <span style="color: #008080;">■</span> P#19 |
| <span style="color: #32CD32;">■</span> P#2 | <span style="color: #DDA0DD;">■</span> P#8  | <span style="color: #008000;">■</span> P#14 | <span style="color: #FFDAB9;">■</span> P#20 |
| <span style="color: #654321;">■</span> P#3 | <span style="color: #FFD700;">■</span> P#9  | <span style="color: #FFFFFF;">■</span> P#15 | <span style="color: #483D8B;">■</span> P#21 |
| <span style="color: #ADD8E6;">■</span> P#4 | <span style="color: #000000;">■</span> P#10 | <span style="color: #DDA0DD;">■</span> P#16 | <span style="color: #000080;">■</span> P#22 |
| <span style="color: #000080;">■</span> P#5 | <span style="color: #FF8C00;">■</span> P#11 | <span style="color: #FFFF00;">■</span> P#17 | <span style="color: #32CD32;">■</span> P#23 |
| <span style="color: #008000;">■</span> P#6 | <span style="color: #FFB6C1;">■</span> P#12 | <span style="color: #A9A9A9;">■</span> P#18 |   |

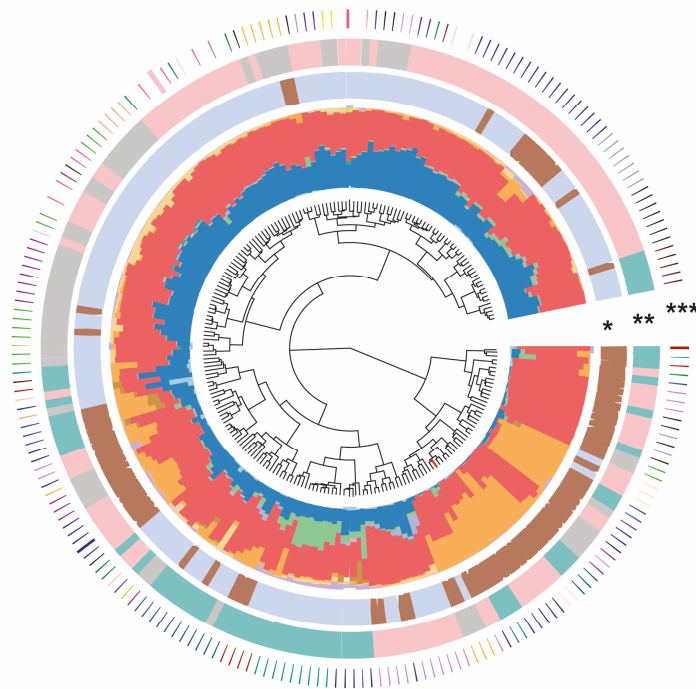


Figure 71: Taxonomic phylogenetic tree of microbes in upper and lower gastrointestinal tract (GIT), stool, and tissue biopsy samples from pigs of different genotypes (#1-23). The tree is color-coded to represent the samples' association with the biopsy location (upper/lower gastrointestinal tract and stool), genotype (Wild-type,  $TNF^{\Delta ARE/+}$ ,  $TNF^{\Delta ARE/\Delta ARE}$ ), and pig number (#1-23). This plot was generated by Dr. Amira Metwaly. Adapted from Winogradzki et al.<sup>163</sup>.

In  $TNF^{\Delta ARE}$  pigs, mucosa-adhering bacterial composition of the ileum was characterised by a higher relative abundance of *Proteobacteria* and a lower relative abundance of *Firmicutes*, whereas in the proximal colon, a relative increase in *Campylobacterota* and *Verrucomicrobiota* at the expense of *Bacteroidota* was observed, especially in  $TNF^{\Delta ARE/\Delta ARE}$  pigs (Figure 72).

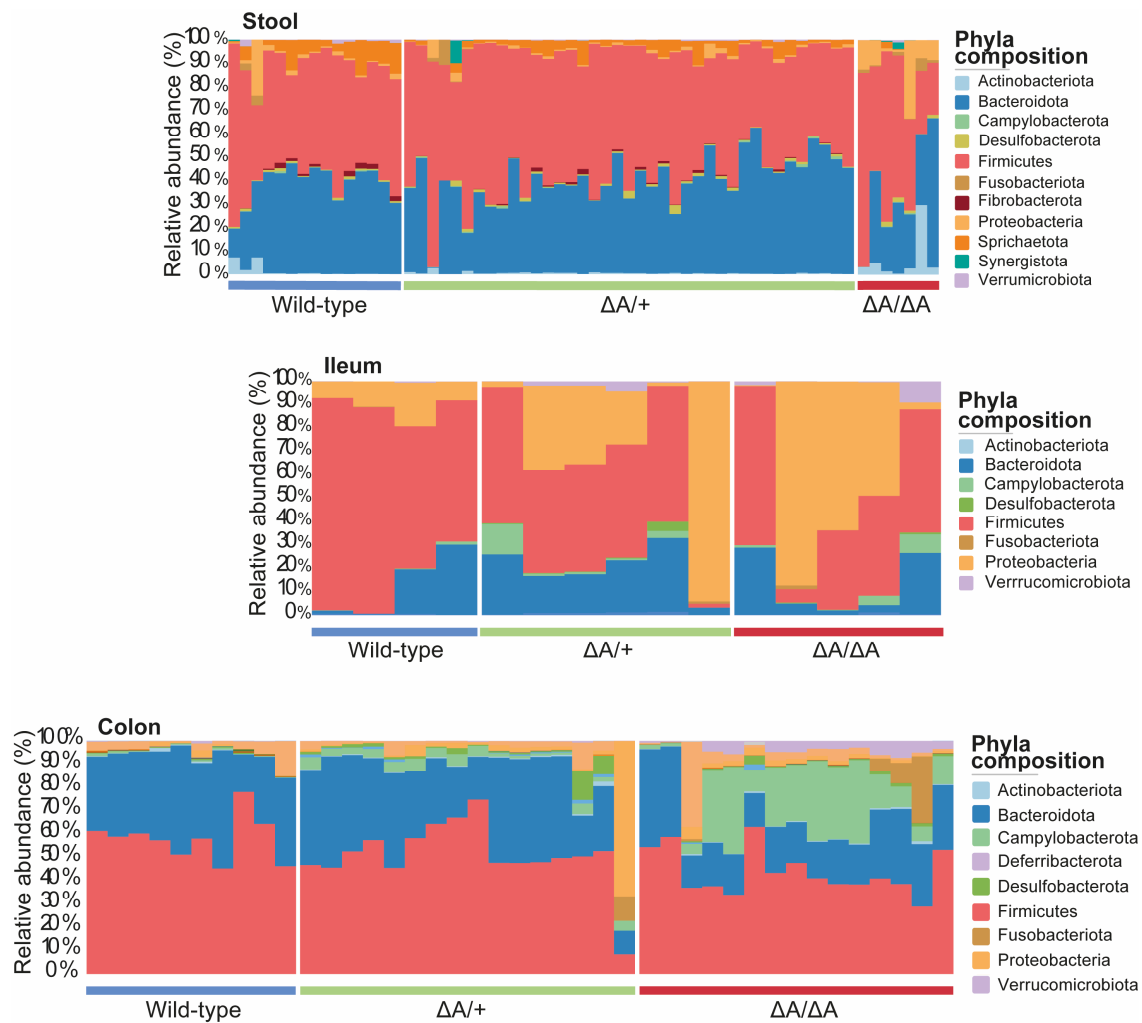


Figure 72: Taxonomic Distribution of microbes in faecal, ileal, and colonic tissue biopsy samples from wild-type,  $TNF^{\Delta ARE/+}$  and  $TNF^{\Delta ARE/\Delta ARE}$  pigs. The color-coded representation of the phyla present in each sample is described in the accompanying legend. Modified from Dr. Amira Metwaly's plot. Adapted from Winogradzki et al.<sup>163</sup>.

LEfSe analysis showed an enrichment in members belonging to *Helicobacter*, *Megasphaera*, *Campylobacter*, *Desulfovibrio*, *Alistipes*, and *Lachnoclostridium* among others in faecal or mucosa-associated bacteria of  $TNF^{\Delta ARE}$  pigs compared to wild-type littermates (Figure S17).

Stratification of microbial profiles by location expectedly showed reduced community richness and alpha diversity in the upper gastrointestinal mucosa-associated microbiota compared to lower GI mucosa-associated and stool microbiota (Figure 73).



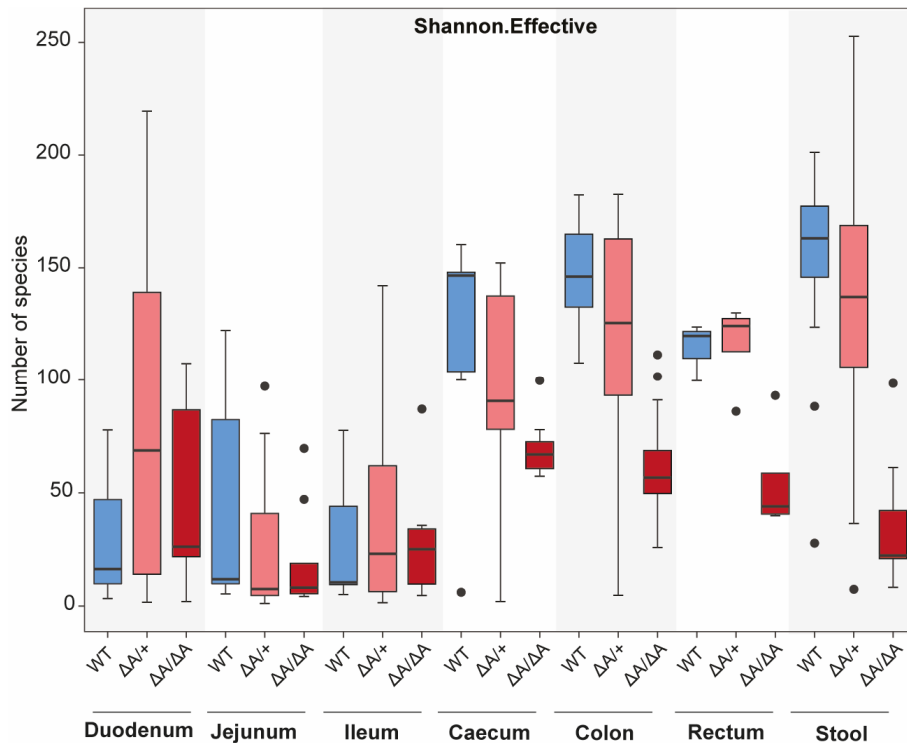


Figure 73: Shannon effective numbers of faecal or duodenal, jejunal, ileal, caecal, colonic, or rectal tissue samples derived from wild-type,  $TNF^{\Delta ARE/+}$  and  $TNF^{\Delta ARE/\Delta ARE}$  swine. Modified from Dr. Amira Metwaly's plot. Adapted from Winogrodzki et al.<sup>163</sup>.

Beta-diversity analysis showed significant separation of microbial profiles in ileal and colonic mucosa of wild-type,  $TNF^{\Delta ARE/+}$  or  $TNF^{\Delta ARE/\Delta ARE}$  pigs, which was weakly reflected in stool, jejunum and duodenum (Figure 74). Comparison of microbiota compositions revealed, that 48 % or 61 % of zOTUs were shared among genotypes in colon and ileum, respectively. zOTU-overlap between  $TNF^{\Delta ARE/+}$  and  $TNF^{\Delta ARE/\Delta ARE}$  pigs in the ileocolitic mucosa was larger compared to mutant and wild-type swine, and this effect was stronger in the colon (Figure S18).

Although only a few luminal samples were 16s rRNA sequenced, results comparable to those obtained with  $\beta$ -diversity analysis of tissue samples were obtained. Bacterial profiles stratified based on genotype showed the strongest differences in the ileocolitic region, particularly in the colon (Figure S19).

In contrast to mucosal bacterial profiles, the biggest overlap of zOTUs was found between  $TNF^{\Delta ARE/+}$  pigs and wild-types (54 % or 37 % of zOTUS for colonic or ileal samples, respectively). When all intestinal sections were considered, the biggest overlap of zOTUs was found for the overlap of all samples (43 %). These findings indicate a gene-dosage dependent disruption of the basal microbiota that is more sensitive on the surface compared to the luminal level (Figure S20).

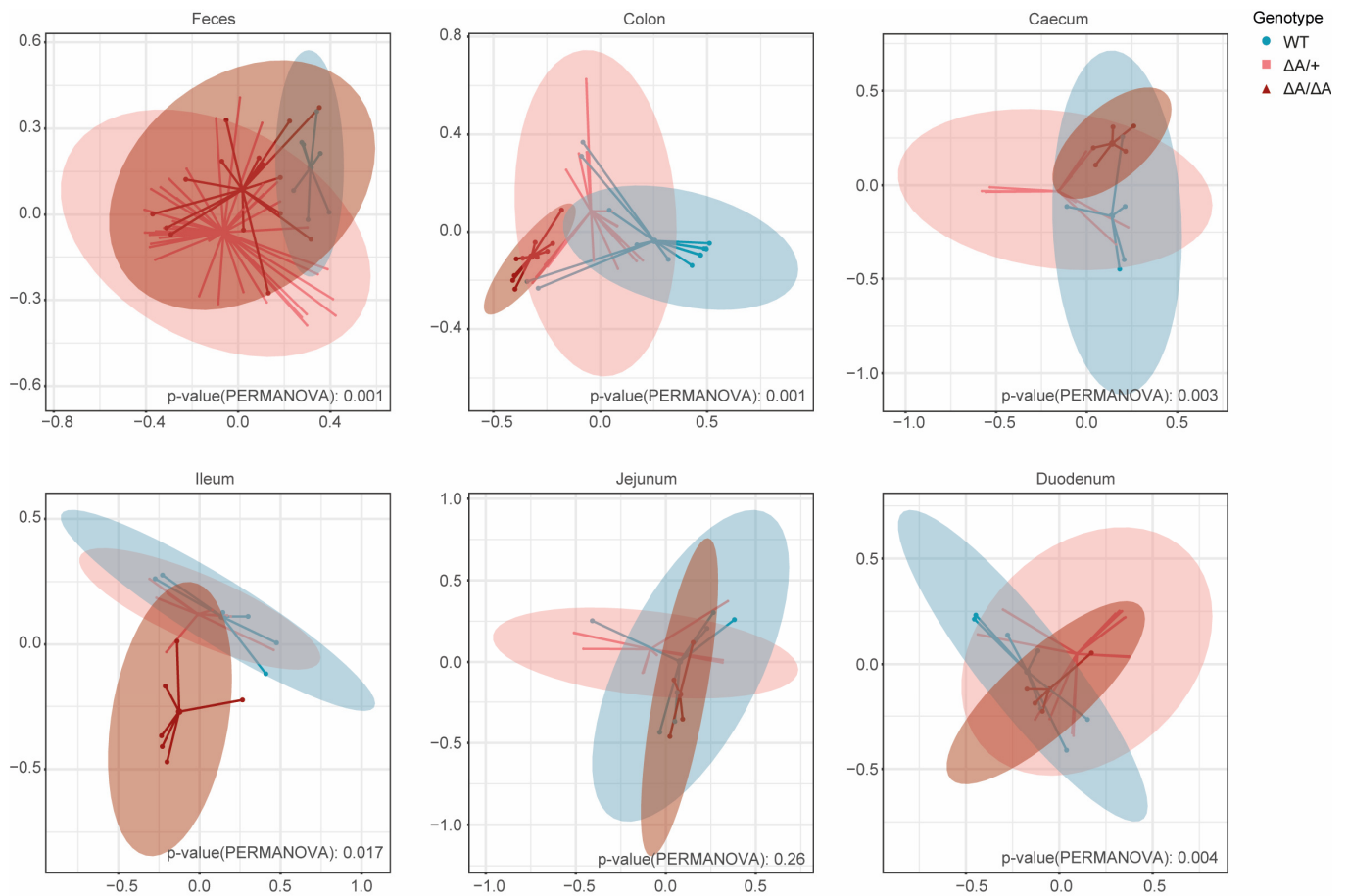


Figure 74: PCoA plots of microbial profiles derived from faecal (top left), colonic (top middle), caecal (top right), ileal (bottom left), jejunal (bottom middle), and duodenal (bottom right) tissue samples stratified by genotype.

To potentially identify discriminative taxa or groups of taxa that might trigger an inflammatory phenotype, a semi-subjective disease score was determined based on the time of disease manifestation, external appearance, and the degree of macroscopic and microscopic intestinal morphological changes (Figure 75).

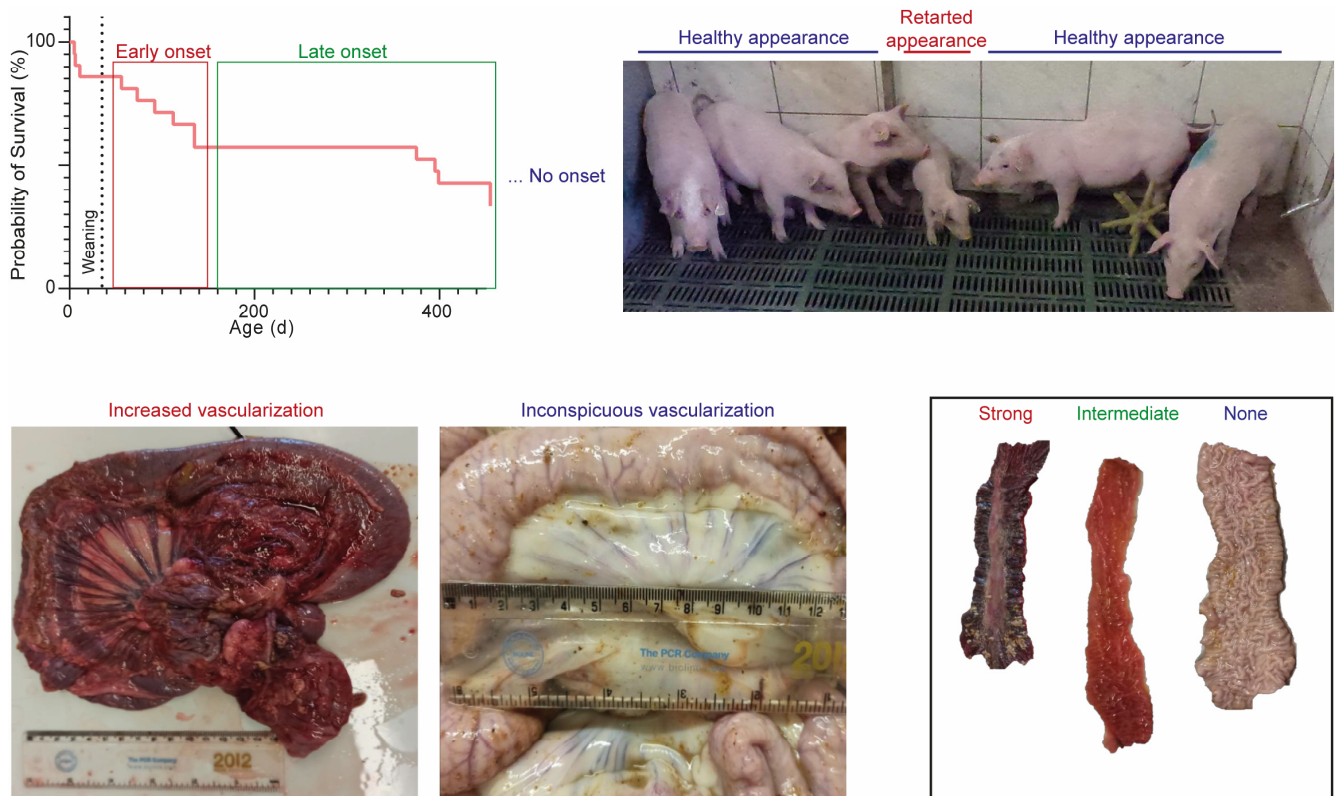


Figure 75: Considered factors for the determination of health status in mutant pigs were the age at the onset of disease (top left), the general appearance (top right), macroscopic intestinal findings, such as vascularization (bottom left and middle) and hemorrhagic coloration (bottom right).

To test the applicability of this semi-subjective classification, a correlation analysis was performed with data from immunohistochemical staining of ileocolonic tissue biopsy specimens. Indeed, a significant correlation was found between the inflammation score and the proportion of Pas/AB<sup>+</sup> cells in the crypt (Pearson's  $r = -0.6802$ ) or IBA1<sup>+</sup> cells in the lamina propria (Pearson's  $r = 0.7342$ ), suggesting that the classification used to classify inflammation is consistent with immunohistochemical markers of inflammation and thus applicable (Figure S21).

Using this semi-subjective approach, 8 % (9/118), 31 % (37/118) and 61 % (72/118) of stool samples were associated with a diseased, intermediate, or healthy phenotype, respectively. Terminal tissue biopsy samples were found to be diseased in 32 % (31/97), mildly diseased in 66 % (64/97) or not diseased at all in 2 % (2/97) of cases. These results were expected as sampling of tissue and luminal specimen was performed when mutant pigs reached a termination criterion, in contrast to faecal sampling that occurred regardless of the disease severity.

Next, a confounder analysis was performed to identify meta variables that might explain observed differences regardless of genotype. The highest  $R^2$  values were calculated for litter (0.1625), gut section (0.0959) and genotype (0.0953). It was found that the subjectively assigned inflammation score was a confounding variable for gut section- and age-related differences (Figure 76). Additionally, it is important to note that the significance of the observed confounding effects could potentially be attributed to a higher statistical power, in addition to the changes induced by mutation.

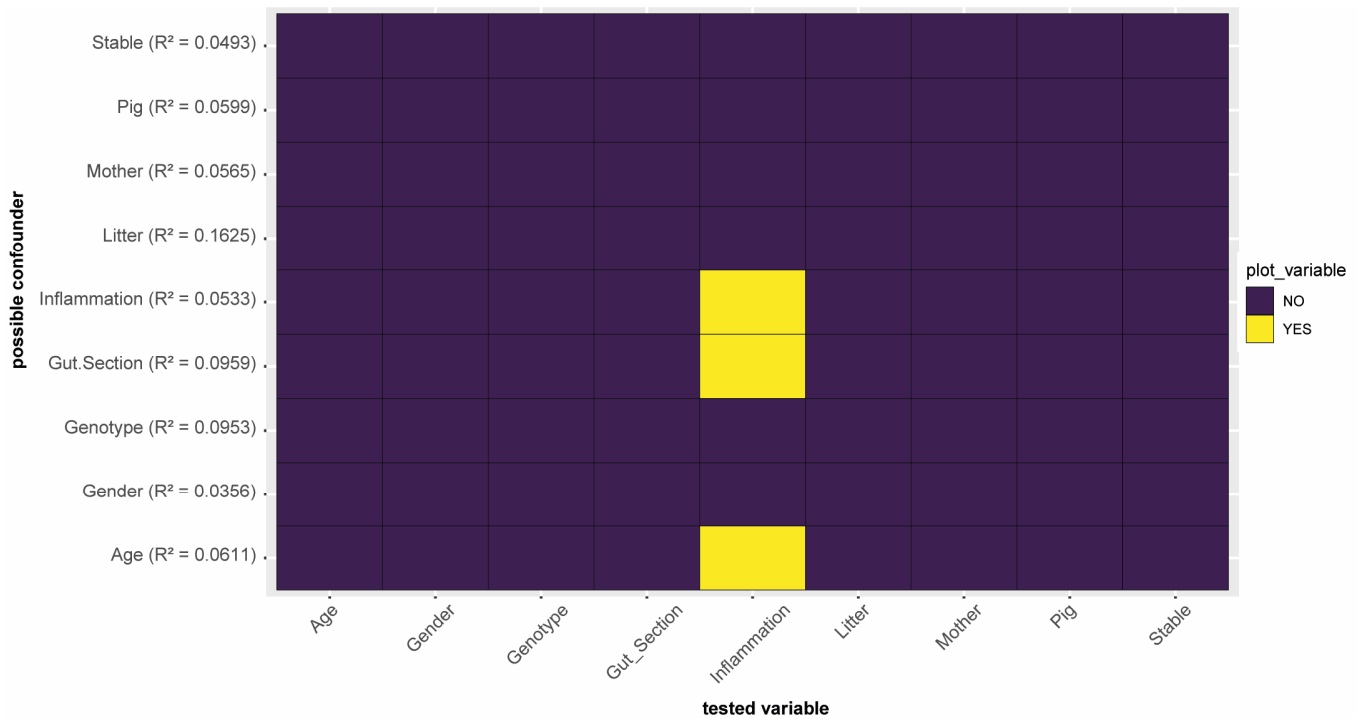


Figure 76: Heatmap showing potential confounding factors for specific variables. Confounding factors are highlighted in yellow. R<sup>2</sup> values of confounding factors are shown.

Of note, there was a weaker separation between samples derived from *TNF<sup>ΔARE/+</sup>* pigs based on their gender when compared to the wild-type controls (Figures S14 and S22).

Since age has been identified as a possible confounder for the severity of disease, microbial shifts during critical periods, e.g. weaning were determined more closely. It was shown that physical and psychological stress, e.g., nutritional or environmental changes at time of weaning, and increased exposure to pathogenic microorganisms can elicit local or systemic immune responses in post-weaning piglets<sup>176, 183</sup>. Intestinal inflammatory response was observed up to 15 days post-weaning, measured by increased IgA-producing cells, and enhanced mucosal levels of IgA, IgM, IFN- $\gamma$ , IL-1 $\alpha$ , IL-8, IL-10, IL-12 $\alpha$ , and TGF- $\beta$ <sup>177</sup>. As animal health is of economic importance for the pig industry this time period has become a research focus<sup>176,178,179</sup>.

The effect of this critical time window on the pathophysiology of *TNF<sup>ΔARE</sup>* pigs has already been shown (Figure 29) most phenotypic disease manifestations were observed shortly after weaning. Stratification of samples based on collection time points (pre-weaning: 16 days; during-weaning: 37 days; post-weaning: 73, 109, 138 and 227 days) revealed significant shifts in bacterial profiles, highlighting the significant compositional changes that occur during this process (Figure 77).

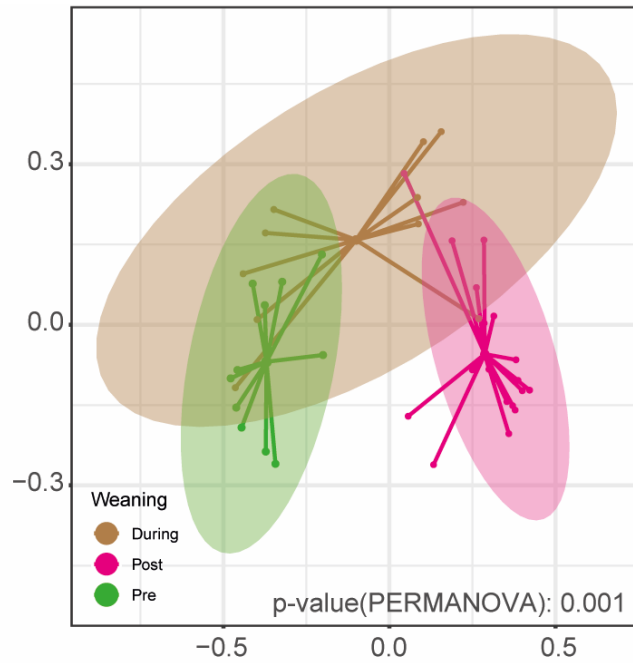


Figure 77: PCoA plots of microbial profiles derived from stool samples stratified by weaning state of wild-type and mutant pigs.

LEfSe analysis revealed a strong association in members belonging to the genera of *Escherichia-Shigella*, *Enterococcus* and *Olsenella* with pigs before weaning, *Synergistaceae*, and *Cloacibacillus* with pigs during weaning and *Treponema*, *(Allo-)Prevotella*, *Prevotellaceae* and *Campylobacter*, among others, with pigs after weaning across genotypes (Figure S23).

In contrast to the *TNF<sup>ΔARE/+</sup>* mouse model<sup>180</sup>, differences in α-diversity were already seen for periods before the onset of disease after weaning, suggesting changes in the microbiota preceding observable inflammatory changes. Of note, pre-weaning and during-weaning bacterial diversity appeared to be higher compared to the post-weaning time-points (Figure 78).

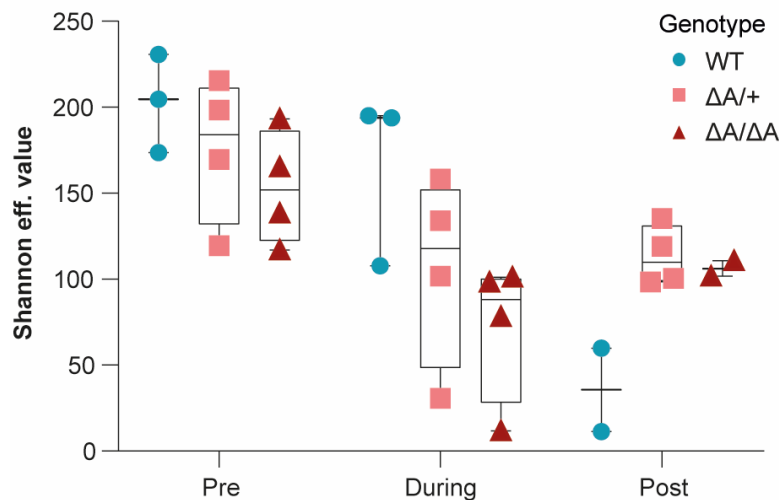


Figure 78: Shannon effective numbers for microbial ecosystems derived from faecal samples of wild-type *TNF<sup>ΔARE/+</sup>*, and *TNF<sup>ΔARE/ΔARE</sup>* pigs pre-, during and post-weaning.

Differential statistical analysis (Wilcoxon test with Bonferroni multiple correction testing) stratified based on the time and genotype identified 6 significantly differing features. Within the post-weaning group, a significantly higher abundance of the complex plant diet-metabolizer *Prevotella* genus was observed in stool derived from  $TNF^{\Delta ARE}$  pigs (Figure 79). This is particularly important when considering that pigs receive a plant-based diet after weaning, indicating a higher plasticity of the gut microbiota, which is in line with an increased alpha-diversity after weaning.

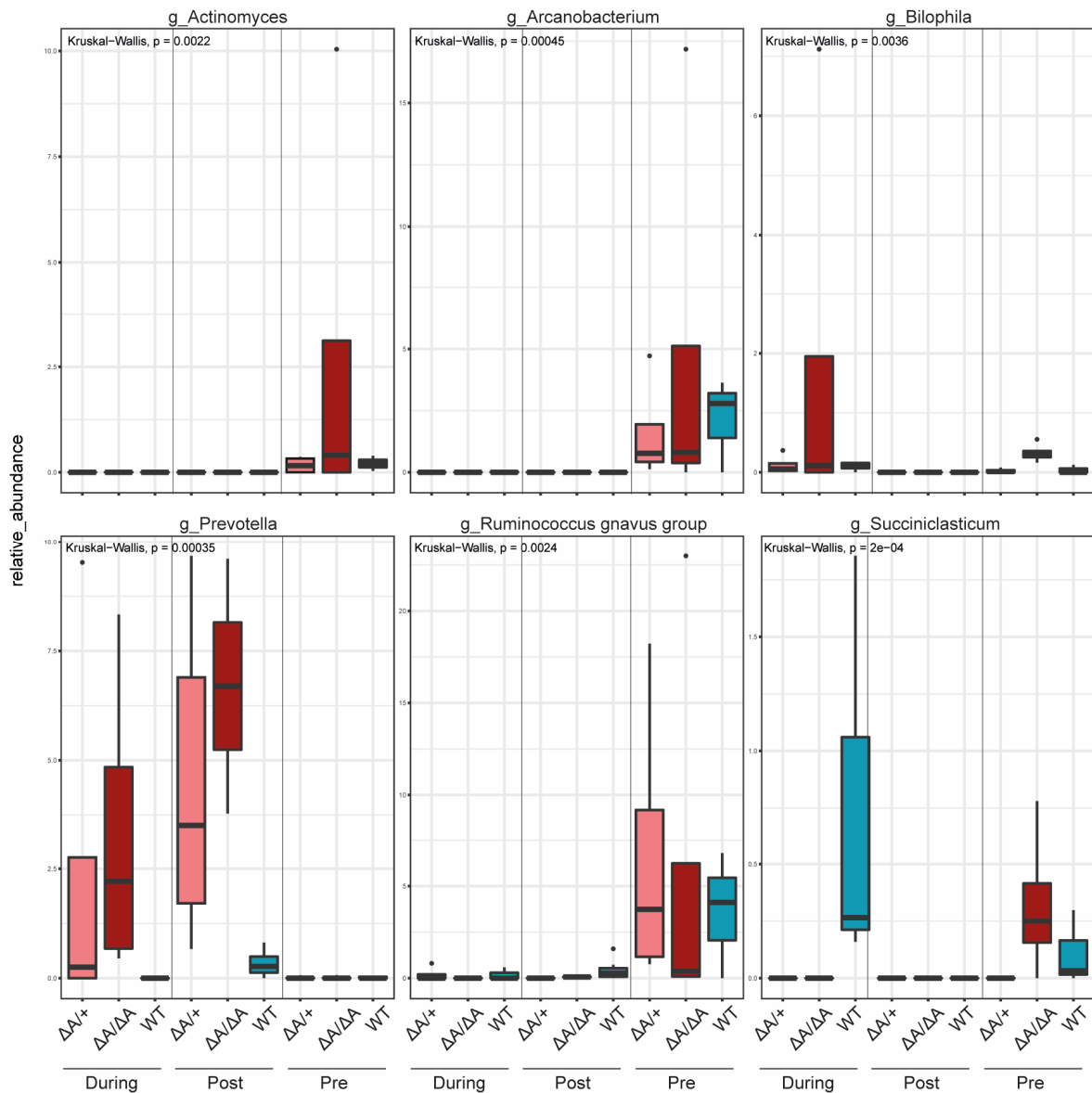


Figure 79: Significantly differentially abundant genera found in faecal samples of wild-type  $TNF^{\Delta ARE/+}$ , and  $TNF^{\Delta ARE/\Delta ARE}$  pigs pre-, during and post-weaning identified by Wilcoxon testing with Bonferroni correction for multiple testing.

Time-series comparison of phyla abundances between genotypes clearly visualized a fast expansion of *Campilobacterota*, *Cyanobacteria*, *Firmicutes*, *Proteobacteria* and *Verrumicrobiota* in  $TNF^{\Delta ARE}$  pigs

compared to wild-type littermates, while *Bacteroidota*, *Fusobacteriota*, *Planctomycetota* and *Spirochaetota* showed a slower and weaker increase. Noteworthy, the number of often obligate anaerobic Firmicutes quickly declined after reaching a maximum during weaning, which aligned with a steady increase in *Bacteroidota*, *Campilobacterota*, *Cyanobacteria*, and *Proteobacteria*, indicating a more favourable environment for these often facultative anaerobic phyla after weaning (Figure 80).

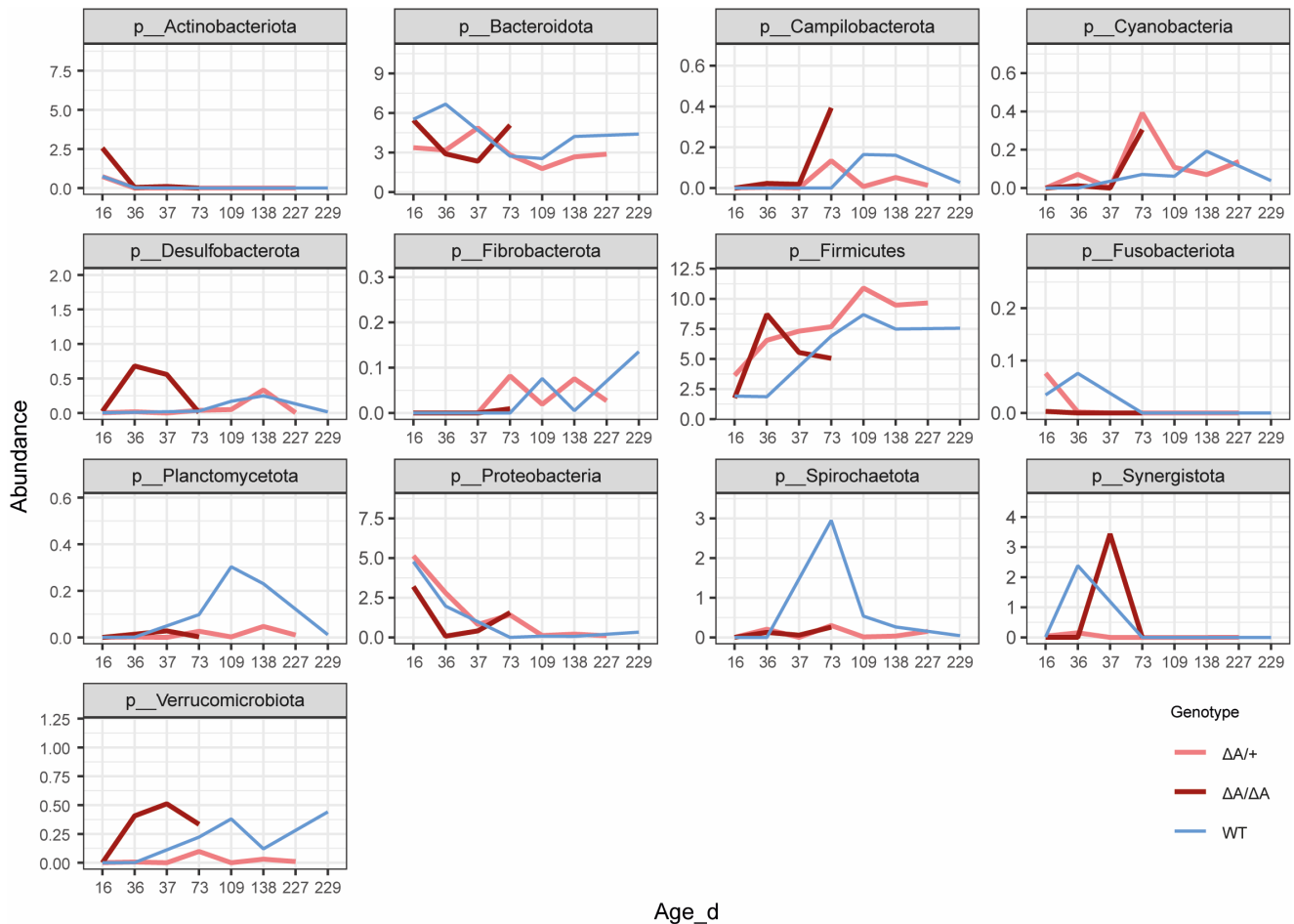


Figure 80: Time-series-analysis of phylum abundances in faecal samples derived from wild-type  $TNF^{AAARE/+}$ , and  $TNF^{\Delta ARE/\Delta ARE}$  pigs.

Evidence of a disturbed intestinal epithelial barrier integrity was found via immunohistochemistry and protein analysis (as shown in Figures 38-40), which could have led to a higher oxygen availability at the mucosal surface and favored the growth of certain facultative anaerobic phyla over obligate anaerobes such as *Firmicutes*.

#### 4.8.4. Exploring the temporal relationship between gut microbiota and inflammation

##### 4.8.4.1. Comparison of faecal consistency and markers of intestinal inflammation across genotypes

To identify whether inflammatory processes precede or follow observed microbial changes, faecal consistency and markers of intestinal inflammation were compared across genotypes for two time points after weaning (ages 50d and 75d) of the same individual. Expectedly,  $TNF^{\Delta\Delta/\Delta\Delta}$  swine showed the highest Bristol stool scores, followed by  $TNF^{\Delta A/+}$  pigs and wild-types. Bristol stool scores correlated with Calprotectin values, although no significant correlation was found presumably due to a low statistical power (Pearson's R: 0.5242) (Figure 81).

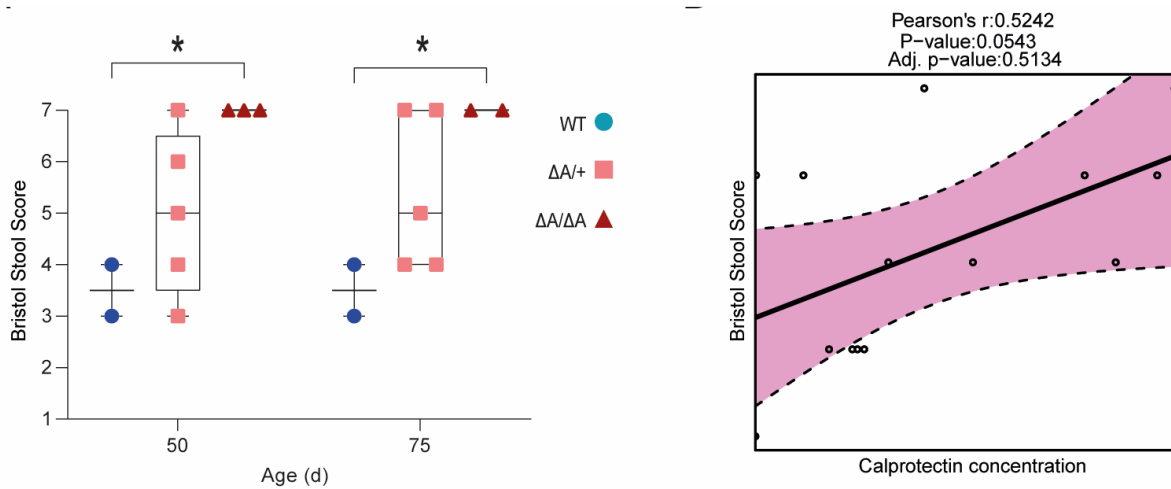


Figure 81: Bristol Stool Scores of faecal samples from wild-type  $TNF^{\Delta A/+}$ , and  $TNF^{\Delta\Delta/\Delta\Delta}$  pigs at two consecutive time points, 50 and 75 days (left) and a correlation analysis for Bristol stool scores and respective faecal calprotectin protein concentrations (right). Adapted from Winogrodzki et al.<sup>163</sup>.

##### 4.8.4.2. Assessing inflammation-associated bacterial profile changes in $TNF^{\Delta A/+}$ pigs.

Next, Calprotectin protein concentrations were evaluated in the faeces of highly and mildly inflamed individuals for the two successive post-weaning time points, t1 (50d) and t2 (75d). Based on the calprotectin content with a threshold of 30 ng/ml, the stool samples were categorized as either highly ("High") or mildly ("Low") inflamed. Two out of seven (29%) and four out of seven (57%) pigs showed calprotectin concentrations above 30 ng/ml in the stool samples at these time points. Overall, calprotectin levels were 1.6-fold (n.s.) greater at time t2 than they were at time t1 (Figure 82).



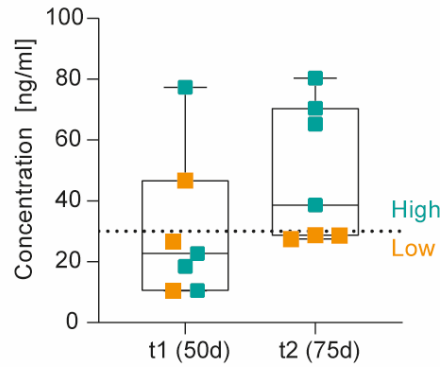


Figure 82: Calprotectin protein concentrations measured in faecal samples from  $TNF^{\Delta ARE/+}$  swine at two consecutive timepoints, t1 (50 days of age) and t2 (75 days of age). Samples were colored according to a high or low inflammatory group depending on the calprotectin protein concentration at t2 (threshold 30ng/ml). Adapted from Winogrodzki et al.<sup>163</sup>.

Although comparatively weak, stratifying samples based on a high or low inflammatory signal revealed an inflammation-associated shift of bacterial profiles (Figure 83).

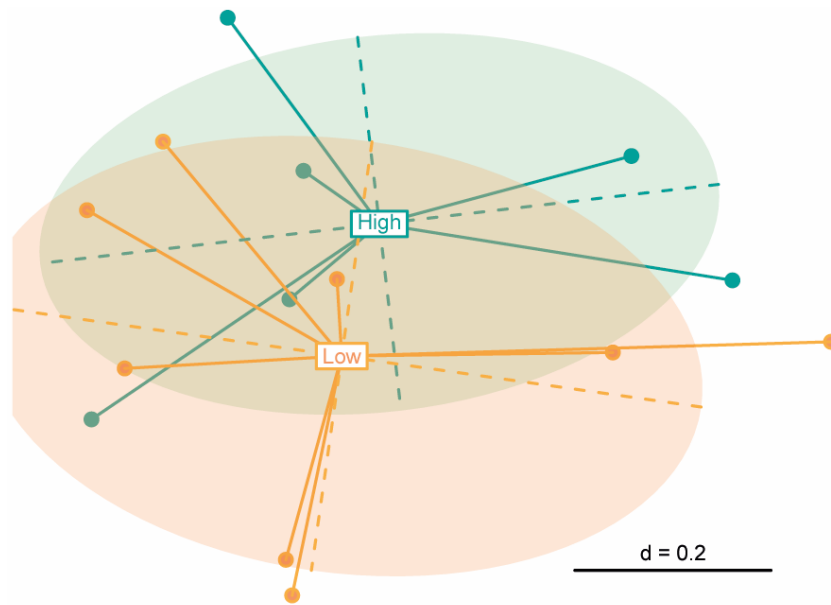


Figure 83: PCoA plot of faecal samples derived from  $TNF^{\Delta ARE/+}$  swine stratified based on their faecal calprotectin protein levels. Samples were grouped as highly (“High”) or low inflamed (“Low”) based on their Calprotectin protein levels (threshold for High: 30 ng/ml). Adapted from Winogrodzki et al.<sup>163</sup>.

#### 4.8.4.3. Temporal relationship between gut microbiota changes and inflammation in $TNF^{\Delta ARE/+}$ pigs

Finally, it was analysed whether inflammation-associated shifts were already observable before the inflammation was measured. To this end, samples were stratified based on the timepoint (T1 or T2) in addition to their inflammation status at T2 (mildly inflamed “MI” or highly inflamed “HI”). It was found that samples T1\_HI clustered more closely with T2\_HI than did T1\_MI with T2\_MI, indicating that a

change in the gut microbiota precedes stool-derived inflammatory markers (Figure 84). However, as mentioned before, stool samples are providing information about surface-level alterations to only a limited extent and should not be over-interpreted.

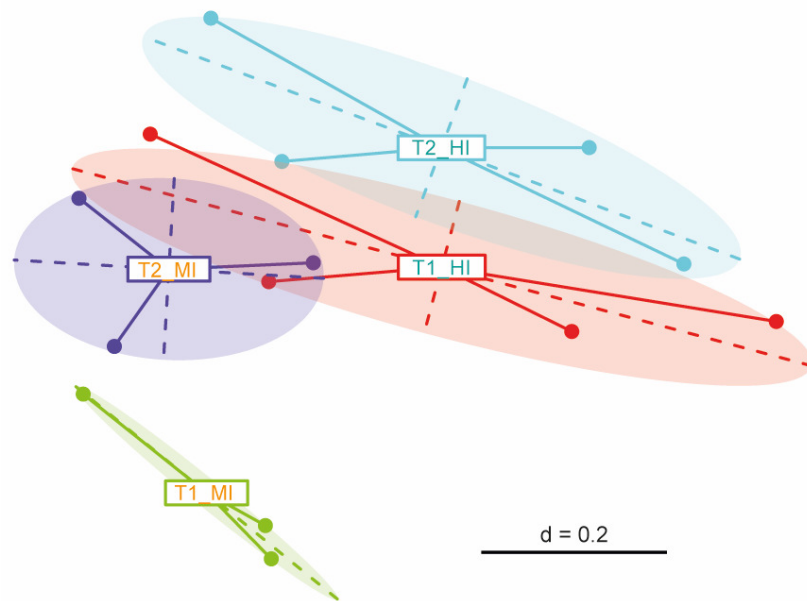


Figure 84: PCoA plot of faecal samples derived from  $TNF^{\Delta ARE/+}$  swine stratified based on their faecal calprotectin protein levels and the respective timepoint of sampling, T1 (50 days of age) and T2 (75 days of age). Samples were grouped as highly (“HI”) or mildly inflamed (“MI”) based on their Calprotectin protein levels at timepoint t2 (threshold for HI: 30 ng/ml). Adapted from Winogrodzki et al.<sup>163</sup>.

#### 4.8.5. Identification of bacterial taxa associated with severely inflamed $TNF^{\Delta ARE/+}$ swine

To potentially identify discriminative taxa or groups of taxa that might trigger an inflammatory pathophenotype, the phenotypically diverse group of  $TNF^{\Delta ARE/+}$  pigs was further investigated by stratifying faecal samples based on disease severity.

No considerable separation of bacterial profile clustering or statistically significant differences in  $\alpha$ -diversity were observed for stool samples when stratified based on the health status. However, Wilcoxon test with Bonferroni multiple correction on different taxonomic levels between sample groups revealed members of the genus *Campylobacter* to be significantly enriched in diseased compared to healthy or intermediate phenotypes. Subsequent analysis of tissue-associated microbiota composition from highly, intermediate and not inflamed  $TNF^{\Delta ARE/+}$  animals showed similar results, supporting a previously reported inflammation-associated role of this gastroenteritis-inducing microorganism<sup>181</sup> (Figure 85). Of note, no phenotype- or genotype-associated differences for segmented filamentous bacteria in faecal samples were found.

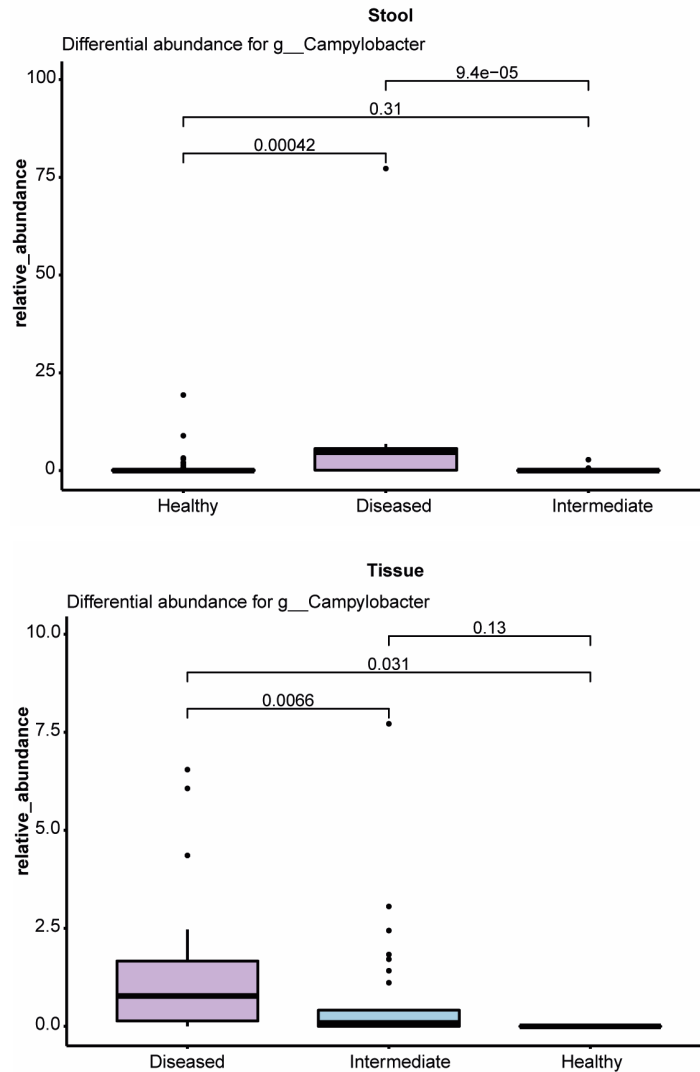


Figure 85: Significantly differentially abundant genera found between healthy, diseased and intermediately inflamed faecal (top) and tissue samples (bottom) identified by Wilcoxon testing with Bonferroni correction for multiple testing.

As for most pigs a phenotypic manifestation was observed after weaning, pre-, during and post-weaning time points were compared with regards to *Campylobacter* abundance and  $\beta$ -diversity. Members of the genus *Campylobacter* were found to be significantly more abundant in stool from post weaning time points, and a clear weaning state-dependent shift of *TNF<sup>ΔARE/+</sup>* pig-derived microbiota profiles was observed (Figure 86). A similar increase in *Campylobacter* in wild-type pigs was not expected as time—series-analysis of phylum abundances showed a steady decline of *Proteobacteria* in contrast to the *TNF<sup>ΔARE</sup>* pigs.

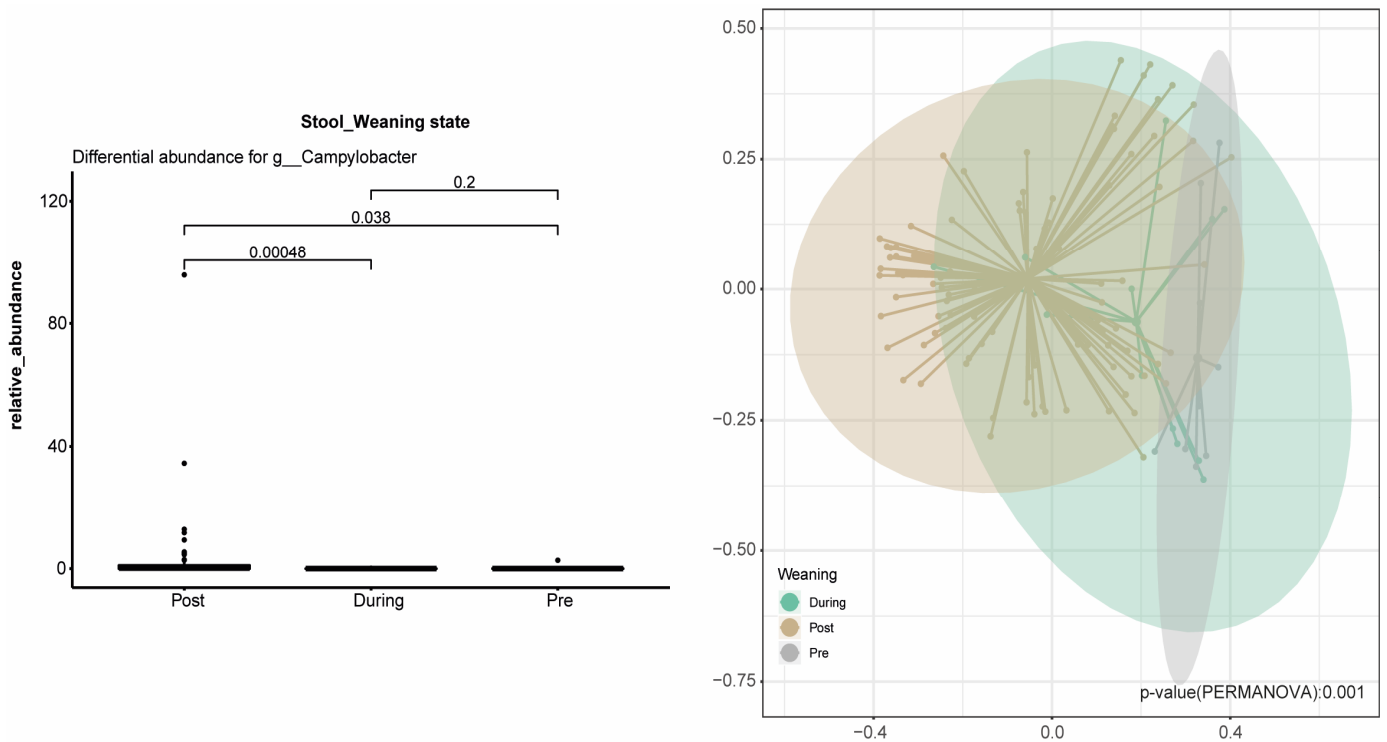


Figure 86: Wilcoxon test with Bonferroni correction of multiple testing for differentially abundant genera in stool obtained from  $TNF^{\Delta ARE/+}$  pigs in a pre-weaning, during-weaning and post-weaning state (left) and PCoA plot showing samples stratified based on the weaning state (right).

In mouse models of intestinal inflammation, mono-associations of ex-GF animals with candidate pathobionts have revealed that in some settings pathology was induced, while in others it was prevented<sup>171,182,183</sup>. Thus, it was hypothesized that not all members of the gut microbiota are similarly sufficient to trigger pathology, but rather interaction with other commensals is required<sup>171</sup>. Consequently, microbiota network analysis was utilized using stool samples to identify co-occurrence networks of *Campylobacter* in  $TNF^{\Delta ARE/+}$  pigs. *Campylobacter* was not identified as a major node in the analysis of the coincidence network, which suggests that a community effect is unlikely.

The attempt to identify the intestinal section with the highest *Campylobacter* abundance was unsuccessful, due to the limited number of samples in each section. Nonetheless, a statistical analysis of the differences in zOTUs between healthy or mildly inflamed and highly inflamed  $TNF^{\Delta ARE/+}$  pigs was conducted, using luminal and tissue samples from various intestinal locations. To determine the gut sections with the most significant variations, the  $-\log(\text{corrected p-value})$  of the respective zOTUs was plotted against the corresponding tissue segments (Figure 87). This analysis revealed that the colon and ileum had the highest number of significant differences, suggesting that the ileocolonic region is the area most impacted by inflammation in  $TNF^{\Delta ARE/+}$  pigs.

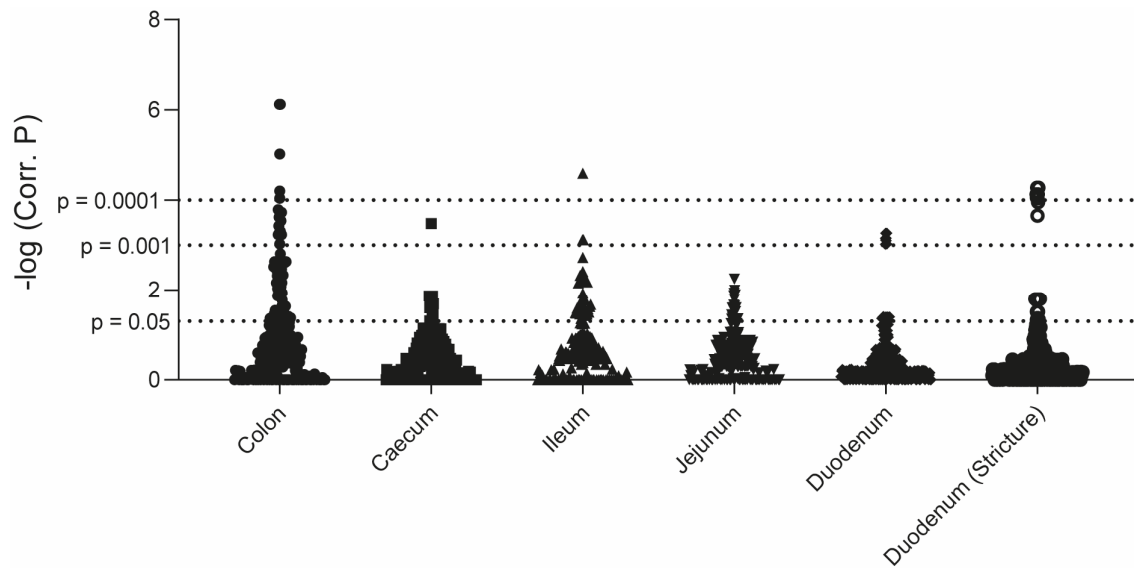


Figure 87: Plot comparing the abundance of different zOTUs in healthy and highly inflamed  $TNF^{\Delta ARE/+}$  pigs across various segments of the intestinal tissue, with the negative logarithm of the corrected p-value plotted against the respective tissue segment. Two segments of the duodenum are included: the duodenum and the duodenum (stricture), which differ in macroscopically observable tissue affection, with the latter resulting from fibrotic, structuring tissue. Dotted lines are used to highlight the significance levels.

Comparison of biopsy samples taken from macroscopically healthy and adjacent fibrotic duodenal tissue (Figure S24) revealed a significantly higher number of zOTUs in the macroscopically abnormal tissue. This indicates the presence of large local microbial differences between the two tissues.

#### 4.8.6. Cross-species comparison of bacterial profiles

IBD research using mouse models has helped identify a model-specific microbial signature for ileitis through comparison of conventionally housed, germ-free, and antibiotics-treated  $TNF^{\Delta ARE/+}$  mice<sup>42</sup>. The phylum-level signature differed from shifts in gut microbiota composition observed in CD patients<sup>42</sup>, however no direct comparison of human and mouse samples was performed. To identify the existence of a species-independent microbial signature of ileitis, publicly available data sets from WT and  $TNF^{\Delta ARE/+}$  mice, as well as from CD patients, were compared with  $TNF^{\Delta ARE}$  pig samples. Dr. Amira Metwaly kindly provided these datasets and performed phylogenetic tree visualization and the PcoA plot of cross-species clustering between porcine and murine samples.

Comparing the luminal microbiota composition in both  $TNF^{\Delta ARE}$  pigs and mice revealed a clear separation between microbiota profiles emphasizing host-specific colonization of bacterial communities in both models and suggesting host-specific functional relevance of microbial dysbiosis in IBD (Figure 88).

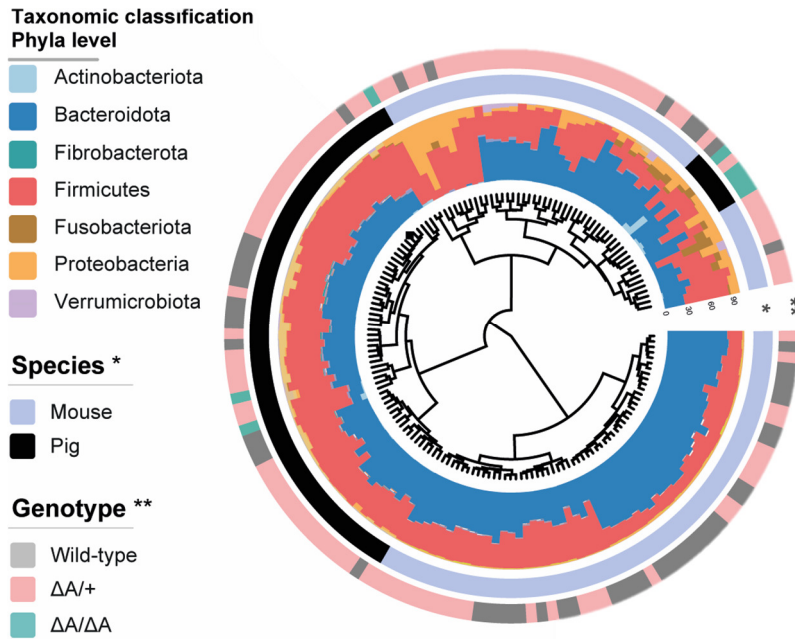


Figure 88: Phylogenetic tree visualizing the similarity of microbiota patterns in luminal ( $n=61$ ) and mucosa-associated ( $n=166$ ) microbiota from 23 pigs (7 wild-type, and 16  $TNF^{\Delta ARE}$ ), based on generalized UniFrac distances. Around the phylogram, stacked bar plots are used to display the taxonomic composition of each each phylum. The innermost ring displays stratification according to sample type, with upper gastrointestinal tract (GIT) samples (blue) and lower GIT and stool samples (brown) and denoted by (\*); the second ring displays stratification according to genotype, with wild-type (grey),  $TNF^{\Delta ARE/+}$  (pink), and  $TNF^{\Delta ARE/\Delta ARE}$  (green) and denoted by (\*\*). Samples from each pig are shown by (\*\*\*) as bars in the outside ring of the figure. Plot generated by Dr. Amira Metwaly. Adapted from Winogrodzki et al.<sup>163</sup>.

Pigs showed significantly higher bacterial community richness and diversity compared to mice, with  $TNF^{\Delta ARE/\Delta ARE}$  pigs showing the least number of species (Figure 89). Linear discriminant analysis Effect Size (LEfSe) identified a set of bacterial genera that are significantly differential between  $TNF^{\Delta ARE/+}$  pigs and mice, characterised by an increased abundance of *Alistipes*, *Bacteroides*, *E. coli*, and *Fusobacterium* in mice. In contrast, an increased abundance of *Prevotella*, *Lactobacillus*, *Treponema*, *Megasphaera* was observed in  $TNF^{\Delta ARE/+}$  pigs (Figure S25).

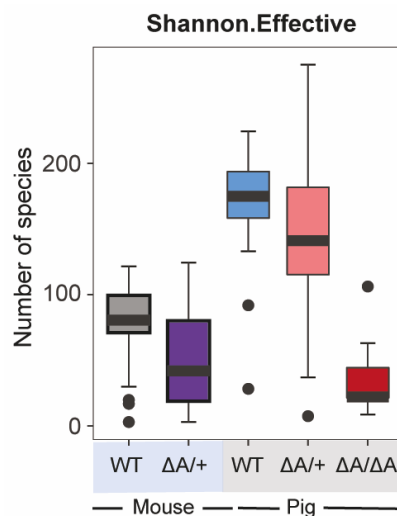


Figure 89: Shannon effective numbers of faecal samples derived from wild-type and  $TNF^{\Delta ARE/+}$  mice, and wild-type,  $TNF^{\Delta ARE/+}$  and  $TNF^{\Delta ARE/\Delta ARE}$  pigs. Modified based on Dr. Amira Metwaly's plot. Adapted from Winogrodzki et al.<sup>163</sup>.

Analysis of faecal samples identified a total 1250 zOTUs in pigs and 1042 in mice indicating a more complex pig intestinal bacterial ecosystem. 544 (31 %) zOTUs were shared among the species, indicating a shared gut microbial composition (Figure 90).

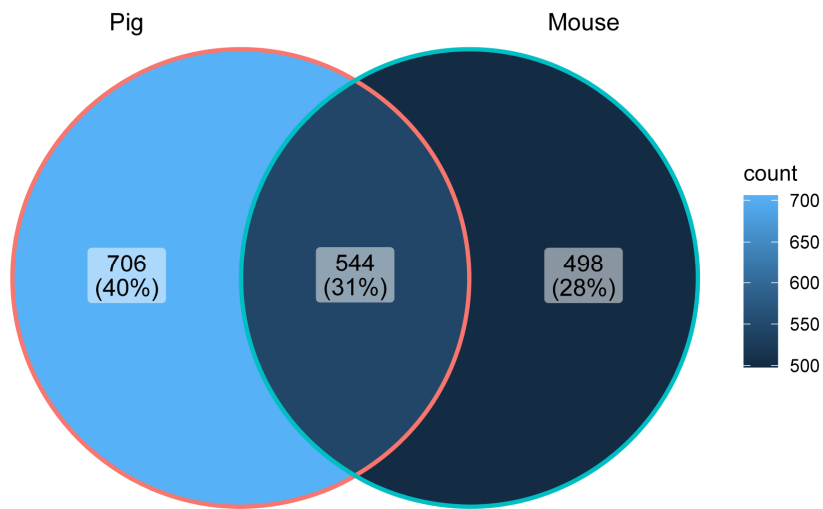


Figure 90: Venn Diagram showing the absolute amount of shared and exclusive zOTUs between porcine and murine faecal samples. A brighter color indicates a larger zOTU count.

In line with these results, the faecal microbiota from a subset of  $TNF^{\Delta ARE/\Delta ARE}$  pigs showed to cluster with  $TNF^{\Delta ARE/+}$  mice, suggesting a potential microbiota clustering based on the severity of inflammation. To identify a cross-species inflammatory microbial signature, stool samples from the pig and mouse, which form a cluster in the taxonomic tree, were compared with non-clustering samples (Figure 91).

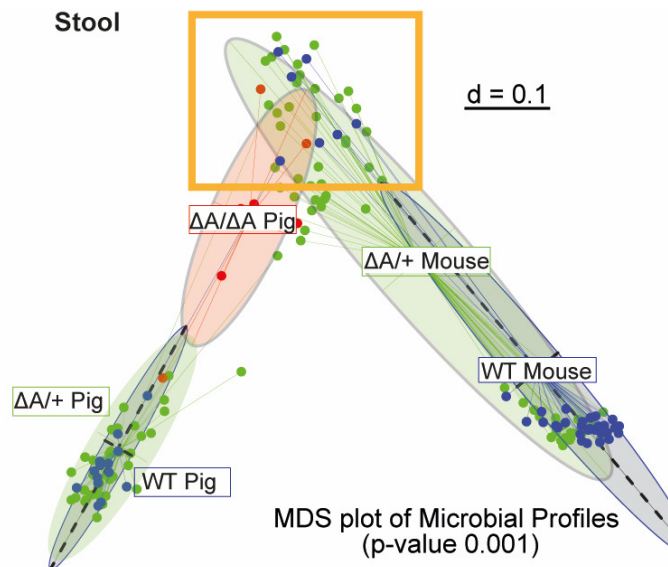


Figure 91: MDS plot of porcine and murine faecal samples derived from wild-type,  $TNF^{\Delta ARE/+}$  and  $TNF^{\Delta ARE/\Delta ARE}$  individuals. Closely clustering sample subsets are highlighted by an orange rectangle. Modified based on Dr. Amira Metwaly's plot. Adapted from Winogradzki et al.<sup>163</sup>.

Comparison between clustered and non-clustered pig samples showed significantly lower  $\alpha$ -diversity ( $p_{adj} > 0.001$ ), and separate clustering of bacterial profiles were observed (Figure 92).



Figure 92: Shannon effective number of porcine and murine faecal samples derived from wild-type,  $TNF^{\Delta ARE/+}$  and  $TNF^{\Delta ARE/\Delta ARE}$  individuals that either cluster (“Yes”) or do not cluster (“No”) together on a MDS plot.

In clustering samples, the abundance of members from *Proteobacteria* (*Escherichia/Shigella*), *Fusobacteria* (*Fusobacteria*), *Firmicutes* (*Veillonella*, *Ruminococcus gnavus*, *Ruminococcus torques*) was higher (Figure S26). In contrast, the non-clustering samples were characterized by an increased relative genus abundance of *Bacteroidetes* (*Prevotella\_9*, *Rikenellaceae\_RC9\_gut\_group*), and *Firmicutes* (*Lactobacillus*) in pigs, and *Bacteroidetes* (*Muribaculaceae*, *Prevotellaceae\_UCG\_001*), and *Firmicutes* (*Lachnospiraceae\_NK4A136\_group*) in mice, respectively. Furthermore, LEfSe analysis revealed a significant association of members from *Firmicutes* (*Clostridium sensu stricto*, *Flavonifractor*, *Enterococcus*, *Lachnoclostridium*, *Ruminococcus gnavus*) and *Proteobacteria* (*Escherichia/Shigella*) with clustering porcine samples, in contrast to a significant association of *Bacteroidetes* (*Prevotella*, *Alloprevotella*, *Rikenellaceae RC9 gut group*) and *Firmicutes* (*Lachnospiraceae NK4A13*) with non-clustering porcine samples. Similar results were obtained for clustering vs. non-clustering mice, with significantly increased abundances of members from *Firmicutes* (*Veillonella*, *Ruminococcus torques*, *Ruminococcus gnavus*, *Flavonifractor*, *Phascolarctobacterium*) compared to *Bacteroidetes* (*Prevotellaceae UCG-001*, *Rikenellaceae RC9 gut group*) and *Firmicutes* (*Lachnospiraceae NK413*) in the latter.

Comparison of clustering mouse with clustering pig samples revealed comparable bacterial diversity and clustering of microbial profiles. Significantly increased abundance of members from *Proteobacteria* (*Campylobacter*), *Firmicutes* (*Enterococcus*, *Lactobacillus*, *Limosilactobacillus*, *Parvimonas*, *Peptococcus*), and *Actinobacteria* (*Actinomyces*, *Olsenella*) were found in porcine feces. In contrast, several members of the phyla *Verrucomicrobia* (*Akkermansia*), *Firmicutes* (*Acidaminococcus*, *Blautia*, *Dialister*, *Roseburia*), *Bacteroidetes* (*Barnesiella*, *Odoribacter*), and *Actinobacteria* (*Actinomyces*) appeared to be increased in murine fecal samples (Figure S26).



More zOTUs were shared among clustering with non-clustering murine samples compared to porcine samples (114 vs. 46). Interestingly, more zOTUs were shared between non-clustering pig samples with clustering samples from mice and pigs, compared to non-clustering mouse samples with clustering samples from mice and pigs (65 vs. 10), highlighting the high complexity of porcine microbial communities (Figure 93).

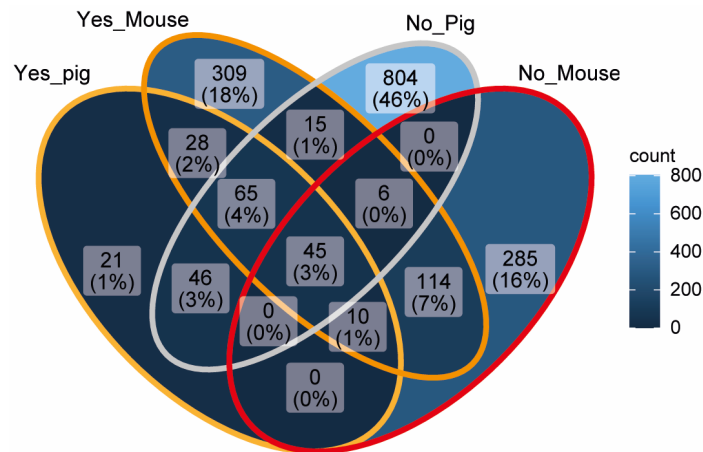


Figure 93: Venn diagram showing exclusively shared zOTUs between murine and porcine faecal samples that either cluster (“Yes”) or do not cluster close together (“No”) on a MDS plot. A brighter color indicates a higher zOTU count.

Next, luminal and mucosal or stool samples derived from  $TNF^{\Delta ARE}$  pigs were compared to samples derived from a human CD patient cohort. The cohort consisted of individuals who had undergone autologous hematopoietic stem cell transplantation (HSCT), a therapeutic intervention that results in long-lasting and significant disease remission in previously unresponsive and severely diseased CD patients, with a subset of patients relapsing over time, most likely due to a correction in exaggerated immune responses towards intestinal bacteria<sup>184,185</sup>. When comparing stool samples, considerably higher bacterial diversity was found in porcine samples (Figure 94), with 497 or 1131 unique zOTUs found in swine or human samples, respectively (Figure 95).

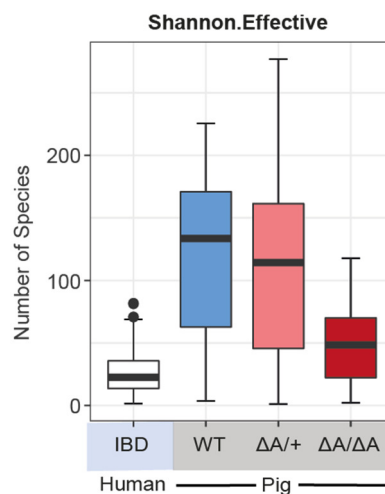


Figure 94: Shannon effective numbers of faecal, luminal and tissue samples derived from human IBD patients, and wild-type,  $TNF^{\Delta ARE/+}$  and  $TNF^{\Delta ARE/\Delta ARE}$  pigs. Modified based on Dr. Amira Metwaly’s plot. Adapted from Winogradzki et al.<sup>163</sup>.

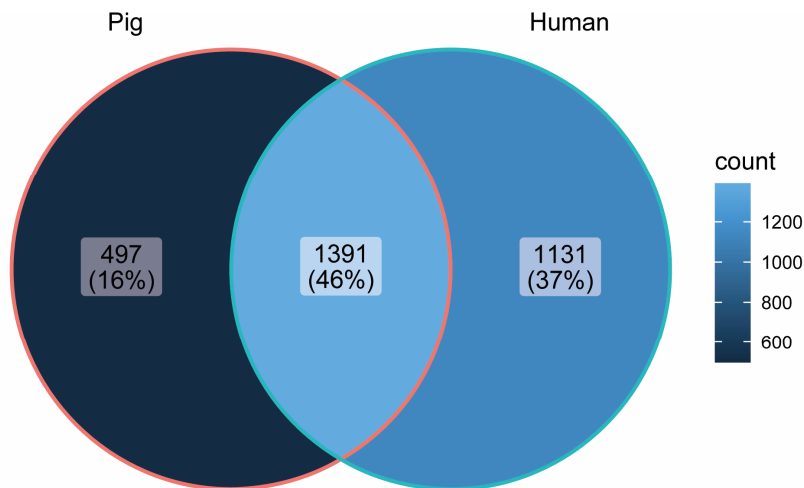


Figure 95: Venn diagram showing exclusive and shared zOTUs between faecal, luminal, and tissue samples derived from porcine wild-type and mutant pigs and human IBD patients.

Bacterial profiles clearly clustered separately based on the species, with a subset of human patient samples clustering with highly inflamed  $TNF^{\Delta ARE/+}$  and  $TNF^{\Delta ARE/\Delta ARE}$  pig samples (Figure 96).

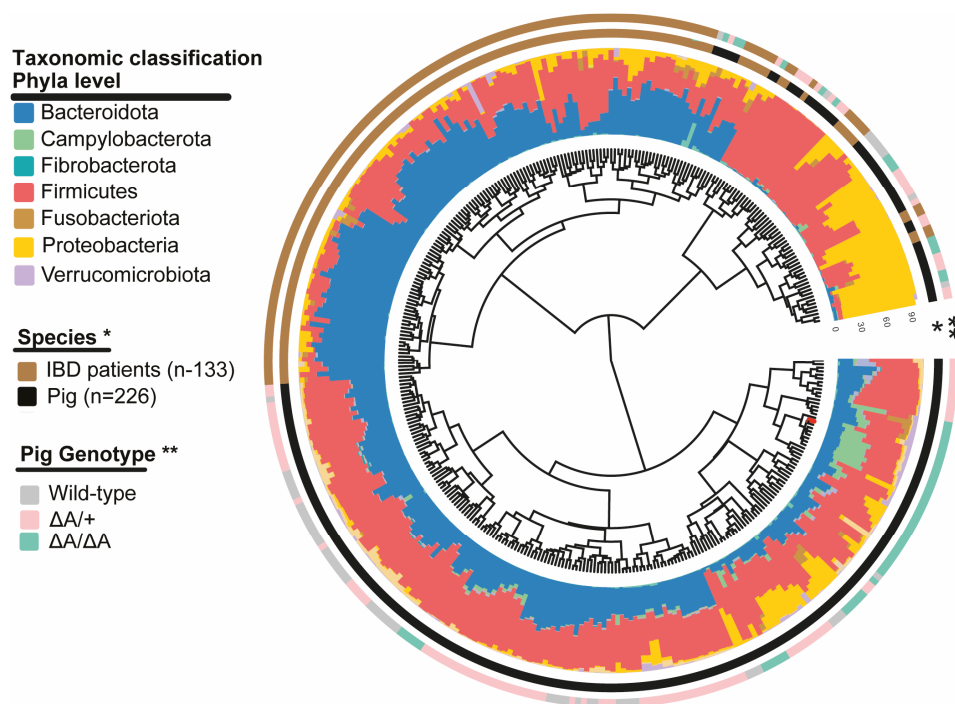


Figure 96: Phylogenetic tree that compares the microbiota profiles of faecal, luminal and tissue samples derived from wild-type and  $TNF^{\Delta ARE}$  pigs and human IBD patients to each other using generalized UniFrac distances. As stacked bar plots around the phylogram, the individual taxonomic makeup at the phylum level is displayed. The outside ring displays stratification based on genotype, wild-type (grey),  $TNF^{\Delta ARE/+}$  (red), and  $TNF^{\Delta ARE/\Delta ARE}$  (green). The innermost ring displays stratification depending on species, either human (pink) or pig (black). This plot was generated by Dr. Amira Metwaly. Adapted from Winogrodzki et al.<sup>163</sup>.

In the original study, human samples were clinically assessed with measurement of the Crohn's disease activity index and biomarkers including C-reactive protein and faecal calprotectin. Before and after the

therapeutic intervention, including periods of active disease, faecal samples were collected longitudinally and 16s rRNA gene amplicon sequencing was performed<sup>184</sup>. A reduced bacterial diversity in CD patients with active disease and a significant separation of microbial profiles between patients with active and inactive disease was found<sup>184</sup>. This finding suggests that samples collected from patients with severe disease activity overlap with  $TNF^{\Delta ARE/\Delta ARE}$  pig samples, like what was seen in the comparison with  $TNF^{\Delta ARE/+}$  mice. To investigate this, amplicon sequencing data was additionally stratified based on the disease activity index (Baseline Active, Remission, or Active (post-HSCT)) (Figure 97).

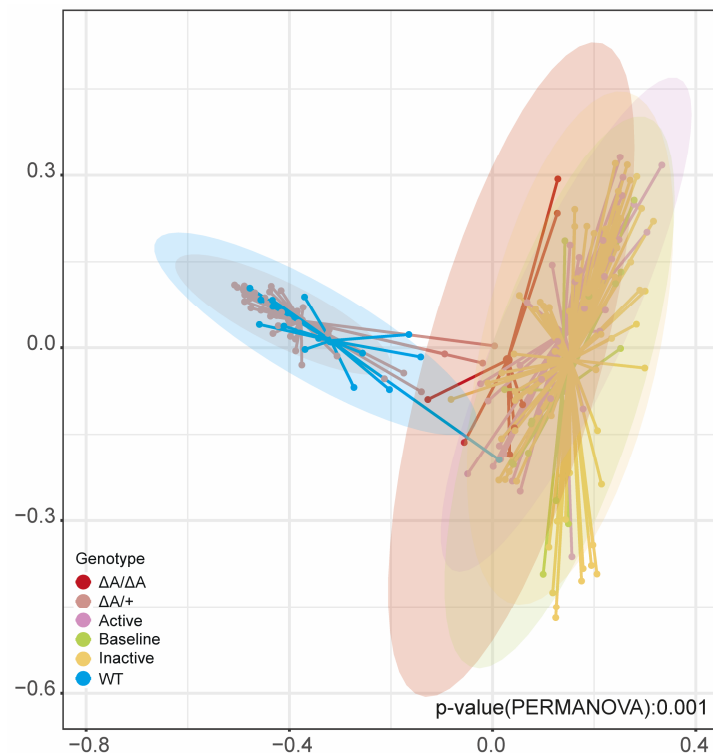


Figure 97: PCoA plot of faecal samples derived from human CD patients with inactive or active disease or at the time of HPST-treatment and wild-type,  $TNF^{\Delta ARE/+}$  and  $TNF^{\Delta ARE/\Delta ARE}$  pigs stratified by genotype (or disease activity state, respectively).

Supporting the assumption of a species-independent microbial signature of chronic intestinal inflammation, the subset of CD patients with active disease (post-HSCT) indeed clustered closer to highly inflamed  $TNF^{\Delta ARE/\Delta ARE}$  pigs. However, it should be noted that clustering of a subset of samples was less pronounced compared to mouse and porcine faecal subsample clustering.

Members of the genera *Escherichia-Shigella*, *Flavonifractor*, *g\_Bacteroides* and *g\_27(f\_Oscillospiraceae)* were found to be enriched in stool of both patients with active disease and of  $TNF^{\Delta ARE/\Delta ARE}$  porcine stool (Figure S27).

Noteworthy, zOTU-overlap analysis revealed that  $TNF^{\Delta ARE/\Delta ARE}$  pigs and IBD patients with active disease do not exclusively share zOTUs, while wild-type pigs exclusively share 3 zOTUs and  $TNF^{\Delta ARE/+}$  pigs 23 zOTUs with this human cohort. In addition,  $TNF^{\Delta ARE/\Delta ARE}$  pig samples only exclusively share 10 zOTUs with all human IBD samples, in contrast to wild-type with 39 and  $TNF^{\Delta ARE/+}$  pigs with 156

exclusively shared zOTUs. These ten exclusively shared zOTUs represent members of the genera *Lachnoclostridium*, *Parabacteroides*, *Eggerthella*, *NK4A214* group and *Epulopiscium* (Figure S28). These finding highlights that not the presence of certain zOTUs, but their abundance defines inflammatory microbial signatures.

Samples found within the cross-species conjunction were characterised by a significantly reduced bacterial diversity (Figure 98).

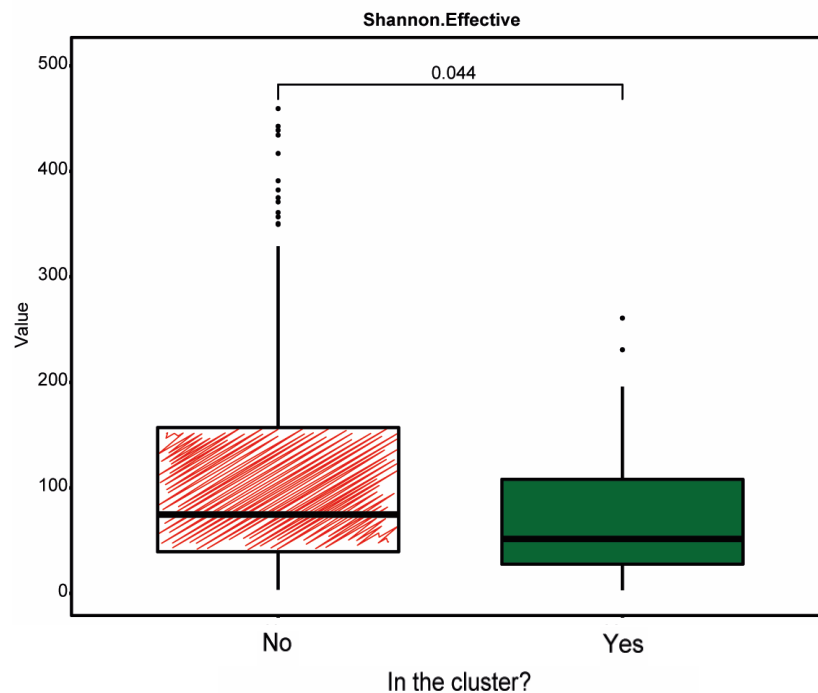


Figure 98: Shannon effective numbers of faecal samples derived from human IBD patients with inactive or active disease or at the time of HPST-treatment and wild-type,  $TNF^{\Delta ARE/+}$  and  $TNF^{\Delta ARE/\Delta ARE}$  pigs that either cluster ("Yes") or do not cluster close together ("No") on a PCoA plot.

LEfSe analysis revealed 71 significantly differing genera between clustering and non-clustering samples. The results showed strong associations with higher levels of *Firmicutes* (*Ruminococcus gnavus* group, *Veillonella*, *Blautia*), *Proteobacteria* (*Escherichia/Shigella*), and *Fusobacteria* (*Fusobacterium*) in clustering samples. In contrast, lower levels of *Bacteroidetes* (*Bacteroides*, *Odoribacter*), *Firmicutes* (*Anaerovibrio*, *Fusicatenibacter*, *Phascolarctobacterium*, *Roseburia*, *Ruminococcus*, *Subdoligranum*), and *Proteobacteria* (*Desulfovibrio*) were observed in clustering samples (Figure S28).

Following the analysis of clustering pig vs. mouse samples and the analysis of clustering pig vs. human samples, the intersection of both clustering analyses showed an increase in *Veillonella*, *Fusobacterium*, and *Bifidobacterium*. This observation implies that these genera exhibit a consistent upregulation in samples derived from individuals with inflammation, when drawing comparisons between pigs and their counterparts in both mice and humans. Noteworthy, *Campylobacter* was found to be more abundant in pig samples that did not cluster together with human patient samples, indicating that either this cluster-based approach to identifying species-independent microbial signatures of inflammation must be taken

with caution, especially when species or strain level comparisons are missing or that the finding of disease-triggering taxa in *TNF<sup>ΔARE/+</sup>* pigs is not applicable for other genotypes or species. However, in line with previous results, *Campylobacter Concisus* and *C. Jejuni* were associated with disease progression in IBD patients<sup>186,187</sup>.

Finally, faecal microbiota derived from all three species was compared within the same analysis. Pig microbial communities in general were more diverse compared to human and mouse samples (Figure 99).

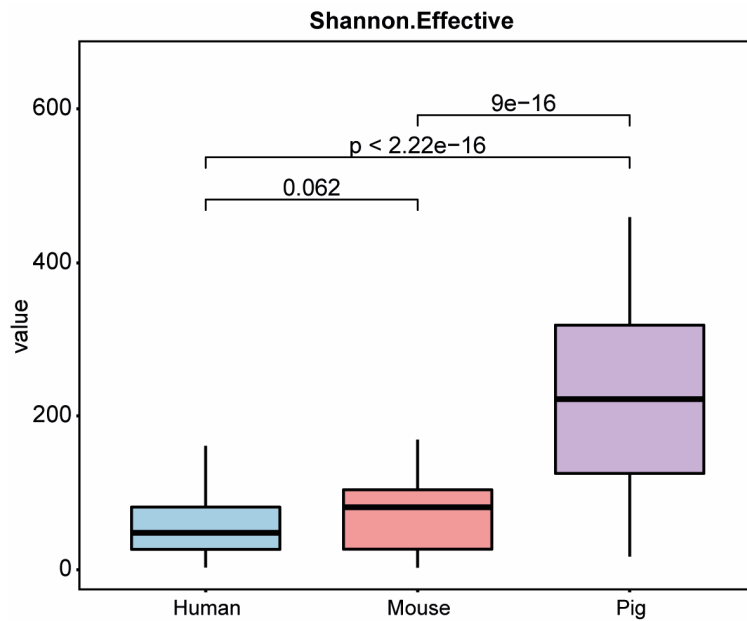


Figure 99: Shannon effective numbers of faecal samples derived from human IBD patients, wild-type and *TNF<sup>ΔARE/+</sup>* mice, and wild-type, *TNF<sup>ΔARE/+</sup>* and *TNF<sup>ΔARE/ΔARE</sup>* pigs.

Microbial profiles stratified by species showed species-specific clustering, with a subset of samples clustering together (Figure 100). Interestingly, the microbial samples from pigs and mice exhibited a greater separation within their respective clusters when compared to the human data. This is likely due to a larger influence of genotypes on the phenotype and microbial composition, as opposed to differing states of activity in manifested inflammatory bowel disease.

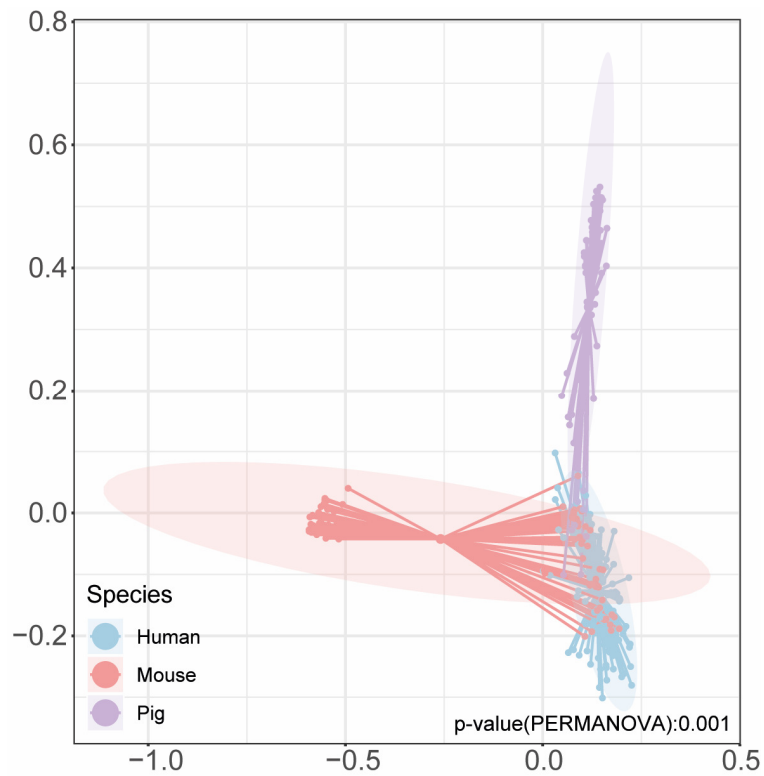


Figure 100: PCoA plot of faecal samples derived from human IBD patients, wild-type and  $TNF^{\Delta ARE/+}$  mice, and wild-type,  $TNF^{\Delta ARE/+}$  and  $TNF^{\Delta ARE/\Delta ARE}$  pigs stratified by their respective species.

Human and porcine samples shared 1036 zOTUs, compared to 55 zOTUs and 373 zOTUs shared between pig and mouse or human and mouse samples, respectively, indicating a larger overlap between human and porcine gut microbiomes (Figure 101).

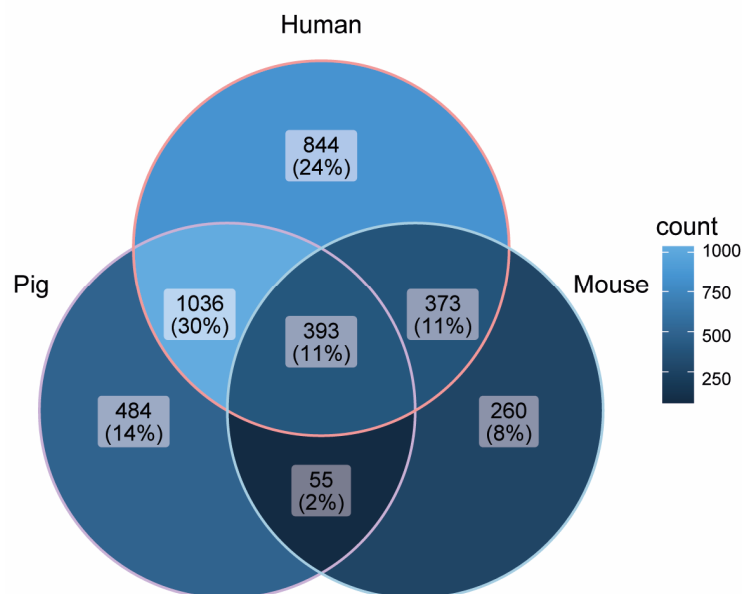


Figure 101: Venn diagram showing exclusive and shared zOTUs of faecal samples derived from human IBD patients, wild-type and  $TNF^{\Delta ARE/+}$  mice, and wild-type,  $TNF^{\Delta ARE/+}$  and  $TNF^{\Delta ARE/\Delta ARE}$  pigs. A brighter color indicates a higher zOTU count.

In line with previous analyses, a subset of samples shared a comparable microbial profile, which was characterised by a lower bacterial diversity compared to non-clustering samples (Figures 102 and 103).

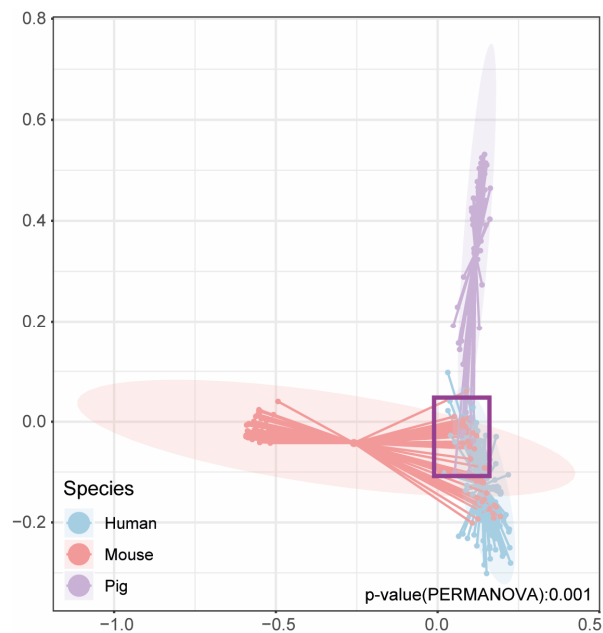


Figure 102: PCoA plot of faecal samples derived from human IBD patients, wild-type and  $TNF^{\Delta ARE/+}$  mice, and wild-type,  $TNF^{\Delta ARE/+}$  and  $TNF^{\Delta ARE/\Delta ARE}$  pigs stratified by their respective species. Closely clustering sample subsets are highlighted by a purple rectangle.

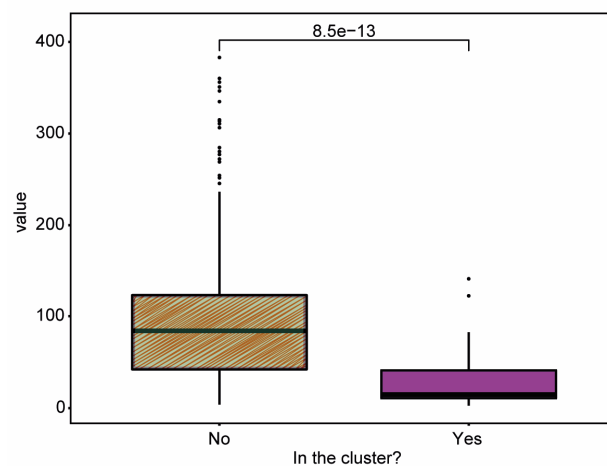


Figure 103: Shannon effective numbers of faecal samples derived from human IBD patients, wild-type and  $TNF^{\Delta ARE/+}$  mice, and wild-type,  $TNF^{\Delta ARE/+}$  and  $TNF^{\Delta ARE/\Delta ARE}$  pigs that either cluster ("Yes") or do not cluster ("No") close together on a PCoA plot.

LEfSe analysis identified a significant association of members of the genera *Parabacteroides*, *Coprobacter* and *Granulicatella*, with clustering samples with *Parabacteroides* and *Granulicatella* being found to be associated with clustering samples of the cross-species comparison of human and pig samples (Figure S30). The reduced number of very common genera appears to correlate with an

increase in the number of compared species. This suggests that cross-species comparisons for identifying inflammation-associated microbial signatures that are independent of species are limited to only a few species, and there is a risk of discovering microbial signatures that are independent of the disease state. Furthermore, the lack of relevant publications on the IBD-relevant role of these microorganisms supports this observation<sup>188,189</sup>.



## 5. Discussion

### 5.1. *TNF<sup>ΔARE</sup>* pigs develop a CD-like ileocolitis pathophenotype that is associated with impaired barrier integrity and hyperresponsive immunity

In this study, a porcine model for inflammatory bowel diseases was generated and characterised with the goal of bridging the gap between murine model-based basic research and human clinical studies. A spontaneously developing Crohn's disease-like patchy ileocolitis pathophenotype with varying disease severity was induced through the deletion of two mRNA-destabilizing regulatory elements (ARE and CDE1) within the 3' UTR of the *TNF* gene in the porcine genome.

Homozygous and about half of heterozygous mutant pigs manifested clinical indications of intestinal inflammation, including chronic and sometimes bloody diarrhea, impaired weight gain, abdominal pain, and increased apathy. These clinical features collectively suggested the presence of severe inflammatory processes in the gut.

As in the corresponding mouse model it was the gastrointestinal tract, that was mainly affected in *TNF<sup>ΔARE</sup>* pigs<sup>58</sup>. The selective organ susceptibility could be further attributed to the varying composition of epithelial barriers and their sensitivity to inflammation. It was shown that a high concentration of TNF in intestinal epithelial cells in combination with increasing IFN $\gamma$  levels leads to *TNFR1*-induced collapse of intestinal epithelial TJs via *myosin light chain kinase (MLCK)* signaling<sup>190</sup>. Sporadically lung inflammation was observed in *TNF<sup>ΔARE</sup>* pigs, which can be explained by a single layered, inflammation-sensitive barrier present in the lungs, and its self-repair capacity mainly maintained through interactions with macrophages, the major secretors of TNF<sup>169,191</sup>. The occurrence of aerogenic microbial stimuli or genetically induced hypersensitivity of the immune system was equally shown to result in *TNF-TNFR*-mediated reduction in barrier integrity<sup>192</sup>.

There is substantial evidence supporting the notion of a compromised intestinal barrier in the IBD pig model. Clinically the *TNF<sup>ΔARE</sup>* pigs exhibited decelerated weight gain and chronic diarrhea indicative of an impaired nutrient and water (re-)absorption. Consistent with these findings, *TNF<sup>ΔARE</sup>* pigs showed an increased urea-creatinine ratio and hypoalbuminemia in whole blood, which provide further evidence of gastrointestinal bleeding and increased bowel disease<sup>193–195</sup>. An elevated serum Cu/Zn ratio, which has been linked to malnutrition, increased oxidative stress, inflammation, and impaired immune status in patients with chronic diseases was also found. The Cu/Zn ratio has recently been suggested as a potential marker for assessing disease activity in IBD patients<sup>41,196,197</sup>. In addition, an increased level of Calprotectin in the stool, reflecting accelerated migration of neutrophils, monocytes, and macrophages into the intestine was detected<sup>198</sup>. Microscopically, several indicators of impaired barrier function were observed, including enhanced cell proliferation markers, an influx of members of the adaptive and innate immunity, and diminished and disorganized TJ proteins. *In vitro* cultivation of M1 macrophages and flow cytometry of PBMCs derived from *TNF<sup>ΔARE</sup>* pigs demonstrated increased *TNF* transcript half-life and expression. Taken together, these results suggest a hyperreactive pro-inflammatory immune response, which may explain the altered intestinal permeability in *TNF<sup>ΔARE</sup>* pigs.

## 5.2. Intestinal inflammation is linked to human IBD-like alterations in the gut microbiome, but occurs earlier in development

Because mucosal immune cells, such as dendritic cells, macrophages, and T lymphocytes, interact directly or indirectly with gut-resident bacteria, microbial factors may also be involved in the progression of the disease. Studies in *TNF<sup>ΔARE/+</sup>* mice have demonstrated that the absence of the pathophenotype occurs under germ-free housing conditions<sup>42</sup>. Significant changes in the gut microbiota associated with intestinal inflammation were also observed in *TNF<sup>ΔARE/+</sup>* pigs. Microbial analysis of wild-type pigs revealed a spatial distribution of microbial communities along the intestinal tract, in line with findings reported in humans<sup>199</sup>. The oxygen-rich sections of the proximal small intestine harbour a higher relative abundance of O<sub>2</sub>-tolerating *Proteobacteria*. *Bacteroidetes* are one of the most abundant bacterial phyla in the large intestine being essential for the production of acetate and propionate and protection against pathogenic bacteria<sup>200–202</sup>. *Firmicutes* are the third major phylum in the healthy porcine gut and are known to be highly beneficial to the host due to their large population of butyrate-producing bacteria, which directly contribute to host health<sup>202</sup>. The microbial diversity in the healthy state was lower in the small intestine compared to the large bowel, which can be attributed to longer transit times and larger volume of the latter<sup>203</sup>. In the chronic inflammatory condition, the highly plastic microbiota composition and loss of microbial diversity reflects a loss of colonization resistance due to changes in the redox potential<sup>204</sup>. This is further supported by the overgrowth of facultative anaerobic *Proteobacteria* and *Campylobacterota* at the expense of *Firmicutes*; a phenomenon also observed in human IBD patients<sup>205,206</sup>. *Proteobacteria* and *Campylobacterota* consist of both obligate and facultative anaerobes and are characterised by a high functional diversity that allows them to cope with a variety of growth conditions and nutrient availability<sup>207</sup>. Notably, intestinal microbiota shifts towards elevated commensal *Escherichia coli* loads resulted in abrogated colonization resistance against *Campylobacter jejuni*, a known causative agent of human enterocolitis<sup>208</sup>, suggesting that a disease-associated microbiome plays a crucial role in modulating colonization resistance against secondary enteric pathogens.

The majority of diseased mutant pigs exhibited a patchy inflammatory phenotype in the small intestine associated with differences in the composition of the microbiota. For example, comparison of structured duodenum with adjacent healthy tissue identified distinct bacterial profiles. This additional layer of microbial complexity is well known from Crohn's disease patients. Studies on IBD and related diseases have shown that the phenotypic divergence may result from differences in immune system signalling of epithelial crypts<sup>209,210</sup>. The clonal expansion of susceptible crypts during inflammatory flare-ups may reciprocally promote a pro-inflammatory microbial environment and thus induce an even more pronounced inflammatory phenotype<sup>209</sup>. Comprehensive longitudinal studies including genomic, immunological, and microbial analyses are necessary to better understand the occurrence of skip lesions. Noteworthy, there are no reports on small intestinal skip lesions in the IBD mouse models. Thus, the *TNF<sup>ΔARE</sup>* pigs are well-suited to investigate this particular disease manifestation.

The onset of disease in *TNF<sup>ΔARE</sup>* pigs occurred shortly after weaning. This differs from humans, where most patients with early-onset IBD are diagnosed at around 10 years of age<sup>38</sup>. It is likely due to a strong genetic predisposition in the *TNF<sup>ΔARE</sup>* pigs. The “weaning reaction” of the immune system in response

to the concomitant microbiota alterations then functions as an early disease trigger. Indeed, in humans and mice, the “weaning reaction” was shown to be a critical time window for potential long-term pathological imprinting that decides on the disease susceptibility in later life<sup>211,212</sup>. During the weaning process, various genes including *Reg3*, defensins, chemokines, cytokine receptors, and structural components of the epithelial barrier are induced by the microbiota and play a crucial role in promoting anti-microbial immunity<sup>212,213</sup>. In 3 weeks old mice, weaning-associated microbiota alterations trigger a rapid increase of pro-inflammatory cytokines, such as TNF and IFN $\gamma$ , mainly produced by T cells<sup>212</sup>. After the weaning, the expression of these cytokines gradually decreased to the levels observed in germ-free mice<sup>212</sup>. Thus, it is likely that the inability to regulate the concomitant upregulation of pro-inflammatory genes throughout the intestine in both *TNF* $\Delta$ ARE mice and pigs might exacerbate the weaning phenotype, resulting in earlier onset of the disease. This was supported, by the rapidly increasing levels of gut inflammation-associated phyla such as *Campylobacterota* and *Proteobacteria* at the expense of *Firmicutes* shortly after weaning in *TNF* $\Delta$ ARE pigs. Noteworthy, higher levels of *Firmicutes* and lower levels of *Proteobacteria* were observed in the stool of *TNF* $\Delta$ ARE/ $\Delta$ ARE pigs compared to controls before weaning. As basal *TNF* transcript levels were found to be increased in mutant macrophages, it is likely that a low-grade *TNF* expression alters the gut microbiota composition even in the absence of intestinal inflammation. The presence of more “beneficial” SCFA-producers before weaning emphasizes the already known concentration-dependent pleiotropic role of *TNF* in health and disease<sup>214–216</sup>. On the other hand, perturbation of the microbiota before weaning is known to cause disruption in immune system development and, as a result, immune response dysregulation later in life<sup>217</sup>. In addition, the observation that faecal microbial changes precede the increase in faecal calprotectin levels suggests that the onset of CD-like intestinal inflammation in this model is highly interactive, has its origins early in the development and is subject to reciprocal elevation/increase of dysregulated pro-inflammatory stimuli from both the host and its environment.

### 5.3. *TNF* $\Delta$ ARE pigs and mice differ in transcript regulation, biogeography of manifestations and pathophenotype-associated differentially abundant taxa

Recently published mouse models to study functional role of TNF in inflammation, in which various regions of the *Tnf* 3'UTR were deleted, have revealed a combinatorial effect of multiple deletions on disease severity<sup>218</sup>. *TNF* transcript half-lives in LPS-challenged pig M1 M $\phi$ s were considerably higher compared to mouse-derived *Tnf* $\Delta$ ARE M $\phi$ s, in which only the ARE sequence was deleted<sup>58</sup>. The deletion of ARE and the single CDE in the murine *Tnf* gene resulted in embryonic lethality in mice<sup>218</sup>. But not so in pigs; pointing towards species- and sequence-specific differences of the models. Most likely the presence of a second CDE element (Figure 16) in the porcine *TNF* 3'UTR is responsible for residual transcript regulation.

However, not only differential transcript kinetics, but also tissue-specific differences between pig and mouse IBD models were observed. *TNF* $\Delta$ ARE pigs show transmural inflammation in the terminal ileum,

but also in the proximal colon, which is similar to the inflammation observed in human ileocolitis patients. This similarity can be attributed to the fact that pigs and humans both have their primary site for ingesta fermentation in the colon, whereas for mice it is the cecum<sup>219</sup>. This difference in the location of fermentation has a direct impact on the constituents of the gut microbiota and microbe-host interactions<sup>219</sup>. A larger organ size and the presence of sacculations and tenia have a similar impact in pigs (and humans), providing a variety of physiological and anatomical niches for gut inhabitants that are absent in mice<sup>219</sup>. Accordingly, microbial diversity in pigs is much higher than in mice, and clear species-specific compositional differences of the gut microbiota were found in this study.

In addition, *Campylobacteria* were identified as potential disease exacerbating agents in heterozygous mutant pigs in contrast to segmented filamentous bacteria in the corresponding mouse model<sup>42</sup>. The latter were present but did not differ between genotypes or disease severities of *TNF<sup>ΔARE</sup>* pigs. In the *TNF<sup>ΔARE/+</sup>* mouse the abundance of SFBs correlates with disease severity<sup>220</sup>. Moreover, mono- or co-colonization of this immunomodulatory microorganism established a causal link and showed that the presence of SFBs is indispensable for disease development in *TNF<sup>ΔARE/+</sup>* and SAMP/Yit mice<sup>220</sup>. In contrast the analysis of longitudinal stool samples from phenotypically diverse *TNF<sup>ΔARE/+</sup>* pigs revealed that a more severe pathophenotype is associated with an increased abundance of *Campylobacteria*. Members of this genus were found to be enriched after weaning, underscoring the significance of the "weaning reaction". However, it is unlikely that they play a similar role in disease aetiology as hypothesized for SFBs, where it was suggested that a maturing effect on the adaptive immunity might provoke disease in genetically susceptible hosts<sup>221</sup>. The correlation between *Campylobacteria* and disease severity in pigs might be explained by a loss of colonization resistance and the generation of niches for secondary enteric pathogens that subsequently exacerbate disease, which has also been observed in mice and humans<sup>181,208</sup>. It remains to be investigated which strain(s) is associated with the disease onset and to what extent this genus plays a role in disease aetiology.

#### 5.4. Microbial similarities in highly inflamed individuals indicate the presence of a species-independent microbial signature of inflammation

Despite observed differences, a subset of samples derived from highly inflamed *TNF<sup>ΔARE</sup>* pigs and mice were found to have overlapping bacterial profiles, indicating a species-independent composition of the microbiota that correlates with inflammation severity. This is supported by similar findings when comparing samples derived from porcine and human or from all three species. Comparable changes in microbial populations have been reported in different animal models of IBD, which are consistent with those in human patients<sup>42,222–224</sup>. However, no cross-species comparison has yet been conducted using comparable disease models to identify a universal microbial signature of inflammation. This approach offers several advantages, including the ability to identify genera that are cultivatable across multiple species, which can aid in subsequent cultivation studies. Furthermore, this approach increases the threshold of significance for a taxon to be identified, highlighting those that are truly important in disease. However, comparing more than two species can increase the likelihood of excluding false negatives

and overlooking species-specific differences and microbial networks. This knowledge would be necessary to fully understand the complexity of a species-specific phenotype. It must also be noted that differentially abundant taxa partially differed for porcine vs. mouse and porcine vs. human stool samples, which likely results from confounding factors such as diet, environment, inbreeding of mouse lines and age. But overall, independent of the species, samples that clustered together displayed lower microbial diversity, with an overrepresentation of gut inflammation-associated taxa, which was consistent with the inflammatory phenotype of the individuals from whom the samples were collected. The consistency of the findings with what is known from patients with active IBD, suggests that the comparative cross-species approach is likely to be suitable for identifying microbial signatures across different species. Notably, several gut inflammation-associated genera, including *Escherichia\_Shigella*<sup>225</sup>, *Dialister*<sup>226</sup>, *Blautia*<sup>227–229</sup>, *Lachnoclostridium*<sup>227</sup> and *Ruminococcus*<sup>227,230</sup> were found to be positively associated with clustering samples to varying degrees. It is worth noting that *Veillonella*, *Fusobacterium*, and *Bifidobacterium* were consistently increased in clustering samples when comparing faecal samples from pigs and mice as well as pigs and humans, indicating their potential involvement in gut inflammation across these species. Although *Veillonella*<sup>231,232</sup> and *Fusobacterium*<sup>233</sup> have been shown to be associated with IBD, reports have been mixed for different members of the *Bifidobacterium* genus<sup>234,235</sup>, making it an important candidate for further functional investigation and highlighting the need for species- and strain-level analyses.

## 5.5. Ease of sampling vs. accuracy: stool-based analyses are a less invasive but only provide weak reflection of intestinal inflammatory hotspots

Stool samples are the primary source for the analysis of IBD-associated microbial alterations in patients. It provides a convenient way to collect specimens for longitudinal analysis and saves patients from more invasive endoscopic procedures. However, the results of this study showed that the use of stool samples was sub-optimal as it largely ignores the complex and distinct patternization of microbial communities that is needed to understand IBD-aetiology. Therefore, the use of stool sample may result in a loss of detailed information regarding spatial interaction events, such as mutual cross-feeding, direct microbe-microbe interactions, and horizontal gene transfer<sup>16,236</sup>.

Comparison of *TNF<sup>ΔARE</sup>* with matched wild-type pigs showed a clear genotype-associated distinct bacterial profiles in ileocolitic tissue and luminal, but not in faecal samples. Comparison of stool, ileal, and colonic samples from heterozygous and homozygous *TNF<sup>ΔARE</sup>* pigs revealed that stool samples from severely inflamed individuals only weakly reflected the bloom of *Proteobacteria* and *Campylobacterota* at sites of active inflammation. Of note, the observed underrepresentation of inflammation-associated changes in stool samples indicates that the analysis of Calprotectin levels in luminal or tissue samples may be more precise in determining the degree of intestinal inflammation. Finally, faecal samples showed a greater number of zOTUs exclusively shared with large intestinal samples than with small intestinal samples, suggesting a low suitability particularly for the analysis of intestinal diseases with ileal involvement, such as Crohn's disease.

The intestinal tissue is advantageous for the study of direct microbe-host-interactions due to their close proximity to the host epithelium, while luminal samples are more suitable for dietary intervention studies as they better reflect environmental changes in each gut section. Recent findings from Cornell University (personal communication) suggest that luminal and tissue-associated bacteria may fluctuate in certain disease-related conditions due to host-secreted pro-inflammatory cytokines that influence the expression of virulence factors of individual *E. coli* and *Prevotella* strains. In addition, when selecting the most appropriate tissue type for studying microbe-host interactions, reproducibility in humans must also be considered. In clinical settings, the human intestine samples are mainly collected endoscopically. While non-invasive options for studying the luminal bowel environment do exist in experimental stages, reproducibility and accuracy in human studies remain challenging<sup>237,238</sup>. In the preclinical phase, repeated endoscopic sampling is feasible in both large and, to some extent, small animal models of IBD. However, the larger sample volume and more frequent sampling opportunities available in large animal models make them a more favourable option. This facilitates subsequent laboratory analyses and may also become significant in the future when considering the use of faecal output for xeno-FMT approaches.

## 5.6. Rodents to Pigs to People: Optimizing Pre-Clinical Testing

Despite extensive research in both basic and clinical settings, IBD remains a persistent global health challenge with increasing incidence and prevalence<sup>38</sup>. While mouse models have proven valuable in elucidating the molecular mechanisms of CD and exploring the relationship between gut epithelium, inflammation, and the microbiome<sup>41,42</sup>, differences between humans and rodents, such as variations in nutrient requirements, GIT physiology, and immunological and metabolic responses, have limited the applicability of these findings to clinical settings<sup>239–243</sup>. To develop more relevant translational models, pigs were considered as suitable animal IBD model, because of the anatomical and physiological similarities to the human GIT. Pigs are widely recognized as models for nutrition research, intestinal microbiota, and gut barrier function<sup>111</sup>. The *TNF<sup>ΔARE</sup>* pig model exhibits characteristics of CD, including chronic diarrhea, weight loss, abnormal intestinal morphology, changes in intestinal epithelial cell composition, with transmural skip lesions and ileocolitic predominance, and associated microbiota alterations similar to those observed in human CD patients<sup>244</sup>.

The translational relevance of the IBD pigs needs to be demonstrated in further studies. However, given the encouraging examples of pig models of gastrointestinal disease, there is good reason for optimism. The *APC<sup>1311/+</sup>* pigs, a disease model for familial adenomatous polyposis<sup>245</sup>, showed a disease pathophenotype similar to human. The *APC<sup>1311/+</sup>* pigs have been successfully used for testing of human-sized endoscopy prototypes and contributed to the development of promising human-relevant procedures for the detection of early colonic dysplasia<sup>246</sup>. In collaboration with the author of this dissertation, porcine *ex vivo APC<sup>1311/+</sup>* enteroid culture was utilized to investigate the tumour-modulating role of the *APC* wild-type allele<sup>247</sup>, a genetic cofactor still understudied in colorectal cancer progression<sup>248</sup>. This successful use of the pig model for basic research highlights its potential for future studies beyond the translational context. Collaborative studies were initiated to analyse the influence of

the gut microbiome on polyp regression, and the generation of *APC*<sup>1311/+</sup> and *TP53*<sup>+/-</sup>:*TNF*<sup>ΔARE</sup> double mutant pigs to model IBD-associated colorectal cancer. This work is expected to strengthen the translational relevance of the pig and increase its acceptance within the microbiome research community.

It is important to note that despite the potential benefits of the pig model for translational research, the mouse remains a valuable model for studying fundamental disease mechanisms due to its ease of genetic modification and simple handling.

Concluding, the value of pig models for digestive disease research has already been demonstrated. Thus, the *TNF*<sup>ΔARE</sup> pigs are likely to be beneficial for translational IBD studies, both because the phenotype of the animals mirrors the main features of the human disease and because they are suitable for longitudinal studies investigating innovative nutritional and technological interventions.

## Supplementary

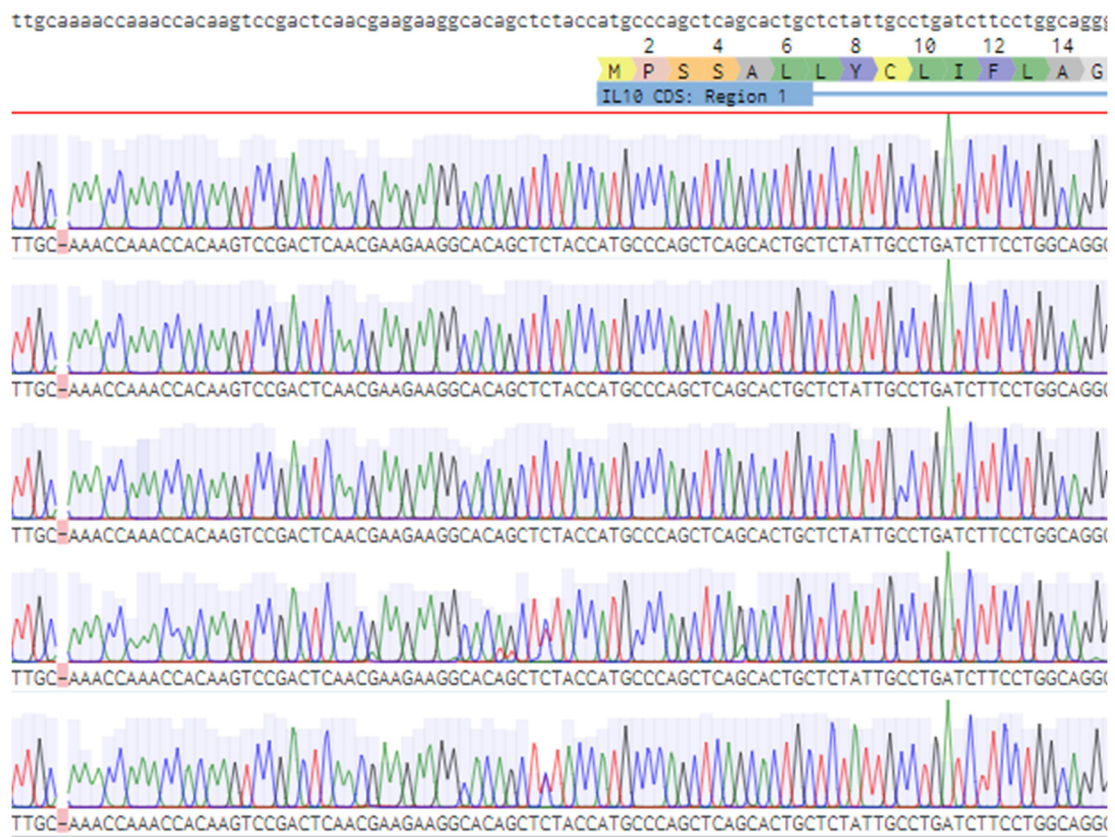


Figure S1: Sanger-sequencing results for the exon 1 of the porcine IL10 gene derived from five randomly selected wild-type pigs (lower rows) compared to the NCBI gene deposit (top). The reference gene additionally shows its amino acid code. The Sanger sequencing quality is shown for each base. A deletion is indicated at position 47 bp upstream of the start codon (ATG) by a highlighted "-".



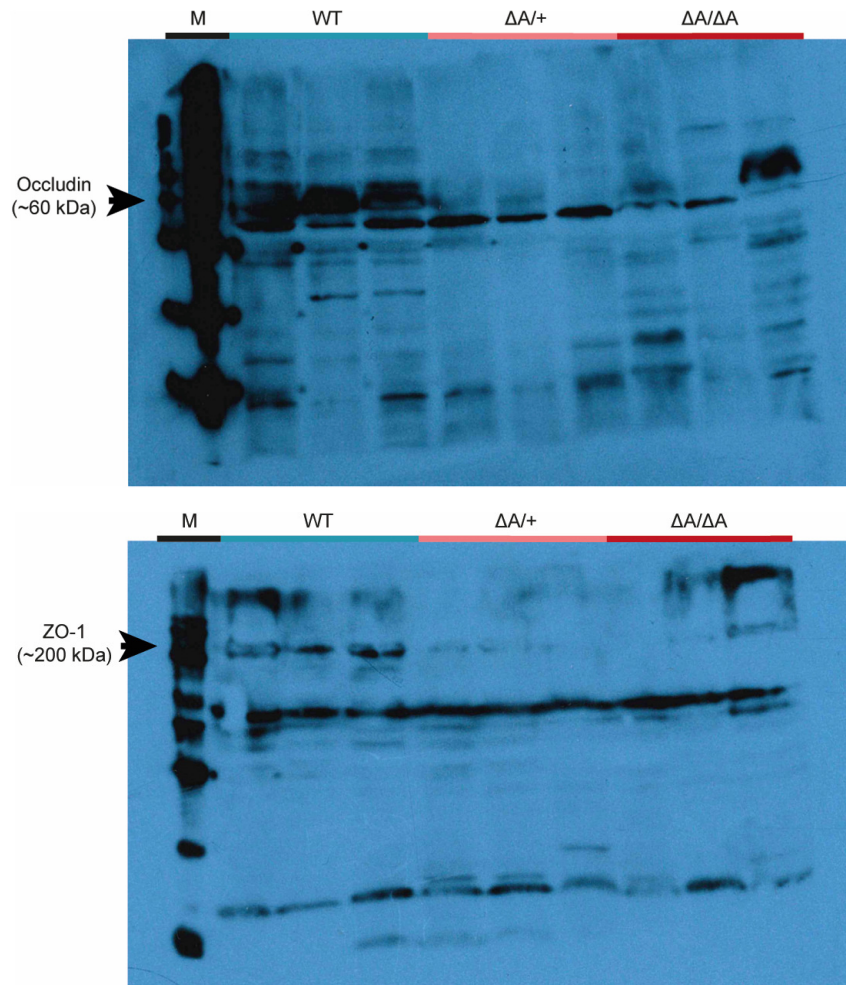


Figure S2: Complete Western blot images for Occludin (top) and ZO-1 (bottom) for colonic tissue isolates from three wild-type, three  $TNF^{\Delta ARE/+}$  and  $TNF^{\Delta ARE/\Delta ARE}$  swine. Band locations and sizes of ZO-1 and Occludin are indicated. M, size marker. Adapted from Winogrodzki et al.<sup>163</sup>.

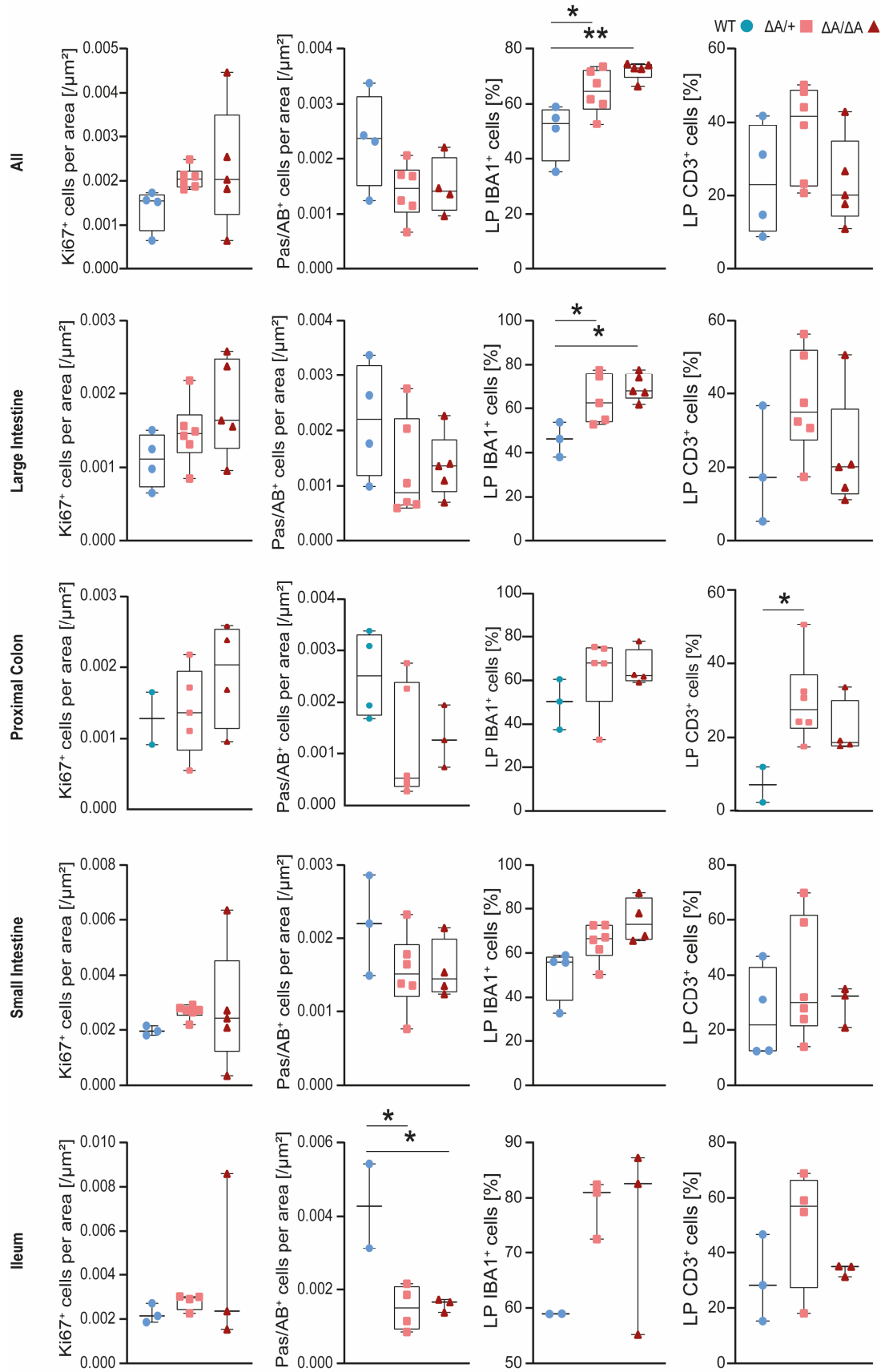


Figure S3: Statistical analysis of immunohistochemically stained tissue sections from wild-type,  $TNF^{\Delta ARE/+}$  and  $TNF^{\Delta ARE/\Delta ARE}$  pigs. The results demonstrate an increase in  $Ki67^+$ ,  $CD3^+$ , and  $IBA1^+$  cells and a decrease in  $Pas/AB^+$  cells. Adapted from Winogrodzki et al.<sup>163</sup>.

Table S1: Raw values of the complete blood count of  $TNF^{\Delta ARE/+}$  and  $TNF^{\Delta ARE/\Delta ARE}$  pigs and wild-type siblings. ). GOT: glutamate-oxalacetate-transaminase; GLDH: glutamate-dehydrogenase; GGT:  $\gamma$ -Glutamyl-Transferase; Bili: Bilirubin; AP: alkaline phosphatase; Chol.: cholesterol; TP: total protein; ALB: albumin; RBC: red blood cells; HCT: haematocrit; HGB: haemoglobin; MCV: mean corpuscular volume; MCHC: Mean corpuscular haemoglobin concentration; RDW: red cell distribution; RETIC: reticulocyte; WBC: white blood cell; NEU: neutrophils; LYM: lymphocytes; MONO: monocytes; EOS: eosinophils; BASO: basophils; PLT: platelets; MPV: mean platelet volume; PCT: procalcitonin.

Parameter	WT 1	WT 2	WT 3	$\Delta A/+$ 1	$\Delta A/+$ 2	$\Delta A/+$ 3	$\Delta A/+$ 4	$\Delta A/\Delta A$ 1	$\Delta A/\Delta A$ 2
GOT [U/l]	27	45	51	33	38	31	31	21	22
GLDH [U/l]	0.7	1.5	2	0.6	0.7	0.8	0.7	1.2	0.8
Ca [mg/dl]	9.8	9.9	10.8	9.9	9.4	9.7	9.6	9	9.1
P [mg/dl]	11.6	10.1	12.1	11.2	11.7	9.4	10.6	9.8	10.6
CK [U/l]	590	2656	1371	643	768	997	857	542	254
Mg [mg/dl]	2.61	2.96	3.05	3.03	2.92	2.91	2.84	2.7	2.83
Harnst. [mg/dl]	15.1	29	26.6	24.1	36.5	16.8	30.9	41	53.1
Fe [ $\mu$ g/dl]	186	127	157	108	52	108	119	95	85
Na [mg/dl]	329	326	329	328	328	323	329	323	318
K [mg/dl]	17.7	19.5	19.2	19.7	17	17.1	16.5	17.2	24.9
Cu [ $\mu$ g/dl]	120	114	124	125	156	122	123	159	166
Zn [ $\mu$ g/dl]	70	81	98	73	53	52	52	37	47
Mn [ $\mu$ g/dl]	0.31	0.3	0.35	0.34	0.23	0.31	0.24	0.23	0.2
Se [ $\mu$ g/l]	131	95	145	99	98	105	90	103	86
GGT [U/l]	60	67	88	87	72	71	75	82	93
TP [g/dl]	4.4	3.8	4.9	3.8	3.9	4.2	3.9	4.2	4.9
Bili [mg/dl]	0.2	0.09	0.11	0.12	0.16	0.12	0.15	0.15	0.17
AP [U/l]	297	346	379	409	261	209	194	201	98
Chol. [mg/dl]	69	60	58	69	74	68	66	72	56
Crea. mg/dl	1.4	1.14	1.05	1.15	1.31	1.27	1.33	1.44	1.53
Cl mg/dl	379	383	383	376	378	386	373	377	371
ALB g/dl	3.6	2.8	3.8	2.6	2.6	2.9	2.8	2.4	2.2
RBC	7.13	5.6	6.02	7.2	6.31	6.44	6.51	5.03	6.94
HCT	41.8	32.9	39.2	39.9	34.9	38.6	41.7	32.3	38.2
HGB	11.4	8.7	10.4	10.1	9.2	10.1	10.9	8.7	10.5
MCV	58.6	58.8	65.1	55.4	55.3	59.9	64.1	64.2	55
MCHC	16	15.5	17.3	14	14.6	15.7	16.7	17.3	15.1
MCHC	27.3	26.4	26.5	25.3	26.4	26.2	26.1	26.9	27.5
RDW	22.6	23.9	25.7	25.5	23.7	22.8	22.6	19.5	24.9
%RETIC	1.1	1.9	2.4	1.7	1	1.3	0.6	1.4	1
RETIC	76.3	104.7	145.7	120.2	60.6	86.3	37.1	71.9	70.1
WBC	20.71	21.89	19.8	24.26	15.73	16.07	18.94	16.95	10.68
%NEU	42	48.8	40.3	50.1	46.7	43.2	49.5	66	6.6
%LYM	53.5	47.3	54.2	47.4	48	52.5	43.9	29.4	81.6

%MONO	3.8	3.1	4.4	1.8	3.1	2.6	5.2	4	11.7
%EOS	0.7	0.8	1	0.7	2.2	1.5	1.4	0.4	0.1
%BASO	0	0	0.1	0	0	0.2	0	0.2	0
NEU	8.68	10.66	7.99	12.15	7.35	6.94	9.37	11.17	0.7
LYM	11.09	10.36	10.73	11.5	7.55	8.44	8.32	4.99	8.72
MONO	0.79	0.68	0.88	0.43	0.49	0.42	0.98	0.68	1.25
EOS	0.14	0.18	0.19	0.18	0.34	0.24	0.27	0.07	0.01
BASO	0.01	0.01	0.01	0	0	0.03	0	0.04	0
PLT	419	437	452	592	438	411	424	298	441
MPV	9.7	10.2	10.3	10.7	10.3	10.6	10.8	9.5	12.1
PDW	12.1	NA	16	NA	14.3	15.5	18	12.7	NA
PCT	0.41	0.45	0.47	0.63	0.45	0.44	0.46	0.28	0.53

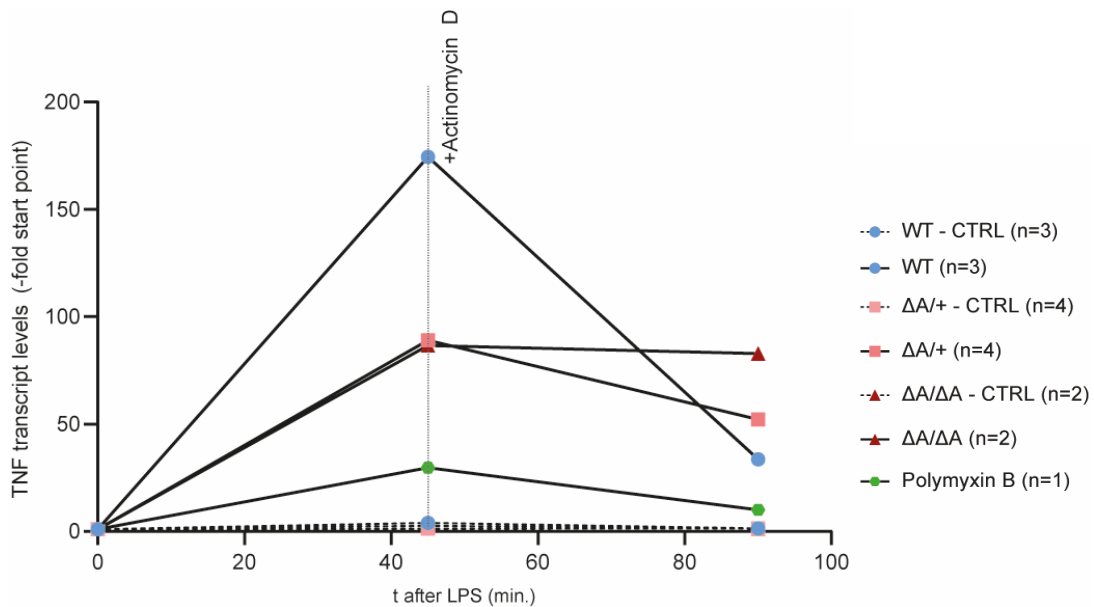


Figure S4: Determination of TNF mRNA levels and half-lives in macrophages from  $TNF^{\Delta ARE}$  and wild-type pigs. Macrophages were subject to LPS challenge alone or LPS+Polymyxin B, followed by co-incubation with actinomycin D from time point 45 minutes to 90 minutes. Untreated macrophages served as control (dotted lines).

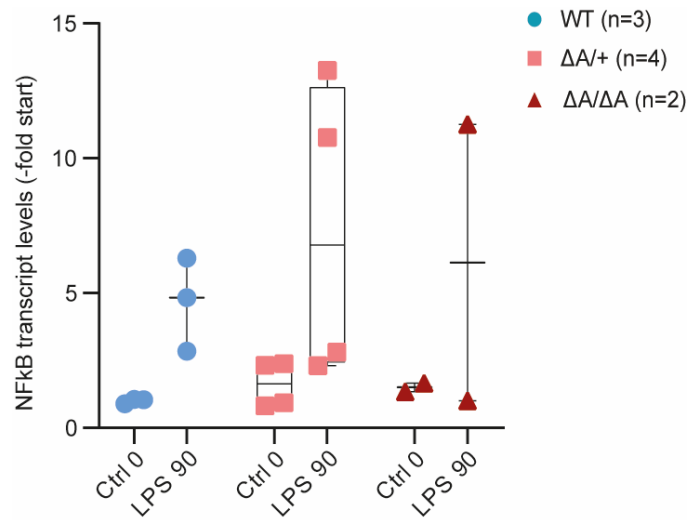


Figure S5: *NFκB* transcript levels of macrophages from wild-type and *TNF<sup>ΔARE</sup>* swine. Transcript levels at timepoints 0 minutes and 90 minutes of incubation with LPS were compared within and between groups.

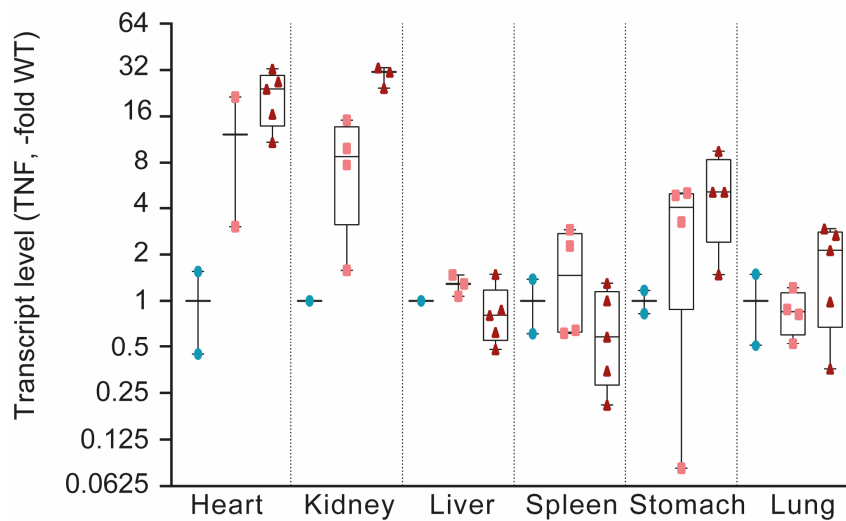


Figure S6: *TNF* mRNA levels in extra-intestinal samples shown as  $\log_2$  multiples of the average wild-type value. Caec., Caecum; Duod., Duodenum; Jej., Jejunum. Adapted from Winogrodzki et al.<sup>163</sup>.

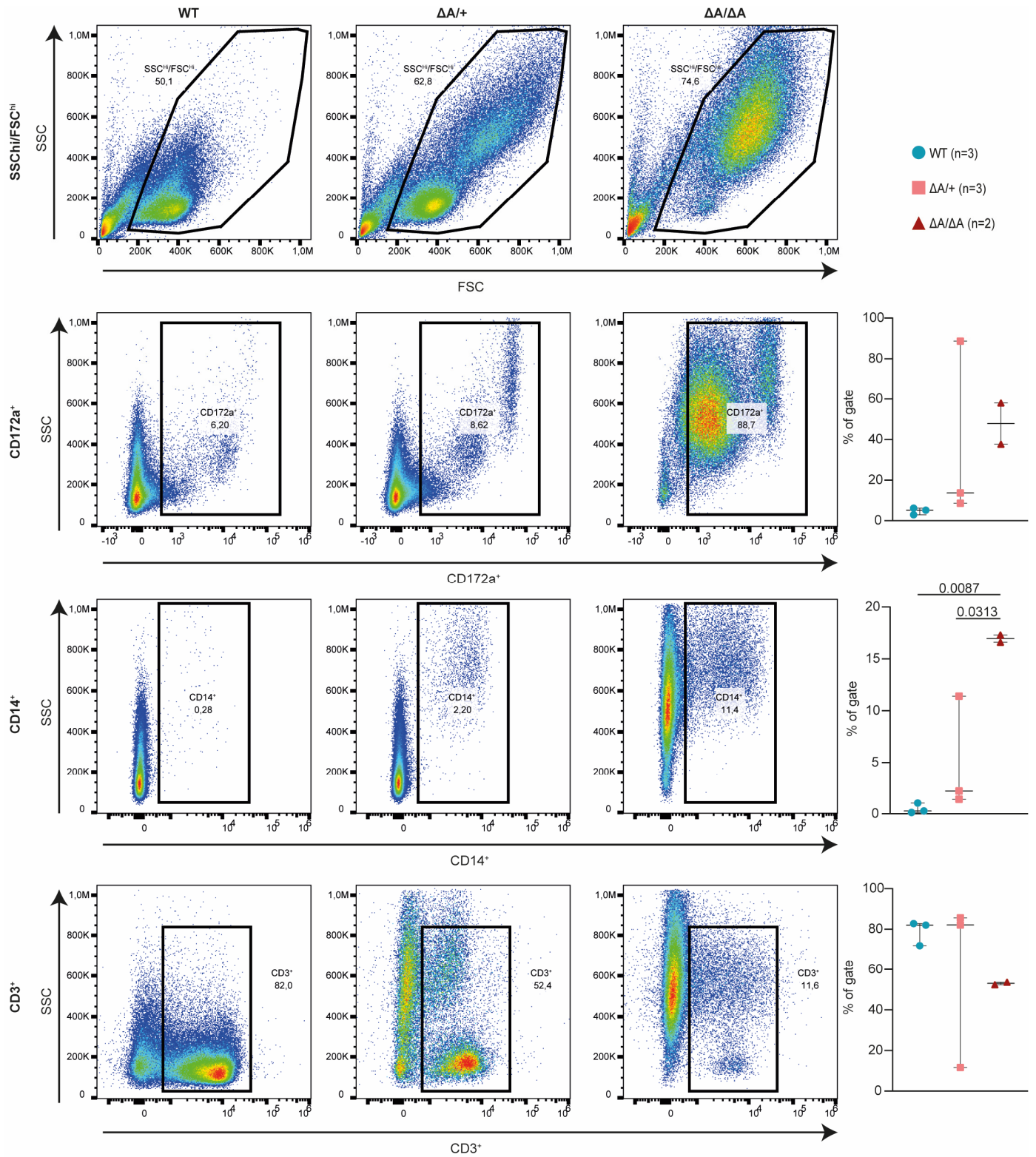
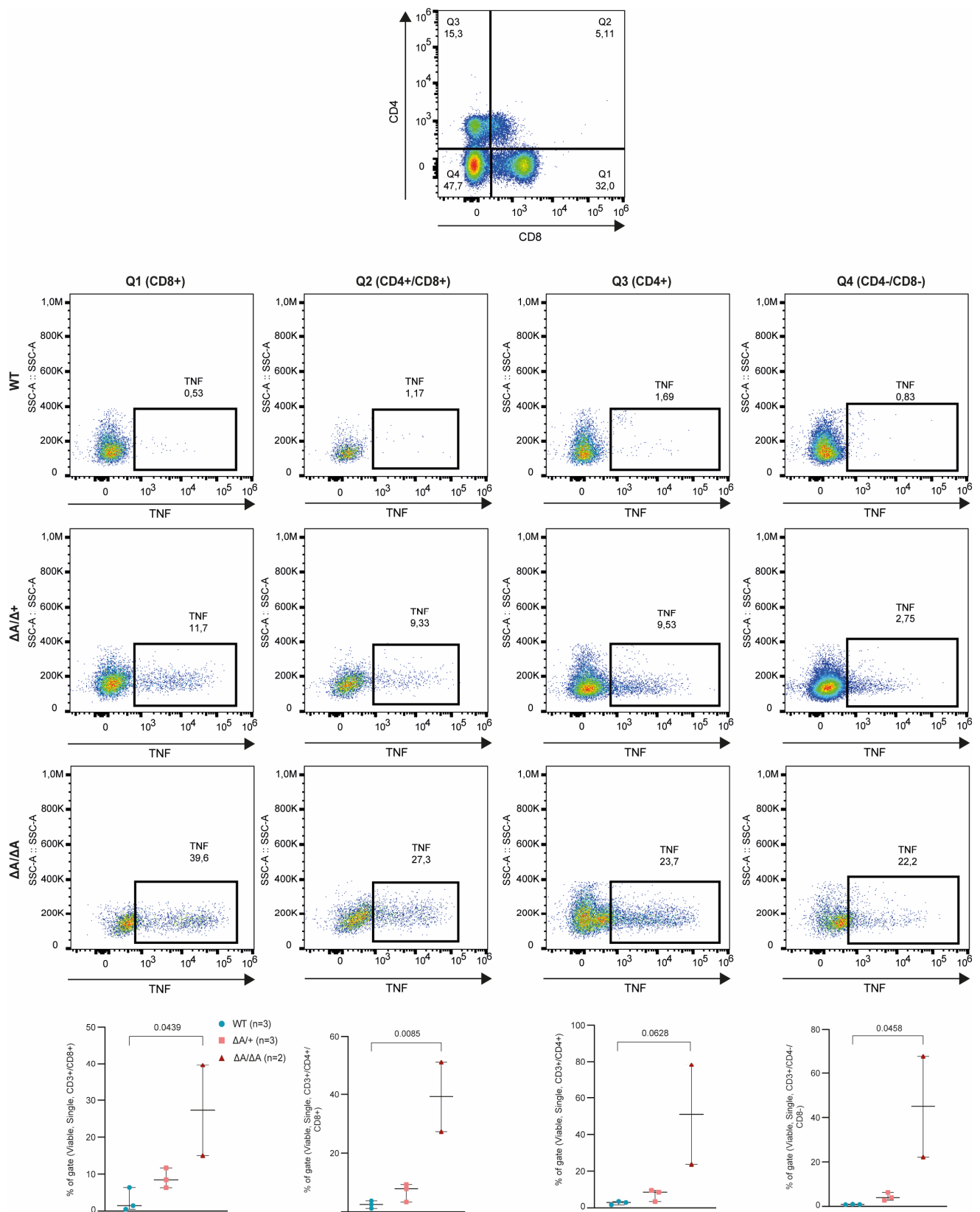


Figure S7: Flow cytometric analysis of viable, single PBMC-derived cell subsets from wild-type,  $TNF^{\Delta ARE/+}$  and  $TNF^{\Delta ARE/\Delta ARE}$  swine showing enhanced ratio of the  $FSC^{high}/SSC^{high}$  cell subset in mutant animals (top). Gating on this cell subset enabled the identification of increased numbers of CD172a<sup>+</sup> (second) and CD14<sup>+</sup> (third) cells, whereas gating on lymphocyte-characteristic FSC/SSC-ratios revealed a decreased number of CD3<sup>+</sup> cells (bottom) in mutant pigs. Statistical evaluation is shown next to respective representative gates.





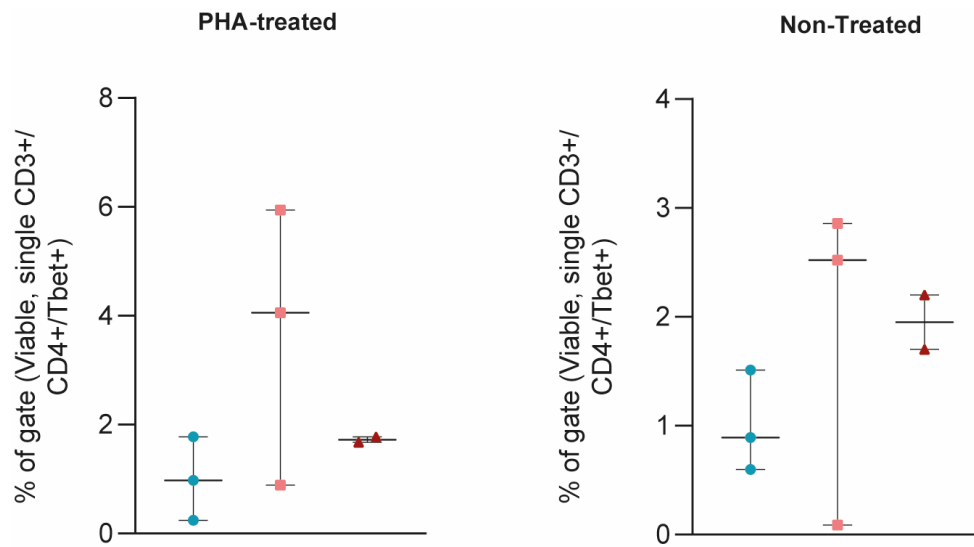


Figure S9: Statistical evaluation of for flow cytometry analysis of TNF<sup>+</sup>/CD3<sup>+</sup>/CD4<sup>+</sup>/Tbet<sup>+</sup> viable, single lymphocytes of PBMCs derived from 3 wild-type, 3 TNF $\Delta$ ARE<sup>+</sup>, and 2 TNF $\Delta$ ARE/ $\Delta$ ARE swine. In addition to results from the PHA-treated immune cells group (left), results from the non-treated group are shown (right).



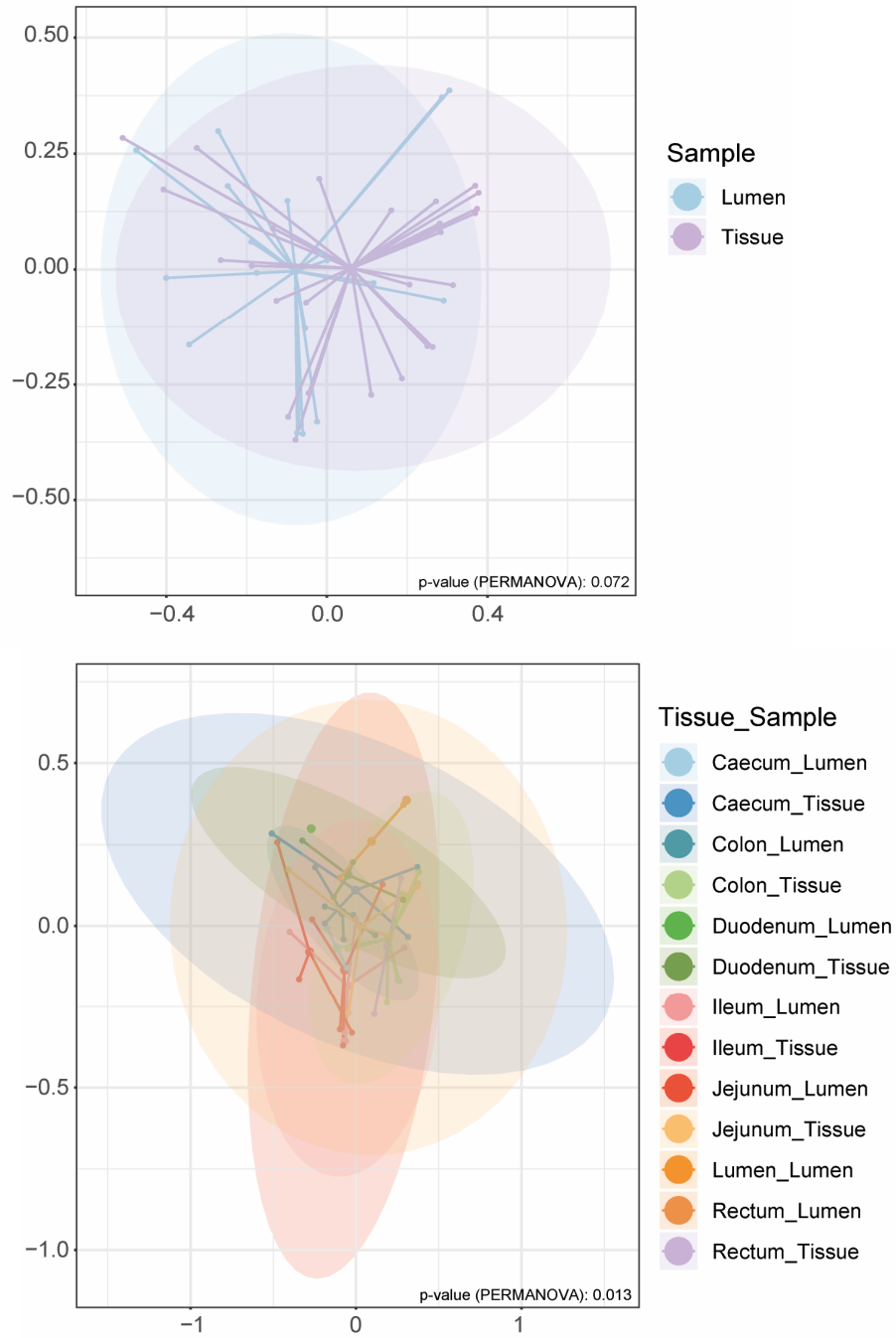


Figure S10: PCoA plots of microbial profiles derived from tissue and luminal rectal, colonic, caecal, ileal, jejunal and duodenal samples stratified by sample type (top) and tissue sections (bottom).

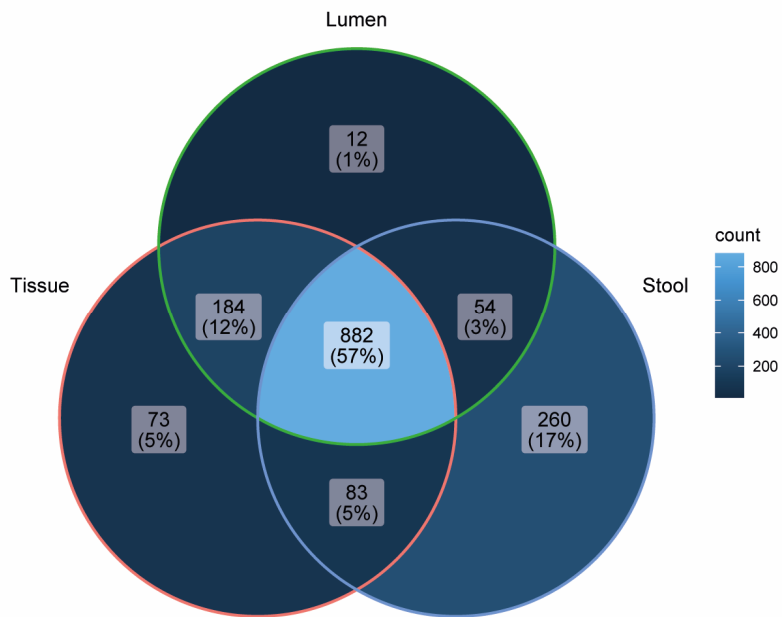


Figure S11: Venn Diagram showing the absolute amount of shared and exclusive zOTUs between stool, luminal and tissue samples. A brighter color indicates a larger overlap.

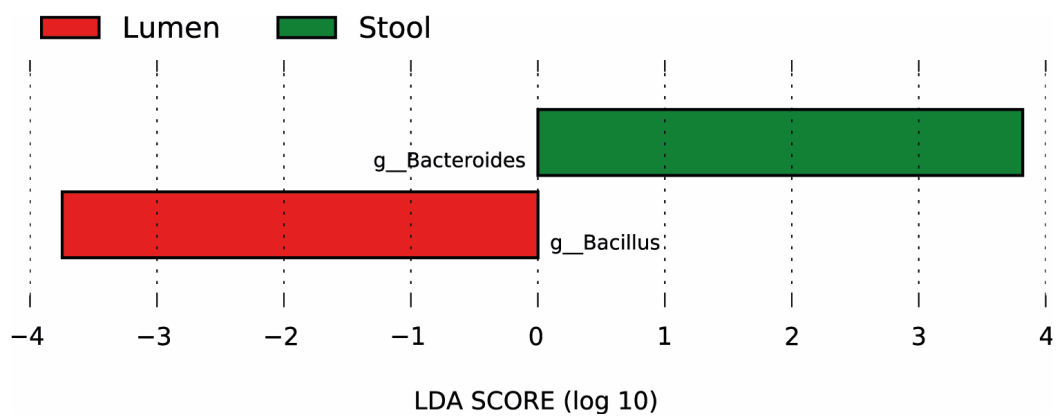
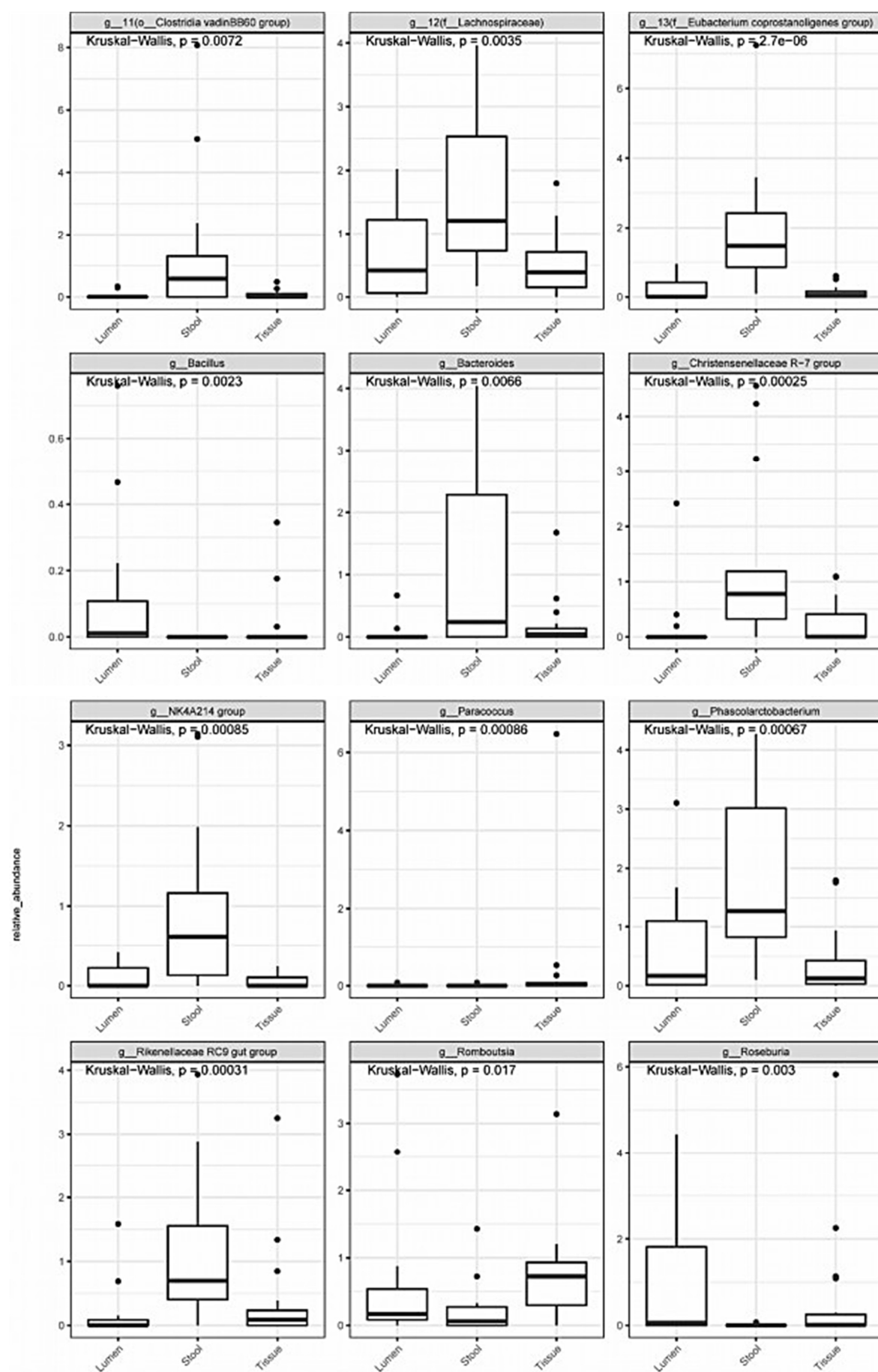
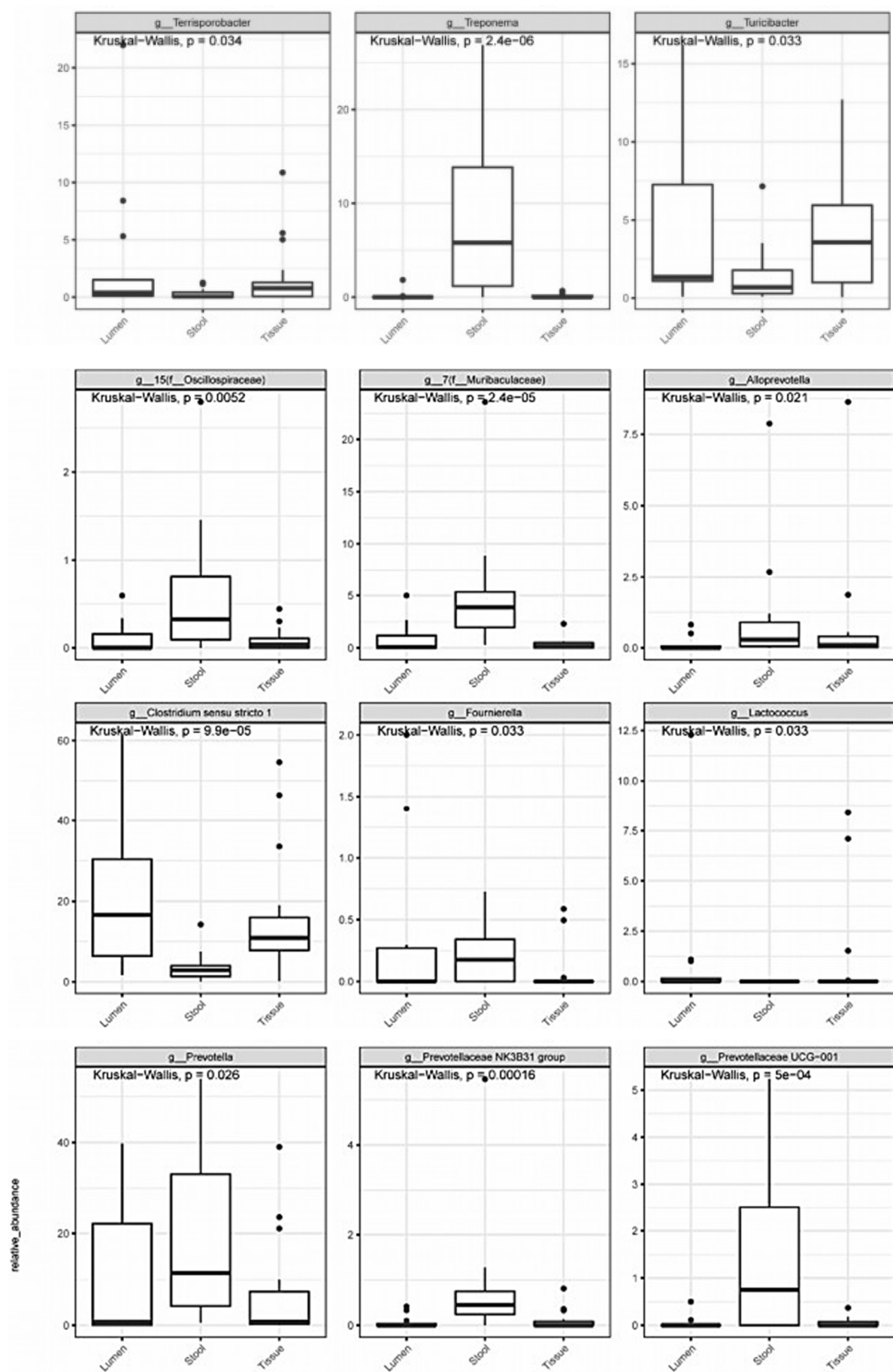


Figure S12: LEfSe analysis of stool, luminal and tissue microbiomes from wild-type samples. The bar lengths illustrate logarithmic fold-changes of differentially abundant genera. The respective LDA linear discriminant analysis score is shown.





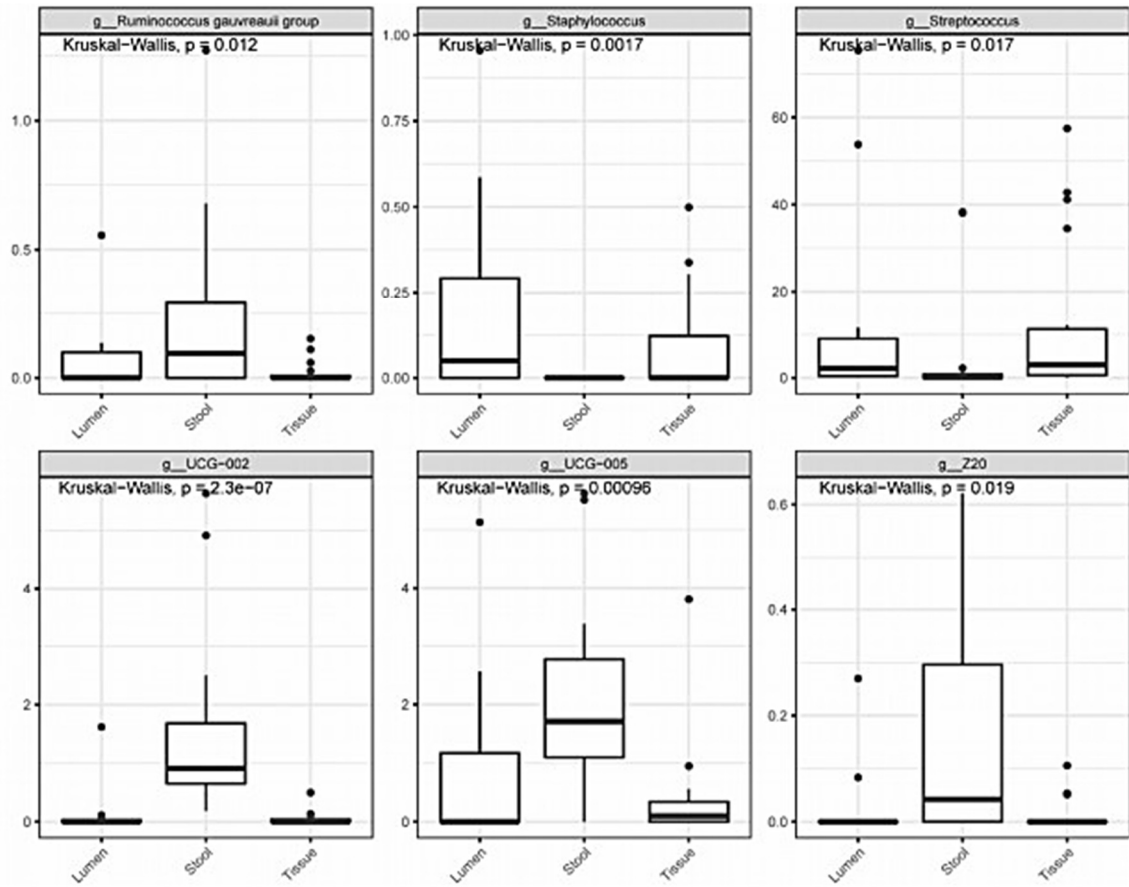


Figure S13: Differentially abundant genera in wild-type luminal, faecal and biopsy tissues.

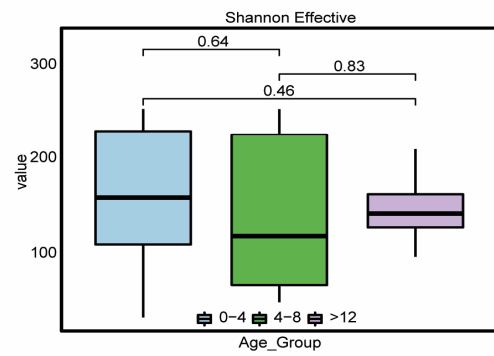
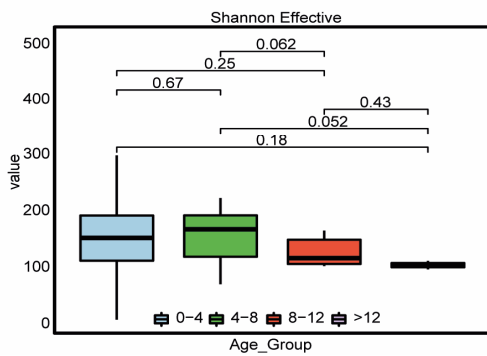
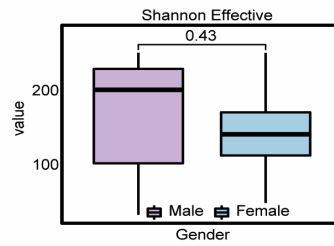
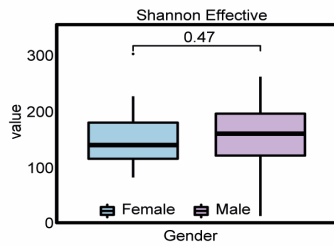
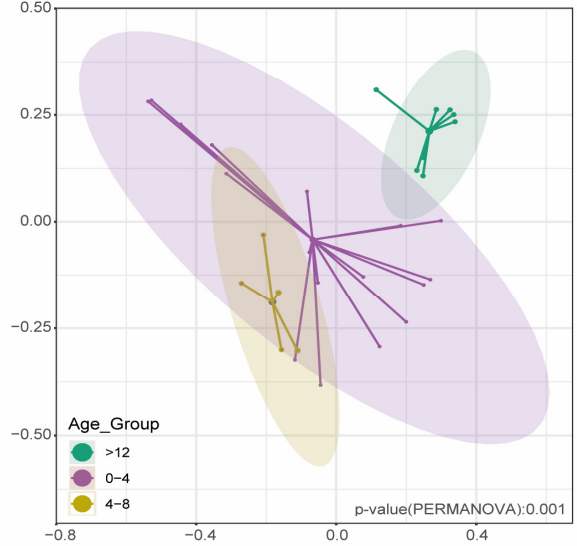
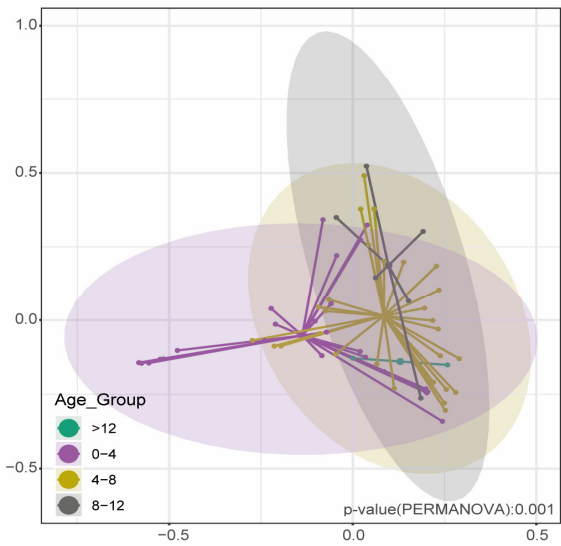
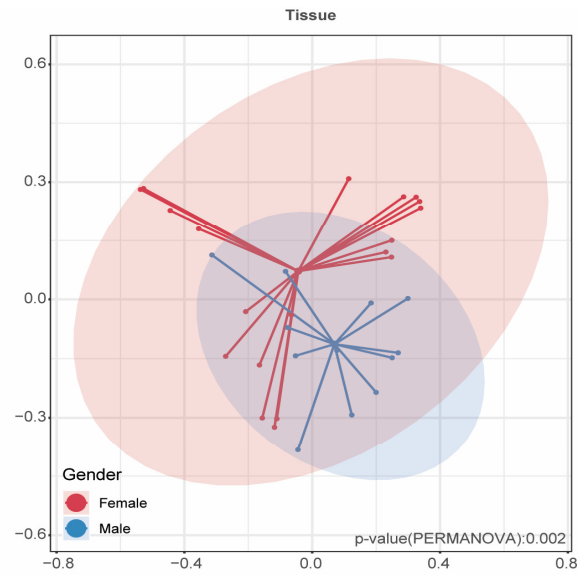
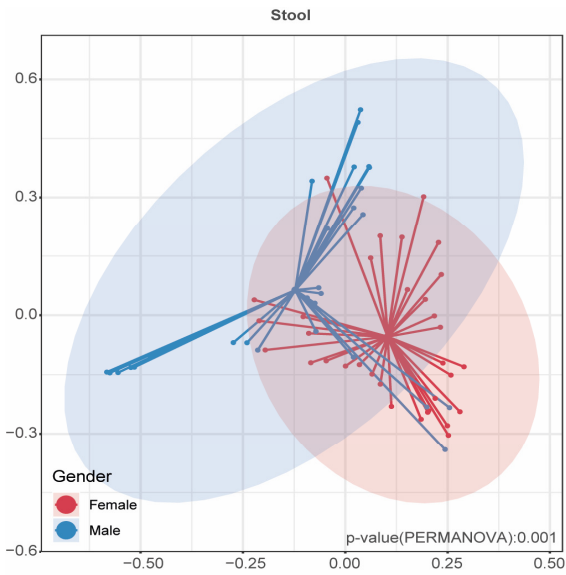


Figure S14: PCoA plots of microbial profiles derived from tissue biopsy and faecal samples stratified by gender (top left) and age group (bottom left) and respective shannon effective numbers displaying alpha-diversity of samples stratified by gender (top right) and age group (bottom right).

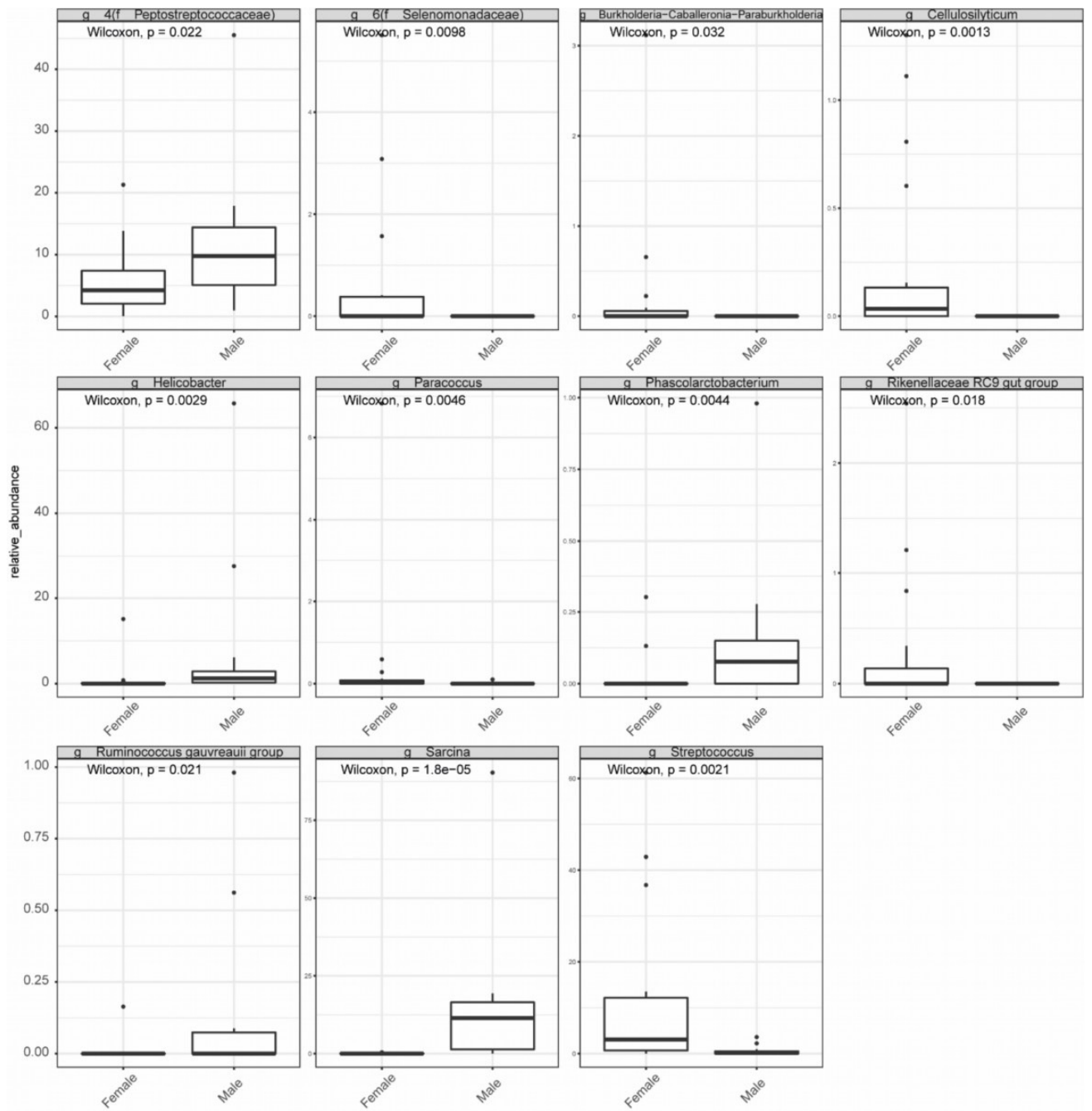


Figure S15: Differentially abundant genera in female and male wild-type tissue biopsies.

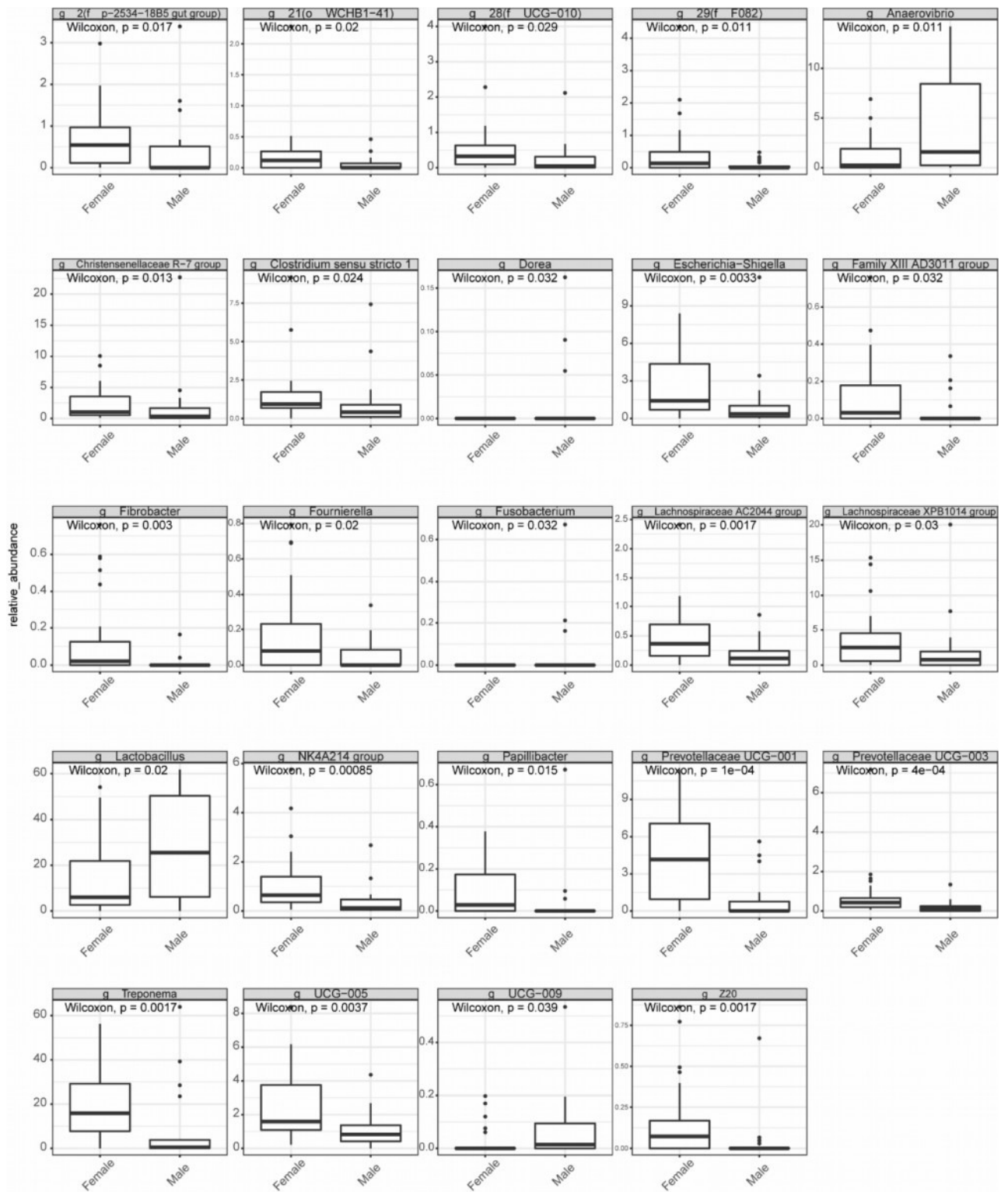


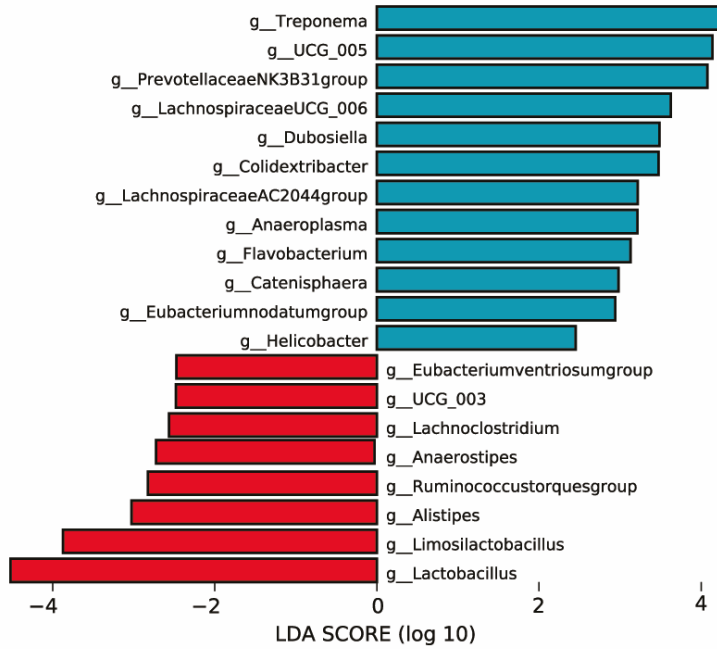
Figure S16: Differentially abundant genera in female and male wild-type faecal samples.



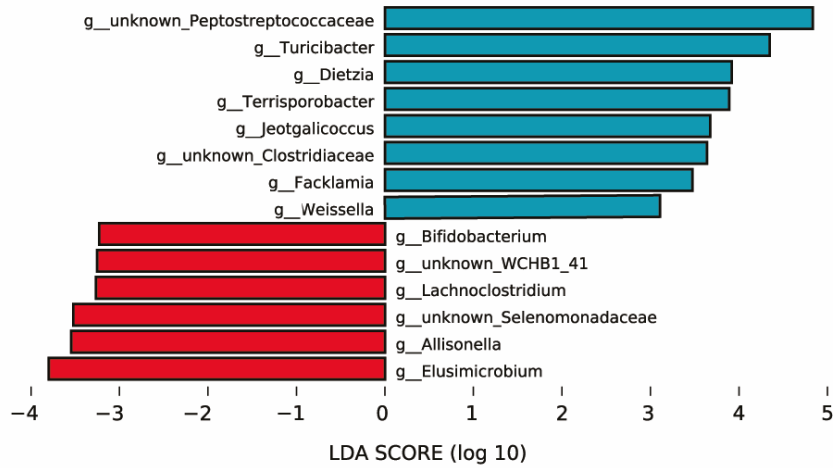
■  $\Delta$ ARE ( $\Delta$ A/+ &  $\Delta$ A/ $\Delta$ A)

■ Wild-type

### Stool



### Ileum



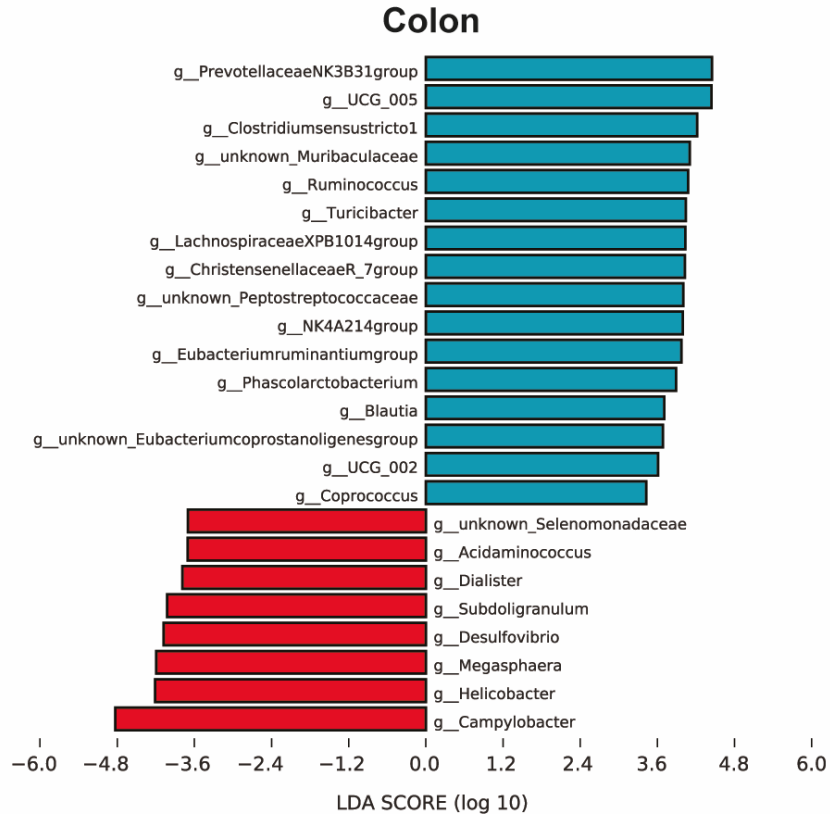


Figure S17: LEfSe analysis plot of microbial taxonomic differences in stool (top), ileal tissue (mid), and colonic tissue biopsy samples (bottom) from mutant pigs (red) and wild-types (blue). The plot shows the differentially abundant taxa and the respective linear discriminant analysis score. Modified based on Dr. Amira Metwaly's plot. Adapted from Winogradzki et al.<sup>163</sup>.

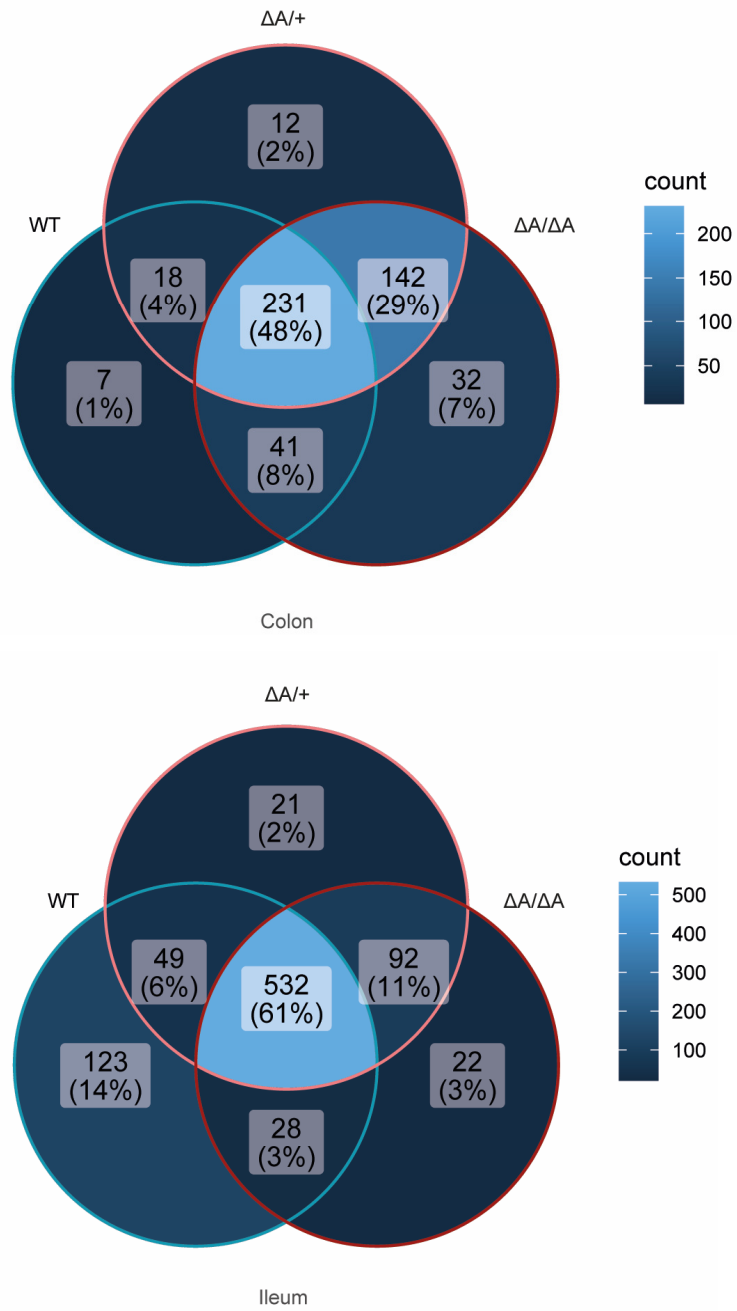


Figure S18: Venn Diagram showing the absolute amount of shared and exclusive zOTUs between colonic (top) and ileal (bottom) tissue samples derived from wild-type and  $TNF^{\Delta ARE}$  swine. A brighter color indicates a larger overlap.

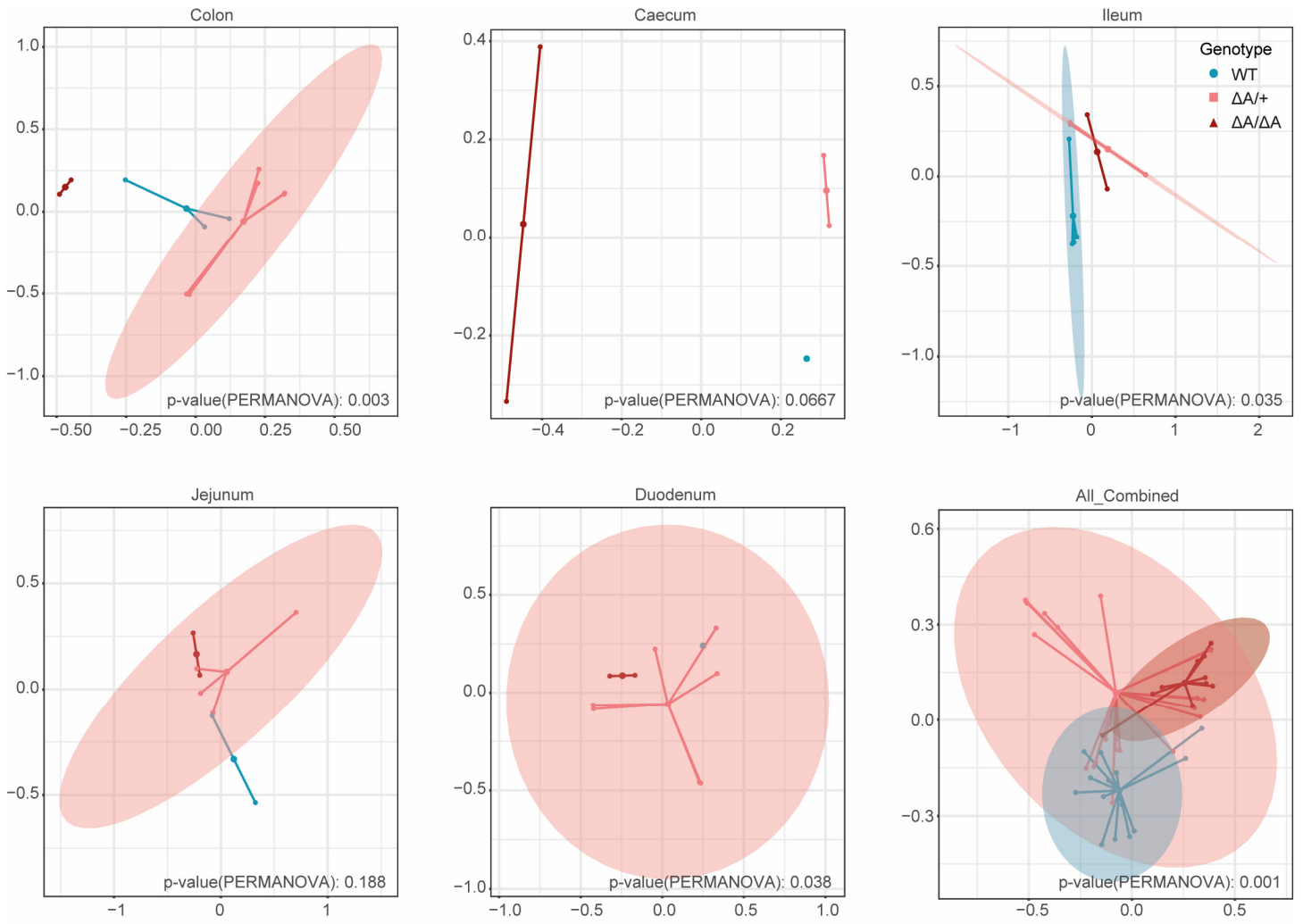


Figure S19: PCoA plots of microbial profiles derived from colonic (top left), caecal (top middle), ileal (top right), jejunal (bottom left), duodenal (bottom middle) and all combined (bottom right) tissue samples stratified by genotype.

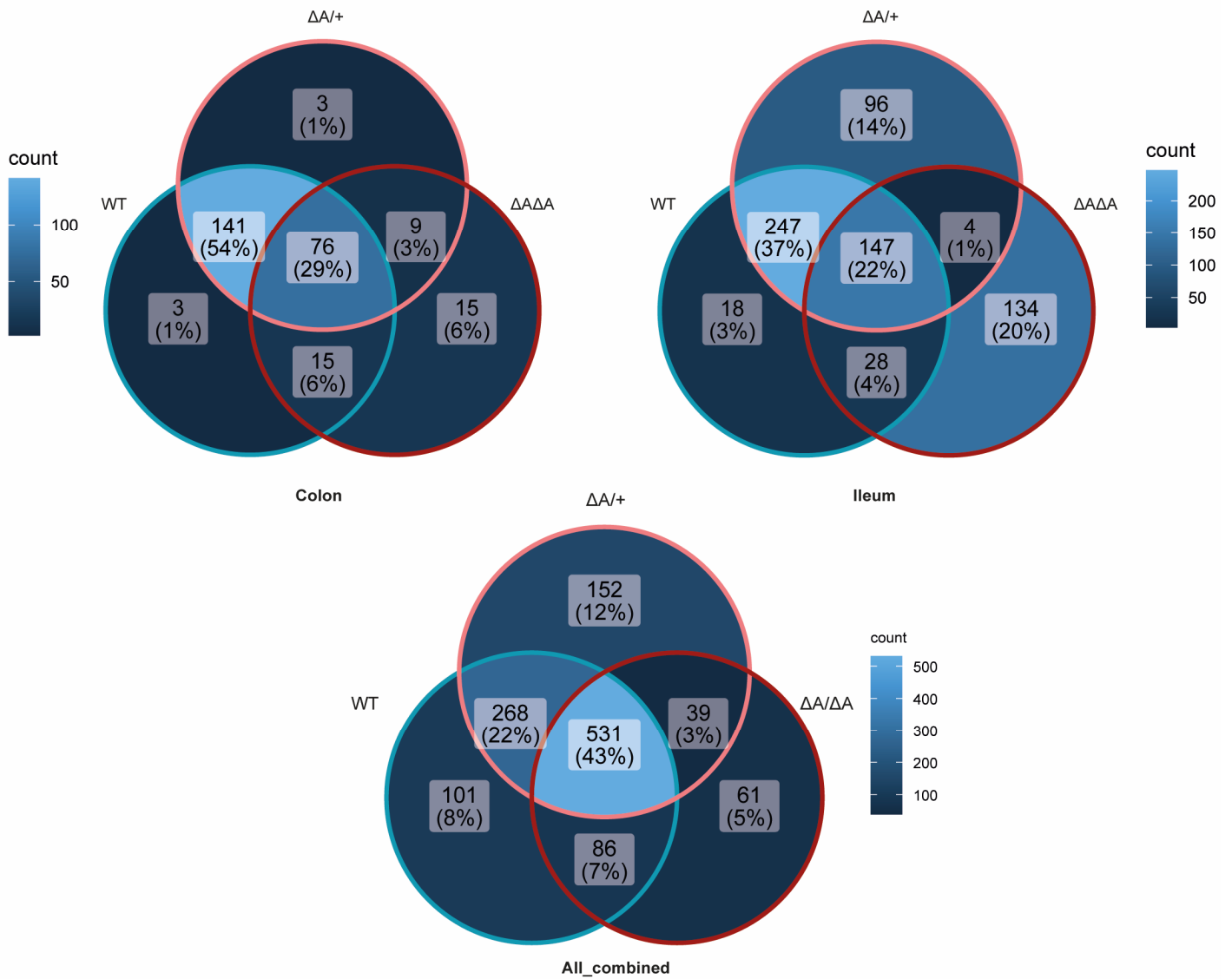


Figure S20: Venn Diagram showing the absolute amount of shared and exclusive zOTUs between colonic (top left), ileal (top right) and all combined (bottom) tissue samples derived from wild-type and  $TNF^{\Delta ARE}$  swine. A brighter color indicates a larger overlap.

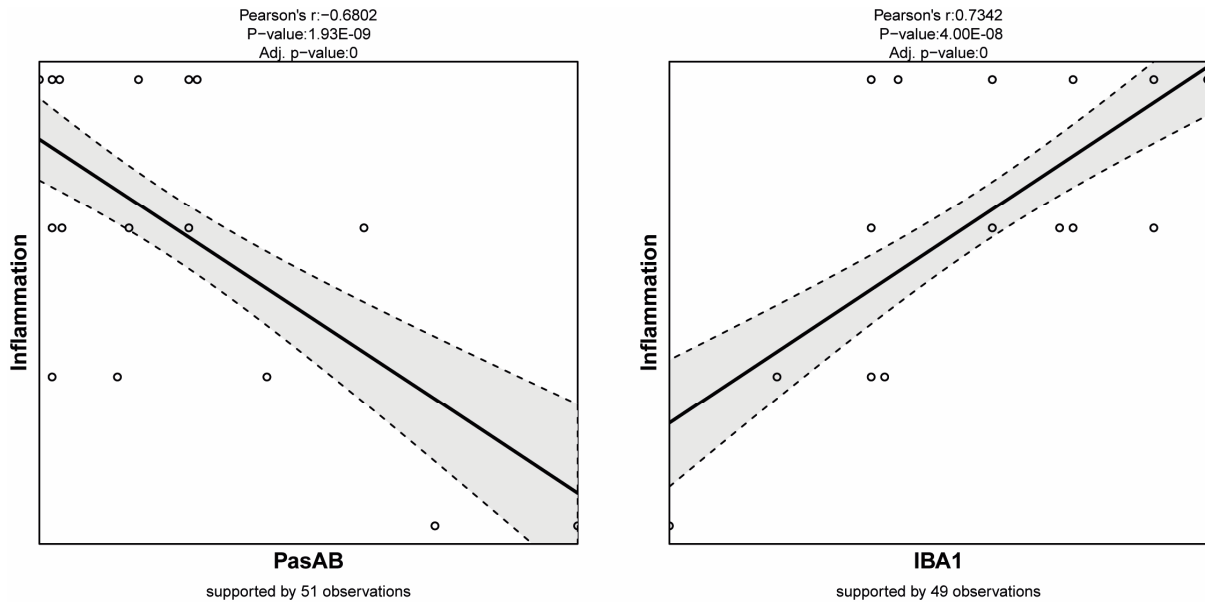


Figure S21: Pearson's correlation analysis for the health status (inflammation) of an individual vs. the amount of Pas/AB<sup>+</sup> per crypt length and vs. the ratio of IBA1<sup>+</sup> to IBA<sup>-</sup> cells in the lamina propria measured in this pig. Shown are individual sample-specific values, lower and upper boundaries of the predicted interval, as determined using the R function predict, and the linear fitted line.

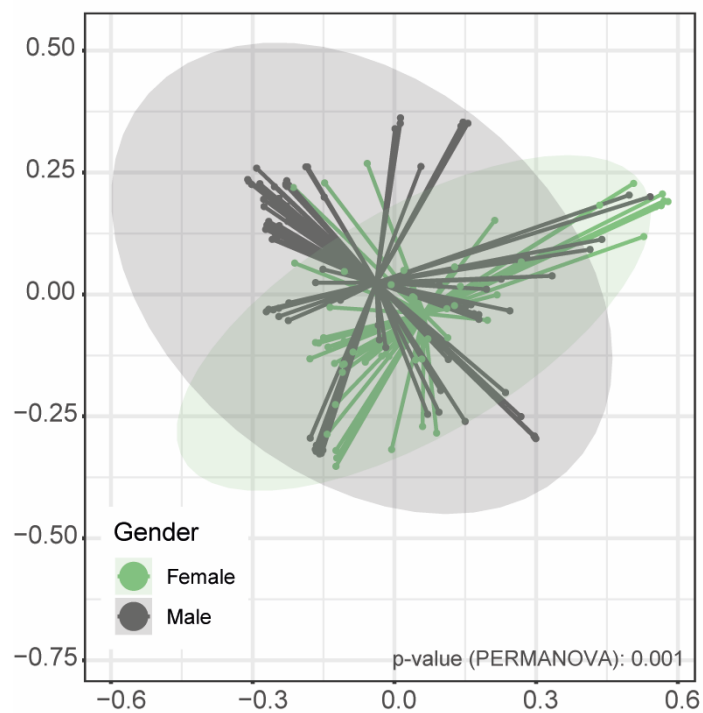


Figure S22: PCoA plots of microbial profiles derived from faecal, luminal and tissue samples of male and female swine.

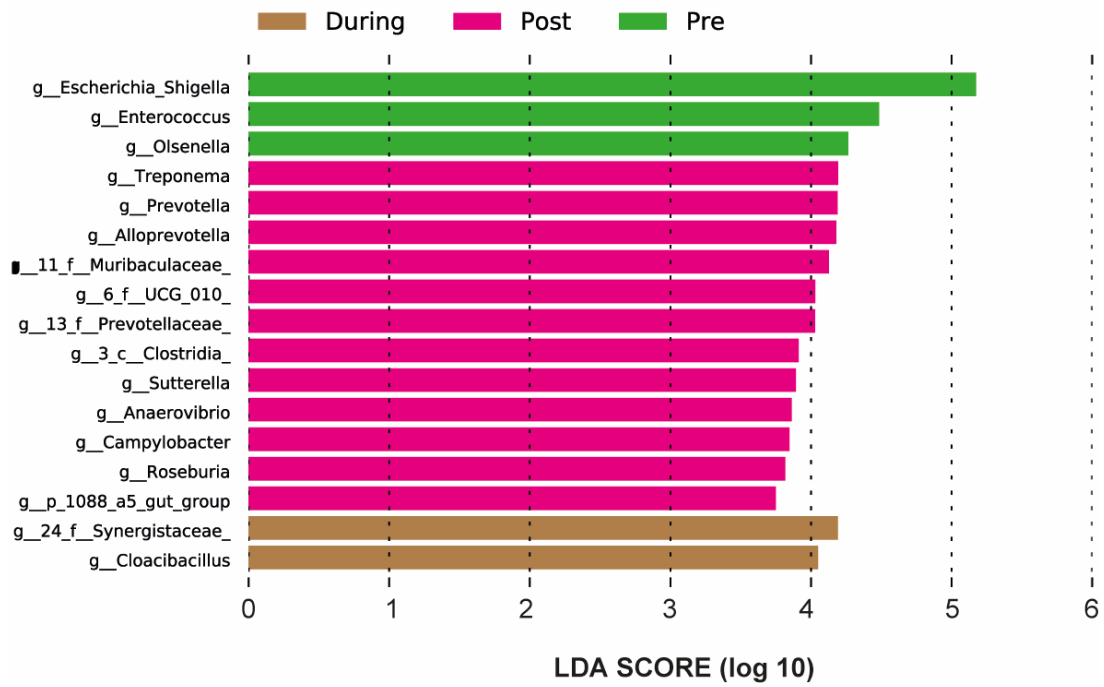


Figure S23: LEfSe analysis plot of microbial taxonomic differences in stool samples pre-, during and post-weaning from mutant pigs and wild-types. The plot shows the differentially abundant taxa and the respective linear discriminant analysis score.

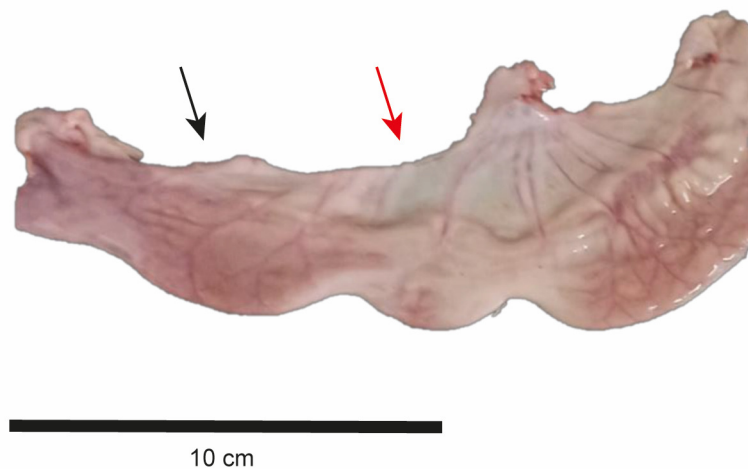


Figure S24: Duodenal section of a heavily inflamed  $TNF^{\Delta ARE/+}$  pig. The image includes two areas of the tissue, one of which is macroscopically unaffected and is indicated by a black arrow, while the other is fibrotic and structuring, indicated by a red arrow.

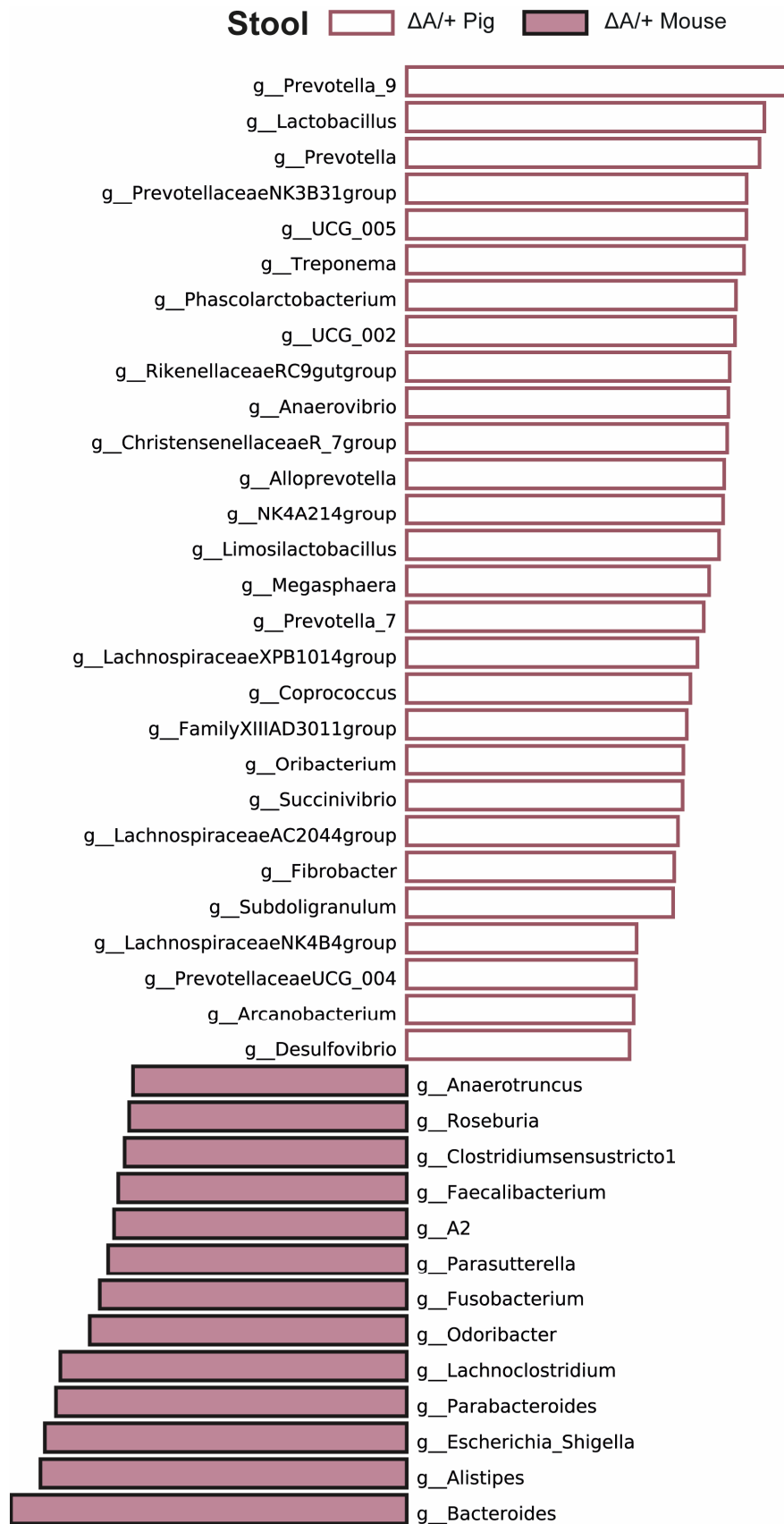


Figure S25: LEfSe analysis of faecal samples derived from wild-type,  $TNF^{\Delta ARE/+}$  and  $TNF^{\Delta ARE/\Delta ARE}$  pigs and  $TNF^{\Delta ARE/+}$  mice. The plot shows the differentially abundant taxa and the respective linear discriminant analysis score. Adapted from Winogradzki et al.<sup>163</sup>.



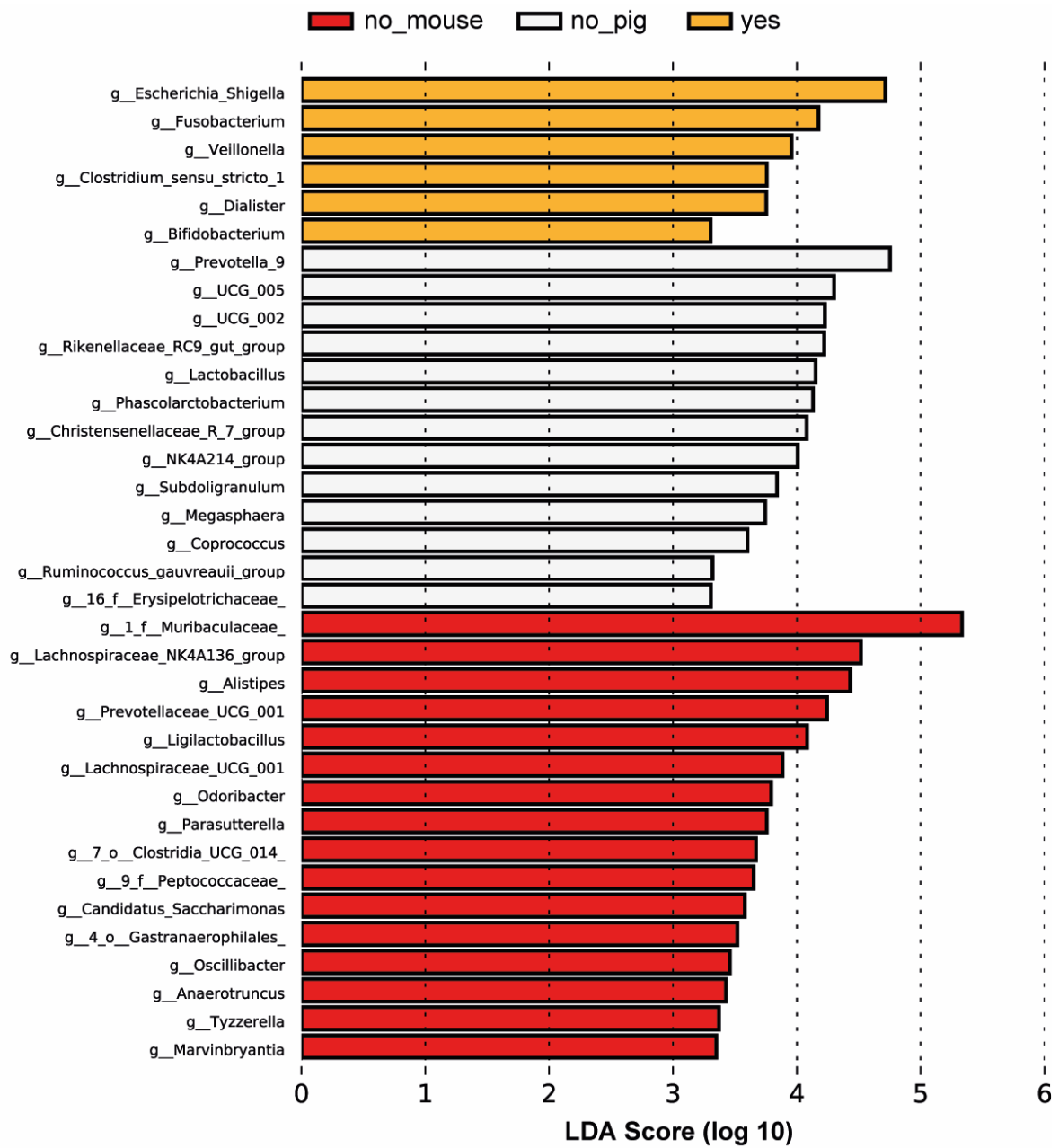


Figure S26: LEfSe analysis plot of microbial taxonomic differences in porcine and murine faecal samples derived from wild-type,  $TNF^{\Delta ARE/+}$  and  $TNF^{\Delta ARE/\Delta ARE}$  individuals that either cluster (“Yes”) or do not cluster (“No”) together on a PCoA plot. The plot shows the differentially abundant taxa and the respective linear discriminant analysis score.

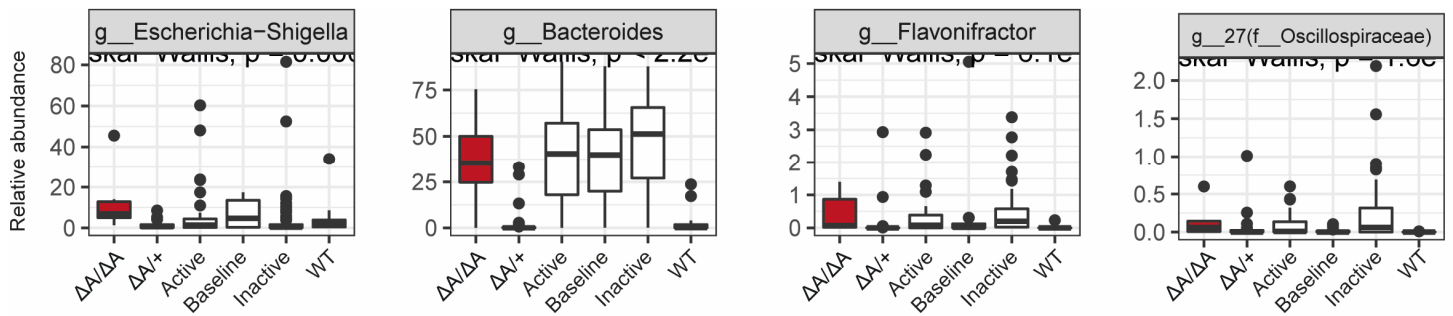


Figure S27: Selection of results from Wilcoxon test with Bonferroni correction for multiple testing identifying significantly differentially abundant genera between human IBD patients with inactive or active disease or at the time of HPSCt-treatment and wild-type,  $TNF^{\Delta ARE/+}$  and  $TNF^{\Delta ARE/\Delta ARE}$  pigs that shows relatively high levels of genera in both  $TNF^{\Delta ARE/\Delta ARE}$  pigs and patients with active disease.

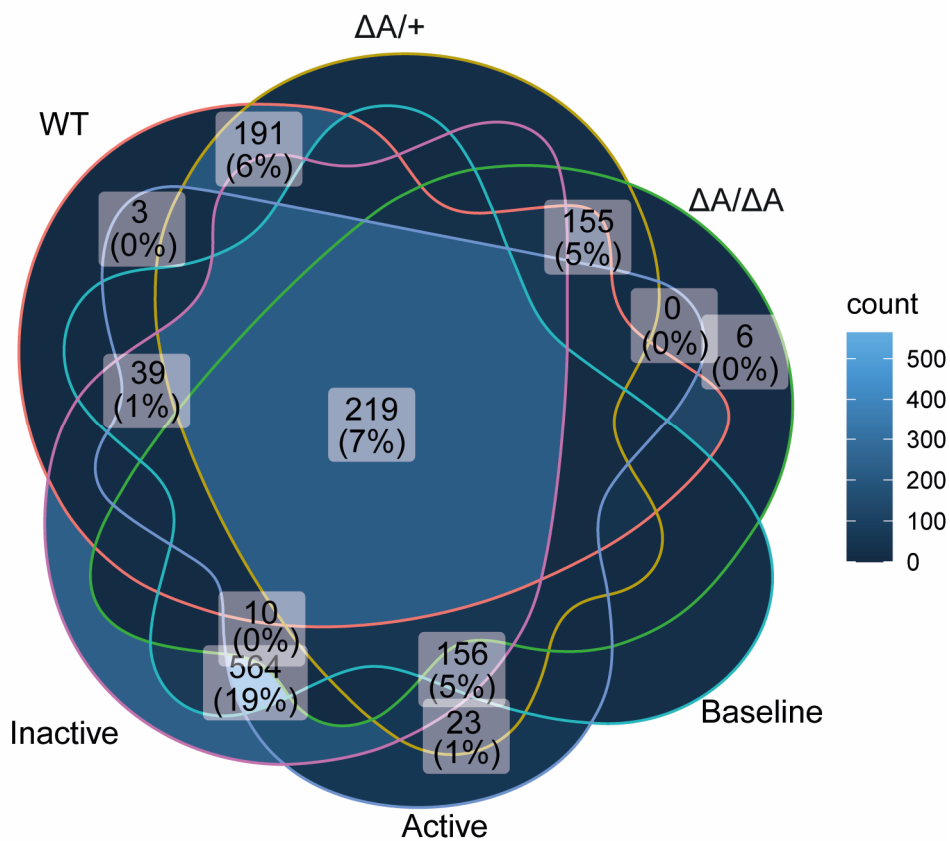


Figure S28: Venn diagram showing the counts of shared and exclusive zOTUs between faecal samples derived from human IBD patients with inactive or active disease or at the time of HPSCt-treatment and wild-type,  $TNF^{\Delta ARE/+}$  and  $TNF^{\Delta ARE/\Delta ARE}$  pigs. Results relevant for the analysis are shown. A brighter color indicates a higher zOTU count.

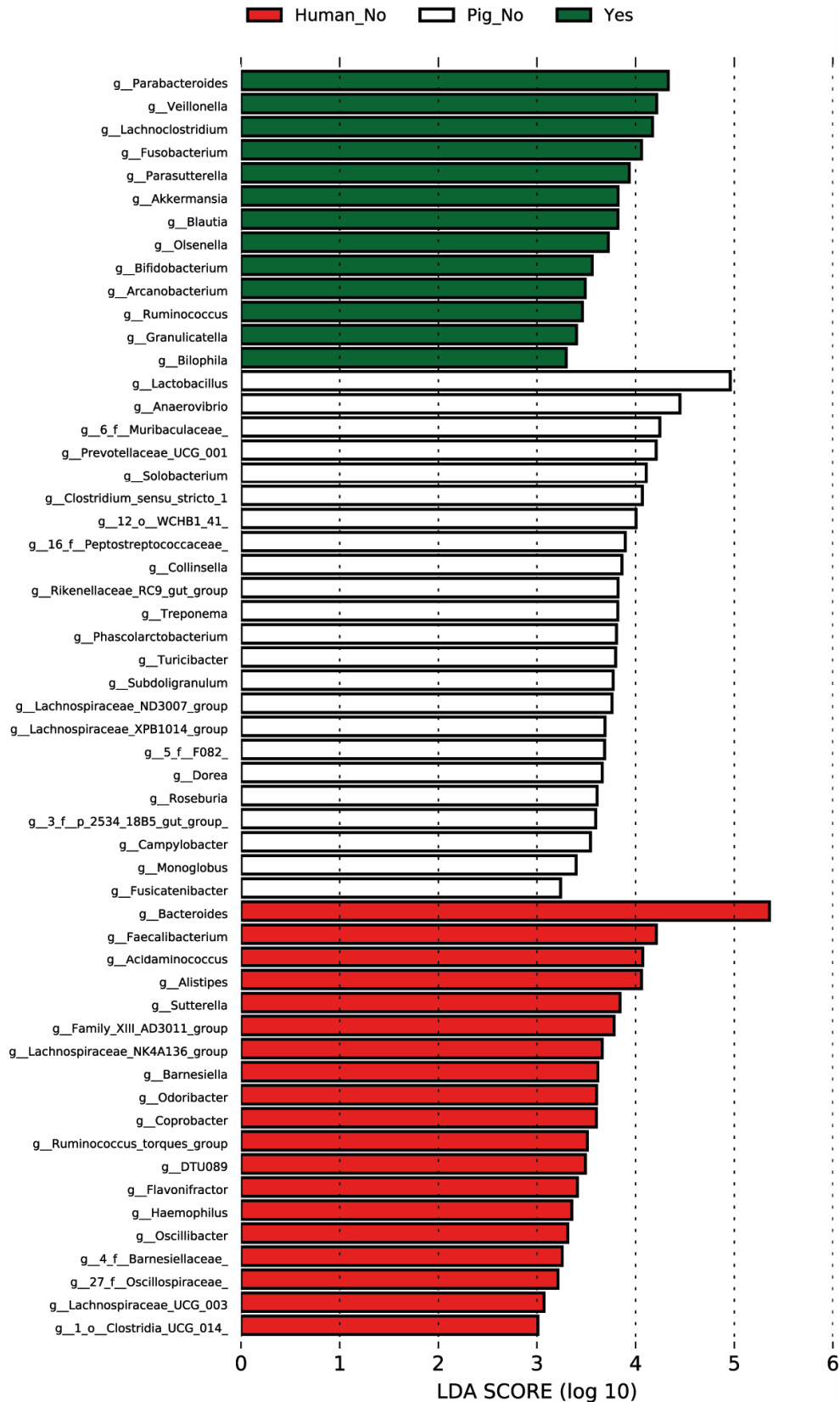


Figure S29: LEfSe analysis of faecal samples derived from human IBD patients with inactive or active disease or at the time of HPSCt-treatment and wild-type,  $TNF^{\Delta ARE/+}$  and  $TNF^{\Delta ARE/\Delta ARE}$  pigs that either cluster (“Yes”) or do not cluster close together (“No”) on a PCoA plot. The plot shows the differentially abundant taxa and the respective linear discriminant analysis score.

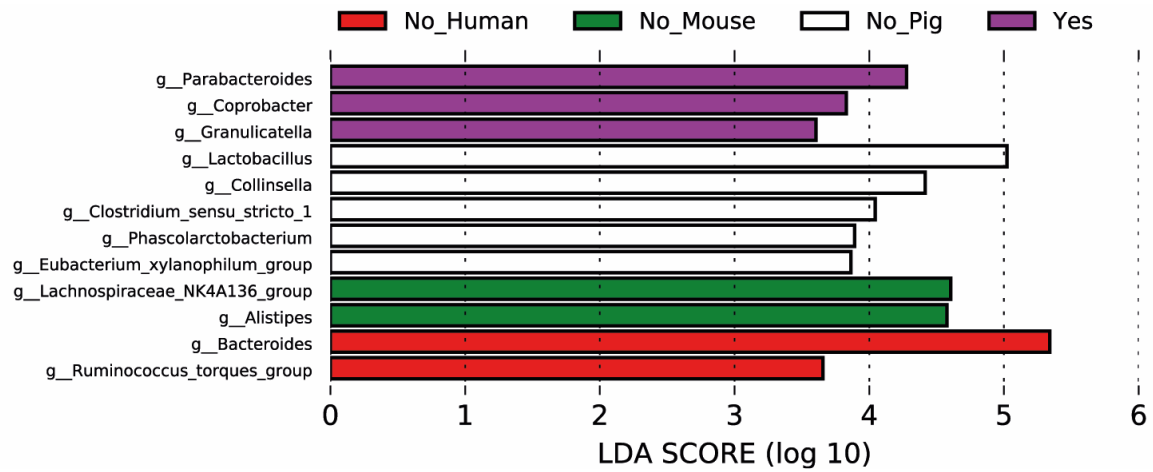


Figure S30: LEfSe analysis of faecal samples derived from human IBD patients, wild-type and  $TNF^{\Delta ARE/+}$  mice, and wild-type,  $TNF^{\Delta ARE/+}$  and  $TNF^{\Delta ARE/\Delta ARE}$  pigs that either cluster (“Yes”) or do not cluster close together (“No”) on a PCoA plot. The plot shows the differentially abundant taxa and the respective linear discriminant analysis score.

## Abbreviations

<b>Abbreviation</b>	<b>Written out</b>
ActD	Actinomycin D
ADAM	A disintegrin and metalloproteinase
APC	Adenomatous polyposis coli
ARE	Au-rich element
ASV	Amplicon sequence variant
ATG16L1	Autophagy-related 16-like 1
AUF1	Au-rich element binding protein 1
B2M	Beta-2-microglobulin
BALT	Bronchus-associated lymphoid tissue
Cas	Crispr-associated
CD	Crohn's disease
CD3	Cluster of differentiation 3
cDC	Conventional dc
CDE	Constitutive decay element
cDNA	Complementary dna
CED	Crohnisch-entzündliche darmerkrankungen
CETAB	Cetyltrimethylammonium bromide
cFLIP	Flice-like inhibitory protein
ciAP	Cellular inhibitor of apoptosis protein
CLR	C-type lectin receptor
COC	Cumulus-oocyte complex
CRISPR	Clustered regularly interspaced short palindromic repeat
crRNA	Crispr rna
Ct	Threshold cycle
CTRL	Control
DAB	3,3'-diaminobenzidine
DAMPS	Damage-associated molecular patterns
DC	Dendritic cell
DD	Death domain
DMEM	Dulbecco's modified eagle medium
DMSO	Dimethylsulfoxide
DNA	Deoxyribonucleic acid
DSB	Double-strand break
DSS	Dextrane sulfate sodium
DUSPs	Dual-specificity phosphatases
ECG	Equine chorionic gonadotropin

EDTA	Ethylendiamintetraacetic acid
ELISA	Enzyme-linked immunosorbent assay
FADD	Fas-associated dd
FCS	Fetal calf serum
FFPE	Formalin-fixed paraffin-embedded
FMO	Fluorescence-minus one
FMT	Faecal microbiota transplantation
FSC	Forward scatter
GALT	Gut-associated lymphatic tissues
GAPDH	Glyceraldehyde-3-phosphate dehydrogenase
GF	Germ-free
GM	Genetically modified
GM-CSF	Granulocyte/macrophage-colony stimulating factor
gRNA	Guide rna
GWAS	Genome-wide association study
HCG	Human chorionic gonadotropin
HDR	Homology-directed repair
HEPES	4-(2-hydroxyethyl)-1-piperazineethanesulfonic acid
HMBS	Hydroxymethylbilane synthase
HPRT	Hypoxanthine phosphoribosyltransferase
HSCT	Hematopoietic stem cell transplantation
HSPCB	Heat-shock protein family c member b
HU	Human antigen
i.m.	Intramuscular
i.v.	Intravenous
IBA1	Ionized calcium-binding adapter molecule 1
IBD	Inflammatory bowel disease
ICE	Inference of crispr edits
IEC	Intestinal epithelial cells
IFN- $\gamma$	Interferon $\gamma$
IgA	Immunoglobulin a
IgM	Immunoglobulin m
IHC	Immunohistochemistry
IL10	Interleukin 1
IL6	Interleukin 6
IL8	Interleukin 6
IMNGS	Integrated microbial next generation sequencing
iNOS	Inducible nitric oxid synthase

IVC	In vitro-cultivation
IVF	In vitro-fertilisation
IVM	In vitro-maturation
Ikk	Inhibitor of ikb kinase
JNK	Jun nh <sub>2</sub> -terminal kinase
Ki67	Kiel67
LDA	Linear discriminant analysis effect size
LEfSe	Linear discriminant analysis
LGR5	Leucine-rich repeat-containing g-protein coupled receptor 5
LPS	Lipopolysaccharide
MAPK	Mitogen-activated protein kinase
MC	Morbus crohn
M-cells	Microfold cells
MFE	Minimal free energy
MII	Metaphase ii
MK2	Mapk-activated protein kinase 2
MLKL	Mixed lineage kinase domain-like
MPO	Myeloperoxidase
mTNF	Membrane-bound tnf
MØs	Macrophages
n.s.	Not significant
NEMO	Nfkb essential modulator
NFkB	Nuclear factor kappa-light chain-enhancer of activated b cells
NGS	Next-generation sequencing
NHEJ	Non-homologous end-joining
NHPs	Non-human primates
NIK	Nfkb-inducing kinase
NLR	Nod-like receptor
NOD	Nucleotide-binding and oligomerization domain
NRE	New regulatory element
NUC	Nuclease
OCLN	Occludin
OD	Optical density
ORF	Open reading frame
OTU	Operational taxonomic unit
PAM	Protospacer-adjacent motif
PAMPs	Pathogen-associated molecular patterns
Pas/AB	Periodic acid/schiff-alcian blue

PBMC	Peripheral blood mononuclear cell
PBS	Phosphate-buffered saline
PCoA	Principal component analysis
PCR	Polymerase chain reaction
PFM	Porcine fertilisation medium
pKDNF	Porcine kidney fibroblasts
PolyB	Polymyxin b
PP	Peyer's patch
PPAR $\gamma$	Peroxisome proliferator-activated receptor gamma
PRRs	Pattern recognition receptors
PZM	Porcine zygote medium
RBP	Rna binding protein
REC	Recognition
RIPK	Receptor-interacting serine/threonine-protein kinase 1
RNA	Ribonucleic acid
RnP	Ribonucleoprotein
RPL	Ribosomal protein l
RSP	Ribosomal protein s28
RT-qPCR	Reverse transcriptase/real time-quantitative pcr
SCFA	Short-chain fatty acid
SCNT	Somatic cell nuclear transfer
SFB	Segmented filamentous bacteria
SG	Stress granule
SNP	Single nucleotide polymorphism
SSC	Side scatter
sTNF	Soluble tnf
TACE	Tnf converting enzyme
TAE	Tris-acetate-edta
TALEN	Transcription activator-like effector nuclease
TBE	Tris-borate-edta
Teff	T effector cell
TGF- $\beta$	Transforming growth factor $\beta$
TH	T helper cell
TIA-1	T-cell intracellular antigen-1
TIAR	Tia-1-related protein
TJ	Tight junction
TLO	Tertiary lymphoid structure
TLR	Toll-like receptor



TNBS	2,4,6-trinitrobenzene sulfonic acid
TNF	Tumor necrosis factor (alpha)
TNFR	Tnf-receptor
tracrRNA	Trans-activating crrna
TRADD	Tnfr1-associated dd
TRAF	Tnfr-associated factor
Treg	Regulatory t-cell
TTE	Tris-taurine-edta
TTP	Tristetraprolin
UC	Ulcerative colitis
UTR	Untranslated region
XIAP	X-linked inhibitor of apoptosis protein
ZFN	Zinc finger nuclease
Zfp	Zinc finger protein
ZO-1	Zona occludens-1
zOTU	Zero-radius otu

## List of figures

Figure 1: Schematic presentation of the small intestinal crypts. The intestinal microbiota and the goblet cell-derived and immunoglobulin A-rich mucus layer are separated by the single epithelial layer from the lamina propria harbouring the gut-associated lymphatic tissue (e.g. Peyer's patches) that senses the gut microbiota directly or indirectly through M-cell-mediated or -independent mechanisms. Lieberkühn-crypts are found throughout the gut and harbour a variety of stem cells, stem cell niche-supporting and antimicrobial peptide- (AMP) secreting cells. Adapted from "Small Intestine Villus Background (Layout)" by BioRender (2023). ..... 9

Figure 2: Differential chemical properties along the gastrointestinal tract favour the growth of specialized bacteria. The pH value and the amount of colony forming units (CFU) per mL increases from stomach to colon, while the oxygen partial pressure ( $pO_2$ ) is decreasing from stomach to colon. Adapted from Clarke et al., 2019<sup>13</sup>. ..... 10

Figure 3: Microbe-Host-Interactions in health and inflammatory bowel disease. In a healthy state, a diverse bacterial population that includes short chain-fatty acids (SCFA)-producing bacteria helps to maintain homeostasis between pro- and anti-inflammatory host responses. This balance is mediated by members of both the innate (such as dendritic cells (DCs) or macrophages (MΦs)) and adaptive immunity (such as T regulatory ( $T_{reg}$ ) or T effector cells ( $T_{eff}$ )), which in turn support the growth of these microorganisms. On the other hand, a dysbiotic state - which may be a cause or consequence of IBD - is characterised by a reduction in bacterial diversity and loss of often obligate facultative SCFA-producers. Dysbiosis fuels chronic pro-inflammatory processes that ultimately lead to impaired barrier integrity and dysfunctional intestinal tissue function. Adapted from "Compare and Contrast Layout - Healthy and Inflamed Epithelium" by BioRender (2023). ..... 13

Figure 4: TNF-mediated pleiotropic function in cell proliferation, cell death and the recruitment of immune cells. (Left) TNF receptor I (TNFRI) binding directly enhances inflammation by activating pro-inflammatory signalling pathways NF $\kappa$ B and p38, which result in the transcriptional upregulation of genes encoding proinflammatory mediators such as cytokines and chemokines. (Right) TNFRI activation also indirectly causes inflammation by inducing cell death. Damage-associated molecular patterns (DAMPs) are released by lytic forms of cell death such as apoptosis, necroptosis (or pyroptosis), which stimulate proinflammatory gene expression in bystander cells. Pattern recognition receptor, PRR. Adapted from van Loo et al., 2022<sup>78</sup>. ..... 16

Figure 5: Schematic view of the two splice variants of the murine Tnf gene. Blue boxes represent exons, light blue boxes mark 5' and 3' untranslated regions (UTRs). The red marking highlights the deletion of the ARE sequence. The extension shows the stop codon (TGA), as well as the AU-rich element (ARE), constitutive decay element (CDE), and the new regulatory element (NRE). The deletion of the ARE sequence is indicated by a red cross. Black lines between the exons represent introns. .... 17

Figure 6: SpCRISPR/Cas9-mediated double-strand break (DSB) results in the activation of two DNA repair pathways, Non-homologous end-joining (NHEJ) and Homology-directed repair (HDR). NHEJ is a highly error-prone repair mechanism, that frequently results in InDel formations. HDR results in

homologous template-based repair of disrupted DNA strands, which enables targeted mutations and knock-in of transgenes. Adapted from Esmée Dragt<sup>130</sup>. ..... 21

Figure 7: Somatic cell nuclear transfer is a cloning technique that involves the transfer of the nucleus from a somatic cell into an enucleated oocyte. The somatic cells are first genetically modified and selected based on the desired modification. Next, single cells are inserted into the perivitelline space of enucleated oocytes in metaphase II (MII)-phase. Electrofusion leads to the transfer of the somatic cell nucleus into the enucleated oocyte and the start of cell division. These reconstructed embryos can then be transferred to a surrogate mother to develop into a cloned offspring with the desired genetic characteristics. .... 23

Figure 8: Microinjection of gene editing vectors into porcine zygotes at the pronuclear stage. First, cumulus-oocyte-complexes (COCs) are aspirated from polycystic ovaries derived from slaughterhouse material. COCs are then in vitro matured (IVM) to the metaphase II (MII)-phase, indicated by polar body extrusion. Next, in vitro fertilisation (IVF) is performed, and zygotes are obtained (7-10 hours post IVF). Subsequently, the vector is microinjected into the cytoplasm in close proximity to the pronuclei, followed by in vitro cultivation (IVC). Microinjected embryos can either be cultured in vitro until the blastocyst stage (7 days) for genotyping and genotoxicity analyses or until the 2-cell stage (1-2 days) for embryo transfer into a surrogate mother to produce mutant offspring. .... 24

Figure 9: Porcine IL10 gene and transcript annotation deposits found in NCBI (A) and Ensemble (B) databases. The IL10 gene was found on porcine chromosome 9 on the reverse strand at position 67,405,777 bp to 67,405,372 bp. In NCBI, dark green boxes represent coding sequences, dark green lines represent introns, light green boxes represent untranslated regions, purple boxes represent exons found within transcripts and purple lines represent introns found within pre-mature transcripts. In Ensemble, red boxes represent coding sequences, red lines represent introns and empty red boxes represent untranslated regions. .... 66

Figure 10: Human IL10 gene and transcript annotation deposits found in NCBI database. The IL10 splice variants were found on human chromosome 1 on the reverse strand at position 206,767,602 bp to 206,772,494 bp (isoform #1) and at position 206,767,602 bp to 206,771,189 bp (isoform #2), respectively. Dark green boxes represent coding sequences, dark green lines represent introns, light green boxes represent untranslated regions, purple boxes represent exons found within transcripts and purple lines represent introns found within pre-mature transcripts. .... 67

Figure 11: Schematic representation of the potential (top) and known (bottom) splice variants of the porcine IL10 transcript. Shown are coding exons (Ex), the untranslated regions (UTRs) and selected primers for the qualitative assessment of the potential second splice variant. The potential second splice variant consists of exons 3-5 of the known splice variant. The primers were selected to amplify the sequence from the novel 5'-UTR in a potential splice variant but not in the known splice variant. Primers: (1) IL10\_IsoformCheck\_Fwd1, (2) IL10\_IsoformCheck\_Fwd2, (3) IL10\_IsoformCheck\_Rev1 and (3) IL10\_IsoformCheck\_Rev2. .... 67

Figure 12: Qualitative RT-PCR for the identification of a porcine alternative IL10 isoform using a cDNA pool derived from various porcine bulk RNA isolates.. Three primer combinations Check\_1, Check\_2 and Check\_3 were used to amplify a potential isoform. H<sub>2</sub>O served as negative control, while the amplification of the actin gene served as positive control. (M) Log2-Marker indicates band sizes. .... 68

Figure 13: Schematic view of the porcine IL10 gene and selected gRNA candidates. Shown are the 3' and 5' untranslated regions (UTR) and exons (Ex) 1-5 represented as boxes. The expanded view shows the base pair sequence of exon 1. Selected gRNA candidate target sequences are marked in red with their respective PAM site marked in purple. .... 69

Figure 14: Schematic view of the porcine IL10 gene and selected gRNAs. Shown are the 3' and 5' untranslated regions (UTR), exons (Ex) 1-5 represented as pink boxes and the excised sequence represented as green box. The expanded view shows the base pair sequence of exon 1. Selected gRNA target sequences are marked in red with their respective PAM site marked in purple. The insertion of a thymidine molecule (Insertion +T) and the deleted sequence are marked in green. The Sanger sequencing result is shown at the bottom. A mismatch to the reference genome is highlighted by a darker coloration. .... 70

Figure 15: Wild-type (WT) and mutant ( $\Delta$ gRNA\_2/1+ gRNA\_3/1) versions of the base pair and amino acid sequences of exon 1 of the IL10 gene. .... 70

Figure 16: Genotyping PCR using primers IL10\_Check\_F2 and IL10\_Check\_R1 of genome edited and wild-type blastocysts following sham-microinjection and microinjection of gRNA 2/1 + 3/1 RnP complexes into in vitro derived zygotes. Expected size for the amplified wild-type IL10 fragment 674 bp, for IL10<sup>A</sup> 627 bp. M, size marker. CTRL, control template. Genotypes are annotated below the respective blastocyst number..... 71

Figure 17: Plasmid map of the CRISPR/Cas9 vector used for the generation of TNF <sup>$\Delta$ ARE</sup> pigs. The plasmid is encoding two gRNAs, gRNA 5' and gRNA 3', each under the control of a separate U6 promoter (U6 prom) and the Cas9 protein under the control of a CAG promoter (CAG enhancer). The plasmid additionally encodes puromycin N-acetyltransferase (Puro), which is co-expressed with Cas9 through T2A-mediated ribosome skipping and enables selection of eukaryotic cells with puromycin, and a beta-lactamase (Amp), which enables selection of prokaryotic cells with ampicillin. .... 72

Figure 18: Strategy for the deletion of ARE and CDE1 in TNF by CRISPR/Cas9-based gene editing. The 3' UTR and the deleted sequence with the gRNA binding sites (marked in green) are shown in the enlarged view. The excised sequence (93 bp) is highlighted in orange, and the ARE, CDE, and NRE elements are displayed as boxes..... 72

Figure 19: Genotyping PCR using primers TNF\_Check\_F2 and TNF\_Check\_R2 of genome edited and wild-type blastocysts. Expected size for the amplified wild-type TNF fragment 524 bp, for the mutated TNF <sup>$\Delta$ ARE</sup> sequence 431 bp. M, size marker. CTRL, control. Genotypes are annotated below the respective blastocyst number..... 73

Figure 20: Sanger sequencing showing the wild-type and mutated ARE/CDE1 sequence. gRNA binding sites are marked in green..... 73

Figure 21: Genotyping PCR of genome edited founder piglets (Pigs# 1688-1694 from 1 of 2 founding litters born). M, size marker, predicts a size of 524 bp for the amplified wild-type TNF fragment and 431 bp for TNF<sup>ΔARE</sup>. CTRL, Control. The genotypes are indicated below the respective animal number... 74

Figure 22: Wild-type, SNP- and ΔARE sequence and RNAfold-predicted RNA structure of the TNF transcript. Color scale shows calculated base-pair probabilities. .... 75

Figure 23: Qualitative PCR for the assessment of potential random integration of the puromycin-N-acetyltransferase gene into the porcine genome. M, size marker. CTRL, control..... 76

Figure 24: Overview of identified SNPs in the TNF gene. Dark blue boxes represent exons, light blue boxes mark 5' and 3' untranslated region (UTR). The ARE/CDE1 sequence is marked in red. The extension shows the stop codon (TGA), and the ARE, CDE1, CDE2, ADE and NRE elements. Black lines between the exons are representing introns. The position and type of SNPs are indicated..... 77

Figure 25: Representative sanger sequencing result of offspring with (bottom) and without (top) inherited mutations in close proximity to the ARE/CDE region. Mutations are highlighted in red. .... 77

Figure 26: Sex distribution of genotypes. Shown are the total number of pigs n (top), the number of wild-types (WT), TNF<sup>ΔARE/+</sup> (ΔA/+) and TNF<sup>ΔARE/ΔARE</sup> pigs (ΔA/ΔA), regardless of further mutations (e.g. including APC<sup>1311/+</sup>x TNF<sup>ΔARE/+</sup>). The numbers of pigs showing an early disease onset per pigs with the same genotype are shown in brackets, only TNF<sup>ΔARE/+</sup> or TNF<sup>ΔARE/ΔARE</sup> pigs were considered (e.g. excluding TNF<sup>ΔARE/+</sup>xAPC<sup>1311/+</sup>)..... 78

Figure 27: Phylogenetic tree visualizing sex, geno- and phenotype distribution for representative litters 1904-1910, 1933-1945 and 2360-2370. .... 79

Figure 28: Wild-type, heterozygous, and homozygous TNF<sup>ΔARE</sup> siblings' weight [kg] ranged from 16 to 39 days..... 80

Figure 29: Kaplan-Meier diagram showing the time at which the animals were killed due to their declining health status. Indicated are the mean survival times for TNF<sup>ΔARE/+</sup> and TNF<sup>ΔARE/ΔARE</sup> pigs that had to be killed. The time point of weaning is indicated at 35 days..... 80

Figure 30: Frequent macroscopic gastrointestinal findings in diseased TNF<sup>ΔARE</sup> pigs. (A) Colonic “creeping” fat patches and (B) a generally more vascularized phenotype were observed frequently. (C) Intestinal mucosal tissue was found to be highly (left) or intermediate (middle) inflamed compared to wild-type tissue (right). (D) Mesenteric lymph nodes were found to be swollen (left) compared to wild-type lymph nodes (right). (E) Stricturing of the small intestine was frequently observed. Size bars are shown..... 81

Figure 31: Representative results from a (left) positive and (right) negative occult test using faecal samples. The presence of blood in the sample leads to a colour change from colourless to blue. .... 82

Figure 32: Illustration of the intestinal tract and areas of inflammation. Increased inflammation is indicated by darker red coloring..... 82

Figure 33: Images showing the inflamed large and small bowel. In the large intestine, there were continuous macroscopically visible symptoms of inflammation; in the small intestine, these signs were segmental..... 83

Figure 34: Crust formation in the caecum of a  $TNF^{\Delta ARE/\Delta ARE}$  pig. The crust was found to consist of diphetic membranes..... 83

Figure 35: Image of a spinal cord of a severely diseased  $TNF^{\Delta ARE/\Delta ARE}$  animal that has been freed from muscle and fat tissue, and ribs. Size bar displays reference size. .... 84

Figure 36: Necrotic colonic mucosal tissue specimen of a severely diseased  $TNF^{\Delta ARE/+}$  animal. Corresponding H&E-stained tissue section is shown. Herniation of crypts and fibrinous exudates are shown in this tissue section..... 85

Figure 37: Representative images of H&E-stained colonic and ileal gut sections. Shown are non-inflamed (left), mildly (middle) and highly inflamed (right) tissue sections of the colon (top) and ileum (bottom). Bars indicate 500  $\mu m$ ..... 86

Figure 38: Image of H&E-stained colonic tissue section with invasive *Balantidium Coli*. Arrows show bacterial localization. Size bars display reference size. Evaluation was performed by Dr. Katja Steiger. .... 86

Figure 39: Western Blot sections displaying band intensities for ZO-1 (top), Occludin (middle) and GAPDH (bottom) for colonic tissue isolates from three wild-type, three  $TNF^{\Delta ARE/+}$  and  $TNF^{\Delta ARE/\Delta ARE}$  swine. .... 87

Figure 40: (Top) Confocal laser scanning microscopy images of occludin and (bottom) ZO-1 immunofluorescence stainings (red) of healthy and highly inflamed colonic tissue, additionally stained with DAPI (blue). Scale bars indicate 100  $\mu m$ . Original signal intensities were adjusted for clear visualization of defined or diffuse antigen localization. Signals captured from tissue sections stained with secondary antibodies and DAPI only served as control. .... 87

Figure 41: Representative images of immune-histological stainings of wild-type,  $TNF^{\Delta ARE/+}$  and  $TNF^{\Delta ARE/\Delta ARE}$  colonic tissue sections. Scale bars indicate 200  $\mu m$ ..... 88

Figure 42: Statistical evaluation of mucosal thickness layer measured from muscularis mucosa to the epithelium for various tissue sections from wild-type,  $TNF^{\Delta ARE/+}$  and  $TNF^{\Delta ARE/\Delta ARE}$  swine. .... 89

Figure 43: Heatmap of the complete blood count of  $TNF^{\Delta ARE/+}$  and  $TNF^{\Delta ARE/\Delta ARE}$  pigs in comparison to wild-type siblings (n=3). GOT: glutamate-oxalacetate-transaminase; GLDH: glutamate-dehydrogenase; GGT:  $\gamma$ -Glutamyl-Transferase; Billi: Bilirubin; AP: alkaline phosphatase; Chol.: cholesterol; TP: total protein; ALB: albumin; RBC: red blood cells; HCT: haematocrit; HGB: haemoglobin; MCV: mean corpuscular volume; MCHC: Mean corpuscular haemoglobin concentration; RDW: red cell distribution; RETIC: reticulocyte; WBC: white blood cell; NEU: neutrophils; LYM: lymphocytes; MONO: monocytes; EOS: eosinophils; BASO: basophils; PLT: platelets; MPV: mean platelet volume; PCT: procalcitonin. \*, significant difference. .... 90

Figure 44: Workflow and pipetting scheme for the analysis of TNF transcript half-lives. EDTA-blood was isolated from the vena jugularis, followed by ficoll-gradient centrifugation to isolate PBMCs. PBMCs were cultured for seven days at 37 °C on a bacteriological petri dish in the presence of poGM-CSF1 before cells were transferred onto a 12-well culture plate in equal cell numbers. Cells were incubated with LPS alone, LPS+Polymyxin B or LPS+Actinomycin D for 0, 45 or 90 minutes. X, wells not used. .... 92

Figure 45: Determination of TNF mRNA levels and half-lives in macrophages from TNF<sup>ΔARE</sup> and wild-type pigs. Macrophages were subject to LPS challenge, followed by co-incubation with the global transcription inhibitor actinomycin D. Extended view shows percentage of TNF transcript levels at time points 90 minutes (after 45 min of co-incubation with actinomycin D) and 45 minutes (before the addition of actinomycin D). .... 93

Figure 46: TNF, IL-6, and IL-8 mRNA levels in intestinal tissue samples shown as log<sub>2</sub> multiples of the average wild-type value. Caec., Caecum; Duod., Duodenum; Jej., Jejunum..... 94

Figure 47: Expression of TNF and GAPDH proteins in ileal (bottom) and colonic (top) samples from 3 wild-type, 3 TNF<sup>ΔARE/+</sup>, and 3 TNF<sup>ΔARE/ΔARE</sup> pigs, respectively. M, size marker. .... 95

Figure 48: Gating strategy for flow cytometry analysis of CD3<sup>+</sup> cell subsets. (From left to right) Viable cells were selected based on low viability dye signal that incorporates into dead cells. Viable cells were further gated based on equal FSC-H/FSC-A-ratio to select single cells. The lymphocyte cell population was selected from viable, single cells based on a characteristic SSC-A/FSC-A-ratio. CD3<sup>+</sup> cells were selected from viable, single lymphocytes based on a high CD3 signal intensity..... 95

Figure 49: Viable, single lymphocyte and monocyte cell populations in (top) wild-type and (bottom) inflamed TNF<sup>ΔARE</sup> pigs. Gates and cell ratios of the gate are shown..... 96

Figure 50: Gating strategy for flow cytometry analysis of TNF<sup>+</sup>CD3<sup>+</sup> viable single lymphocytes of PBMCs derived from 3 wild-type, 3 TNF<sup>ΔARE/+</sup>, and 3 TNF<sup>ΔARE/ΔARE</sup> swine (top) and statistical analysis (bottom). .... 97

Figure 51: Statistical analysis of CD3<sup>+</sup>/CD4<sup>+</sup>/CD8<sup>-</sup> (top left), CD3<sup>+</sup>/CD4<sup>-</sup>/CD8<sup>+</sup> (top right), CD3<sup>+</sup>/CD4<sup>+</sup>/CD8<sup>+</sup> (bottom left), CD3<sup>+</sup>/CD4<sup>-</sup>/CD8<sup>-</sup> (bottom right) cell subsets derived from 3 wild-type, 3 TNF<sup>ΔARE/+</sup>, and 2 TNF<sup>ΔARE/ΔARE</sup> swine. .... 98

Figure 52: Statistical analysis of TNF<sup>+</sup>CD4<sup>+</sup>CD8<sup>+</sup>, TNF<sup>+</sup>CD4<sup>-</sup>CD8<sup>+</sup>, TNF<sup>+</sup>CD4<sup>+</sup>CD8<sup>-</sup>, and TNF<sup>+</sup>CD4<sup>-</sup>CD8<sup>-</sup> viable single lymphocytes derived from 3 wild-type, 3 TNF<sup>ΔARE/+</sup>, and 2 TNF<sup>ΔARE/ΔARE</sup> swine. .... 99

Figure 53: Gating strategy for flow cytometry analysis of TNF<sup>+</sup>/CD3<sup>+</sup>/CD4<sup>+</sup>/CD25<sup>+</sup>/FOXP3<sup>+</sup> viable, single lymphocytes of PBMCs derived from 3 wild-type, 3 TNF<sup>ΔARE/+</sup>, and 2 TNF<sup>ΔARE/ΔARE</sup> swine (top) and statistical analysis (bottom). .... 100

Figure 54: Statistical evaluation of for flow cytometry analysis of TNF<sup>+</sup>/CD3<sup>+</sup>/CD4<sup>+</sup>/Tbet<sup>+</sup> viable, single lymphocytes of PBMCs derived from 3 wild-type, 3 TNF<sup>ΔARE/+</sup>, and 2 TNF<sup>ΔARE/ΔARE</sup> swine. .... 101

Figure 55: Gating strategy for flow cytometry analysis of TNF <sup>+</sup> /CD3 <sup>+</sup> /TCR15 <sup>+</sup> viable, single lymphocytes of PBMCs derived from 3 wild-type, 3 TNF <sup>ΔARE/+</sup> , and 2 TNF <sup>ΔARE/ΔARE</sup> swine (top) and statistical analysis (bottom). .....	101
Figure 56: Gating strategy for flow cytometry analysis of TNF <sup>+</sup> /CD3 <sup>+</sup> /CD4 <sup>+</sup> /CD8 <sup>+</sup> /IFN $\gamma$ <sup>+</sup> viable, single lymphocytes of PBMCs derived from 3 wild-type, 3 TNF <sup>ΔARE/+</sup> , and 2 TNF <sup>ΔARE/ΔARE</sup> swine (top) and statistical analysis (bottom). .....	102
Figure 57: Overview of analysed porcine, murine and human samples for microbiome analysis. ....	104
Figure 58: Alpha-Diversity analysis (Shannon effective) of five randomly selected luminal, tissue, stool, and polyp samples with ambient air, buffer, and washing solution controls. ....	105
Figure 59: Taxonomic binning of phyla showing taxonomic differences between luminal samples derived from various intestinal sections. ....	105
Figure 60: Shannon effective number of small and large intestinal luminal samples derived from wild-type pigs. ....	106
Figure 61: PCoA plot of microbial profiles derived from luminal rectal, colonic, caecal, ileal, jejunal and duodenal samples stratified by tissue sections. The separation of luminal colon and small intestine samples is highlighted by framing the respective samples. ....	106
Figure 62: PCoA plot of microbial profiles derived from tissue rectal, colonic, caecal, ileal, jejunal and duodenal samples stratified by tissue sections. ....	107
Figure 63: Taxonomic binning of phyla showing taxonomic differences between tissue samples derived from various intestinal sections. ....	107
Figure 64: Venn Diagram showing the absolute amount of shared and exclusive zOTUs between luminal and tissue samples. ....	108
Figure 65: LEfSe analysis of luminal and tissue microbiomes from wild-type samples. The bar lengths illustrate logarithmic fold-changes of differentially abundant genera. The respective LDA linear discriminant analysis score is shown. ....	108
Figure 66: Taxonomic binning of phyla showing taxonomic differences between luminal and tissue samples derived from various intestinal sections. ....	109
Figure 67: Shannon effective numbers of stool, intestinal tissue-associated and luminal bacteria derived from wild-type pigs. ....	110
Figure 68: PCoA plot of microbial profiles derived from stool, tissue and luminal samples stratified by sample type. ....	110
Figure 69: Venn Diagram showing the absolute amount of shared and exclusive zOTUs between stool, and large intestinal (rectum, colon, caecum) or small intestinal (ileum, jejunum, duodenum) luminal and tissue samples derived from wild-type pigs. A brighter color indicates a larger overlap. ....	111



Figure 70: Explained variation plot representing individual groups that are plotted over their negative log 10 p-value and R<sup>2</sup> value derived from a confounding analysis. P-values and R<sup>2</sup> values are shown. .... 112

Figure 71: Taxonomic phylogenetic tree of microbes in upper and lower gastrointestinal tract (GIT), stool, and tissue biopsy samples from pigs of different genotypes (#1-23). The tree is color-coded to represent the samples' association with the biopsy location (upper/lower gastrointestinal tract and stool), genotype (Wild-type, TNF<sup>ΔARE/+</sup>, TNF<sup>ΔARE/ΔARE</sup>), and pig number (#1-23). This plot was generated by Dr. Amira Metwaly. .... 114

Figure 72: Taxonomic Distribution of microbes in faecal, ileal, and colonic tissue biopsy samples from wild-type, TNF<sup>ΔARE/+</sup> and TNF<sup>ΔARE/ΔARE</sup> pigs. The color-coded representation of the phyla present in each sample is described in the accompanying legend. Modified from Dr. Amira Metwaly's plot. .... 115

Figure 73: Shannon effective numbers of faecal or duodenal, jejunal, ileal, caecal, colonic, or rectal tissue samples derived from wild-type, TNF<sup>ΔARE/+</sup> and TNF<sup>ΔARE/ΔARE</sup> swine. Modified from Dr. Amira Metwaly's plot. .... 116

Figure 74: PCoA plots of microbial profiles derived from faecal (top left), colonic (top middle), caecal (top right), ileal (bottom left), jejunal (bottom middle), and duodenal (bottom right) tissue samples stratified by genotype. .... 117

Figure 75: Considered factors for the determination of health status in mutant pigs were the age at the onset of disease (top left), the general appearance (top right), macroscopic intestinal findings, such as vascularization (bottom left and middle) and hemorrhagic coloration (bottom right). .... 118

Figure 76: Heatmap showing potential confounding factors for specific variables. Confounding factors are highlighted in yellow. R<sup>2</sup> values of confounding factors are shown. .... 119

Figure 77: PCoA plots of microbial profiles derived from stool samples stratified by weaning state of wild-type and mutant pigs. .... 120

Figure 78: Shannon effective numbers for microbial ecosystems derived from faecal samples of wild-type TNF<sup>ΔARE/+</sup>, and TNF<sup>ΔARE/ΔARE</sup> pigs pre-, during and post-weaning. .... 120

Figure 79: Significantly differentially abundant genera found in faecal samples of wild-type TNF<sup>ΔARE/+</sup>, and TNF<sup>ΔARE/ΔARE</sup> pigs pre-, during and post-weaning identified by Wilcoxon testing with Bonferroni correction for multiple testing. .... 121

Figure 80: Time-series-analysis of phylum abundances in faecal samples derived from wild-type TNF<sup>ΔARE/+</sup>, and TNF<sup>ΔARE/ΔARE</sup> pigs. .... 122

Figure 81: Bristol Stool Scores of faecal samples from wild-type TNF<sup>ΔARE/+</sup>, and TNF<sup>ΔARE/ΔARE</sup> pigs at two consecutive time points, 50 and 75 days (left) and a correlation analysis for Bristol stool scores and respective faecal calprotectin protein concentrations (right). .... 123

Figure 82: Calprotectin protein concentrations measured in faecal samples from TNF<sup>ΔARE/+</sup> swine at two consecutive timepoints, t1 (50 days of age) and t2 (75 days of age). Samples were colored according

to a high or low inflammatory group depending on the calprotectin protein concentration at t2 (threshold 30ng/ml). ..... 124

Figure 83: PCoA plot of faecal samples derived from from TNF<sup>ΔARE/+</sup> swine stratified based on their faecal calprotectin protein levels. Samples were grouped as highly (“High”) or low inflamed (“Low”) based on their Calprotectin protein levels (threshold for High: 30 ng/ml). ..... 124

Figure 84: PCoA plot of faecal samples derived from from TNF<sup>ΔARE/+</sup> swine stratified based on their faecal calprotectin protein levels and the respective timepoint of sampling, T1 (50 days of age) and T2 (75 days of age). Samples were grouped as highly (“HI”) or mildly inflamed (“MI”) based on their Calprotectin protein levels at timepoint t2 (threshold for HI: 30 ng/ml). ..... 125

Figure 85: Significantly differentially abundant genera found between healthy, diseased and intermediately inflamed faecal (left) and tissue samples (right) identified by Wilcoxon testing with Bonferroni correction for multiple testing. .... 126

Figure 86: Wilcoxon test with Bonferroni correction of multiple testing for differentially abundant genera in stool obtained from TNF<sup>ΔARE/+</sup> pigs in a pre-weaning, during-weaning and post-weaning state (left) and PCoA plot showing samples stratified based on the weaning state (right). ..... 127

Figure 87: Plot comparing the abundance of different zOTUs in healthy and highly inflamed TNF<sup>ΔARE/+</sup> pigs across various segments of the intestinal tissue, with the negative logarithm of the corrected p-value plotted against the respective tissue segment. Two segments of the duodenum are included: the duodenum and the duodenum (stricture), which differ in macroscopically observable tissue affection, with the latter resulting from fibrotic, structuring tissue. Dotted lines are used to highlight the significance levels. .... 128

Figure 88: Phylogenetic tree visualizing the similarity of microbiota patterns in luminal (n=61) and mucosa-associated (n=166) microbiota from 23 pigs (7 wild-type, and 16 TNF<sup>ΔARE</sup>), based on generalized UniFrac distances. Around the phylogram, stacked bar plots are used to display the taxonomic composition of each each phylum. The innermost ring displays stratification according to sample type, with upper gastrointestinal tract (GIT) samples (blue) and lower GIT and stool samples (brown) and denoted by (\*); the second ring displays stratification according to genotype, with wild-type (grey), TNF<sup>ΔARE/+</sup> (pink), and TNF<sup>ΔARE/ΔARE</sup> (green) and denoted by (\*\*). Samples from each pig are shown by (\*\*\*) as bars in the outside ring of the figure. Plot generated by Dr. Amira Metwaly. .... 129

Figure 89: Shannon effective numbers of faecal samples derived from wild-type and TNF<sup>ΔARE/+</sup> mice, and wild-type, TNF<sup>ΔARE/+</sup> and TNF<sup>ΔARE/ΔARE</sup> pigs. Modified based on Dr. Amira Metwaly’s plot. .... 129

Figure 90: Venn Diagram showing the absolute amount of shared and exclusive zOTUs between porcine and murine faecal samples. A brighter color indicates a larger zOTU count. .... 130

Figure 91: MDS plot of porcine and murine faecal samples derived from wild-type, TNF<sup>ΔARE/+</sup> and TNF<sup>ΔARE/ΔARE</sup> individuals. Closely clustering sample subsets are highlighted by an orange rectangle. Modified based on Dr. Amira Metwaly’s plot. .... 130

Figure 92: Shannon effective number of porcine and murine faecal samples derived from wild-type,  $TNF^{\Delta ARE/+}$  and  $TNF^{\Delta ARE/\Delta ARE}$  individuals that either cluster (“Yes”) or do not cluster (“No”) together on a MDS plot..... 131

Figure 93: Venn diagram showing exclusively shared zOTUs between murine and porcine faecal samples that either cluster (“Yes”) or do not cluster close together (“No”) on a MDS plot. A brighter color indicates a higher zOTU count..... 132

Figure 94: Shannon effective numbers of faecal, luminal and tissue samples derived from human IBD patients, and wild-type,  $TNF^{\Delta ARE/+}$  and  $TNF^{\Delta ARE/\Delta ARE}$  pigs. Modified based on Dr. Amira Metwaly’s plot. .... 132

Figure 95: Venn diagram showing exclusive and shared zOTUs between faecal, luminal, and tissue samples derived from porcine wild-type and mutant pigs and human IBD patients. .... 133

Figure 96: Phylogenetic tree that compares the microbiota profiles of faecal, luminal and tissue samples derived from wild-type and  $TNF^{\Delta ARE}$  pigs and human IBD patients to each other using generalized UniFrac distances. As stacked bar plots around the phylogram, the individual taxonomic makeup at the phylum level is displayed. The outside ring displays stratification based on genotype, wild-type (grey),  $TNF^{\Delta ARE/+}$  (red), and  $TNF^{\Delta ARE/\Delta ARE}$  (green). The innermost ring displays stratification depending on species, either human (pink) or pig (black). This plot was generated by Dr. Amira Metwaly. .... 133

Figure 97: PCoA plot of faecal samples derived from human CD patients with inactive or active disease or at the time of HPSCT-treatment and wild-type,  $TNF^{\Delta ARE/+}$  and  $TNF^{\Delta ARE/\Delta ARE}$  pigs stratified by genotype (or disease activity state, respectively). .... 134

Figure 98: Shannon effective numbers of faecal samples derived from human IBD patients with inactive or active disease or at the time of HPSCT-treatment and wild-type,  $TNF^{\Delta ARE/+}$  and  $TNF^{\Delta ARE/\Delta ARE}$  pigs that either cluster (“Yes”) or do not cluster close together (“No”) on a PCoA plot. .... 135

Figure 99: Shannon effective numbers of faecal samples derived from human IBD patients, wild-type and  $TNF^{\Delta ARE/+}$  mice, and wild-type,  $TNF^{\Delta ARE/+}$  and  $TNF^{\Delta ARE/\Delta ARE}$  pigs. .... 136

Figure 100: PCoA plot of faecal samples derived from human IBD patients, wild-type and  $TNF^{\Delta ARE/+}$  mice, and wild-type,  $TNF^{\Delta ARE/+}$  and  $TNF^{\Delta ARE/\Delta ARE}$  pigs stratified by their respective species. .... 137

Figure 101: Venn diagram showing exclusive and shared zOTUs of faecal samples derived from human IBD patients, wild-type and  $TNF^{\Delta ARE/+}$  mice, and wild-type,  $TNF^{\Delta ARE/+}$  and  $TNF^{\Delta ARE/\Delta ARE}$  pigs. A brighter color indicates a higher zOTU count. .... 137

Figure 102: PCoA plot of faecal samples derived from human IBD patients, wild-type and  $TNF^{\Delta ARE/+}$  mice, and wild-type,  $TNF^{\Delta ARE/+}$  and  $TNF^{\Delta ARE/\Delta ARE}$  pigs stratified by their respective species. Closely clustering sample subsets are highlighted by a purple rectangle. .... 138

Figure 103: Shannon effective numbers of faecal samples derived from human IBD patients, wild-type and  $TNF^{\Delta ARE/+}$  mice, and wild-type,  $TNF^{\Delta ARE/+}$  and  $TNF^{\Delta ARE/\Delta ARE}$  pigs that either cluster (“Yes”) or do not cluster (“No”) close together on a PCoA plot. .... 138

Figure S1: Sanger-sequencing results for the exon 1 of the porcine IL10 gene derived from five randomly selected wild-type pigs (lower rows) compared to the NCBI gene deposit (top). The reference gene additionally shows its amino acid code. The Sanger sequencing quality is shown for each base. A deletion is indicated at position 47 bp upstream of the start codon (ATG) by a highlighted “-“..... 147

Figure S2: Complete Western blot images for Occludin (top) and ZO-1 (bottom) for colonic tissue isolates from three wild-type, three TNF $\Delta$ ARE/+ and TNF $\Delta$ ARE/ $\Delta$ ARE swine. Band locations and sizes of ZO-1 and Occludin are indicated. M, size marker. .... 148

Figure S3: Statistical analysis of immunohistochemically stained tissue sections from wild-type, TNF $\Delta$ ARE/+ and TNF $\Delta$ ARE/ $\Delta$ ARE pigs. The results demonstrate an increase in Ki67+, CD3+, and IBA1+ cells and a decrease in Pas/AB+ cells. .... 149

Figure S4: Determination of TNF mRNA levels and half-lives in macrophages from TNF $\Delta$ ARE and wild-type pigs. Macrophages were subject to LPS challenge alone or LPS+Polymyxin B, followed by co-incubation with actinomycin D from time point 45 minutes to 90 minutes. Untreated macrophages served as control (dotted lines)..... 151

Figure S5: NF $\kappa$ B transcript levels of macrophages from wild-type and TNF $\Delta$ ARE swine. Transcript levels at timepoints 0 minutes and 90 minutes of incubation with LPS were compared within and between groups..... 152

Figure S6: TNF mRNA levels in extra-intestinal samples shown as log2 multiples of the average wild-type value. Caec., Caecum; Duod., Duodenum; Jej., Jejunum. .... 152

Figure S7: Flow cytometric analysis of viable, single PBMC-derived cell subsets from wild-type, TNF $\Delta$ ARE/+ and TNF $\Delta$ ARE/ $\Delta$ ARE swine showing enhanced ratio of the FSChigh/SSChigh cell subset in mutant animals (top). Gating on this cell subset enabled the identification of increased numbers of CD172a+ (second) and CD14+ (third) cells, whereas gating on lymphocyte-characteristic FSC/SSC-ratios revealed a decreased number of CD3+ cells (bottom) in mutant pigs. Statistical evaluation is shown next to respective representative gates..... 153

Figure S8: Gating strategy for flow cytometry analysis of TNF+CD4+CD8+, TNF+CD4-CD8+, TNF+CD4+CD8-, and TNF+CD4-CD8- viable single lymphocytes of PBMCs derived from 3 wild-type, 3 TNF $\Delta$ ARE/+, and 2 TNF $\Delta$ ARE/ $\Delta$ ARE swine. .... 154

Figure S9: Statistical evaluation of for flow cytometry analysis of TNF+/CD3+/CD4+/Tbet+ viable, single lymphocytes of PBMCs derived from 3 wild-type, 3 TNF $\Delta$ ARE/+, and 2 TNF $\Delta$ ARE/ $\Delta$ ARE swine. In addition to results from the PHA-treated immune cells group (left), results from the non-treated group are shown (right). .... 155

Figure S10: MDS plot of microbial profiles derived from tissue and luminal rectal, colonic, caecal, ileal, jejunal and duodenal samples stratified by sample type (top) and tissue sections (bottom)..... 156

Figure S11: Venn Diagram showing the absolute amount of shared and exclusive zOTUs between stool, luminal and tissue samples. A brighter color indicates a larger overlap..... 157

Figure S12: LEfSe analysis of stool, luminal and tissue microbiomes from wild-type samples. The bar lengths illustrate logarithmic fold-changes of differentially abundant genera. The respective LDA linear discriminant analysis score is shown. ....	157
Figure S13: Differentially abundant genera in wild-type luminal, faecal and biopsy tissues. ....	160
Figure S14: MDS plots of microbial profiles derived from tissue biopsy and faecal samples stratified by gender (top left) and age group (bottom left) and respective shannon effective numbers displaying alpha-diversity of samples stratified by gender (top right) and age group (bottom right). ....	162
Figure S15: Differentially abundant genera in female and male wild-type tissue biopsies. ....	162
Figure S16: Differentially abundant genera in female and male wild-type faecal samples. ....	163
Figure S17: LEfSe analysis plot of microbial taxonomic differences in stool (top), ileal tissue (mid), and colonic tissue biopsy samples (bottom) from mutant pigs (red) and wild-types (blue). The plot shows the differentially abundant taxa and the respective linear discriminant analysis score. ....	165
Figure S18: Venn Diagram showing the absolute amount of shared and exclusive zOTUs between colonic (top) and ileal (bottom) tissue samples derived from wild-type and TNF $\Delta$ ARE swine. A brighter color indicates a larger overlap. ....	166
Figure S19: MDS plots of microbial profiles derived from colonic (top left), caecal (top middle), ileal (top right), jejunal (bottom left), duodenal (bottom middle) and all combined (bottom right) tissue samples stratified by genotype. ....	167
Figure S20: Venn Diagram showing the absolute amount of shared and exclusive zOTUs between colonic (top left), ileal (top right) and all combined (bottom) tissue samples derived from wild-type and TNF $\Delta$ ARE swine. A brighter color indicates a larger overlap. ....	168
Figure S21: Pearson's correlation analysis for the health status (inflammation) of an individual vs. the amount of Pas/AB+ per crypt length and vs. the ratio of IBA1+ to IBA- cells in the lamina propria measured in this pig. Shown are individual sample-specific values, lower and upper boundaries of the predicted interval, as determined using the R function predict, and the linear fitted line. ....	169
Figure S22: MDS plots of microbial profiles derived from faecal, luminal and tissue samples of male and female swine. ....	169
Figure S23: LEfSe analysis plot of microbial taxonomic differences in stool samples pre-, during and post-weaning from mutant pigs and wild-types. The plot shows the differentially abundant taxa and the respective linear discriminant analysis score. ....	170
Figure S24: Duodenal section of a heavily inflamed TNF $\Delta$ ARE/+ pig. The image includes two areas of the tissue, one of which is macroscopically unaffected and is indicated by a black arrow, while the other is fibrotic and structuring, indicated by a red arrow. ....	170
Figure S25: LEfSe analysis of faecal samples derived from wild-type, TNF $\Delta$ ARE/+ and TNF $\Delta$ ARE/ $\Delta$ ARE pigs and TNF $\Delta$ ARE/+ mice The plot shows the differentially abundant taxa and the respective linear discriminant analysis score. ....	171

FigureS26: LEfSe analysis plot of microbial taxonomic differences in porcine and murine faecal samples derived from wild-type, TNFΔARE/+ and TNFΔARE/ΔARE individuals that either cluster (“Yes”) or do not cluster (“No”) together on a PCoA plot. The plot shows the differentially abundant taxa and the respective linear discriminant analysis score. .... 172

Figure S27: Selection of results from Wilcoxon test with Bonferroni correction for multiple testing identifying significantly differentially abundant genera between human IBD patients with inactive or active disease or at the time of HPSCT-treatment and wild-type, TNFΔARE/+ and TNFΔARE/ΔARE pigs that shows relatively high levels of genera in both TNFΔARE/ΔARE pigs and patients with active disease. .... 173

Figure S28: Venn diagram showing the counts of shared and exclusive zOTUs between faecal samples derived from human IBD patients with inactive or active disease or at the time of HPSCT-treatment and wild-type, TNFΔARE/+ and TNFΔARE/ΔARE pigs. Results relevant for the analysis are shown. A brighter color indicates a higher zOTU count. .... 173

Figure S29: LEfSe analysis of faecal samples derived from human IBD patients with inactive or active disease or at the time of HPSCT-treatment and wild-type, TNFΔARE/+ and TNFΔARE/ΔARE pigs that either cluster (“Yes”) or do not cluster close together (“No”) on a PCoA plot. The plot shows the differentially abundant taxa and the respective linear discriminant analysis score. .... 174

Figure S30: LEfSe analysis of faecal samples derived from human IBD patients, wild-type and TNFΔARE/+ mice, and wild-type, TNFΔARE/+ and TNFΔARE/ΔARE pigs that either cluster (“Yes”) or do not cluster close together (“No”) on a PCoA plot. The plot shows the differentially abundant taxa and the respective linear discriminant analysis score. .... 175

## List of tables

Table 1: Laboratory equipment .....	26
Table 2: Consumables .....	28
Table 3: Chemicals .....	29
Table 4: Enzymes and enzyme buffers.....	34
Table 5: Antibodies .....	35
Table 6: Kits .....	37
Table 7: Prokaryotic cells .....	38
Table 8: Eukaryotic cells .....	38
Table 9: Primers.....	39
Table 10: gRNA oligonucleotides.....	41
Table 11: Molecular cloning vectors and DNA constructs .....	41
Table 12: Software and webtools.....	42
Table 13: Length and molecular weight standards .....	43
Table 14: Buffers and solutions .....	43
Table 15: Components for restriction digest .....	47
Table 16: Components for DNA ligation .....	48
Table 17: Pipetting scheme for GoTaq-PCR. Shown is the pipetting scheme for a single reaction.....	48
Table 18: GoTaq-PCR program. Duration of denaturation within the cycle is determined by the origin of template DNA, 30" for plasmids and 45" for genomic DNA. Duration of elongation within the cycle is determined by template DNA size. ....	49
Table 19: Pipetting scheme for Eurofinsgenomics-sequence samples.....	50
Table 20: Clinical parameters for severity scoring for pigs predisposed to IBD. ....	57
Table 21: Pipetting scheme for qPCR.....	60
Table 22: Extended information for selected gRNA candidates. ....	69
Table 23: Highest ranked predicted off-targets of TNF 5' gRNA (top) and 3' gRNA (bottom).....	75
Table 24: Values for standard deviation and coefficient of correlation (coeff. of corr.) for selected housekeeper candidates calculated using Bestkeeper. Values are based on qPCR results using cDNA pools from three each of wild-type, TNF <sup>ΔARE/+</sup> and TNF <sup>ΔARE/ΔARE</sup> animals. ....	91

Table 25: Values for stability value and standard error for selected housekeeper candidates calculated using Normfinder. Values are based on qPCR results using cDNA pools from three each of wild-type, TNF<sup>ΔARE/+</sup> and TNF<sup>ΔARE/ΔARE</sup> animals. .... 91

Table 26: Summary of findings from flow cytometric analyses of PBMCs. Upward (↑) and downward (↓) arrows indicate increase and decrease, respectively, relative to the wild-type group (n=3). ..... 103

Table S1: Raw values of the complete blood count of TNF<sup>ΔARE/+</sup> and TNF<sup>ΔARE/ΔARE</sup> pigs and wild-type siblings. ). GOT: glutamate-oxalacetate-transaminase; GLDH: glutamate-dehydrogenase; GGT: γ-Glutamyl-Transferase; Billi: Bilirubin; AP: alkaline phosphatase; Chol.: cholesterol; TP: total protein; ALB: albumin; RBC: red blood cells; HCT: haematocrit; HGB: haemoglobin; MCV: mean corpuscular volume; MCHC: Mean corpuscular haemoglobin concentration; RDW: red cell distribution; RETIC: reticulocyte; WBC: white blood cell; NEU: neutrophils; LYM: lymphocytes; MONO: monocytes; EOS: eosinophils; BASO: basophils; PLT: platelets; MPV: mean platelet volume; PCT: procaltitonin. .... 150



## References

1. Reinus, J. & Simon, D. (eds.). *Gastrointestinal anatomy and physiology. The essentials ; [with website]* (Wiley Blackwell, Chichester, 2014).
2. Mowat, A. M. & Agace, W. W. Regional specialization within the intestinal immune system. *Nature reviews. Immunology* **14**, 667–685; 10.1038/nri3738 (2014).
3. Kiela, P. R. & Ghishan, F. K. Physiology of Intestinal Absorption and Secretion. *Best practice & research. Clinical gastroenterology* **30**, 145–159; 10.1016/j.bpg.2016.02.007 (2016).
4. Rees, W. D., Tandun, R., Yau, E., Zachos, N. C. & Steiner, T. S. Regenerative Intestinal Stem Cells Induced by Acute and Chronic Injury: The Saving Grace of the Epithelium? *Frontiers in Cell and Developmental Biology* **8**, 583919; 10.3389/fcell.2020.583919 (2020).
5. Haller, D. & Hörmannspurger, G. *Darmgesundheit und Mikrobiota. Ein Überblick über die Bedeutung der Darmbakterien für die Gesundheit* (Springer Spektrum, Wiesbaden, 2015).
6. Pietrzak, B., Tomela, K., Olejnik-Schmidt, A., Mackiewicz, A. & Schmidt, M. Secretory IgA in Intestinal Mucosal Secretions as an Adaptive Barrier against Microbial Cells. *International Journal of Molecular Sciences* **21**; 10.3390/ijms21239254 (2020).
7. Donaldson, G. P., Lee, S. M. & Mazmanian, S. K. Gut biogeography of the bacterial microbiota. *Nature reviews. Microbiology* **14**, 20–32; 10.1038/nrmicro3552 (2016).
8. Haller, D. (ed.). *The gut microbiome in health and disease* (Springer, Cham, 2018).
9. Ley, R. E. *et al.* Evolution of mammals and their gut microbes. *Science (New York, N.Y.)* **320**, 1647–1651; 10.1126/science.1155725 (2008).
10. Sender, R., Fuchs, S. & Milo, R. Revised Estimates for the Number of Human and Bacteria Cells in the Body. *PLoS biology* **14**, e1002533; 10.1371/journal.pbio.1002533 (2016).
11. Zheng, D., Liwinski, T. & Elinav, E. Interaction between microbiota and immunity in health and disease. *Cell research* **30**, 492–506; 10.1038/s41422-020-0332-7 (2020).
12. Worsøe, J. *et al.* Gastric transit and small intestinal transit time and motility assessed by a magnet tracking system. *BMC gastroenterology* **11**, 145; 10.1186/1471-230X-11-145 (2011).
13. Clarke, G. *et al.* Gut Reactions: Breaking Down Xenobiotic-Microbiome Interactions. *Pharmacological reviews* **71**, 198–224; 10.1124/pr.118.015768 (2019).
14. Turnbaugh, P. J. *et al.* A core gut microbiome in obese and lean twins. *Nature* **457**, 480–484; 10.1038/nature07540 (2009).
15. Qin, J. *et al.* A human gut microbial gene catalogue established by metagenomic sequencing. *Nature* **464**, 59–65; 10.1038/nature08821 (2010).

16. Goyal, A., Wang, T., Dubinkina, V. & Maslov, S. Ecology-guided prediction of cross-feeding interactions in the human gut microbiome. *Nature communications* **12**, 1335; 10.1038/s41467-021-21586-6 (2021).
17. Koh, A., Vadder, F. de, Kovatcheva-Datchary, P. & Bäckhed, F. From Dietary Fiber to Host Physiology: Short-Chain Fatty Acids as Key Bacterial Metabolites. *Cell* **165**, 1332–1345; 10.1016/j.cell.2016.05.041 (2016).
18. Topping, D. L. & Clifton, P. M. Short-chain fatty acids and human colonic function: roles of resistant starch and nonstarch polysaccharides. *Physiological reviews* **81**, 1031–1064; 10.1152/physrev.2001.81.3.1031 (2001).
19. Vos, W. M. de, Tilg, H., van Hul, M. & Cani, P. D. Gut microbiome and health: mechanistic insights. *Gut* **71**, 1020–1032; 10.1136/gutjnl-2021-326789 (2022).
20. Visekruna, A. & Luu, M. The Role of Short-Chain Fatty Acids and Bile Acids in Intestinal and Liver Function, Inflammation, and Carcinogenesis. *Frontiers in Cell and Developmental Biology* **9**, 703218; 10.3389/fcell.2021.703218 (2021).
21. Schilderink, R. *et al.* The SCFA butyrate stimulates the epithelial production of retinoic acid via inhibition of epithelial HDAC. *American journal of physiology. Gastrointestinal and liver physiology* **310**, G1138-46; 10.1152/ajpgi.00411.2015 (2016).
22. Stagg, A. J. Intestinal Dendritic Cells in Health and Gut Inflammation. *Frontiers in immunology* **9**, 2883; 10.3389/fimmu.2018.02883 (2018).
23. Huang, G., Wang, Y. & Chi, H. Control of T cell fates and immune tolerance by p38 $\alpha$  signaling in mucosal CD103+ dendritic cells. *Journal of immunology (Baltimore, Md. : 1950)* **191**, 650–659; 10.4049/jimmunol.1300398 (2013).
24. Ng, S. C. *et al.* Relationship between human intestinal dendritic cells, gut microbiota, and disease activity in Crohn's disease. *Inflammatory bowel diseases* **17**, 2027–2037; 10.1002/ibd.21590 (2011).
25. Izcue, A., Coombes, J. L. & Powrie, F. Regulatory T cells suppress systemic and mucosal immune activation to control intestinal inflammation. *Immunological reviews* **212**, 256–271; 10.1111/j.0105-2896.2006.00423.x (2006).
26. Kawamoto, S. *et al.* Foxp3(+) T cells regulate immunoglobulin a selection and facilitate diversification of bacterial species responsible for immune homeostasis. *Immunity* **41**, 152–165; 10.1016/j.immuni.2014.05.016 (2014).
27. Litvak, Y., Byndloss, M. X., Tsois, R. M. & Bäumler, A. J. Dysbiotic Proteobacteria expansion: a microbial signature of epithelial dysfunction. *Current opinion in microbiology* **39**, 1–6; 10.1016/j.mib.2017.07.003 (2017).

28. Singh, V. *et al.* Butyrate producers, "The Sentinel of Gut": Their intestinal significance with and beyond butyrate, and prospective use as microbial therapeutics. *Frontiers in microbiology* **13**, 1103836; 10.3389/fmicb.2022.1103836 (2022).
29. Kelly, C. J. *et al.* Crosstalk between Microbiota-Derived Short-Chain Fatty Acids and Intestinal Epithelial HIF Augments Tissue Barrier Function. *Cell host & microbe* **17**, 662–671; 10.1016/j.chom.2015.03.005 (2015).
30. Winter, S. E. *et al.* Host-derived nitrate boosts growth of *E. coli* in the inflamed gut. *Science (New York, N.Y.)* **339**, 708–711; 10.1126/science.1232467 (2013).
31. Fan, Y.-Y. *et al.* A bioassay to measure energy metabolism in mouse colonic crypts, organoids, and sorted stem cells. *American journal of physiology. Gastrointestinal and liver physiology* **309**, G1-9; 10.1152/ajpgi.00052.2015 (2015).
32. Hansen, I. S. *et al.* FcαRI co-stimulation converts human intestinal CD103+ dendritic cells into pro-inflammatory cells through glycolytic reprogramming. *Nature communications* **9**, 863; 10.1038/s41467-018-03318-5 (2018).
33. Cerovic, V. *et al.* Hyporesponsiveness of intestinal dendritic cells to TLR stimulation is limited to TLR4. *Journal of immunology (Baltimore, Md. : 1950)* **182**, 2405–2415; 10.4049/jimmunol.0802318 (2009).
34. Askenase, M. H. *et al.* Bone-Marrow-Resident NK Cells Prime Monocytes for Regulatory Function during Infection. *Immunity* **42**, 1130–1142; 10.1016/j.immuni.2015.05.011 (2015).
35. Jakubzick, C. V., Randolph, G. J. & Henson, P. M. Monocyte differentiation and antigen-presenting functions. *Nature reviews. Immunology* **17**, 349–362; 10.1038/nri.2017.28 (2017).
36. Kaplan, G. G. & Windsor, J. W. The four epidemiological stages in the global evolution of inflammatory bowel disease. *Nature Reviews. Gastroenterology & Hepatology* **18**, 56–66; 10.1038/s41575-020-00360-x (2021).
37. Abraham, C. & Cho, J. H. Inflammatory bowel disease. *The New England journal of medicine* **361**, 2066–2078; 10.1056/NEJMra0804647 (2009).
38. Ng, S. C. *et al.* Worldwide incidence and prevalence of inflammatory bowel disease in the 21st century: a systematic review of population-based studies. *Lancet (London, England)* **390**, 2769–2778; 10.1016/S0140-6736(17)32448-0 (2017).
39. Turpin, W., Goethel, A., Bedrani, L. & Croitoru MdcM, K. Determinants of IBD Heritability: Genes, Bugs, and More. *Inflammatory bowel diseases* **24**, 1133–1148; 10.1093/ibd/izy085 (2018).
40. Ramos, G. P. & Papadakis, K. A. Mechanisms of Disease: Inflammatory Bowel Diseases. *Mayo Clinic proceedings* **94**, 155–165; 10.1016/j.mayocp.2018.09.013 (2019).
41. Khaloian, S. *et al.* Mitochondrial impairment drives intestinal stem cell transition into dysfunctional Paneth cells predicting Crohn's disease recurrence. *Gut* **69**, 1939–1951; 10.1136/gutjnl-2019-319514 (2020).

42. Schaubeck, M. *et al.* Dysbiotic gut microbiota causes transmissible Crohn's disease-like ileitis independent of failure in antimicrobial defence. *Gut* **65**, 225–237; 10.1136/gutjnl-2015-309333 (2016).
43. Nguyen, H. T. T., Lapaquette, P., Bringer, M.-A. & Darfeuille-Michaud, A. Autophagy and Crohn's disease. *Journal of Innate Immunity* **5**, 434–443; 10.1159/000345129 (2013).
44. Larabi, A., Barnich, N. & Nguyen, H. T. T. New insights into the interplay between autophagy, gut microbiota and inflammatory responses in IBD. *Autophagy* **16**, 38–51; 10.1080/15548627.2019.1635384 (2020).
45. Olszak, T. *et al.* Microbial exposure during early life has persistent effects on natural killer T cell function. *Science (New York, N.Y.)* **336**, 489–493; 10.1126/science.1219328 (2012).
46. Cholanpranee, A. & Ananthakrishnan, A. N. Environmental Hygiene and Risk of Inflammatory Bowel Diseases: A Systematic Review and Meta-analysis. *Inflammatory bowel diseases* **22**, 2191–2199; 10.1097/MIB.0000000000000852 (2016).
47. Ananthakrishnan, A. N. *et al.* A prospective study of long-term intake of dietary fiber and risk of Crohn's disease and ulcerative colitis. *Gastroenterology* **145**, 970–977; 10.1053/j.gastro.2013.07.050 (2013).
48. Lee, M. & Chang, E. B. Inflammatory Bowel Diseases (IBD) and the Microbiome-Searching the Crime Scene for Clues. *Gastroenterology* **160**, 524–537; 10.1053/j.gastro.2020.09.056 (2021).
49. Lloyd-Price, J. *et al.* Multi-omics of the gut microbial ecosystem in inflammatory bowel diseases. *Nature* **569**, 655–662; 10.1038/s41586-019-1237-9 (2019).
50. Schnupf, P. *et al.* Growth and host interaction of mouse segmented filamentous bacteria in vitro. *Nature* **520**, 99–103; 10.1038/nature14027 (2015).
51. Metwaly, A. *et al.* P059 Diet controls segmented filamentous bacteria in driving Crohn's disease-like inflammation in TNFdeltaARE mice. *Journal of Crohn's and Colitis* **16**, i168-i168; 10.1093/ecco-jcc/jjab232.188 (2022).
52. Palma, G. de *et al.* Transplantation of fecal microbiota from patients with irritable bowel syndrome alters gut function and behavior in recipient mice. *Science translational medicine* **9**; 10.1126/scitranslmed.aaf6397 (2017).
53. Matsumoto, M. *et al.* Cerebral low-molecular metabolites influenced by intestinal microbiota: a pilot study. *Frontiers in systems neuroscience* **7**, 9; 10.3389/fnsys.2013.00009 (2013).
54. Iliopoulou, L. & Kollias, G. Harnessing murine models of Crohn's disease ileitis to advance concepts of pathophysiology and treatment. *Mucosal immunology* **15**, 10–26; 10.1038/s41385-021-00433-3 (2022).
55. Katsandegwaza, B., Horsnell, W. & Smith, K. Inflammatory Bowel Disease: A Review of Pre-Clinical Murine Models of Human Disease. *International Journal of Molecular Sciences* **23**; 10.3390/ijms23169344 (2022).

56. Wirtz, S. *et al.* Chemically induced mouse models of acute and chronic intestinal inflammation. *Nature protocols* **12**, 1295–1309; 10.1038/nprot.2017.044 (2017).
57. Wahida, A. *et al.* XIAP restrains TNF-driven intestinal inflammation and dysbiosis by promoting innate immune responses of Paneth and dendritic cells. *Science immunology* **6**, eabf7235; 10.1126/sciimmunol.abf7235 (2021).
58. Kontoyiannis, D., Pasparakis, M., Pizarro, T. T., Cominelli, F. & Kollias, G. Impaired On/Off Regulation of TNF Biosynthesis in Mice Lacking TNF AU-Rich Elements. *Immunity* **10**, 387–398; 10.1016/S1074-7613(00)80038-2 (1999).
59. Moss, M. L. *et al.* Cloning of a disintegrin metalloproteinase that processes precursor tumour-necrosis factor-alpha. *Nature* **385**, 733–736; 10.1038/385733a0 (1997).
60. Black, R. A. *et al.* A metalloproteinase disintegrin that releases tumour-necrosis factor-alpha from cells. *Nature* **385**, 729–733; 10.1038/385729a0 (1997).
61. Yang, S., Wang, J., Brand, D. D. & Zheng, S. G. Role of TNF-TNF Receptor 2 Signal in Regulatory T Cells and Its Therapeutic Implications. *Frontiers in immunology* **9**, 784; 10.3389/fimmu.2018.00784 (2018).
62. Gough, P. & Myles, I. A. Tumor Necrosis Factor Receptors: Pleiotropic Signaling Complexes and Their Differential Effects. *Frontiers in immunology* **11**, 585880; 10.3389/fimmu.2020.585880 (2020).
63. Arijs, I. *et al.* Mucosal gene expression of cell adhesion molecules, chemokines, and chemokine receptors in patients with inflammatory bowel disease before and after infliximab treatment. *The American journal of gastroenterology* **106**, 748–761; 10.1038/ajg.2011.27 (2011).
64. Watson, A. J. M. & Hughes, K. R. TNF- $\alpha$ -induced intestinal epithelial cell shedding: implications for intestinal barrier function. *Annals of the New York Academy of Sciences* **1258**, 1–8; 10.1111/j.1749-6632.2012.06523.x (2012).
65. Su, L. *et al.* TNFR2 activates MLCK-dependent tight junction dysregulation to cause apoptosis-mediated barrier loss and experimental colitis. *Gastroenterology* **145**, 407–415; 10.1053/j.gastro.2013.04.011 (2013).
66. McElroy, S. J. *et al.* Tumor necrosis factor receptor 1-dependent depletion of mucus in immature small intestine: a potential role in neonatal necrotizing enterocolitis. *American journal of physiology. Gastrointestinal and liver physiology* **301**, G656-66; 10.1152/ajpgi.00550.2010 (2011).
67. Naudé, P. J. W., Boer, J. A. den, Luiten, P. G. M. & Eisel, U. L. M. Tumor necrosis factor receptor cross-talk. *The FEBS journal* **278**, 888–898; 10.1111/j.1742-4658.2011.08017.x (2011).
68. Hsu, H., Xiong, J. & Goeddel, D. V. The TNF receptor 1-associated protein TRADD signals cell death and NF-kappa B activation. *Cell* **81**, 495–504; 10.1016/0092-8674(95)90070-5 (1995).
69. Hsu, H., Huang, J., Shu, H. B., Baichwal, V. & Goeddel, D. V. TNF-dependent recruitment of the protein kinase RIP to the TNF receptor-1 signaling complex. *Immunity* **4**, 387–396; 10.1016/s1074-7613(00)80252-6 (1996).

70. Shu, H. B., Takeuchi, M. & Goeddel, D. V. The tumor necrosis factor receptor 2 signal transducers TRAF2 and c-IAP1 are components of the tumor necrosis factor receptor 1 signaling complex. *Proceedings of the National Academy of Sciences of the United States of America* **93**, 13973–13978; 10.1073/pnas.93.24.13973 (1996).
71. Haas, T. L. *et al.* Recruitment of the linear ubiquitin chain assembly complex stabilizes the TNF-R1 signaling complex and is required for TNF-mediated gene induction. *Molecular cell* **36**, 831–844; 10.1016/j.molcel.2009.10.013 (2009).
72. Micheau, O. & Tschopp, J. Induction of TNF receptor I-mediated apoptosis via two sequential signaling complexes. *Cell* **114**, 181–190; 10.1016/s0092-8674(03)00521-x (2003).
73. Li, H., Kobayashi, M., Blonska, M., You, Y. & Lin, X. Ubiquitination of RIP is required for tumor necrosis factor alpha-induced NF-kappaB activation. *The Journal of biological chemistry* **281**, 13636–13643; 10.1074/jbc.M600620200 (2006).
74. Newton, K. & Manning, G. Necroptosis and Inflammation. *Annual review of biochemistry* **85**, 743–763; 10.1146/annurev-biochem-060815-014830 (2016).
75. Tummers, B. & Green, D. R. Caspase-8: regulating life and death. *Immunological reviews* **277**, 76–89; 10.1111/imr.12541 (2017).
76. Kaiser, W. J. *et al.* Toll-like receptor 3-mediated necrosis via TRIF, RIP3, and MLKL. *The Journal of biological chemistry* **288**, 31268–31279; 10.1074/jbc.M113.462341 (2013).
77. Kearney, C. J. & Martin, S. J. An Inflammatory Perspective on Necroptosis. *Molecular cell* **65**, 965–973; 10.1016/j.molcel.2017.02.024 (2017).
78. van Loo, G. & Bertrand, M. J. M. Death by TNF: a road to inflammation. *Nature reviews. Immunology*, 1–15; 10.1038/s41577-022-00792-3 (2022).
79. Medler, J. & Wajant, H. Tumor necrosis factor receptor-2 (TNFR2): an overview of an emerging drug target. *Expert opinion on therapeutic targets* **23**, 295–307; 10.1080/14728222.2019.1586886 (2019).
80. Fischer, R., Kontermann, R. E. & Pfizenmaier, K. Selective Targeting of TNF Receptors as a Novel Therapeutic Approach. *Frontiers in Cell and Developmental Biology* **8**, 401; 10.3389/fcell.2020.00401 (2020).
81. Sun, S.-C. The non-canonical NF-κB pathway in immunity and inflammation. *Nature reviews. Immunology* **17**, 545–558; 10.1038/nri.2017.52 (2017).
82. Kim, E. Y., Priatel, J. J., Teh, S.-J. & Teh, H.-S. TNF receptor type 2 (p75) functions as a costimulator for antigen-driven T cell responses in vivo. *Journal of immunology (Baltimore, Md. : 1950)* **176**, 1026–1035; 10.4049/jimmunol.176.2.1026 (2006).
83. Musicki, K., Briscoe, H., Tran, S., Britton, W. J. & Saunders, B. M. Differential requirements for soluble and transmembrane tumor necrosis factor in the immunological control of primary and

- secondary *Listeria monocytogenes* infection. *Infection and immunity* **74**, 3180–3189; 10.1128/IAI.02004-05 (2006).
84. Nair, A. P. K., Hirsch, H. H., Colombi, M. & Moroni, C. Cyclosporin A Promotes Translational Silencing of Autocrine Interleukin-3 via Ribosome-Associated Deadenylation. *Molecular and cellular biology* **19**, 889–898; 10.1128/MCB.19.1.889 (1999).
85. Zhang, T., Kruys, V., Huez, G. & Gueydan, C. AU-rich element-mediated translational control: complexity and multiple activities of trans-activating factors. *Biochemical Society transactions* **30**, 952–958; 10.1042/bst0300952 (2002).
86. Langa, F. *et al.* Healthy mice with an altered c-myc gene: role of the 3' untranslated region revisited. *Oncogene* **20**, 4344–4353; 10.1038/sj.onc.1204482 (2001).
87. Barreau, C., Paillard, L. & Osborne, H. B. AU-rich elements and associated factors: are there unifying principles? *Nucleic acids research* **33**, 7138–7150; 10.1093/nar/gki1012 (2005).
88. Liang, J. *et al.* RNA-destabilizing Factor Tristetraprolin Negatively Regulates NF- $\kappa$ B Signaling. *Journal of Biological Chemistry* **284**, 29383–29390; 10.1074/jbc.M109.024745 (2009).
89. Renner, F. & Schmitz, M. L. Autoregulatory feedback loops terminating the NF- $\kappa$ B response. *Trends in Biochemical Sciences* **34**, 128–135; 10.1016/j.tibs.2008.12.003 (2009).
90. Dumitru, C. D. *et al.* TNF- $\alpha$  Induction by LPS Is Regulated Posttranscriptionally via a Tpl2/ERK-Dependent Pathway. *Cell* **103**, 1071–1083; 10.1016/S0092-8674(00)00210-5 (2000).
91. Stoecklin, G. *et al.* MK2-induced tristetraprolin:14-3-3 complexes prevent stress granule association and ARE-mRNA decay. *EMBO J* **23**, 1313–1324; 10.1038/sj.emboj.7600163 (2004).
92. Chen, C.-Y. *et al.* AU Binding Proteins Recruit the Exosome to Degrade ARE-Containing mRNAs. *Cell* **107**, 451–464; 10.1016/S0092-8674(01)00578-5 (2001).
93. Brooks, S. A., Connolly, J. E. & Rigby, W. F. C. The Role of mRNA Turnover in the Regulation of Tristetraprolin Expression: Evidence for an Extracellular Signal-Regulated Kinase-Specific, AU-Rich Element-Dependent, Autoregulatory Pathway. *The Journal of Immunology* **172**, 7263–7271; 10.4049/jimmunol.172.12.7263 (2004).
94. Mahmoud, L., Moghrabi, W., Khabar, K. S. A. & Hitti, E. G. Bi-phased regulation of the post-transcriptional inflammatory response by Tristetraprolin levels. *RNA Biology* **16**, 309–319; 10.1080/15476286.2019.1572437 (2019).
95. Kontoyiannis, D. *et al.* Genetic dissection of the cellular pathways and signaling mechanisms in modeled tumor necrosis factor-induced Crohn's-like inflammatory bowel disease. *The Journal of experimental medicine* **196**, 1563–1574; 10.1084/jem.20020281 (2002).
96. Cominelli, F., Arseneau, K. O., Rodriguez-Palacios, A. & Pizarro, T. T. Uncovering Pathogenic Mechanisms of Inflammatory Bowel Disease Using Mouse Models of Crohn's Disease-Like Ileitis: What is the Right Model? *Cellular and molecular gastroenterology and hepatology* **4**, 19–32; 10.1016/j.jcmgh.2017.02.010 (2017).

97. Núñez-Sánchez, M. A. *et al.* Crohn's Disease, Host-Microbiota Interactions, and Immunonutrition: Dietary Strategies Targeting Gut Microbiome as Novel Therapeutic Approaches. *International Journal of Molecular Sciences* **23**; 10.3390/ijms23158361 (2022).
98. Petersen, A. M. *et al.* Ciprofloxacin and probiotic *Escherichia coli* Nissle add-on treatment in active ulcerative colitis: a double-blind randomized placebo controlled clinical trial. *Journal of Crohn's and Colitis* **8**, 1498–1505; 10.1016/j.crohns.2014.06.001 (2014).
99. Nguyen, T. L. A., Vieira-Silva, S., Liston, A. & Raes, J. How informative is the mouse for human gut microbiota research? *Dis Model Mech* **8**, 1–16; 10.1242/dmm.017400 (2015).
100. Rosshart, S. P. *et al.* Laboratory mice born to wild mice have natural microbiota and model human immune responses. *Science (New York, N.Y.)* **365**; 10.1126/science.aaw4361 (2019).
101. Ericsson, A. C. & Franklin, C. L. The gut microbiome of laboratory mice: considerations and best practices for translational research. *Mammalian genome : official journal of the International Mammalian Genome Society* **32**, 239–250; 10.1007/s00335-021-09863-7 (2021).
102. Alpert, C., Sczesny, S., Gruhl, B. & Blaut, M. Long-term stability of the human gut microbiota in two different rat strains. *Current issues in molecular biology* **10**, 17–24 (2008).
103. Seewoo, B. J. *et al.* Changes in the rodent gut microbiome following chronic restraint stress and low-intensity rTMS. *Neurobiology of stress* **17**, 100430; 10.1016/j.ynstr.2022.100430 (2022).
104. Liou, A. P. *et al.* Conserved shifts in the gut microbiota due to gastric bypass reduce host weight and adiposity. *Science translational medicine* **5**, 178ra41; 10.1126/scitranslmed.3005687 (2013).
105. Zhang, S. L. *et al.* Human and rat gut microbiome composition is maintained following sleep restriction. *Proceedings of the National Academy of Sciences of the United States of America* **114**, E1564-E1571; 10.1073/pnas.1620673114 (2017).
106. Ziegler, A., Gonzalez, L. & Blikslager, A. Large Animal Models: The Key to Translational Discovery in Digestive Disease Research. *Cellular and molecular gastroenterology and hepatology* **2**, 716–724; 10.1016/j.jcmgh.2016.09.003 (2016).
107. Swanson, K. S. *et al.* Phylogenetic and gene-centric metagenomics of the canine intestinal microbiome reveals similarities with humans and mice. *The ISME journal* **5**, 639–649; 10.1038/ismej.2010.162 (2011).
108. Coelho, L. P. *et al.* Similarity of the dog and human gut microbiomes in gene content and response to diet. *Microbiome* **6**, 72; 10.1186/s40168-018-0450-3 (2018).
109. Allenspach, K. *et al.* Evaluation of mucosal bacteria and histopathology, clinical disease activity and expression of Toll-like receptors in German shepherd dogs with chronic enteropathies. *Veterinary microbiology* **146**, 326–335; 10.1016/j.vetmic.2010.05.025 (2010).
110. Suchodolski, J. S., Dowd, S. E., Wilke, V., Steiner, J. M. & Jergens, A. E. 16S rRNA gene pyrosequencing reveals bacterial dysbiosis in the duodenum of dogs with idiopathic inflammatory bowel disease. *PloS one* **7**, e39333; 10.1371/journal.pone.0039333 (2012).



111. Roura, E. *et al.* Critical review evaluating the pig as a model for human nutritional physiology. *Nutrition research reviews* **29**, 60–90; 10.1017/S0954422416000020 (2016).
112. Hart, E. A. *et al.* Lessons learned from the initial sequencing of the pig genome: comparative analysis of an 8 Mb region of pig chromosome 17. *Genome Biol* **8**, R168; 10.1186/gb-2007-8-8-r168 (2007).
113. Ibrahim, Z. *et al.* Selected physiologic compatibilities and incompatibilities between human and porcine organ systems. *Xenotransplantation* **13**, 488–499; 10.1111/j.1399-3089.2006.00346.x (2006).
114. Lunney, J. K. *et al.* Importance of the pig as a human biomedical model. *Science translational medicine* **13**, eabd5758; 10.1126/scitranslmed.abd5758 (2021).
115. Klymiuk, N. *et al.* Tailored Pig Models for Preclinical Efficacy and Safety Testing of Targeted Therapies. *Toxicologic pathology* **44**, 346–357; 10.1177/0192623315609688 (2016).
116. Pang, X. *et al.* Inter-species transplantation of gut microbiota from human to pigs. *The ISME journal* **1**, 156–162; 10.1038/ismej.2007.23 (2007).
117. Xiao, L. *et al.* A reference gene catalogue of the pig gut microbiome. *Nature microbiology* **1**, 16161; 10.1038/nmicrobiol.2016.161 (2016).
118. Wylensek, D. *et al.* A collection of bacterial isolates from the pig intestine reveals functional and taxonomic diversity. *Nature communications* **11**, 6389; 10.1038/s41467-020-19929-w (2020).
119. Yang, H. *et al.* ABO genotype alters the gut microbiota by regulating GalNAc levels in pigs. *Nature*; 10.1038/s41586-022-04769-z (2022).
120. Fischer, K. *et al.* Viable pigs after simultaneous inactivation of porcine MHC class I and three xenoreactive antigen genes GGTA1, CMAH and B4GALNT2. *Xenotransplantation* **27**, e12560; 10.1111/xen.12560 (2020).
121. Rieblinger, B. *et al.* Cas9-expressing chickens and pigs as resources for genome editing in livestock. *Proceedings of the National Academy of Sciences of the United States of America* **118**; 10.1073/pnas.2022562118 (2021).
122. Li, S. *et al.* Dual fluorescent reporter pig for Cre recombination: transgene placement at the ROSA26 locus. *PLoS one* **9**, e102455; 10.1371/journal.pone.0102455 (2014).
123. Kurome, M., Kessler, B., Wuensch, A., Nagashima, H. & Wolf, E. Nuclear transfer and transgenesis in the pig. *Methods in molecular biology (Clifton, N.J.)* **1222**, 37–59; 10.1007/978-1-4939-1594-1\_4 (2015).
124. Flisikowska, T., Kind, A. & Schnieke, A. Genetically modified pigs to model human diseases. *Journal of applied genetics* **55**, 53–64; 10.1007/s13353-013-0182-9 (2014).

125. Preisinger, D., Winogrodzki, T., Klinger, B., Schnieke, A. & Rieblinger, B. Genome Editing in Pigs. *Methods in molecular biology (Clifton, N.J.)* **2631**, 393–417; 10.1007/978-1-0716-2990-1\_19 (2023).
126. Cortez, C. CRISPR 101: Homology Directed Repair. Addgene Blog. Available at <https://blog.addgene.org/crispr-101-homology-directed-repair> (2015).
127. Zhang, J.-P. *et al.* Efficient precise knockin with a double cut HDR donor after CRISPR/Cas9-mediated double-stranded DNA cleavage. *Genome Biol* **18**, 35; 10.1186/s13059-017-1164-8 (2017).
128. Lieber, M. R. The mechanism of double-strand DNA break repair by the nonhomologous DNA end-joining pathway. *Annual review of biochemistry* **79**, 181–211; 10.1146/annurev.biochem.052308.093131 (2010).
129. Ma, Y. *et al.* A biochemically defined system for mammalian nonhomologous DNA end joining. *Molecular cell* **16**, 701–713; 10.1016/j.molcel.2004.11.017 (2004).
130. Addgene (ed.). *CRISPR 101: A Desktop Resource. Chapter 3: Using CRISPR in your experiments* (2017).
131. Rouet, P., Smih, F. & Jasin, M. Introduction of double-strand breaks into the genome of mouse cells by expression of a rare-cutting endonuclease. *Mol. Cell. Biol.* **14**, 8096–8106; 10.1128/MCB.14.12.8096 (1994).
132. Rouet, P., Smih, F. & Jasin, M. Expression of a site-specific endonuclease stimulates homologous recombination in mammalian cells. *Proceedings of the National Academy of Sciences* **91**, 6064–6068; 10.1073/pnas.91.13.6064 (1994).
133. Wang, H., La Russa, M. & Qi, L. S. CRISPR/Cas9 in Genome Editing and Beyond. *Annual review of biochemistry* **85**, 227–264; 10.1146/annurev-biochem-060815-014607 (2016).
134. Urnov, F. D., Rebar, E. J., Holmes, M. C., Zhang, H. S. & Gregory, P. D. Genome editing with engineered zinc finger nucleases. *Nature reviews. Genetics* **11**, 636–646; 10.1038/nrg2842 (2010).
135. Joung, J. K. & Sander, J. D. TALENs: a widely applicable technology for targeted genome editing. *Nature reviews. Molecular cell biology* **14**, 49–55; 10.1038/nrm3486 (2013).
136. Carroll, D. Genome engineering with zinc-finger nucleases. *Genetics* **188**, 773–782; 10.1534/genetics.111.131433 (2011).
137. Boch, J. *et al.* Breaking the code of DNA binding specificity of TAL-type III effectors. *Science (New York, N.Y.)* **326**, 1509–1512; 10.1126/science.1178811 (2009).
138. Liu, X., Wu, S., Xu, J., Sui, C. & Wei, J. Application of CRISPR/Cas9 in plant biology. *Acta pharmaceutica Sinica. B* **7**, 292–302; 10.1016/j.apsb.2017.01.002 (2017).

139. Mojica, F. J. M., Díez-Villaseñor, C., García-Martínez, J. & Soria, E. Intervening sequences of regularly spaced prokaryotic repeats derive from foreign genetic elements. *Journal of molecular evolution* **60**, 174–182; 10.1007/s00239-004-0046-3 (2005).
140. Jinek, M. *et al.* A programmable dual-RNA-guided DNA endonuclease in adaptive bacterial immunity. *Science (New York, N.Y.)* **337**, 816–821; 10.1126/science.1225829 (2012).
141. Wright, A. V., Nuñez, J. K. & Doudna, J. A. Biology and Applications of CRISPR Systems: Harnessing Nature's Toolbox for Genome Engineering. *Cell* **164**, 29–44; 10.1016/j.cell.2015.12.035 (2016).
142. Tang, Y. & Fu, Y. Class 2 CRISPR/Cas: an expanding biotechnology toolbox for and beyond genome editing. *Cell & bioscience* **8**, 59; 10.1186/s13578-018-0255-x (2018).
143. Nishimasu, H. *et al.* Crystal structure of Cas9 in complex with guide RNA and target DNA. *Cell* **156**, 935–949; 10.1016/j.cell.2014.02.001 (2014).
144. Shah, S. A., Erdmann, S., Mojica, F. J. M. & Garrett, R. A. Protospacer recognition motifs: mixed identities and functional diversity. *RNA Biology* **10**, 891–899; 10.4161/rna.23764 (2013).
145. Lander, E. S. The Heroes of CRISPR. *Cell* **164**, 18–28; 10.1016/j.cell.2015.12.041 (2016).
146. Le Cong *et al.* Multiplex genome engineering using CRISPR/Cas systems. *Science (New York, N.Y.)* **339**, 819–823; 10.1126/science.1231143 (2013).
147. Cho, S. W., Lee, J., Carroll, D., Kim, J.-S. & Lee, J. Heritable gene knockout in *Caenorhabditis elegans* by direct injection of Cas9-sgRNA ribonucleoproteins. *Genetics* **195**, 1177–1180; 10.1534/genetics.113.155853 (2013).
148. Zuris, J. A. *et al.* Cationic lipid-mediated delivery of proteins enables efficient protein-based genome editing in vitro and in vivo. *Nature biotechnology* **33**, 73–80; 10.1038/nbt.3081 (2015).
149. Ryu, J., Prather, R. S. & Lee, K. Use of gene-editing technology to introduce targeted modifications in pigs. *Journal of animal science and biotechnology* **9**, 5; 10.1186/s40104-017-0228-7 (2018).
150. Niemann, H., Tian, X. C., King, W. A. & Lee, R. S. F. Epigenetic reprogramming in embryonic and foetal development upon somatic cell nuclear transfer cloning. *Reproduction (Cambridge, England)* **135**, 151–163; 10.1530/REP-07-0397 (2008).
151. Lagkouvardos, I., Fischer, S., Kumar, N. & Clavel, T. Rhea: a transparent and modular R pipeline for microbial profiling based on 16S rRNA gene amplicons. *PeerJ* **5**, e2836; 10.7717/peerj.2836 (2017).
152. Schlapschy, M. & Lerchner. *Kurspraktikum Biomolekulare Spektroskopie. Versuch Nr. 1 - Absorptionsspektroskopie (UV/VIS)* ,
153. Gstraunthaler, G. & Lindl, T. *Zell- und Gewebekultur. Allgemeine Grundlagen und spezielle Anwendungen*. 7th ed. (Springer Berlin Heidelberg, Berlin, Heidelberg, s.l., 2013).

154. Albl, B. *et al.* Tissue Sampling Guides for Porcine Biomedical Models. *Toxicologic pathology* **44**, 414–420; 10.1177/0192623316631023 (2016).
155. Gruber, A. R., Lorenz, R., Bernhart, S. H., Neuböck, R. & Hofacker, I. L. The Vienna RNA websuite. *Nucleic acids research* **36**, W70-4; 10.1093/nar/gkn188 (2008).
156. Bazanella, M. *et al.* Randomized controlled trial on the impact of early-life intervention with bifidobacteria on the healthy infant fecal microbiota and metabolome. *The American journal of clinical nutrition* **106**, 1274–1286; 10.3945/ajcn.117.157529 (2017).
157. Lagkouvardos, I. *et al.* Gut metabolites and bacterial community networks during a pilot intervention study with flaxseeds in healthy adult men. *Molecular nutrition & food research* **59**, 1614–1628; 10.1002/mnfr.201500125 (2015).
158. Lagkouvardos, I. *et al.* IMNGS: A comprehensive open resource of processed 16S rRNA microbial profiles for ecology and diversity studies. *Scientific reports* **6**, 33721; 10.1038/srep33721 (2016).
159. Dietrich, A. *et al.* *Namco: A microbiome explorer* (2021).
160. Edgar, R. C., Haas, B. J., Clemente, J. C., Quince, C. & Knight, R. UCHIME improves sensitivity and speed of chimera detection. *Bioinformatics (Oxford, England)* **27**, 2194–2200; 10.1093/bioinformatics/btr381 (2011).
161. Quast, C. *et al.* The SILVA ribosomal RNA gene database project: improved data processing and web-based tools. *Nucleic acids research* **41**, D590-6; 10.1093/nar/gks1219 (2013).
162. Kumar, S., Stecher, G., Li, M., Knyaz, C. & Tamura, K. MEGA X: Molecular Evolutionary Genetics Analysis across Computing Platforms. *Molecular biology and evolution* **35**, 1547–1549; 10.1093/molbev/msy096 (2018).
163. Winogrodzki, T. *et al.* TNF  $\Delta$ ARE pigs: a translational Crohn`s Disease model. *Journal of Crohn's and Colitis*; 10.1093/ecco-jcc/jjad034 (2023).
164. Mortimer, S. A., Kidwell, M. A. & Doudna, J. A. Insights into RNA structure and function from genome-wide studies. *Nature reviews. Genetics* **15**, 469–479; 10.1038/nrg3681 (2014).
165. Ha, C. W. Y. *et al.* Translocation of Viable Gut Microbiota to Mesenteric Adipose Drives Formation of Creeping Fat in Humans. *Cell* **183**, 666-683.e17; 10.1016/j.cell.2020.09.009 (2020).
166. Rogler, G., Singh, A., Kavanaugh, A. & Rubin, D. T. Extraintestinal Manifestations of Inflammatory Bowel Disease: Current Concepts, Treatment, and Implications for Disease Management. *Gastroenterology* **161**, 1118–1132; 10.1053/j.gastro.2021.07.042 (2021).
167. Pfaffl, M. W., Tichopad, A., Prgomet, C. & Neuvians, T. P. Determination of stable housekeeping genes, differentially regulated target genes and sample integrity: BestKeeper--Excel-based tool using pair-wise correlations. *Biotechnology letters* **26**, 509–515; 10.1023/b:bile.0000019559.84305.47 (2004).

168. Andersen, C. L., Jensen, J. L. & Ørntoft, T. F. Normalization of real-time quantitative reverse transcription-PCR data: a model-based variance estimation approach to identify genes suited for normalization, applied to bladder and colon cancer data sets. *Cancer research* **64**, 5245–5250; 10.1158/0008-5472.CAN-04-0496 (2004).
169. Parameswaran, N. & Patial, S. Tumor necrosis factor- $\alpha$  signaling in macrophages. *Critical reviews in eukaryotic gene expression* **20**, 87–103; 10.1615/critreveukargeneexpr.v20.i2.10 (2010).
170. Bauquier, J. R., Tennent-Brown, B. S., Tudor, E. & Bailey, S. R. Effects of polymyxin-B on TNF- $\alpha$  production in equine whole blood stimulated with three different bacterial toxins. *Journal of veterinary pharmacology and therapeutics* **41**, e35-e39; 10.1111/jvp.12445 (2018).
171. Buttó, L. F., Schaubeck, M. & Haller, D. Mechanisms of Microbe-Host Interaction in Crohn's Disease: Dysbiosis vs. Pathobiont Selection. *Frontiers in immunology* **6**, 555; 10.3389/fimmu.2015.00555 (2015).
172. Haverson, K., Bailey, M. & Stokes, C. R. T-cell populations in the pig intestinal lamina propria: memory cells with unusual phenotypic characteristics. *Immunology* **96**, 66–73; 10.1046/j.1365-2567.1999.00658.x (1999).
173. Clough, J. N., Omer, O. S., Tasker, S., Lord, G. M. & Irving, P. M. Regulatory T-cell therapy in Crohn's disease: challenges and advances. *Gut* **69**, 942–952; 10.1136/gutjnl-2019-319850 (2020).
174. Catalan-Serra, I., Sandvik, A. K., Bruland, T. & Andreu-Ballester, J. C. Gammadelta T Cells in Crohn's Disease: A New Player in the Disease Pathogenesis? *Journal of Crohn's and Colitis* **11**, 1135–1145; 10.1093/ecco-jcc/jjx039 (2017).
175. Holderness, J., Hedges, J. F., Ramstead, A. & Jutila, M. A. Comparative biology of  $\gamma\delta$  T cell function in humans, mice, and domestic animals. *Annual review of animal biosciences* **1**, 99–124; 10.1146/annurev-animal-031412-103639 (2013).
176. Kim, K., Song, M., Liu, Y. & Ji, P. Enterotoxigenic Escherichia coli infection of weaned pigs: Intestinal challenges and nutritional intervention to enhance disease resistance. *Frontiers in immunology* **13**, 885253; 10.3389/fimmu.2022.885253 (2022).
177. Moeser, A. J., Ryan, K. A., Nighot, P. K. & Blikslager, A. T. Gastrointestinal dysfunction induced by early weaning is attenuated by delayed weaning and mast cell blockade in pigs. *American journal of physiology. Gastrointestinal and liver physiology* **293**, G413-21; 10.1152/ajpgi.00304.2006 (2007).
178. McCracken, B. A., Spurlock, M. E., Roos, M. A., Zuckermann, F. A. & Gaskins, H. R. Weaning anorexia may contribute to local inflammation in the piglet small intestine. *The Journal of nutrition* **129**, 613–619; 10.1093/jn/129.3.613 (1999).
179. Humphrey, B., Zhao, J. & Faris, R. Link between intestinal immunity and practical approaches to swine nutrition. *Animal : an international journal of animal bioscience* **13**, 2736–2744; 10.1017/S1751731119001861 (2019).

180. Roulis, M. *et al.* Host and microbiota interactions are critical for development of murine Crohn's-like ileitis. *Mucosal immunology* **9**, 787–797; 10.1038/mi.2015.102 (2016).
181. Kaakoush, N. O., Castaño-Rodríguez, N., Mitchell, H. M. & Man, S. M. Global Epidemiology of Campylobacter Infection. *Clinical Microbiology Reviews* **28**, 687–720; 10.1128/CMR.00006-15 (2015).
182. Steck, N. *et al.* Enterococcus faecalis metalloprotease compromises epithelial barrier and contributes to intestinal inflammation. *Gastroenterology* **141**, 959–971; 10.1053/j.gastro.2011.05.035 (2011).
183. Kim, S. C. *et al.* Variable phenotypes of enterocolitis in interleukin 10-deficient mice monoassociated with two different commensal bacteria. *Gastroenterology* **128**, 891–906; 10.1053/j.gastro.2005.02.009 (2005).
184. Metwaly, A. *et al.* Integrated microbiota and metabolite profiles link Crohn's disease to sulfur metabolism. *Nature communications* **11**, 4322; 10.1038/s41467-020-17956-1 (2020).
185. López-García, A. *et al.* Autologous Haematopoietic Stem Cell Transplantation for Refractory Crohn's Disease: Efficacy in a Single-Centre Cohort. *Journal of Crohn's and Colitis* **11**, 1161–1168; 10.1093/ecco-jcc/jjx054 (2017).
186. Kaakoush, N. O. *et al.* The pathogenic potential of Campylobacter concisus strains associated with chronic intestinal diseases. *PloS one* **6**, e29045; 10.1371/journal.pone.0029045 (2011).
187. Castaño-Rodríguez, N., Kaakoush, N. O., Lee, W. S. & Mitchell, H. M. Dual role of Helicobacter and Campylobacter species in IBD: a systematic review and meta-analysis. *Gut* **66**, 235–249; 10.1136/gutjnl-2015-310545 (2017).
188. Sheh, A. *et al.* Analysis of gut microbiome profiles in common marmosets (*Callithrix jacchus*) in health and intestinal disease. *Scientific reports* **12**, 4430; 10.1038/s41598-022-08255-4 (2022).
189. Chen, D., Chen, G., Chen, C., Zeng, X. & Ye, H. Prebiotics effects in vitro of polysaccharides from tea flowers on gut microbiota of healthy persons and patients with inflammatory bowel disease. *International journal of biological macromolecules* **158**, 968–976; 10.1016/j.ijbiomac.2020.04.248 (2020).
190. Suzuki, M. *et al.* Myosin Light Chain Kinase Expression Induced via Tumor Necrosis Factor Receptor 2 Signaling in the Epithelial Cells Regulates the Development of Colitis-Associated Carcinogenesis. *PloS one* **9**, e88369; 10.1371/journal.pone.0088369 (2014).
191. Bhattacharya, J. & Westphalen, K. Macrophage-epithelial interactions in pulmonary alveoli. *Seminars in Immunopathology* **38**, 461–469; 10.1007/s00281-016-0569-x (2016).
192. Lipke, A. B. *et al.* Febrile-range hyperthermia augments lipopolysaccharide-induced lung injury by a mechanism of enhanced alveolar epithelial apoptosis. *The Journal of Immunology* **184**, 3801–3813; 10.4049/jimmunol.0903191 (2010).

193. Zia Ziabari, S. M. *et al.* Blood Urea Nitrogen to Creatinine ratio in Differentiation of Upper and Lower Gastrointestinal Bleedings; a Diagnostic Accuracy Study. *Archives of Academic Emergency Medicine* **7**, e30 (2019).
194. Felber, S., Rosenthal, P. & Henton, D. The BUN/creatinine ratio in localizing gastrointestinal bleeding in pediatric patients. *Journal of pediatric gastroenterology and nutrition* **7**, 685–687; 10.1097/00005176-198809000-00011 (1988).
195. Khan, N., Patel, D., Shah, Y., Trivedi, C. & Yang, Y.-X. Albumin as a prognostic marker for ulcerative colitis. *World Journal of Gastroenterology* **23**, 8008–8016; 10.3748/wjg.v23.i45.8008 (2017).
196. Guo, C.-H., Chen, P.-C., Yeh, M.-S., Hsiung, D.-Y. & Wang, C.-L. Cu/Zn ratios are associated with nutritional status, oxidative stress, inflammation, and immune abnormalities in patients on peritoneal dialysis. *Clinical biochemistry* **44**, 275–280; 10.1016/j.clinbiochem.2010.12.017 (2011).
197. Schneider, T. *et al.* The Copper/Zinc Ratio Correlates With Markers of Disease Activity in Patients With Inflammatory Bowel Disease. *Crohn's & colitis* **360** **2**, otaa001; 10.1093/crocol/otaa001 (2020).
198. Pathirana, W. G. W., Chubb, S. P., Gillett, M. J. & Vasikaran, S. D. Faecal Calprotectin. *The Clinical biochemist. Reviews* **39**, 77–90 (2018).
199. Zhang, Z. *et al.* Spatial heterogeneity and co-occurrence patterns of human mucosal-associated intestinal microbiota. *The ISME journal* **8**, 881–893; 10.1038/ismej.2013.185 (2014).
200. Wexler, H. M. Bacteroides: the good, the bad, and the nitty-gritty. *Clinical Microbiology Reviews* **20**, 593–621; 10.1128/CMR.00008-07 (2007).
201. Zafar, H. & Saier, M. H. Gut Bacteroides species in health and disease. *Gut microbes* **13**, 1–20; 10.1080/19490976.2020.1848158 (2021).
202. Parada Venegas, D. *et al.* Short Chain Fatty Acids (SCFAs)-Mediated Gut Epithelial and Immune Regulation and Its Relevance for Inflammatory Bowel Diseases. *Frontiers in immunology* **10**, 277; 10.3389/fimmu.2019.00277 (2019).
203. Henze, L. J. *et al.* Characterization of gastrointestinal transit and luminal conditions in pigs using a telemetric motility capsule. *European journal of pharmaceutical sciences : official journal of the European Federation for Pharmaceutical Sciences* **156**, 105627; 10.1016/j.ejps.2020.105627 (2021).
204. Shin, N.-R., Whon, T. W. & Bae, J.-W. Proteobacteria: microbial signature of dysbiosis in gut microbiota. *Trends in biotechnology* **33**, 496–503; 10.1016/j.tibtech.2015.06.011 (2015).
205. Morgan, X. C. *et al.* Dysfunction of the intestinal microbiome in inflammatory bowel disease and treatment. *Genome Biol* **13**, R79; 10.1186/gb-2012-13-9-r79 (2012).

206. Mahendran, V. *et al.* Prevalence of Campylobacter species in adult Crohn's disease and the preferential colonization sites of Campylobacter species in the human intestine. *PLoS one* **6**, e25417; 10.1371/journal.pone.0025417 (2011).
207. Bradley, P. H. & Pollard, K. S. Proteobacteria explain significant functional variability in the human gut microbiome. *Microbiome* **5**, 36; 10.1186/s40168-017-0244-z (2017).
208. Haag, L.-M. *et al.* Intestinal microbiota shifts towards elevated commensal Escherichia coli loads abrogate colonization resistance against Campylobacter jejuni in mice. *PLoS one* **7**, e35988; 10.1371/journal.pone.0035988 (2012).
209. Olafsson, S. *et al.* Somatic Evolution in Non-neoplastic IBD-Affected Colon. *Cell* **182**, 672-684.e11; 10.1016/j.cell.2020.06.036 (2020).
210. Patman, G. Crohn's disease: suppression of p21Rac1 signalling contributes to skip-lesion phenotype in Crohn's disease. *Nature Reviews. Gastroenterology & Hepatology* **11**, 332; 10.1038/nrgastro.2014.72 (2014).
211. Guo, F. *et al.* How Early-Life Gut Microbiota Alteration Sets Trajectories for Health and Inflammatory Bowel Disease? *Frontiers in nutrition* **8**, 690073; 10.3389/fnut.2021.690073 (2021).
212. Al Nabhani, Z. *et al.* A Weaning Reaction to Microbiota Is Required for Resistance to Immunopathologies in the Adult. *Immunity* **50**, 1276-1288.e5; 10.1016/j.immuni.2019.02.014 (2019).
213. Mao, K. *et al.* Innate and adaptive lymphocytes sequentially shape the gut microbiota and lipid metabolism. *Nature* **554**, 255–259; 10.1038/nature25437 (2018).
214. Flynn, J. L. *et al.* Tumor necrosis factor- $\alpha$  is required in the protective immune response against Mycobacterium tuberculosis in mice. *Immunity* **2**, 561–572; 10.1016/1074-7613(95)90001-2 (1995).
215. Wang, Y. *et al.* Protective role of tumor necrosis factor (TNF) receptors in chronic intestinal inflammation: TNFR1 ablation boosts systemic inflammatory response. *Laboratory investigation; a journal of technical methods and pathology* **93**, 1024–1035; 10.1038/labinvest.2013.89 (2013).
216. Ninnemann, J. *et al.* TNF hampers intestinal tissue repair in colitis by restricting IL-22 bioavailability. *Mucosal immunology* **15**, 698–716; 10.1038/s41385-022-00506-x (2022).
217. Gensollen, T., Iyer, S. S., Kasper, D. L. & Blumberg, R. S. How colonization by microbiota in early life shapes the immune system. *Science (New York, N.Y.)* **352**, 539–544; 10.1126/science.aad9378 (2016).
218. Clayer, E. *et al.* Severe Impairment of TNF Post-transcriptional Regulation Leads to Embryonic Death. *iScience* **23**, 101726; 10.1016/j.isci.2020.101726 (2020).
219. Rose, E. C., Blikslager, A. T. & Ziegler, A. L. Porcine Models of the Intestinal Microbiota: The Translational Key to Understanding How Gut Commensals Contribute to Gastrointestinal Disease. *Frontiers in veterinary science* **9**, 834598; 10.3389/fvets.2022.834598 (2022).



220. Metwaly, A. *et al.* Diet prevents the expansion of segmented filamentous bacteria and ileo-colonic inflammation in a model of Crohn's disease (2022).
221. Hedblom, G. A., Reiland, H. A., Sylte, M. J., Johnson, T. J. & Baumler, D. J. Segmented Filamentous Bacteria - Metabolism Meets Immunity. *Frontiers in microbiology* **9**, 1991; 10.3389/fmicb.2018.01991 (2018).
222. Yang, I. *et al.* Intestinal microbiota composition of interleukin-10 deficient C57BL/6J mice and susceptibility to *Helicobacter hepaticus*-induced colitis. *PloS one* **8**, e70783; 10.1371/journal.pone.0070783 (2013).
223. Håkansson, Å. *et al.* Immunological alteration and changes of gut microbiota after dextran sulfate sodium (DSS) administration in mice. *Clinical and experimental medicine* **15**, 107–120; 10.1007/s10238-013-0270-5 (2015).
224. Jiminez, J. A., Uwiera, T. C., Douglas Inglis, G. & Uwiera, R. R. E. Animal models to study acute and chronic intestinal inflammation in mammals. *Gut pathogens* **7**, 29; 10.1186/s13099-015-0076-y (2015).
225. Mirsepasi-Lauridsen, H. C., Vallance, B. A., Krogfelt, K. A. & Petersen, A. M. *Escherichia coli* Pathobionts Associated with Inflammatory Bowel Disease. *Clinical Microbiology Reviews* **32**; 10.1128/CMR.00060-18 (2019).
226. Schirmer, M. *et al.* Dynamics of metatranscription in the inflammatory bowel disease gut microbiome. *Nature microbiology* **3**, 337–346; 10.1038/s41564-017-0089-z (2018).
227. Tedjo, D. I. *et al.* The fecal microbiota as a biomarker for disease activity in Crohn's disease. *Scientific reports* **6**, 35216; 10.1038/srep35216 (2016).
228. Lee, C. *et al.* P926 *Blautia Obeum* Aggravates Colitis in a Murine Model. *Journal of Crohn's and Colitis* **17**, i1035-i1035; 10.1093/ecco-jcc/jjac190.1056 (2023).
229. Lo Presti, A. *et al.* Fecal and Mucosal Microbiota Profiling in Irritable Bowel Syndrome and Inflammatory Bowel Disease. *Frontiers in microbiology* **10**, 1655; 10.3389/fmicb.2019.01655 (2019).
230. Hall, A. B. *et al.* A novel *Ruminococcus gnavus* clade enriched in inflammatory bowel disease patients. *Genome medicine* **9**, 103; 10.1186/s13073-017-0490-5 (2017).
231. Rojas-Tapias, D. F. *et al.* Inflammation-associated nitrate facilitates ectopic colonization of oral bacterium *Veillonella parvula* in the intestine. *Nature microbiology* **7**, 1673–1685; 10.1038/s41564-022-01224-7 (2022).
232. Zhan, Z. *et al.* Overabundance of *Veillonella parvula* promotes intestinal inflammation by activating macrophages via LPS-TLR4 pathway. *Cell death discovery* **8**, 251; 10.1038/s41420-022-01015-3 (2022).

233. Strauss, J. *et al.* Invasive potential of gut mucosa-derived *Fusobacterium nucleatum* positively correlates with IBD status of the host. *Inflammatory bowel diseases* **17**, 1971–1978; 10.1002/ibd.21606 (2011).
234. Kato, K. *et al.* Randomized placebo-controlled trial assessing the effect of bifidobacteria-fermented milk on active ulcerative colitis. *Alimentary pharmacology & therapeutics* **20**, 1133–1141; 10.1111/j.1365-2036.2004.02268.x (2004).
235. Wang, W. *et al.* Increased proportions of Bifidobacterium and the Lactobacillus group and loss of butyrate-producing bacteria in inflammatory bowel disease. *Journal of clinical microbiology* **52**, 398–406; 10.1128/JCM.01500-13 (2014).
236. Brito, I. L. Examining horizontal gene transfer in microbial communities. *Nature reviews. Microbiology* **19**, 442–453; 10.1038/s41579-021-00534-7 (2021).
237. Kotula, J. W. *et al.* Programmable bacteria detect and record an environmental signal in the mammalian gut. *Proceedings of the National Academy of Sciences of the United States of America* **111**, 4838–4843; 10.1073/pnas.1321321111 (2014).
238. Schmidt, F., Cherepkova, M. Y. & Platt, R. J. Transcriptional recording by CRISPR spacer acquisition from RNA. *Nature* **562**, 380–385; 10.1038/s41586-018-0569-1 (2018).
239. Kurtz, C. B. *et al.* An engineered *E. coli* Nissle improves hyperammonemia and survival in mice and shows dose-dependent exposure in healthy humans. *Science translational medicine* **11**; 10.1126/scitranslmed.aau7975 (2019).
240. Taylor, N. P. Synlogic scraps ammonia-lowering drug after early phase fail. Available at <https://www.fiercebiotech.com/biotech/synlogic-scraps-ammonia-lowering-drug-after-early-phase-fail> (2019).
241. Moser, A. *et al.* ApcMin: A mouse model for intestinal and mammary tumorigenesis. *European Journal of Cancer* **31**, 1061–1064; 10.1016/0959-8049(95)00181-H (1995).
242. Lehr, H. A., Menger, M. D. & Granger, D. N. Ischemia-reperfusion injury: enthusiasm in laboratory research but dilemma in clinical trials? *Circulation* **90**, 1580 (1994).
243. Rogers, C. S. *et al.* Production of CFTR-null and CFTR-DeltaF508 heterozygous pigs by adeno-associated virus-mediated gene targeting and somatic cell nuclear transfer. *The Journal of Clinical Investigation* **118**, 1571–1577; 10.1172/JCI34773 (2008).
244. Chang, J. T. Pathophysiology of Inflammatory Bowel Diseases. *The New England journal of medicine* **383**, 2652–2664; 10.1056/NEJMra2002697 (2020).
245. Flisikowska, T. *et al.* A porcine model of familial adenomatous polyposis. *Gastroenterology* **143**, 1173-1175.e7; 10.1053/j.gastro.2012.07.110 (2012).
246. Rogalla, S. *et al.* Biodegradable fluorescent nanoparticles for endoscopic detection of colorectal carcinogenesis. *Advanced functional materials* **29**; 10.1002/adfm.201904992 (2019).

247. Flisikowski, K. *et al.* Wild-type APC Influences the Severity of Familial Adenomatous Polyposis. *Cellular and molecular gastroenterology and hepatology* **13**, 669-671.e3; 10.1016/j.jcmgh.2021.11.002 (2022).
248. Jorissen, R. N. *et al.* Wild-type APC predicts poor prognosis in microsatellite-stable proximal colon cancer. *British journal of cancer* **113**, 979–988; 10.1038/bjc.2015.296 (2015).

## Acknowledgement

Ich möchte mich von ganzem Herzen bei Prof. Angelika Schnieke für die kontinuierliche Unterstützung, sowohl in professioneller als auch persönlicher Hinsicht, bedanken. Ich bin dankbar für die kritische Auseinandersetzung mit meinen Fortschritten und Plänen aber auch für die großartige Atmosphäre am Lehrstuhl. Besonderer Dank gilt auch Prof. Benjamin Schusser, der unseren Lehrstuhl als kommissarischer Gruppenleiter übernommen und mich mit vollem Einsatz bei meinen Zukunftsplänen unterstützt hat.

Ein großes Dankeschön geht selbstverständlich auch an unsere wichtigsten Labormitarbeiter Lea, Alex, Peggy, Bärbel, Kristina, Marlene, Sara, Johanna, Monika und Sulith! Die Zusammenarbeit mit euch und eure Freundschaft haben meinen Aufenthalt am Lehrstuhl unvergesslich gemacht.

Außerhalb des Labors möchte ich dem gesamten Ampertshausen-Team, vor allem aber Viola und Steffen für die großartige Zusammenarbeit am Tier danken. Euer unermüdlicher Einsatz und der dabei nie verloren gegangene Humor haben mich motiviert selbst über meine Grenzen hinauszugehen. Danke auch für die großartigen Grillabende und den lehrreichen Ausflug zu euren Honigbienen!

I would also like to extend my heartfelt appreciation to all former and current Ph.D. students and Postdocs at the BTN and BTR chairs. In particular, I would like to thank my friends Bernhard, Wei, Krzysztof, Tatiana, Dave, Aga, Theresa, and Laura (& Alex), who have been a tremendous source of support during my time at the chair, especially during our free time. I will never forget the memories we made while lifting, hiking, swimming, climbing, cycling, cooking and forging our current and future careers in the Bierstüberl until dawn. Special thanks also to Mohammed, Hicham, and Tom for mentoring me regarding current steps and future milestones.

I am grateful to Sevanna, Eva, Mo, Adam, Nico, Amira, and Dirk from the Chair of Nutrition and Immunology for their continuous intellectual support and enriching discussions.

Chciałbym również podziękować mojemu mentorowi, Krzysztof, i jego wspaniałej żonie Tatianie, którzy wspierali mnie swoją wiedzą techniczną, intelektualnymi dyskusjami, a także Lebensweisheiten, własnymi doświadczeniami i możliwością przedyskutowania moich nieskończonych opcji.

Z całego serca dziękuję mojej rodzinie, czy to w Polsce, Niemczech, Irlandii Północnej czy Bułgarii. Dziękuję, że zawsze mogę na was liczyć/Von ganzem Herzen möchte ich mich bei meiner Familie bedanken, egal ob in Polen, Deutschland, Nordirland oder Bulgarien. Danke, dass ich immer auf euch zählen kann/От цялото си сърце искам да благодаря на семейството си, независимо дали е в Полша, Германия, Северна Ирландия или България. Благодаря ви, че винаги мога да разчитам на вас.

Das größte Dankeschön geht an meine Lea - mit deiner wunderbaren Art hast du mir jeden noch so stressigen Tag verschönert. Danke, dass du mich immer unterstützt und ich dich zum Lachen bringen darf.

Abschließend möchte ich den Beitrag von Tieren in Forschung und Lehre würdigen.

# Curriculum Vitae

## Persönliche Daten

- Name: Thomas Winogrodzki
- Geburtsdatum: 31.01.1992
- Geburtsort: Weißenburg i. Bay., Deutschland

## Ausbildung

- 2019-2023  
Lehrstuhl für Biotechnologie der Nutztiere, TU München, Freising-Weihenstephan, Deutschland  
**Promotion in der Nutztierbiotechnologie**  
Betreuerin: Prof. Angelika Schnieke, PhD  
Integrated Research Training Group of CRC1371  
Dissertation: "The generation and characterisation of a physiologically relevant porcine model of inflammatory bowel disease "
- 2016-2019  
TU München, Freising-Weihenstephan, Deutschland  
**M. Sc., Molekulare Biotechnologie**  
Thesis: "Optimierung des Gen-Targeting durch CRISPR/Cas9 unter Verwendung somatischer Zellen des Schweins".
- 2012-2015  
TU München, Freising-Weihenstephan, Deutschland  
**B. Sc., Molekulare Biotechnologie**  
Thesis: "Charakterisierung von ABA-Korezeptoren in *Populus*".

## Publikationen

- **Winogrodzki**, Metwaly, et al., "TNFΔARE pigs: a translational Crohn`s Disease model". *Journal of Crohn's and Colitis*, 2023; jjad034, <https://doi.org/10.1093/ecco-jcc/jjad034>
- Flisikowski, ... , **Winogrodzki**, ..., Schnieke. "Wild-type APC Influences the Severity of Familial Adenomatous Polyposis". *Cell Mol Gastroenterol Hepatol*. 2022;13(2):669-671.e3. doi: 10.1016/j.jcmgh.2021.11.002
- Preisinger, D., **Winogrodzki, T.**, et al., Genome Editing in Pigs. In: Saunders, T.L. (eds) *Transgenesis. Methods in Molecular Biology*, vol 2631. Humana, New York, NY, 2023. [https://doi.org/10.1007/978-1-0716-2990-1\\_19](https://doi.org/10.1007/978-1-0716-2990-1_19)

- Just, S., Mondot, S., Ecker, J. *et al.* "The gut microbiota drives the impact of bile acids and fat source in diet on mouse metabolism". *Microbiome* 6, 134 (2018).  
<https://doi.org/10.1186/s40168-018-0510-8>  
(Anerkannt als studentische Unterstützung)

### **Konferenzen/Präsentationen**

- *TNF<sup>ΔARE</sup>* pigs: a translational Crohn`s Disease model"  
Posterpräsentation auf der Digestive Disease Week 2023, Chicago, USA (Mai 2023)
- "TNF<sup>ΔARE</sup> pigs: a translational Crohn`s Disease model"  
Vortrag und Posterpräsentation auf der 4. Meeting of the Ghent Gut Inflammation Group, Gent, Belgien (Februar 2023)
- "A porcine model of inflammatory bowel disease"  
Vortrag und Posterpräsentation auf der Konferenz "Pigs in Biomedical Research" 2022, Madison, WI, USA (ausgezeichnet mit 1000 \$ Rednerpreis)
- "A porcine model of IBD"  
Posterpräsentation auf der Seeon-Konferenz 2022, Seeon, Deutschland
- "Red Meat Allergy – development and impact of microbiome in α-1,3-Gal-knockout pigs"  
Elevator Pitch und Posterpräsentation am 5. HEFagrar PhD Symposium 2019 (ausgezeichnet als bester Elevator Pitch)
- "Does size matter? Pig models for microbiome research"  
Vortrag beim ZIELklaus Nutrition & Microbiome 2019
- Verschiedene Vorträge und Posterpräsentationen bei CRC1371-internen halbjährlichen Treffen

### **Lehrerfahrung**

- Supervisor für "Einführung in die Kultivierung von Säugetierzellen" - halbjährliches Studentenpraktikum
- Supervisor für "Assistierte Reproduktionstechnologie" - halbjährliches Studentenpraktikum
- Supervisor für "Epigenetik" Studentenpraktikum
- Supervisor von 3 Bachelor- and Masterstudenten
- Bezahlte Nachhilfe für Schüler aller Schularten, Fächer und Klassenstufen bis zum Abitur bei der Schülerhilfe Nachhilfe, München (2017-2018)

### Praktika und Hilfwissenschaftlertätigkeiten (HiWi)

- 2018-2019  
**Lehrstuhl für Ernährung und Immunologie**, TU München, Freising-Weihenstephan, Deutschland  
HiWi für Dr. Eva Rath  
*Mt-UPR in Mausmodellen chronisch-entzündlicher Darmerkrankungen (qPCRs, immunoblotting, IHC, ex vivo enteroid Kulturen)*
- 2017  
**Institut für neuronale Zellbiologie**, TU München, München, Deutschland  
HiWi für Dr. Leanne Godinho und Prof. Thomas Misgeld  
*Genotypisierung neuer Mauslinien und live cell imaging.*
- 2016  
**Clariant AG**, Planegg, Deutschland  
Praktikum im Bereich des Genome Engineerings von *Bacillus subtilis* (Dr. Helge Jochens)  
*Arbeit an Projekten zur Steigerung des Sekretionsvolumens von rekombinanten Proteinen und zur Vermeidung der gleichzeitigen Sekretion von Proteasen in B. subtilis-Produktionsstämmen*

### Nebentätigkeiten

- 2006-2016: Maurer, Metzger, Rettungsschwimmer, Kinomitarbeiter, Ladendekorateur, Kellner, Reifenmonteur, PR-Mitarbeiter, Küchenhilfe, Tellerwäscher, Nachhilfelehrer, Werkhofsarbeiter, Zusteller, Nebendarsteller in Werbespots und Unterhaltungssendungen, Pizzabäcker

### Ehrenamt

- Buddy Programm der TUM  
*Austauschstudenten dabei helfen, sich in München zurechtzufinden (2014 - 2015)*
- Mentor für Arbeiterkind.de  
*Unterstützung für (angehende) Studierende, die als erste in ihrer Familie eine akademische Karriere anstreben (seit 2021)*
- TUM Senior PhD buddy  
*Unterstützung von neuen Doktoranden bei der Bewältigung ihres Promotionsstudiums (seit 2021)*
- Stellvertretender Sprecher der Promovierenden und Mitglied im Graduiertenrat an der TU München.  
*Vertretung der Mitglieder des Graduiertenzentrums für die School of Life Sciences an der TU München-Weihenstephan (2021-2023).*